EXPERIMENTS IN TURBULENT BUNDLE FLOWS

by

SURESH KUMAR SITARAMAN

A thesis
presented to the University of Ottawa
in fulfillment of the
thesis requirement for the degree of
MASTER OF APPLIED SCIENCE
in
MECHANICAL ENGINEERING

ISBN 0-315-30949-0

ABSTRACT

An experimental study of a single-phase, isothermal, turbulent water flow through a model of the 37-rod CANDU PHW reactor bundle is presented. Measurements were conducted in the entrance, developing and fully developed regions of the bundle model. The study was focussed mainly on the central square subchannel with a pitch over diameter ratio equal to 1.14.

In the first phase of the research, experiments were carried out in a single bundle model with bare rods at Reynolds numbers of 50000 and 62000. Measured quantities include mean static pressure, mean streamwise velocity, wall shear stress and turbulence characteristics such as turbulence intensities, turbulent shear stresses, autocorrelation coefficients, length scales, probability density functions and certain derivative statistics of the streamwise and transverse velocity fluctuations.

In the second phase of the research, experiments were conducted at a Reynolds number of 45000 in the test-bundle preceded by another bundle model with different orientation. Mean streamwise velocity, mean static pressure and wall shear stress were measured.

It is found that mean velocity profiles, turbulence intensities and friction factor in the central square subchannel are comparable to those in a pipe flow, and that the transverse turbulence intensity is about 60% of the streamwise turbulent intensity, as in other turbulent shear flows. The eddy viscosity, estimated using gradient transport model, is typically one or two orders of magnitude larger than the kinematic viscosity. Integral length scales and Taylor microscales are about 20-30% and 5-8% of the square subchannel hydraulic diameter respectively. The presence of a misoriented upstream bundle enhances faster attainment of fully developed conditions in the test-bundle.

ACKNOWLEDGEMENTS

It is with pleasure that I express my gratitude to Dr. S. Tavoularis for his invaluable guidance and supervision throughout the work. His encouraging words, especially during my frustrating moments with hot-film probes, are greatly appreciated. Also, I am thankful to him for perusing the manuscript and providing numerous comments which contributed significantly to the quality.

I thank Dr. E. Stapountzis for helping me get acquainted with the operation of the system in the initial stage of the researcn and Dr. P. Prinos who worked with me in the final phase. Frequent interactions with the staff at the Advance Engineering Branch and the Thermalhydraulics Development Branch of the Atomic Energy of Canada Limited, Chalk River Nuclear Laboratories, Chalk River, Ontario, were also essential; a special mention is due to Mr. D. F. D'Arcy for his constructive suggestions and feedback on our project reports.

Thanks are also due to Messrs. L. Boukhriss, O. Dalnoki, J. Zika and G. Spak for constructing and implementing later modifications in the experimental facility. The general assistance provided by Mr. D. Seaman, whenever sought, is gratefully acknowledged.

The research was funded by the Atomic Energy of Canada Limited.

NOMENCLATURE

A	test-section flow cross-section
A_{FC}	flow-cell flow cross-section
a	flow-cell radial coordinate
D_h	test-section hydraulic diameter
d	rod diameter
d_p	circular pipe diameter, pressure tube diameter
dA	elementary area of flow-cell
E_1, E_2	anemometer output voltages
e_1, e_2	fluctuating anemometer output voltages
f	friction factor
f_p	circular pipe friction factor
L	bundle length
L_u, L_v	test-section axial, radial Eulerian integral length scales along axial direction
P	static pressure, probability density
p	pitch to diameter ratio (s/d)
Q	volume flow rate
R	test-section radius
R_u, R_v	spatial autocorrelation coefficients of test-section axial, radial fluctuating velocities along axial direction
$\mathcal{R}_u, \mathcal{R}_v$	temporal autocorrelation coefficients of axial, radial fluctuating velocities
R_λ	turbulence Reynolds number
r	test-section radial coordinate

Re_{bh}	square subchannel equivalent-pipe Reynolds number
Re_{bp}	circular pipe Reynolds number
Re_{bs}	square subchannel Reynolds number
Re_{bt}	test-section Reynolds number
s	pitch distance
T	temperature
T_f	fluid temperature
T_{op}	hot-film operating temperature
t	time
U, V, W	test-section axial, radial, peripheral velocity components
U_{bh}	square subchannel equivalent-pipe bulk velocity
$U_{b\ell}$	elementary area bulk velocity
U_{bp}	circular pipe bulk velocity
U_{bt}	test-section bulk velocity
U_c	subchannel centreline velocity, pipe centreline velocity
U_J	water-jet velocity (calibration), air-jet velocity (yaw-effect test)
U_x, U_a, U_ϕ	flow-cell axial, radial, peripheral velocity components
u, v, ω	test-section axial, radial, peripheral fluctuating velocities
u_x, u_a, u_ϕ	flow-cell axial, radial, peripheral fluctuating velocities
u^*	friction velocity
u_+	dimensionless velocity
x	test-section (or flow-cell) axial (streamwise) coordinate
y	radial distance from the rod surface
y_h	hydraulic diameter of elementary area

y_o	radial distance from the rod surface to the line of symmetry

GREEK SYMBOLS

α	separation distance along axial direction
Δp	pressure difference between Preston tube and static pressure hole
ϵ	dissipation rate
η_K	Kolmogoroff's length scale
λ_u, λ_v	test-section axial, radial Taylor microscales
μ	dynamic viscosity
ν	kinematic viscosity
ν_K	Kolmogoroff's velocity scale
ν_T	eddy viscosity
$\nu_{Ta}^{u_x}, \nu_{T\phi}^{u_x}$	flow-cell radial, peripheral eddy viscosities of axial momentum
$\nu_{Tr}^{u}, \nu_{T\psi}^{u}$	test-section radial, peripheral eddy viscosities of axial momentum
ψ	test-section peripheral coordinate
ρ	water density, correlation coefficient
σ	standard deviation
τ	separation time
τ_K	Kolmogoroff's time scale
τ_ω	wall shear stress
ϕ	flow-cell peripheral coordinate

SUBSCRIPTS AND SUPERSCRIPTS

$(\ )_{av}$	representation of subchannel or flow-cell average
$\overline{(\ )}$	representation of time-averaged value
$(\ )'$	representation of root mean square value

CONTENTS

LIST OF TABLES

LIST OF FIGURES

Chapter I

INTRODUCTION

1.1 GENERAL BACKGROUND

From the time it was known that sustained chain reaction of nuclear fission could produce enormous amount of energy, man has attempted to harness that energy for various purposes; today, the nuclear power is regarded as an important alternative to conventional modes of electricity production in several parts of the world, where other resources are scarce or fast depleting. With the progress and spread of commercial nuclear technology, nuclear reactors have undergone significant modifications over the past four decades.

Nuclear reactors can be generally classified into Pressurized Water Reactors (PWRs), Boiling Water Reactors (BWRs), Gas Cooled Reactors (GCRs) and Pressurized Heavy Water Reactors (PHWRs), depending on the type and state of the coolant used in the reactor core. Both PWRs and BWRs, originally developed in the USA, have also been in West Germany, France, Japan and U.S.S.R. These reactors use enriched uranium as fuel and light water as moderator as well as as coolant (in liquid state in PWRs and in boiling state in BWRs). GCRs, developed in Britain and France, use unenriched uranium fuel moderated by graphite and cooled by carbon dioxide gas. The only standardized commercial model of PHWRs is the CANDU (CANada Deuterium Uranium) reactor, developed by the Atomic Energy of Canada Limited (AECL). CANDU reactors are widely known for their practical maturity and high performance capablities.

Figure 1 presents a typical 600 MW(e) CANDU Nuclear Power System. A large, horizontally-oriented cylindrical, stainless steel reactor vessel (Calandria) contains the cool, low pressure heavy water moderator. About 380 identical pressure tubes, containing the natural uranium fuel bundles and the pressurized (~9.6 MPa), high temperature heavy water coolant, pass through this reactor vessel. The pressure tubes, made of Zirconium alloy, are about 6 m long and 100 mm in diameter and have a wall thickness of 4 mm; each pressure tube contains a string of twelve 37-Rod fuel bundles (Figure 2) stacked end to end. The consecutive bundles in a fuel channel are randomly oriented. The coolant circuits essentially transfer heat from the fuel elements to steam generators to produce light water steam which is fed to the turbine-generator system to produce electricity.

The fuel bundle geometry used in the CANDU reactors has undergone significant evolution since the first reactor went into operation. The 7-rod fuel bundles used in the first reactor were subsequently replaced by 18-, 19- and 28-rod bundles in later reactors, and finally by 37-rod bundles in the recent reactors. In all bundles, the rods are mostly arranged in triangular or triangular and square arrays.

By increasing the number of fuel rods in a bundle, it is possible to increase the effective heat transfer to the coolant. This would, however, increase the flow resistance and thereby require more power to circulate the coolant. Also, with a denser packing of fuel rods, the circumferential variations of temperature would become more pronounced. These variations are predominantly important not only in estimating the heat transfer rate, but also in determining the fuel bundle lifetime based on thermal stresses, creep strain rates and corrosion rates. Further, the knowledge of temperature distribution around the fuel rods would help to eliminate hot-spots or dryout spots on any particular fuel rod. In order to evaluate the temperature variation around fuel rods, it is essential to study the turbulent flow structure in the various subchannels.

The radioactive environment inside the reactor, augmented with high operating pressure and temperature, makes in-situ experiments with the reactor in operation generally cumbersome and expensive. Collection of necessary information can be done easier using laboratory models simulating, as closely as possible, the actual reactor bundle.

Studies which are concerned with thermohydraulic aspects of the reactor would generally have to simulate the actual thermal environment in their models, using electrical or other source of heating; also, the operating pressure inside such models should simulate that in the actual pressure tube. The construction and operation of such models is tedious and expensive. As a first step in the determination of flow structure in reactor bundles, models which do not necessarily reproduce the actual thermal environment can be used; although it may be desirable to have the same operating pressure as in the actual reactor, the fluid pressure inside these models could be near atmospheric, since the flow structure would be least affected by the difference in pressure conditions. The experimental fluid could be light water or air, as long as the study is restricted to single-phase flow. Although the temperature, the pressure and the experimental fluid can be different from the actual ones, it is essential to keep other important flow parameters, mainly the Reynolds number, as closely as possible to those in the reactor bundle.

1.2 OBJECTIVES AND SCOPE OF THE CURRENT RESEARCH

The present research aims at collecting detailed information about the flow structure in an isothermal, water flow through a model of the 37-rod CANDU-PHW fuel bundle. The study is conducted in a double scale, 60° sector model of the bundle, at a mass flux rate approximating that in the actual reactor bundle. The choice of a 60° sector, instead of a full bundle, was made in order to reduce pumping requirements and materials for the test-section; the model was constructed at double-scale so as to facilitate probe traversing and measurement, especially in the narrow gaps between rods, and also to permit the generation of sufficiently large Reynolds number flow at relatively low water speeds. The current investigation also studies, in a limited scale, the effect of the orientation of an upstream bundle on the flow through the test bundle. During the planning of the study, it was proposed to employ the use of laser-Doppler anemometry and provide a mapping of the entire turbulent flow field, after matching the index of refraction of fluid with that of the model walls that were made of clear perspex (see section 4.2). For budgetary reasons, however, the study had to be done using the less expensive hot-film anemometry.

In the first phase of the research, measurements were conducted in a single bundle model, preceded and followed by empty sections. The bundle was supported on realistic endplates (Figures 8 and 9), but had no rod-spacers, wearpads and other geometrical complications encountered in reactor bundles. The centreplane distribution and the downstream evolution of mean pressure and mean axial velocity were measured using total and static pressure tubes; the azimuthal variation of wall shear stress around the periphery of representative rods was obtained with Preston tubes. Later an extensive study on the centreplane distribution and downstream evolution of mean axial velocity, turbulence intensities, correlation coefficients and length scales was done using hot-film anemometers. Measurements of univariate and bivariate probability density functions and some derivative statistics of the velocity fields were also conducted.

In the second phase of the research, a second 60° bundle model was placed upstream of the test bundle, such that the corresponding rods were rotated by 30° about the bundle axis, and also the endplates of both bundles were equipped with asymmetric radial ribs to simulate more accurately the actual fuel channel which contains a string of misaligned bundles. Few typical mean flow parameters were measured in the downstream bundle in order to evaluate the effect of the upstream bundle and radial ribs.

The motive behind the current investigation is to provide direct information about flow structure, which might help designers in understanding better the performance characteristics of the reactor system; thus, this information might contribute to improvements in the design and operation of future reactor bundles. Further, the present results, obtained in a simple, square subchannel, with symmetric entrance conditions and without wearpads and rod spacers, would contribute to the general knowledge about rod-subchannel flow, and in particular, could serve as test cases for computer codes which try to predict the distribution of various flow parameters in subchannels.

1.3 SURVEY OF LITERATURE ON BUNDLE FLOW STUDIES

1.3.1 Experiments in 37-Rod Bundle Models

The Advance Engineering Branch and the Thermalhydraulics Development Branch of the Atomic Energy of Canada Limited, Chalk River Nuclear Laboratories, Chalk River, Ontario, have been the chief investigators of the flow and thermalhydraulics aspects of turbulent flow through 37-rod bundle models. A comprehensive summary of all related projects has been compiled by Groeneveld (1984). The present section reviews mainly the studies on isothermal bundle flows, which are relevant to our work. Hackett (1984) has reported measurement of mean axial velocity in a single phase water flow using isokinetic sampling technique and has found that mean axial velocity distribution had a systematic variation along the centreplane, with maxima near subchannel centres and minima near rod gaps. The study also analyzes the effect of 30° and 15° misaligned upstream bundles on the mean axial velocity distribution of the downstream test bundle. Bugg (1984) has used a twin needle conductance probe to measure local void fraction and bundle velocity at representative locations in a two-phase, two-component (water and air) flow. D'Arcy and Schenk (1985) have conducted studies in bundles in tandem with misaligned rods and with misaligned endplates, using laser-Doppler anemometry, and have measured mean axial velocity and axial turbulent intensity in square, triangular and wall subchannels of the 37-rod bundle. Groeneveld (1984) reports measurements of axial pressure drop in a 37-rod bundle model facility, using separately water and Freon-12 as the operating fluids, aimed at evaluating the effects of deliberately introduced obstructions. An advanced subchannel computer code, capable of predicting flow and thermal conditions in the various subchannels of a CANDU reactor bundle, has also been developed at Chalk River Nuclear Laboratories (private communication).

In the initial stage of the current investigation, using essentially the same test-section facility, Tavoularis and Stapountzis (1983) have demonstrated the possiblity of studying flow mixing between subchannels, using flow visualization techniques. They concluded that interchannel mixing between adjacent subchannels could be enhanced by introducing small blockages into the flowstream. Experiments have also been carried out at Westinghouse Canada (private communication) in subsections of the 37-rod reactor bundle model, studying the velocity, shear stress and temperature distribution in a single phase water flow through a heated 6-rod, two square array bundle using laser-Doppler anemometry. Finally, a team at Ecole Polytechnique, Montreal (private communication), has measured local pressure, void fraction and mass flux in air and water flow through two identical interconnected square subchannels in vertical and horizontal orientations.

1.3.2 Experiments in Square Array Rod Bundles

The series of experiments conducted at Pacific Northwest Laboratory, Richland, Washington, appear to be the only main source of reference for flow through square array subchannels, that is available in the open literature. Rowe (1973) has measured the distribution of mean axial velocity, turbulence intensity and the Eulerian integral length scales in a turbulent water flow through square array rod bundles using laser-Doppler anemometry; those measurements were conducted at Reynolds numbers of 50000 and 200000. Using the same test-section and instrumentation, Rowe and Chapman (1973) have evaluated the effect of grid spacers on flow structure and on cross flow mixing between subchannels. They have also measured mean axial velocity, turbulence intensity and integral length scales at a Reynolds number of 100000. From their measurements, they concluded that the interchannel mixing was enhanced, to some extent, by the presence of grid spacers. Rowe et al. (1973), using the same test-section and equipment, have studied the effect of sleeve and plate type blockages on the flow structure, and found that the effects of these blockages persisted for relatively long downstream distances. The effect of varying pitch to diameter ratios (s/d) on turbulent flows through square arrays has been evaluated by Rowe et al. (1975); they measured mean axial velocity, axial turbulence intensity, autocorrelation functions and longitudinal integral length scales in arrays with s/d = 1.25 and 1.125 and at Reynolds numbers of 50000 and 200000. They concluded that a smaller rod gap spacing would increase turbulence intensity, integral length scale and dominant frequency of turbulence. They found these turbulent parameters to be independent of the Reynolds number of the flow. Creer et al. (1975, 1976 & 1979) studied flow through 7x7 bundle, consisting of only square arrays with flow blockages, and measured mean axial velocity and turbulence intensity in air and water flow using laser-Doppler techniques. Their experiments were conducted at Reynolds numbers between 14000 and 58000 for water flow and 10000 for air flow. They found that the results of the air tests were in excellent agreement with those obtained from water tests.

1.3.3 Experiments in Triangular and Other Bundle Geometries

Palmer and Swanson (1961) measured mean axial velocity distributions for air flow through a tricuspid channel with s/d = 1.015 at a Reynolds numbe of 20000 using a pitot tube and a kiel probe. Ibragimov et al. (1966), under the assumption that the effective turbulent transport of momentum was due to eddies of all sizes and also due to convective transport, developed a general semi-empirical expression for the distribution of wall shear stress in a straight, smooth channel using their experimental velocity velocity distribution (with pitot tubes) in eight arbitrarily shaped cross-sections. Nijsing et al. (1966) predicted theoretically mean axial velocity, wall shear stress and eddy viscosity distributions in a triangular subchannel. Using an adjustable test section, Eifler and Nijsing (1967) determined experimentally mean axial velocity distributions employing pitot tubes, and found that their results agreed well with their earlier theoretical predictions; their measurements were conducted in triangular arrays with s/d = 1.05, 1.10 and 1.15 at Reynolds numbers of 15000, 30000 and 50000. Levchenko et al. (1967), using air flow through a triangular array with s/d = 1.00, showed that the peripheral variation of wall shear stress remained independent of Reynolds number, in the range between 14000 and 95000, and that velocity distributions measured along normals to the wall were in good agreement with experimental data on circular pipes.

Turbulence measurements in rod bundles were first reported by Kjellstrom (1971) in his comprehensive study on flow through triangular arrays with s/d = 1.217. Besides wall shear stress (with Preston tubes), he measured axial and secondary flow velocities, turbulence intensities and Reynolds stresses using constant temperature hot-wire anemometry at Reynolds numbers of 149000, 271000 and 355000. He found that secondary velocities were less than 1% of the average axial velocity. A detailed study by Trupp and Azad (1975) reports measurements of friction factors, local wall shear stresses and the distributions of mean axial velocity, Reynolds stresses and eddy diffusivities in isothermal air flows through triangular array rod bundles, with s/d = 1.2, 1.35 and 1.50, using static pressure tubes, Pitot tubes, Preston tubes and hot-wire anemometry; their experiments were performed at Reynolds numbers ranging from 12000 to 84000. Fakory and Todreas (1979) concluded from their measurements in a triangular array of s/d = 1.1 using Preston tubes that the local wall shear stress around the rod periphery peaked in the largest flow area.

Several researchers have analyzed interchannel mixing using various techniques. Among them, Rogers and Todreas (1968) have identified turbulent interchange as the basic natural mixing mechanism between rod bundle subchannels. Tahir and Rogers (1975, 1979) have conducted an experimental investigation of turbulent mixing of air in a triangular array by a gas tracer (ethane) technique, and proposed turbulent interchange correlations for three basic (square-square, square-triangular and triangular-triangular) arrays. They have concluded that at small clearance to diameter ratios, secondary flows and large scale eddies enhance turbulent interchange by reducing the mixing distance.

The anisotropic nature of turbulence in closely packed rod bundles has been demonstrated by a few authors. Rehme (1978, 1980, 1982), using his measurements in wall and central square subchannels with s/d = 1.07 at a Reynolds number of 87000, has shown that the peripheral eddy viscosity is at least one order of magnitude higher than the radial eddy viscosity. Tahir and Rogers (1986) have confirmed this claim from their experiments conducted in air flow through triangular arrays with s/d = 1.06 at a Reynolds number of 36000.

Chapter II

BACKGROUND INFORMATION ON MEASURED PARAMETERS

2.1 HYDRAULIC DIAMETER AND BULK QUANTITIES

A common simplification in the study of flow through channels and ducts with non-circular cross-sections is to consider a circular pipe flow with equivalent flow characteristics. The diameter of such a pipe is called hydraulic diameter, and is normally defined as four times the channel cross-sectional area divided by its wetted perimeter. Obviously, this approach cannot describe peripheral variation of various parameters, as it can only provide a rough estimate of the average variation of such parameters along the channel. However, such a description may be useful as a reference for comparisons with measurements in the actual geometry.

For the test-section used in the current investigation (Figure 3; detailed description is given in section 4.2.), the equivalent pipe hydraulic diameter, D_h, is

$$D_h = \frac{\pi\,(4R^2 - 37d^2)}{2R\,(6+\pi) + d\,(37\pi - 30)} \qquad (2\text{-}1)$$

where **R** is the nominal radius of the test-section and **d** is the diameter of the bundle rod.

For a square subchannel (Figure 3), the hydraulic diameter, d_h, is

$$d_h = d\left(\frac{4p^2}{\pi} - 1\right) \qquad (2\text{-}2)$$

where p is the pitch to diameter ratio (s/d).

In a bundle flow, the flow through individual subchannels is described primarily by the local flow conditions. Nevertheless, parameters averaged over the entire test-section can be useful as a reference. The test-section bulk velocity can be defined as

$$U_{bt} = \frac{Q}{A} \qquad (2\text{-}3)$$

where Q is the total flow rate through the test-section and A is its flow cross-section area. For any section with uniform flow cross-section area, U_{bt} is constant along the streamwise direction.

The Reynolds number, which represents the ratio between the inertial forces and viscous forces, is the most commonly used dimensionless parameter to characterize a flow. For the test-section, a Reynolds number can be estimated as

$$Re_{bt} = \frac{U_{bt}\ D_h}{\nu} \qquad (2\text{-}4)$$

where ν is the kinematic viscosity of the fluid.

A rough estimate of the subchannel Reynolds number can be based on the test-section bulk velocity, as

$$Re_{bs} = \frac{U_{bt}\ d_h}{\nu} \qquad (2\text{-}5)$$

However, a consistent definition of the subchannel Reynolds number should be based on the subchannel bulk velocity, U_{bh}, which may be somewhat different from U_{bt}, such that

$$Re_{bh} = \frac{U_{bh}\, d_h}{\nu} \qquad (2\text{-}6)$$

Although U_{bh} cannot be measured exactly in the present facility, it can be estimated from measured local parameters, such as the friction velocity and the centreline mean velocity, using the universal velocity profile equations developed for fully developed, turbulent pipe flow. A detailed discussion on the estimation of U_{bh} is provided in later sections.

Another simplification in the study of subchannels is the division of subchannels into geometrically identical flow-cells. A square subchannel can be divided into eight identical isosceles triangular flow-cells similar to the one shown in Figure 4. Although all flow-cells are geometrically equal, a slight variation in the flow within different cells might be expected, if they are adjacent to different bundle subchannels. It must be noted that each flow-cell has the same hydraulic diameter as the square subchannel. Thus, in an ideal flow situation, the bulk velocity and the streamwise mean pressure drop should be the same for both; hence, the average quantities defined for the square subchannel would also apply to each flow-cell.

For the flow-cell shown in Figure 4, the basic dimensions can be evaluated using simple trigonometry. Defining y_o as the radial distance from the wall surface to the line of symmetry and ϕ as the peripheral angle measured in the counterclockwise direction, it can be shown that

$$y_o(\phi) = \frac{d}{2}\left(\frac{p}{\cos\phi} - 1\right) \tag{2-7}$$

Obviously, $y_{o\,min}$ corresponds to $\phi = 0$ and $y_{o\,max}$ to $\phi = \pi/4$. An average radial distance from the rod surface to the line of symmetry, $y_{o\,av}$, can then be determined as

$$\begin{aligned} y_{o\,av} &= \frac{1}{\phi_{max}}\int_0^{\phi_{max}} \frac{d}{2}\left(\frac{p}{\cos\phi} - 1\right) d\phi \\ &= \frac{d}{2}\left(\frac{4p}{\pi}\ln(\sqrt{2}+1) - 1\right) \end{aligned} \tag{2-8}$$

Dividing the flow-cell into elementary areas, dA one can define a local hydraulic diameter as,

$$y_h(\phi) = d\left(\frac{p^2}{\cos^2\phi} - 1\right) \tag{2-9}$$

The local hydraulic diameter increases monotonically from a minimum $d(p^2-1)$ at the rod gaps ($\phi = 0$) to a maximum $d(2p^2-1)$ at the subchannel center ($\phi = \pi/4$).

The average local hydraulic diameter of all elementary areas in the the flow-cell, defined as

$$y_{h_{av}} = \frac{1}{\phi_{max}}\int_0^{\phi_{max}} y_h(\phi)\, d\phi = d\left(\frac{4p^2}{\pi} - 1\right) \tag{2-10}$$

is equal to the hydraulic diameter, d_h, of the square subchannel, defined by equation (2.2).

2.2 · WALL SHEAR STRESS DISTRIBUTION

Wall shear stress is defined as the tangential force, created by a fluid flowing over a solid surface per unit area. For Newtonian fluids it is expressed as

$$\tau_w = \mu \left.\frac{\partial \bar{U}}{\partial y}\right)_{y=0} \qquad (2\text{-}11)$$

where μ is the dynamic viscosity of the fluid and $\partial \bar{U}/\partial y$ is the mean velocity gradient normal to the wall surface.

In a circular pipe, the wall shear stress is uniform around the perimeter and the total drag force exerted on a circular pipe of diameter, d_p, over a short streamwise length, Δx, will be equal to $(\tau_w)(\pi d_p)(\Delta x)$. In a steady flow, this force is proportional to the pressure drop, ΔP, along the pipe. Equating the drag force to the pressure force, one gets

$$(\tau_w)(\pi d_p)(\Delta x) = \left(\frac{\pi d_p^2}{4}\right)\left(-\Delta P\right)$$

and hence,

$$\tau_w = \frac{d_p}{4}\left(\frac{-\Delta P}{\Delta x}\right) \qquad (2\text{-}12)$$

When Δx is sufficiently small ($\Delta x \to 0$), the above equation is simplified to

$$\tau_w = \frac{d_p}{4}\left(\frac{-\partial P}{\partial x}\right) \qquad (2\text{-}13)$$

Unlike in a circular pipe flow, the local wall shear stress in a rod bundle subchannel varies around its periphery. For the square subchannel shown in Figure 3, an average wall shear stress, $\tau_{w_{av}}$, can defined as the average value of the local wall shear stress over the entire wetted perimeter. Alternatively, $\tau_{w_{av}}$, is equal to the total drag force per unit streamwise length, divided by the wetted perimeter. The average wall shear stress can be estimated from an average streamwise pressure gradient, using equivalent-pipe principle as (e.g. Davies, 1972),

$$\tau_{w_{av}} = \frac{d_h}{4}\left(-\frac{\partial P}{\partial x}\right)_{av} \qquad (2-14)$$

It should be recalled that any average value of a parameter defined or estimated for the entire square subchannel should, in principle, be equal to the average value for each flow-cell, and therefore, no distinction will be made between these values throughout the current study.

Several relations are available for the description of the local wall shear stress distribution around the rod periphery in various geometries. Ibragimov et al. (1966) have suggested the semi-empirical relation,

$$\frac{\tau_w(\phi)}{\tau_{w_{av}}} = C\left(1 - e^{X^{-\frac{7.7}{0.8}} \cdot \frac{y_o(\phi)}{y_{o\,av}}}\right) \qquad (2-15)$$

where $$X = \frac{A_{FC}}{y_{o_{av}}^2}$$

and

$$\frac{1}{C} = \frac{1}{\phi_{max}} \int_0^{\phi_{max}} \left(1 - e^{x^{-\frac{7.7}{0.8} \cdot \frac{y_o(\phi)}{y_{o\,av}}}} \right) d\phi$$

where A_{FC} is the flow cross-section of the flow-cell. This relationship is applicable to the distribution of local wall shear stress around the periphery of any arbitrarily shaped cross-section.

Another available relation,

$$\frac{\tau_w(\phi)}{\tau_{w\,av}} = 1 - 1.0073 \cos 6\phi - 0.1059 \cos 12\phi + 0.0991 \cos 18\phi + 0.0318 \cos 24\phi \qquad (2\text{-}16)$$

developed by Levchenko et al. (1967) using experimental data in a triangular array with s/d = 1, may not be accurate in square arrays.

2.3 FRICTION FACTOR DISTRIBUTION

Two parameters closely associated with the study of wall shear stress are friction velocity and friction factor. Friction velocity, also known as shear stress velocity, is a common scaling parameter in the description of various velocity profiles, and is defined as

$$u^* = \left(\frac{\tau_w}{\rho} \right)^{1/2} \qquad (2\text{-}17)$$

Friction factor, on the other hand, is a dimensionless measure of wall shear stress. For a smooth wall surface and a given cross-sectional shape, it depends only on the Reynolds number of the flow, and is particularly useful as a basis for comparison of flows in pipes and channels of different sizes and shapes. For a circular pipe, the friction factor (D'Arcy) is defined as (e.g. Hinze, 1975)

$$f_p = \frac{8\tau_w}{\rho U_{bp}^2} \qquad (2\text{-}18)$$

where U_{bp} is the bulk velocity in the pipe. u^* and f_p can be related to the streamwise pressure gradient, using equations (2-13), (2-17) and (2-18), as

$$u^* = \left[\frac{d_p}{4\rho}\left(-\frac{\partial P}{\partial x}\right)\right]^{1/2} \qquad (2\text{-}19)$$

$$f_p = \frac{2 d_p}{\rho U_{bp}^2}\left(-\frac{\partial P}{\partial x}\right) \qquad (2\text{-}20)$$

Friction factor in a smooth circular pipe can be estimated for a given flow Reynolds number, using empirical relations, such as (e.g. Reynolds, 1974)

(1) Blasius equation :

$$f_p = 0.316\, Re_{bp}^{-0.25} \qquad (2\text{-}21)$$

for $Re_{bp} < 100000$.

(2) Karman-Nikuradse Law of Friction :

$$\frac{1}{\sqrt{f_p}} = 0.87 \ln\left[\frac{Re_{bp}\sqrt{f_p}}{2}\right] - 0.2 \qquad (2\text{-}22)$$

$$3000 < Re_{bp} < 3000000,$$

where $Re_{bp} = \frac{U_{bp}\ d_p}{\nu}$.

In a circular pipe flow, friction velocity and friction factor are essentially constant around the periphery. In a rod bundle subchannel, however, the friction velocity and the friction factor vary around the subchannel periphery. For the square subchannel (Figure 3), one can define u^*_{av} and f_{av} , as the average values of local friction velocity and the local friction factor, respectively, over the entire wetted perimeter. It can be shown following equivalent-pipe principle (e.g. Tennekes and Lumley, 1972), that

$$u^*_{av} = \left(\frac{\tau_{w\,av}}{\rho} \right)^{1/2} \qquad (2\text{-}23)$$

and

$$f_{av} = \left(\frac{8\,\tau_{w\,av}}{\rho\ U_{bh}^2} \right) \qquad (2\text{-}24).$$

In the current investigation, the distribution of local wall shear stress, $\tau_w(\phi)$, was experimentally determined. In incompressible flow, the variation of local friction velocity, $u^*(\phi)$, can be directly determined as

$$u^*(\phi) = \left(\frac{\tau_w\ (\phi)}{\rho} \right)^{1/2} \qquad (2\text{-}25)$$

The local friction factor, $f(\phi)$, cannot be easily determined from $\tau_w(\phi)$, since it involves another unknown quantity, $U_{b\ell}$, the local bulk velocity of the elementary area, dA, as (Nijsing et al., 1966)

$$f(\phi) = \frac{8\tau_w(\phi)}{\rho U_{b\ell}^2} \tag{2-26}$$

Only few investigators have been able to estimate the local friction factor variation in a rod bundle subchannel; empirical equations are available mostly for determining the average friction factor. Ibragimov (1967) postulates that

$$\frac{f_{av}}{f_p} = \left(0.58 + 0.42\, e^{-0.021 K^3}\right) \times \left(1 + 0.1\,(\beta+1)^{4/3}\right) \tag{2-27}$$

where f_p is the friction factor of a circular pipe at the same Reynolds number and K is a geometrical factor, defined as

$$K = \frac{y_{o\,max} - y_{o\,min}}{y_{o\,av}} \left(\frac{A_{FC}}{y_{o\,av}^2}\right)^{0.25}$$

and

$$\beta = \pm \frac{2\, y_{o\,av}}{d}$$

with + for a concave surface and - for a convex surface.

Subbotin et al. (1971) suggest another expression as

$$\frac{f_{av}}{f_p} = 0.57 + \frac{s}{d}\left(1 - e^{-112(s/d - 1)}\right)\left(\log \frac{s}{d}\right)^{0.27\frac{s}{d}} \tag{2-28}$$

for $1.0 < s/d < 1.22$

Trupp and Azad (1975) provide a least square fit equation from their experimental data as

$$f_{av} = C\, Re_{bh}^{-n} \qquad (2\text{-}29)$$

for $1.2 < s/d < 1.50$ and $10000 < Re_{bh} < 100000$

where

$$C = 0.287 \left(\frac{d_h}{d} - 0.30 \right)^{-1/2}$$

and

$$n = 0.368 \left(\frac{s}{d} \right)^{-1.358}$$

2.4 MEAN VELOCITY DISTRIBUTION

In bounded turbulent flows, the region close to the wall (wall layer) is characterized by the suppression of turbulence and contains large velocity gradients. The wall layer is commonly subdivided into a 'viscous (pseudo-laminar) sublayer', immediately adjacent to the wall, and a 'buffer layer' between the viscous sublayer and the outer region.

In the viscous sublayer, the velocity profile is approximately linear and viscous forces are dominant. In the buffer layer, the viscous stresses and Reynolds stresses are of the same order of magnitude. In the outer region, the flow is fully turbulent and the Reynolds stresses outweigh viscous stresses; in the outer region, the velocity profile is nearly logarithmic and, for this reason, this region is also called the 'logarithmic layer'.

The mean velocity distribution within the three regions has been determined by several authors, both theoretically and experimentally. A common practice is to define a dimensionless velocity as $u_+ = \overline{U}/u^*$ and a dimesionless distance from the wall as $y_+ = yu^*/\nu$. The following mean velocity profiles are generally acceptable for large Reynolds number, turbulent boundary layers over smooth walls (see e.g. Reynolds, 1974 and Hinzè, 1975).

(1) Viscous Sublayer

$$u_+ = y_+ \qquad 0 < y_+ < 5$$

(2) Buffer Layer

$$u_+ = 5.00 \ln y_+ - 3.05 \qquad 5 < y_+ < 30 \tag{2-30}$$

(3) Logarithmic Layer

$$u_+ = 2.5 \ln y_+ + 5.5 \qquad y_+ > 30$$

The expression presented for the buffer layer is due to von Karman; several alternative relations have been suggested for the buffer layer by Rannie, Diessler, Reichardt, Hanna and van Driest. The constants (2.5, 5.5) of the logarithmic layer expression are those determined by Nikuradse from his experiments in pipe flow (e.g. Reynolds, 1974; Hinze, 1975).

From a practical engineering point of view, the logarithmic velocity profile represents fairly accurately the actual velocity profile, even when applied near the core region of a pipe flow. The exact velocity near the centre of the pipe, however, is slightly higher than the predicted velocity. Improved estimates, known as velocity defect laws, can be obtained by adding a correction function to the logarithmic profile. For example, the velocity defect law, based on Coles' (1956) wake function, is written as (e.g. Tennekes and Lumley, 1972)

$$\overline{U} = \overline{U}_c + u^* \left[2.5 \ \ln \frac{2y}{d_p} - 1 + \frac{1}{2} \left(\sin \pi \left(\frac{2y}{d_p} - \frac{1}{2} \right) + 1 \right) \right] \qquad (2-31)$$

$\overline{U}_c$ in the above expression represents the centreline velocity in a circular pipe. Empirical expressions approximating the mean velocity distribution in the entire pipe are also available. The power law profile (e.g. Hinze, 1975), among the common ones, is written as

$$\frac{\overline{U}}{\overline{U}_c} = \left(1 - \frac{2y}{d_p} \right)^{1/n} \qquad (2-32)$$

where n = 6 at Re_{bp} = 4000, n = 7 at Re_{bp} = 100000, n = 9 at Re_{bp} = 1000000 and n = 10 at Re_{bp} = 3000000, according to the measurements by Nikuradse.

The bulk velocity through the pipe can be theoretically determined by integrating respective velocity profiles from wall surface to the centre of the pipe. A widely used rough estimate of the bulk velocity is (e.g. Tennekes and Lumley, 1972)

$$\frac{U_{bp}}{u^*} = 2.5 \ln \frac{d_p u^*}{2\nu} + 1.5 \qquad (2\text{-}33)$$

A more accurate estimate, relating the bulk velocity to the centreline mean velocity, is due to Karman and Nikuradse (e.g. Reynolds, 1974). This expression, which accounts for the velocity defect as well as for the variation of some of the constants with Reynolds number, is given as

$$U_{bp} = \overline{U}_c - \frac{3A}{2} u^* \qquad (2\text{-}34)$$

where A = 2.46, when Re_{bp} is in the range of about 3000-3000000, and A = 2.5, when Re_{bp} is higher than 1000000.

The circular pipe velocity profile equations (except the power law) and the resulting bulk velocity equations are based on the concept of universality of law of the wall and should be, in principle, applicable also to the square rod subchannel. However, a few important points must be considered before using the velocity profile equations in the subchannel.

In a pipe flow, the scaling parameter, i.e. the friction velocity, is constant around the periphery. Therefore, it is sufficient to determine the velocity profile along any one radius. In the square subchannel, however, the friction velocity varies around the periphery, and therefore, separate velocity profiles must be computed along each radial axis, at least for one flow-cell. The velocity field evaluated for one flow-cell can be used for all the other flow-cells of the subchannel, but only under the assumption that the subchannel is part of an infinite array of identical subchannels; in practice, of course, this condition is not satisfied.

In a circular pipe flow, all lines normal to the wall surface meet at the centre of the pipe, so that there is a unique centreline velocity. But in the square subchannel, the lines normal to the rod surface intersect the line of symmetry at different points. Therefore, the concept of unique centreline velocity is no longer valid for a subchannel flow, since individual centreline velocities corresponding to $y = y_o$ (Figure 4) have to be considered for each elementary area dA. Furthermore, since the hydraulic diameter of each elementary area varies, the parametrization of the problem also varies for each one of them.

The determination of the entire flow field in the square subchannel is clearly beyond the scope of the current undertaking. However, an overall estimate of the subchannel bulk velocity, U_{bp} , can be obtained by applying the equivalent-pipe principle to the entire subchannel. From the mean velocity at the geometrical centre of the subchannel, $\overline{U}_c$,and the average value of the friction velocity, u^*_{av} , the bulk velocity can be evaluated as

$$U_{bh} = \overline{U}_c - \frac{3A}{2} u^*_{av} \qquad (2-35)$$

where the value of A can be taken equal to that in equation (2-34).

2.5 TWO-POINT CORRELATIONS

The components of a general two-point correlation tensor in the Cartesian coordinate system (x_1, x_2, x_3) can be defined as

$$R_{ij}\,(\alpha_1, \alpha_2, \alpha_3; \tau) = \frac{\overline{u_i\,(x_k;t)\;u_j\,(x_k+\alpha_m;\,t+\tau)}}{u'_i\,(x_k)\,.\;\;u'_j\,(x_k+\alpha_m)} \qquad (2-36)$$

$$i,\; j,\; k,\; m = 1,\; 2,\; 3$$

Spatial correlations are obtained when τ is fixed, temporal correlations when α_1, α_2 and α_3 are fixed, and space-time correlations when τ as well as α_1, α_2 and α_3 vary. R_{ij} is called autocorrelation coefficient when $i = j$ and cross-correlation coefficient when $i \neq j$.

Since in the current investigation only a few components of the correlation coefficient tensor were evaluated, a simpler notation will be used for them, as

$$
\begin{aligned}
R_u(\alpha) &= R_{11}(\alpha, 0, 0; 0) \\
R_v(\alpha) &= R_{22}(\alpha, 0, 0; 0) \\
\mathcal{R}_u(\tau) &= R_{11}(0, 0, 0; \tau) \\
\mathcal{R}_v(\tau) &= R_{22}(0, 0, 0; \tau)
\end{aligned}
\qquad (2-37)
$$

where u and v are the axial and radial fluctuating velocity components of the test-section.

In practice, $R_u(\alpha)$ and $R_v(\alpha)$ are often estimated, for convenience, from $\mathcal{R}_u(\tau)$ and $\mathcal{R}_v(\tau)$ respectively, employing Taylor's "frozen flow" approximation, namely the assumption that the flow structure remains unchanged, while being conducted by the mean speed past the measuring probe. Taylor's approximation is accurate only when the turbulence intensity $u'/\bar{U}$ is relatively low (typically below 10%), a condition satisfied in the fully developed bundle flow. Therefore, $R_u(\alpha)$ and $R_v(\alpha)$ can be determined as

$$
\begin{aligned}
R_u(\alpha) &= \mathcal{R}_u(\tau) \\
R_v(\alpha) &= \mathcal{R}_v(\tau)
\end{aligned}
\qquad (2-38)
$$

with $\alpha = \overline{U}\,\tau$.

2.6 LENGTH SCALES OF TURBULENCE

Any turbulent flow can be perceived to be consisting of a large number of eddies of different sizes, and the total turbulent kinetic energy of the flow as the sum of individual energies of all eddies. The maximum possible size any eddy can have is determined by the physical dimensions of the flow, while the size of the smallest eddies is determined by the mechanism of dissipation of kinetic energy into heat by molecular motions. There is a continuous energy transfer between these eddies. The prevailing theory of energy cascade postulates that in a large Reynolds number turbulent shear flows, the large eddies extract energy from the mean field and transfer it to smaller and smaller eddies, where it is dissipated into heat. The following subsections introduce the length scales that are commonly used in the description of turbulence.

2.6.1 Integral Length Scale

The integral length scale is a measure of the typical size of the most energetic eddies in the flow. Although several distinct Lagrangian and Eulerian integral length scales have been defined, the easiest to measure and most commonly reported scale is the Eulerian integral length scale of the streamwise velocity component, along the streamwise direction, defined as (e.g. Tennekes and Lumley, 1972)

$$L_u = \int_0^{\infty} R_u(\alpha)\, d\alpha \qquad (2\text{-}39)$$

Using Taylor's hypothesis, the Eulerian integral length scale, L_u, can be determined from the Eulerian integral time scale, as

$$T_u = \int_0^{\infty} R_u(\tau)\, d\tau \qquad (2\text{-}40)$$

as

$$L_u = \overline{U}\, T_u \qquad (2\text{-}41)$$

Following a similar approach, the Eulerian integral length scale of the transverse fluctuating velocity, L_v, along the streamwise direction can be computed as

$$L_v = \overline{U}\, T_v \qquad (2\text{-}42)$$

where

$$T_v = \int_0^{\infty} R_v(\tau)\, d\tau \qquad (2\text{-}43)$$

2.6.2 Taylor Microscale

The curvature of the two-point correlation coefficient at $\alpha = 0$ is determined by the small scales of turbulence. Since $R_u(\alpha)$ is an even function (e.g. Tennekes and Lumley, 1972), it can approximated, at small α, by a parabola. Then, one can define a relevant characteristic length λ_u, known as Taylor's microscale, as

$$R_u(\alpha) \approx 1 - \left(\frac{\alpha}{2\lambda_u}\right)^2_{\text{at } \alpha = 0} \qquad (2-44)$$

so that λ_u corresponds to the intersection between the osculating parabola and the α-axis.

Alternatively, λ_u can be estimated from the variance and spatial derivative of u, as (Hinze, 1975)

$$\lambda_u = \left[\overline{u^2} \Big/ \overline{\left(\frac{\partial u}{\partial x}\right)^2} \right]^{1/2} \qquad (2-45)$$

Using Taylor's approximation, expressed as

$$\frac{\partial u}{\partial x} \approx \frac{1}{\overline{U}} \left(\frac{\partial u}{\partial t} \right) \qquad (2-46)$$

the microscale can be estimated as

$$\lambda_u \approx \overline{U} \left[\overline{u^2} \Big/ \overline{\left(\frac{\partial u}{\partial t}\right)^2} \right]^{1/2} \qquad (2-47)$$

Following a similar procedure, the transverse microscale, λ_v, can be estimated as

$$\lambda_v \approx \overline{U} \left[\overline{v^2} \Big/ \overline{\left(\frac{\partial v}{\partial t}\right)^2} \right]^{1/2} \qquad (2-48)$$

Taylor's microscales are larger than the scales where the dissipation of kinetic energy into heat mostly occurs; however, they are useful among others, in the estimation of the turbulent kinetic energy dissipation rate, ϵ , since in isotropic turbulence,

$$\epsilon = 15\nu \overline{\left(\frac{\partial u}{\partial x}\right)^2} = 15\nu \frac{\overline{u^2}}{\lambda_u^2} \qquad (2\text{-}49)$$

Although the bundle flow is not isotropic, expression (2-49) represents a reasonable approximation of ϵ , verified in a variety of other shear flows at comparable Reynolds numbers.

2.6.3 Local Isotropy and Kolmogoroff's Hypotheses

The practical application of isotropic turbulence theory, i.e. the assumption that turbulence statistics are independent of the orientation of the coordinate system, appears to be quite limited, since most turbulent flows are not even approximately isotropic. On the other hand, turbulent flows are very diverse and do not permit a single universal description of turbulent phenomena. However, at large enough Reynolds numbers, the larger eddies break down to smaller and smaller eddies, until the local Reynolds number of the smaller eddies decreases below the critical value and these eddies become stable. At this small Reynolds number, viscous forces become dominant and they continuously dissipate kinetic energy into heat. Kolmogoroff (1938), postulating that the motion of such small eddies (fine turbulent structure) is essentially independent of the mean flow and the large-scale turbulence, has originated the locally isotropic turbulence theory, also known as the universal equilibrium theory, in the form of two hypotheses:

(A) At large Reynolds numbers, the characteristic length, velocity and time scales can be uniquely determined by ϵ and ν ; by dimensional analysis, these scales can be expressed as (e.g. Tennekes and Lumley, 1972)

$$\begin{aligned} &\text{Kolmogoroff's length scale :} \quad \eta_k = (\nu^3/\epsilon)^{1/4} \\ &\text{Kolmogoroff's velocity scale :} \quad \nu_k = (\nu\epsilon)^{1/4} \qquad (2\text{-}50) \\ &\text{Kolmogoroff's time scale :} \quad \tau_k = (\nu/\epsilon)^{1/2} \end{aligned}$$

It has been found by several investigators that a requirement for the approximate validity of local isotropy is

$$R_\lambda \geq 100 \qquad (2\text{-}51)$$

where

$$R_\lambda = \frac{u' \lambda_u}{\nu}$$

(B) At large Reynolds numbers, if there is an intermediate range of scales which are much smaller than the physical scales and also much larger than the Kolmogoroff's scales, then, in that range, all statistical quantities depend only on ϵ and are independent of ν. This range later came to be known as the inertial subrange. A condition for the existence of an inertial subrange is $\eta_k \ll L_u$, typically, $\eta_k / L_u < 0.01$.

2.7 TURBULENT VISCOSITY

2.7.1 Closure Problem

It is generally accepted that the motion of fluids such as air and water is governed by the continuity and momentum equations, also known as Navier-Stokes equations, and that these equations apply to both laminar and turbulent flow. Although this set of equations is closed, if one considers the instantaneous velocity components and pressure as unknowns, the equations are inconvenient to use in turbulent flows, due to the time-dependence of all parameters. Following the procedure suggested by Osborne Reynolds (1898), it has been a common practice to decompose all instantaneous values in the equations into mean and fluctuating quantities and to derive separate equations for each component. Omitting intermediate steps, the mean flow continuity and momentum equations in stationary (i.e. with statistics independent of time), incompressible flow can be written in cylindrical coordinates as (x, r and ψ represent the axial, radial and peripheral coordinates respectively. U, V and W the corresponding instantaneous velocity components; e.g. Hinze, 1975)

$$\frac{\partial \bar{U}}{\partial x} + \frac{\partial \bar{V}}{\partial r} + \frac{1}{r}\frac{\partial \bar{W}}{\partial \psi} = 0 \qquad (2-52)$$

$$\rho\left(D\bar{V} - \frac{\bar{W}^2}{r}\right) = -\frac{\partial \bar{P}}{\partial r} + \mu\left(\nabla^2\bar{V} - \frac{\bar{V}}{r^2} - \frac{2}{r^2}\frac{\partial \bar{W}}{\partial \psi}\right)$$
$$- \rho/r \cdot \frac{\partial}{\partial r}\overline{rv^2} - \rho\frac{\partial}{r\partial\phi}\overline{\omega v} - \rho\frac{\partial}{\partial x}\overline{uv} + \rho\frac{\overline{\omega^2}}{r}$$

$$\rho\left(D\bar{W} + \frac{\bar{V}\bar{W}}{r}\right) = -\frac{\partial \bar{P}}{r\partial\psi} + \mu\left(\nabla^2\bar{W} - \frac{\bar{W}}{r^2} + \frac{2}{r^2}\frac{\partial \bar{V}}{\partial \psi}\right)$$
$$-\rho\frac{\partial}{r^2\partial\psi}\overline{\omega^2} - \rho\frac{\partial}{\partial r}\overline{\omega v} - \rho\frac{\partial}{\partial x}\overline{u\omega} - \frac{2\rho\,\overline{\omega v}}{r}$$

$$\rho\, D\bar{U} = -\frac{\partial \bar{P}}{\partial x} + \mu\nabla^2\bar{U} - \rho\frac{\partial \overline{u^2}}{\partial x} - \rho/r \cdot \frac{\partial}{\partial r}r\,\overline{uv}$$
$$-\rho\frac{\partial}{r\partial\psi}\overline{u\omega} \qquad (2-53)$$

where

$$D = \bar{V}\frac{\partial}{\partial r} + \frac{\bar{W}}{r}\frac{\partial}{\partial\psi} + \bar{U}\frac{\partial}{\partial x}$$

and

$$\nabla^2 = \frac{\partial^2}{\partial r^2} + \frac{\partial}{r\partial r} + \frac{\partial^2}{r^2\partial\psi^2} + \frac{\partial^2}{\partial x^2}$$

The above set of four equations for the mean flow contains six unknowns, the so called Reynolds stresses ($\rho\overline{u^2}$, $\rho\overline{v^2}$, and $\rho\overline{\omega^2}$ represent normal stresses; $-\rho\overline{uv}$, $-\rho\overline{v\omega}$ and $-\rho\overline{\omega u}$ represent shear stresses), in addition to the three components of mean velocity ($\bar{U}$, $\bar{V}$ and $\bar{W}$) and the mean pressure, $\bar{P}$. To resolve this closure problem, it is necessary to introduce a model of turbulence, namely to establish additional relations between the Reynolds stresses and the mean fields. "Gradient transport" models are among the simplest and most utilized turbulence models; they are formulated by analogy to the proportionality between the viscous stress and the mean velocity gradient in Newtonian fluids. In the simplest case of nearly parallel flows, it is possible to introduce proportionality constants, called eddy viscosities, by assuming linear relations between the dominant Reynolds shear stresses and the corresponding mean velocity gradients as

$$-\rho\,\overline{uv} = \rho\,\nu_{T\,r}^{\,u}\left(\frac{\partial \overline{U}}{\partial r}\right) \qquad (2\text{-}54)$$

and

$$-\rho\,\overline{uw} = \rho\,\nu_{T\,\psi}^{\,u}\left(\frac{1}{r}\,\frac{\partial \overline{U}}{\partial \psi}\right) \qquad (2\text{-}55)$$

where $\nu_{T\,r}^{\,u}$ is the radial eddy viscosity of axial momentum and $\nu_{T\,\psi}^{\,u}$ is the peripheral eddy viscosity of axial momentum. More sophisticated turbulence models have been developed by many investigators, but their coverage is beyond the scope of the present study.

2.7.2 Prandtl's Mixing Length Model

Prandtl's mixing length model attempts to justify equations (2-54) and (2-55) by physical arguments. It proposes that in a shear flow, fluid elements moving from regions of low mean velocity to regions of higher mean velocity, preserve their initial momentum, and therefore, appear to have a momentum deficit. Similarly, fluid elements moving from higher mean velocity regions to lower mean velocity regions, appear to have a momentum surplus. The average distance a fluid element travels before losing its identity has been termed the mixing length, ℓ. Prandtl's theory relates the average turbulent momentum flux to the mixing length as (e.g. Tennekes and Lumley, 1972)

$$-\rho\,\overline{uv} = C_1 \rho\, v' \ell \,\frac{\partial \overline{U}}{\partial r} \qquad (2\text{-}56)$$

where v' is the root mean squared velocity in the r direction. Then the eddy viscosity can be expressed in terms of the mixing length as

$$\nu_{T\,r}^{\,u} = C_1 v' \ell \qquad (2\text{-}57)$$

where C_1 is a constant, presumably of an order of magnitude of 1. Equation (2-56) was based on the assumption that the mean velocity gradient is nearly constant over distances much larger than the mixing length. This condition is violated in many situations, especially in flows with asymmetric maxima in their mean velocity profiles; the failure of gradient transport models in such cases has clearly been documented (see, for example Eskinazi and Erian, 1960). Nevertheless, due to its simplicity and reasonable success in many situations, gradient transport and, in particular, the mixing length model is widely used.

2.7.3 Other Estimates of Eddy Viscosity

Certain theoretical expressions are available to estimate eddy viscosity in rod bundle subchannels from the local friction velocity and the normal distance from the wall surface. Although developed for particular subchannels, some of these theoretical predictions are based on universal velocity distribution, and therefore, could, in principle, be used in other subchannel geometries.

(A) Radial Eddy Viscosity of Axial Momentum (Figure 5) :

Rapier and Redman (1964) assumed universal velocity distributions to postulate that

$$\frac{\nu_{Ta}^{u_x}}{y_0 u^*} = \frac{1}{2.5}\,\frac{y}{y_0}\left(1 - \frac{y}{y_0}\right) \qquad 0 < y < y_0/2 \qquad (2\text{-}58)^*$$

and

$$\frac{\nu_{Ta}^{u_x}}{y_0 u^*} = 0.1 \qquad y > y_0/2$$

---

*The nomenclature used for cylindrical coordinates in this section is different from the one used in sections 2.7.1 and 2.7.2. The difference is intentional for reasons explained in Chapters VI and VII

(B) Peripheral Eddy Viscosity of Axial Momentum (Figure 5) :

An approximation for peripheral eddy viscosity of axial momentum has been derived by Rapier(1964) as

$$\nu_{T\phi}^{u_z} = \left(\nu_{Ta}^{u_z}\right)_{max} = \frac{u^* y_0}{10} \qquad (2\text{-}59)$$

Nijsing et al. (1966) have derived two theoretical expressions for $\nu_{T\phi}^{u_z}$ based on different assumptions. Assuming that the peripheral eddy viscosity of axial momentum is uniquely determined by local flow conditions and varies around the rod periphery, they predict that

$$\nu_{T\phi}^{u_z} = \nu\left(0.0115\ \frac{y_h}{d_h}\ Re_{bh}^{7/8}\right) \qquad (2\text{-}60)$$

while assuming that $\nu_{T\phi}^{u_z}$ does not vary around the rod periphery but is determined by the average flow conditions, they propose that

$$\nu_{T\phi}^{u_z} = \nu\left(0.0115\ Re_{bh}^{7/8}\right) \qquad (2\text{-}61)$$

Kjellstrom (1971) proposes the following expression for the variation of peripheral eddy viscosity of axial momentum along the radial axis, derived by least-square fitting on his measurements in a triangular array with s/d = 1.22.

$$\frac{\nu_{T\phi}^{u_z}}{u^* y_0} = 0.51 - 0.42\ \frac{y}{y_0} \qquad (2\text{-}62)$$

He also proposes a relation for the ratio between peripheral and radial eddy viscosities of axial momentum as

$$\frac{\nu_{T\,\phi}^{\,u_z}}{\nu_{T\,a}^{\,u_z}} = 4.79\, e^{0.99\,(0.40 - y/y_0)} \tag{2-63}$$

Since these two expressions are based on experiments in a triangular subchannel, they can only be used as rough bases for comparison with measurements in the square subchannel.

A general expression for the computation of eddy viscosity of axial momentum, based on universal velocity equations, due to Kattchee and Reynolds (1962), is

$$\frac{\nu_T}{\nu} = \frac{u^* d_h}{2\nu} \tag{2-64}$$

The authors do not specify whether this expression applies to peripheral direction or to radial direction.

Chapter III

AN OVERVIEW OF EXPERIMENTAL TECHNIQUES

3.1 PROBLEMS ASSOCIATED WITH BUNDLE FLOW MEASUREMENT

In any heat exchanger system, the amount of heat transfer can be enhanced by increasing the contact area between the heater and the coolant. Reactor bundles, aimed at increasing the heat transfer between the fuel and the coolant, are designed with a dense packing of fuel rods; consequently, the physical access to interior subchannels of reactor bundle models becomes difficult. Also, the narrow gaps between rods necessitate the use of non-intrusive techniques and, if they are not available, the use of probes with extremely slim yet rigid stems. Additional problems encountered in the present closed circuit water tunnel were a continuous rise of the water temperature of the fluid with operation time and a continuous build-up of rust and other impurities in the system between cleanups. Furthermore, slight water leakage through flanges and other joints in the system at low flow rates and air suction at higher flow rates was extremely difficult to eliminate, although this problem was somewhat reduced by installing a mobile pressurizing tank. All such problems as well as financial and time limitations were taken into consideration in selecting appropriate experimental techniques for the measurement of pressure, velocity and wall shear stress in the test-section. The following sections provide a brief review of instruments and techniques which are available for the measurement of such quantities, with emphasis on those used in the present investigation. They included pressure tubes, orifices, hot-film anemometers and Preston tubes. Justification for their selection over other suitable techniques and devices has been provided in later chapters.

3.2 THE MEASUREMENT OF PRESSURE

Common simple devices for monitoring mean wall static pressure and mean in-flow static pressure are, respectively, surface orifices and static pressure tubes. Local static pressure is transmitted through hollow tubing to a manometer or pressure transducer for its measurement. Details about static pressure measurement procedures can be found in the book by Benedict (1977).

3.3 THE MEASUREMENT OF VELOCITY

3.3.1 Pressure Tubes

Total and static pressure tubes, because of their simple construction and operation, are among the most widely used instruments for measuring mean flow velocity. With the use of incompressible momentum equation, the flow velocity can be readily computed from the difference between total and static pressure tube readings.

Bechwith and Buck (1961), and Chue (1975) have provided exhaustive studies of various available configurations of pressure tubes and errors associated with their measurements.

3.3.2 Flow Tracing

By introducing small quantities of tracer particles into flow streams and following their motion visually, it is possible to identify the flow pattern even in complex geometries. In addition to obtaining a global picture of the flow, such techniques can be used in conjunction with chronophotography, to provide quantitative measurements. The capabilities of these techniques have been greatly enhanced with the introduction of digital image processing of visualization records.

Substances used to visualize the flow of air include smoke, helium bubbles and aerosols. Dyes, solid spheres and hydrogen bubbles are common tracers for water flow. Flow visualization has a significant advantage over transducer techniques, that it is essentially non-intrusive. Reviews of flow visualization techniques can be found in the books by Merzkirch (1974) and Mueller (1983).

3.3.3 Laser-Doppler Anemometry

Laser-Doppler anemometry operates on the principle that laser beam light scattered by moving particles has a frequency shifted from the incident frequency by an amount proportional to the particle velocity. This technique is non-intrusive and has been used for a variety of fluid compositions and flow geometries. Its disadvantages compared to thermal anemometry (see the ensuing section) are higher cost and complication of operation. A detailed review of this technique can be found, among others, in the book by Durst et al. (1981).

3.3.4 Thermal Anemometers

Thermal (hot-wire and hot-film) anemometers measure flow velocity through its relationship to the heat transfer rate from a heated body immersed in the flowing fluid. An expression, relating the heat transfer to the fluid velocity and the temperature difference termed commonly as King's law (its early version was proposed by King, 1915) is

$$\frac{Q}{T_{op} - T_f} = A + B\,U^n \qquad (3\text{-}1)$$

where Q is the heat transfer rate, $T_{op} - T_f$, is the difference between the operating temperature of the sensor and the fluid temperature, U is the velocity normal to the sensor and A, B and n are empirical constants.

Thermal anemometers can be operated either in constant temperature mode or in constant current mode. In the prevailing constant temperature mode, the operating resistance and, as a result, the operating temperature of the sensor is kept constant utilizing a feedback controlled bridge circuit. This technique provides good frequency response, minimal chance for sensor burnout and permits relatively simple correction for temperature sensitivity. Hot-wire sensors are suitable for clean, non-conductive fluids. The need for turbulence measurements in water and other electrically conductive liquids led to the development of hot-film probes in the late 1950s. These usually consist of a thin platinum or nickel film deposited on a quartz or mica substrate in the form of a cylinder, wedge or cone and insulated with a thin quartz coating.

Theories and operational procedures that were originally developed for hot-wire anemometry have also been applied to hot-film anemometry, despite the general knowledge that hot-film response is complicated by heat conduction to the substrate, significant flow obstruction and possibility of dirt accumulation.

Ling (1955) designed conical, wedge and cylindrical shaped hot-films, and compared the dynamic response of hot-film probes with that of hot-wire probes at identical flow conditions. Bankoff and Rosler (1962) found that non-cylindrical sensors measured lower velocity fluctuations than did a hot-wire, and attributed this to the heat conduction into the substrate. Bellhouse and Schultz (1966) developed one-dimensional theoretical model to account for hot-film sensitivity dependence upon frequency. Their classical model assumed a flat substrate with a sensor placed only on one side, but with heat convection occurring at both sides of the model. Briston et al. (1979) developed a two-dimensional model with heat convection as well as axial heat conduction using finite-element analysis. Freymuth (1978,1981) extended his dynamic theory for constant temperature hot-wire anemometers to constant temperature hot-film anemometers and further showed that non-linear effects of large velocity fluctuations were similar for both anemometers. A detailed bibliography on thermal anemometry has been compiled by Freymuth (1978).

3.4 THE MEASUREMENT OF WALL SHEAR STRESS

The exact determination of wall shear stress plays a significant role in the design and performance-analysis of any fluid mechanical system. A brief survey of methods which are available for the measurement of the local wall shear stress, directly or indirectly, is given in the following sections.

3.4.1 Direct Measurement

In most skin friction balances, a floating element with its face aligned with the test surface is used to measure the local wall shear stress directly as a force per unit area, although, in some cases, the wall shear stress is estimated indirectly from the displacement of the floating element. The first skin friction balance was due to Schultz-Grunow (1940). Fenter and Lyons (1957) used balances in rockets. MacArthur (1963) supported the floating element in a piezoelectric crystal and was able to determine very small forces by detecting the displacement of the floating element. The popular Kistler probe (Patos, 1970), once available commercially, was able to measure wall shear stress under linear acceleration. In most cases the floating elements were supported on mechanical linkages, although air bearings have also been used (Ozarapoglu, 1973).

One important constraint in the use of skin friction balances is the need for perfect alignment of the floating element surface with the contour of the test section, since any protrusion or depression would lead to significant errors,(O'Donnell, 1964; O'Donnell and Westkaemper, 1965; Allen, 1976)

3.4.2 The Preston Tube Technique

Preston (1954) developed a simple method for determining the local turbulent wall shear stress utilizing a pitot tube resting on the surface. This method was based on the assumption of universality of 'law of the wall' in turbulent boundary layers. Preston tested circular pitot tubes with different sizes and inner to outer diameter ratio of 0.6 and proposed a universal relationship as

$$\frac{\Delta p \, d_p^2}{4 \rho \nu^2} = F\left(\frac{\tau_w \, d_p^2}{4 \rho \nu^2}\right) \qquad (3\text{-}2)$$

where Δp is the difference between the pitot pressure and the wall static pressure, d_p is the outer diameter of the pitot tube and τ_w is the local wall shear stress. The function 'F' can, presumably, be determined from measurements in a flow where the wall shear stress is known, for example in fully developed pipe flow. Soon after Preston's method was published, many researchers questioned its universality (e.g. Hsu, 1955). Some independent tests (Staff of the Aerodynamics Division, National Physical Laboratory, 1958) indicated that Preston's method underestimated the skin friction by nearly 14%. Patel (1965) used fourteen different size pitot tubes with varying internal to external diameter ratios, and produced a calibration that has been accepted widely. Defining two parameters as $x^* = \log(\Delta p \, d_p^2 / 4\rho\nu^2)$ and $y^* = \log(\tau_w d_p^2 / 4\rho\nu^2)$

he proposed that

$$y^* = \frac{1}{2} x^* + 0.037 \qquad y^* < 1.5$$

$$y^* = 0.8287 - 0.1381 x^* + 0.1437 x^{*2} - 0.0060 x^{*3}$$

$$1.5 < y^* < 3.5 \qquad (3-3)$$

$$x^* = y^* + 2 \log (1.95 y^* + 4.10)$$

These equations roughly correspond to the viscous sublayer, the buffer layer and the logarithmic region of a turbulent boundary layer respectively. The equation for the outer layer is somewhat cumbersome to use because of its implicit form. Furthermore, Patel's expressions are discontinuous at interfaces between regions. To overcome such drawbacks, Head and Vasanta Ram (1971) presented a simple chart with $\Delta p\, d^2/\rho \nu^2$ and $\Delta p/\tau_\omega$ as the variables. Bradshaw and Unsworth (1974) proposed a single equation for Preston tube calibration as

$$\frac{\Delta p}{\tau_\omega} = 96 + 60 \log \frac{d_p u^*}{50 \nu} + 23.7 \left(\log \frac{d_p u^*}{50 \nu} \right)^2 \qquad (3-4)$$

$$50 < \frac{d_p u^*}{\nu} < 1000$$

which was also of an the implicit form.

In the current investigation Preston tubes have been used in the developing flow region as well as in the fully developed region. Since almost all Preston tube calibration equations have been developed based on experiments conducted in fully developed regions, the use of such equations in a developing region is often questioned. Head and Rechenberg (1962) have showed that for a given wall shear stress value, the Preston tube reading was the same in the developing and the fully developed regions; the corollary is that if one could use standard calibration equations for determining wall shear stress from a particular Preston tube reading in the fully developed region, the same could be done in the developing region also.

In the current study Preston tubes are used in locations where there is a favourable pressure gradient, especially in the developing region. Patel (1965) has studied the effects of both adverse and favourable pressure gradients on Preston tube readings. Defining $\Delta = \nu/\rho u^{*3} \left(\partial P/\partial x \right)$, he concluded that in flows with favourable pressure gradient, the maximum error in τ_w was 3% for

$$0 > \Delta > -0.005, \quad \frac{u^* d_p}{\nu} \leqslant 200, \quad \frac{\partial \Delta}{\partial x} < 0 \tag{3-5}$$

and 6% for

$$0 > \Delta > -0.007, \quad \frac{u^* d_p}{\nu} \leqslant 200, \quad \frac{\partial \Delta}{\partial x} < 0$$

The use of tubes with different shapes for the measurement of wall shear stress has been investigated by Quarmby and Das (1969), who studied the response of rectangular tubes with flat elliptical front shape and Prahlad (1972), who analyzed the yaw characteristics of Preston tubes with openings cut off obliquely at 45°.

3.4.3 Obstacles in the Flow

Wall shear stress can be estimated by measuring pressure drop past a small obstacle protruding from the wall. Such obstacles are normally confined within the viscous sublayer (sublayer fence). This technique requires calibration in a flow with known wall shear stress. Tests of this technique have been reported by Konstantinov (1955), Head and Rechenberg (1962) and Vagt and Fernholz (1973).

3.4.4 Heat Transfer Techniques

Fage and Falkner (1930) first investigated the relation between the local skin friction coefficient and the heat transfer from thin platinum strips embedded on the wall surface. Ludwieg (1949) confirmed that the heat flux was proportional to 1/3rd power of local wall shear stress, provided that the heated length was sufficiently small and that its thermal layer was confined within the viscous sublayer of the wall.

A variation of this method is the pulsed heated film technique. Two films are kept perpendicular to the flow direction and the upstream one is heated by a short electric pulse. The local wall shear stress, according to Çinder and Bradbury (1973), can be measured from the time interval between the electric pulse and the change of resistance of the downstream film. These authors used two sensor films, located on either side of the pulsed film, in order to measure shear stress in separating and reattaching flows.

3.4.5 Other Techniques

Stanton et al. (1920) used a rectangular pitot tube with the test wall forming the inner surface of the tube to determine the shear stress. Later, this became known as Stanton tube. Hool (1955) modified the system by attaching a piece of a razor blade over a static pressure hole. Calibration procedures for this technique are given in the study by East (1966), who also introduced magnetic support of the razor blades.

Wall shear stress has also been estimated from the pressure difference between two static pressure holes with different diameters. Mass transfer techniques, similar to heat transfer technique, relate local wall shear stress to the mass flux rate from a finite region on the test surface to the outer region. Detailed reviews of all methods available for measuring wall shear stress have been compiled by Winter (1977) and Hanratty and Campbell (1983).

Chapter IV

EXPERIMENTAL FACILITIES AND INSTRUMENTATION

4.1 THE WATER TUNNEL

The flow field was generated in a closed return water tunnel, shown in Figure 6. Briefly, it consists of a water pump (Berkeley B2TPM 10 BHF), a 3-phase industrial electric motor driving the pump (Baldor 10 HP), a working section in 3 pieces of equal length made from transparent acrylic material, and the contraction and expansion sections from fibreglass. Other features of the channel include a mobile pressurizing tank, a plenum chamber, a by-pass branch with two butterfly valves for the accurate control of the flow rate through the test section, two steel bellows for isolation from vibrations and thermal expansion, an orifice plate for the measurement of the flow rate, various valves and a water filtering system.

The plenum chamber was added to the circuit in order to reduce the recirculating water temperature rise; it was equipped with a honeycomb and a screen which helped straighten the swirly flow from the upstream elbow before entering the test-section. Finally, the relatively long water residence time in the plenum chamber helped deaeration of some of the air bubbles and pockets present in the system. The addition of the pressurizing tank also improved the system operation. The range of pressures within the water tunnel varied relatively widely, depending on the operating conditions. At low flow rates, some water leakage was observed, while at high flow rates, the substantial pressure drop in the bundle resulted in slight air suction through flanges and probe insertion ports. Furthermore, the design and materials of the test-section (see the following section) would not withstand high pressure differences, and for this purpose, the mobile pressurizing tank was introduced to adjust the tunnel pressure and maintain it near atmospheric during tunnel operations. The tank could be slided along a vertical track of about 5m height, using a manual ratchet and cable mechanism. A floating device indicated the water level in the tank. Besides reducing air suction, pressurization of the tunnel acted favourably against cavitation risk, especially at the pump inlet and also behind the bundle endplates and probe stems.

4.2 THE TEST-SECTION

The test-section (Figure 7) was a double scaled model of the 37-rod fuel bundle of the CANDU-PHW reactor. In order to avoid excessively large pump size and economize on materials, only a symmetrical, 60° circular sector of the bundle was constructed; the study was focused mainly on the central square subchannel, where side wall effects were expected to be negligible. The walls as well as most of the rods were made of clear perspex (except for rods A and B which were made of aluminium), thus permitting optical access to the entire flow. The rods were firmly supported at both ends on endplates (Figure 8), which were geometrically similar to those in the reactor bundle (Figure 9)*, except for the location of the radial ribs: in the model, end plate radial ribs were positioned symmetrically, adjacent to the side walls, while in the actual bundle they were positioned in asymmetric positions; symmetry was considered beneficial at this stage, where the flow conditions were simplified as much as possible. Most measurements were conducted with a single bundle model inserted in the middle section of the water tunnel. Inlet ports for probe insertion were available at three streamwise locations (x/L = 0.08, 0.50 and 0.91; x is the distance of the port from the entry to the bundle and L is the length of the bundle; this also can be expressed as x/d_h = 3, 20 and 35) along the test-section.

Table 1 compares flow conditions and physical dimensions of the test-section with those of the reactor bundle. The value provided for s/d in Table 1 was an average over the values corresponding to the four full rods, which formed an approximate but not exact square subchannel; the maximum variation of s/d was less than 1%. The reported value of

---

* CANDU reactor fuel rods are currently supported on this endplate, which has symmetrically located radial ribs; Figure 2 represents an earlier version.

hydraulic diameter, d_h , was based on trapezoidal approximation of the square subchannel.

In the second stage of the research, another 60° sector bundle (Figure 10), but rotated 30° clockwise with respect to the test-section bundle, was inserted in the empty upstream section. The bare aluminium rods of the new bundle were supported at both ends on two more endplates. Figure 11 is a projection of both the bundle cross-sections superimposed on each other; it demonstrates that the amount of resulting subchannel interference was relatively large for the 30° rotation. This choice was the first step in a series of experiments to be conducted in the future with various other relative orientations (e.g. at 0° and 15°)

The adjoining endplates between upstream bundle and test-section bundle were equipped with radial ribs (Figures 12a and 12b), in the same arrangement as that in the actual fuel bundle (Figure 9). When Figures 12(a) and 12(b) are kept facing each other, the azimuthal angle between the radial ribs is 30°, equal to the angle of rotation.

4.3 THE TRAVERSING SYSTEM AND THE MOUNT

A rigid, horizontal steel railing built parallel to the flow axis of the test-section was used to support and guide the traversing system axially. The traversing system with the probe mount (Figure 13) could be traversed manually through the railing and positioned against any inlet port on the test section. Probes (pressure tubes and hot-films) held by the mount were traversed along the test-section radial axis through the inlet port; the design of the mount ensured proper alignment of the probe axis with the flow direction and also a smooth traversing. The radial traversing system (Mitutoyo Height gage) had a resolution of 0.01 mm.

4.4 THE CALIBRATION FACILITY

A separate calibration nozzle was designed and constructed for the calibration of hot-film probes. The jet was capable of providing a stable, laminar vertical column of water with centreline speeds in the range of 2 to 12 m/s (Figures 14 and 15). The jet speed was monitored from the pressure drop between two points upstream and downstream of the contraction, and was checked using a total head tube. There were provisions at the exit of nozzle for mounting the hot-film probe with its tip near the centre of the jet and about 5 mm outside the nozzle (Figure 16a).

At a later stage of the project, a cylindrical piece (Figure 16b), equipped with an inlet port similar to those in the test-section, was attached to the exit of the nozzle. This facilitated the use of the same probe mount described in the previous section, thus avoiding the need for removal of the probe from the mount between calibrations and measurements.

4.5 PRESSURE INSTRUMENTATION

The flow rate through the test section was measured by means of pressure drop through a standard orifice plate, inserted in the straight, returning pipe of the water tunnel. Figure 17 presents the calibration of the orifice plate. Figures 18 and 19 show the corresponding range of the test-section bulk velocity and the test-section Reynolds number respectively.

In-flow static pressure was measured using home-made stainless steel static tubes with a tip outer diameter of 1.2 mm (Figure 20a) and rounded tip front. Four static pressure holes with diameter of about 0.3 mm were drilled radially around the circumference, near the center of the tip, where nose effects and stem effects were expected to nearly cancel each other (see section 5.1.2).

The total pressure tubes, shown in Figure 20(b), had the same shape and size as the static tubes. The tube tip had a square-cut nose and an inner to outer diameter ratio roughly equal to 0.6.

A Validyne DP 108 variable reluctance, diaphragm-type, pressure transducer was used for measuring all the pressures. It was connected to a Validyne CD 23 demodulator and then to a TSI 1076 Integrating voltmeter or through the analog-to-digital converter to the microcomputer. The D.C. ranges of the voltmeter were 10 and 100 volts with 0.05% full-scale accuracy. The integrating time could be set to

0.1, 1.0, 10 or 100 seconds. The choice of transducer diaphragm that would provide the optimum accuracy for the entire measurement range was based on preliminary tests using a mercury manometer under the desired experimental conditions. The transducer installed with thus selected diaphragm was calibrated using a sequence of water columns, measured within ± 0.01 mm with the height gage. A linear relation between the water head ΔH and the voltmeter reading $\bar{E}$. was found valid for the entire diaphragm range (Figure 21).

4.6 PRESTON TUBE INSTRUMENTATION

The two aluminium rods, A and B, located diagonally with respect to the central square subchannel, were equipped with a total of 10 sets of Preston tube and wall static pressure hole combinations (inner rod with 6 sets and outer with 4; 30 peripheral separation between sets) as shown in Figures 22 and 23. Each set constituted 4 straight stainless steel tubes of 1.2 mm outside diameter glued into a long axial slot milled on the rod; two tubes per set were used for upstream wall shear stress measurement, while the other two for downstream measurement. Surface pressure holes with diameter 0.3 mm were drilled about 15 mm directly upstream of the Preston tube mouths in order to minimize the effect of Preston tubes on surface pressure readings. The upstream and downstream Preston tube-pressure hole combinations were at about 20% and 60% of the bundle length. The circumferential position of the hole and Preston tubes was such as to provide the static pressure and wall shear stress distribution mainly within the central subchannel region. The downstream ends of the steel tubes were led out of the test section following mostly end-plate ribs in order to cause minimum possible flow blockage (Figure 24) and were connected through clear plastic tubing to a specially designed pressure manifold for selective pressure measurement, using the pressure transducer.

4.7 HOT-FILM INSTRUMENTATION

All turbulence quantities were measured with hot-film anemometers. Conical hot-film probes (TSI 1246 BJW; Figure 25a) were selected initially, since they were considered sturdy and less sensitive to flow impurities. Two conical probes were purchased and calibrated successfully in the water jet. Unfortunately, no useful results were collected with these probes because the first one was mechanically damaged during preliminary tests in the water tunnel, and the second was apparently burnt, while conducting measurements at water speeds of about 6 m/s. Burnout was verified by microscopic examination of the sensor surface. Considering the manufacturers' specifications and the fact that the probes operated without problems in the calibration jet for water speeds between 2 and 12 m/s, we speculate that the burnout was enhanced by the reduced pressure in the test-section, which facilitated cavitation with resulting large temperature variations across the sensor surface. Because conical probes were not repairable, and also because they could resolve only the streamwise velocity component, cross-film probes were used in subsequent experiments.

The cross-film probes (1249 AC-20W; Figures 25b and 25c), capable of resolving simultaneously two orthogonal velocity components, were constructed to our specifications by TSI, Minnesota, U. S. A. Each probe consisted of two cylindrical hot-film sensors (diameter 0.025 mm), at right angles with each other and at 45° with the probe axis.

Two TSI 1050 constant temperature anemometer modules, powered by a TSI 1051 2D4 Monitor and Power Supply, were used for operating cross-films. The anemometer modules contained built-in square wave generators with frequencies 1 kHz or 20 kHz for checking the frequency response of the sensors and also high frequency low pass filters to cut off frequencies above 100 kHz or 400 kHz. They had provisions for operating in constant current mode or in constant temperature mode. The 4 1/2 digit panel meter of the Monitor and Power Supply unit had a range of 0-20 V with an accuracy of 0.01% of full scale, reading ± 1 digit. Two TSI 1052 linearizers were also available in the same housing for linearizing the anemometer outputs, but they were used only in preliminary stages of the current study.

Anemometer output signals were monitored in the D-13 CRT display unit of a Tektronix 5113 dual beam storage oscilloscope. The two 5A22N differential amplifiers in the oscilloscope were used to amplify and condition the signals. The amplifiers were equipped with a low pass filter (selectable from 0.1 kHz to 1 MHz in a 7 step, 1-3-10 sequence) and a high pass filter (selectable from DC to 10 kHz in a 7 step, 1-10-100 sequence), both with 3 db off per octave. The available amplifier gains ranged from 0.1 to 50000 in an 18 step, 1-2-5 sequence. The DC offset range could be set between ± 0.5 V or ± 50 V, depending on the gains used. The 5B10N time base of the amplifier, used to change the width of the display, had sweep rates from 1 s/div to 5 s/div in a 21 step, 1-2-5 sequence.

Chapter V

EXPERIMENTAL PROCEDURES AND ACCURACIES

5.1 METHODOLOGY FOR PRESSURE TUBE MEASUREMENTS

5.1.1 Measuring Procedure

Pressure tubes were used to measure mean pressure and mean velocity fields in the test-section. This data was particularly useful for the selection of hot-film probes, and also, served as a basis for comparisons with results obtained from Preston tubes and hot-film probes.

In order to eliminate the need for partially emptying and refilling the tunnel, and in order to carry out the measurements at the different downstream ports under, as much as possible, identical operating conditions, it was decided to manufacture sets of several identical static and total pressure tubes. First, identical static pressure tubes were simultaneously inserted at all three inlet ports (x/L = 0.08, 0.5 and 0.91) of the test-section. The tunnel was filled and operated until a steady state was reached; then the in-flow static pressure was measured against a reference wall static pressure tap in the upstream empty section, by traversing one tube at a time along the test-section radial axis at 5 mm intervals. When one tube was in operation, the other idle tubes were traversed to their outmost position, in contact with the curved channel wall, in order to eliminate any probe interference. Observation of the flow behind probe stems did not reveal any apparent cavitation even at the highest flow rate.

After the completion of all static pressure measurements, the tunnel had to be partially emptied, and after replacing static pressure tubes by total pressure tubes, refilled. Total pressure distribution was measured at the same locations and under the same flow conditions, as the static pressure. The flow rate (indicated by the orifice plate) and the gage pressure of the reference wall pressure tap, were adjusted to values, which were as close as possible to those during static tube measurements. The mean axial velocity was then estimated from the difference between the total pressure and the static pressure, using the steady state Bernoulli's equation

$$\bar{U} = \sqrt{\frac{2(\bar{P}_0 - \bar{P})}{\rho}} \qquad (5\text{-}1)$$

5.1.2 Error Analysis for In-Flow Static Pressure Measurements

(1) Nose and Stem Effects

In the home made static head probes, pressure holes were located near the centre of the tip, about 4 diameters away from the nose as well as from the stem. At this location nose effects on static pressure readings were expected to be less than 0.5% of the dynamic pressure (Ower and Johansen, 1925; Merriam and Spaulding, 1935). Stem effects were expected to be more significant, and as a result, the static pressure could have been overestimated by nearly 2% of the dynamic pressure (Ower and Johansen, 1925; Merriam and Spaulding, 1935).

(2) Yaw Effects

Yaw (misalignment of the probe axis with the flow direction) effects have generally been found significant on static tube measurements. With the use of the carefully designed traversing system and mount, it was possible to align the probe axis with the flow direction within ± 2°; the corresponding maximum error was estimated to be 0.7% of the actual static pressure (Ower and Pankhurst, 1977).

(3) Other Effects

The effects of turbulence and of the size of the tube relative to the typical eddy size have not yet been completely understood. For example, according to Goldstein (1936), in a turbulent flow, the static head tube would read by an amount equal to $\frac{1}{2}\rho\left(\frac{1}{2}\left(\overline{v^2} + \overline{w^2}\right)\right)$ higher than the actual static pressure ($\overline{v^2}$, $\overline{w^2}$ are mean square transverse turbulent velocities). Such errors are normally less than 1%, when the turbulent intensity is less than 15%.

5.1.3 Error Analysis for Total Pressure Measurements

(1) Wall Proximity Effects

Total head tubes tend to overestimate the impact pressure in the vicinity of the wall; this effect is quite significant when the distance of the tube centre from the wall is less than about 3 tube diameters (MacMillan, 1957).

In the test-section, the rod gaps were 3.4-3.6 mm wide, and the pressure tube diameter was 1.2 mm. When readings were taken along the centreline in rod gaps, the tube was, in effect, only about 1.5 diameters away from either rod surface.* Eifler and Nijsing (1967) have modified MacMillan's (1957) numerical results, and have estimated such dual wall effects in bundle flow. These results provide a maximum error 2.2% of mean axial velocity for impact tube measurements in the minimum rod gaps.

(2) Effect of Shear

In a shear flow, pressure tubes generally read a total pressure corresponding to an effective pressure centre displaced by a distance, δ_{A}, from the geometrical centre toward the higher velocity side. For circular tubes with inner to outer diameter ratio of 0.6, the displacement is approximately equal to 0.18 tube outer diameter (Young and Maas, 1936). In the maximum shear region between the rod gap and the maximum flow area of the subchannel, the

---

* Most of the available studies have determined single wall proximity errors; it is not obvious how to apply these results in a rod gap geometry.

displacement would then amount to 0.2 mm for the 1.2 mm diameter tube; this means that the measured velocity at points between rod gaps and subchannel centres would more likely correspond to a point 0.2 mm displaced from the point of measurement toward the subchannel centre.

(3) Yaw Effects

Yaw effects on total head tubes are somewhat less severe compared to those on static head tubes. For square-ended total head tubes with inner to outer diameter ratio of about 0.6, this error, according to Davies (1957), is negligible for yaw angles upto $\pm$ 10°.

(4) Turbulence Effects

As said before, the effects of turbulence and the size of the tube relative to typical eddy size have not yet been completely understood. For example, according to Goldstein (1936), in incompressible turbulent flow, an impact pressure tube would read $\overline{P} + \frac{1}{2}\rho\overline{U}^2 + \frac{1}{2}\rho(\overline{u^2} + \overline{v^2} + \overline{w^2})$ rather than $\overline{P} + \frac{1}{2}\rho\overline{U}^2$. Therefore, the mean axial velocity evaluated from the difference between the total and static pressures using equation (5-1), would in fact, contain turbulent components also, and corrections should be introduced for the effect of turbulence.

5.2 METHODOLOGY FOR THE MEASUREMENT OF WALL SHEAR STRESS

Of the various techniques available to measure local wall shear stress, the Preston tube method was chosen in the current investigation to determine wall shear stress around the convex periphery of the bundle rods. Preston tubes are relatively simple to install and operate and have been used almost exclusively for wall shear stress measurements in bundle flow studies (e.g. Kjellström, 1971; Trupp and Azad, 1975). These studies contend that Preston tube calibration equations developed in a pipe flow (or any concave surface) would be applicable to a convex surface also, since the Preston tube technique is based on the assumed universality of the 'Law of the wall' for turbulent boundary layers over any smooth wall surface. In the current investigation, it was, therefore, decided to use a standard calibration equation, rather than constructing a separate calibration facility and then calibrating the Preston tube on a rod surface with wall shear stress known by other analytical or experimental procedures. Preston tube measurements were checked against the wall shear stress estimated from the measured pressure drop data and also from various empirical equations outlined in Chapter II

A constraint in the use of Preston tubes is that the radius of curvature of the test surface should be at least 10 times the radius of the Preston tube (e.g. Patel, 1965). For the present test-section rods, this ratio was slightly more than 21.

The local wall shear stress distribution around the periphery of rods A and B at two streamwise locations (x/L = 0.20 and 0.60) was estimated from the difference between the impact pressure read by the Preston tube and the corresponding surface pressure hole, using equation (3-3).

The surface pressure holes were also used separately against the reference pressure tap to provide the peripheral wall static pressure distribution around the same rods.

5.2.1 Error Analysis for Surface Pressure Measurements

The exact wall static pressure can be measured, in principle, only by an infinitesimally small, clean, burr-free, square-edged surface pressure hole with its axis perpendicular to the flow direction. Since such a hole is extremely difficult to machine, and since its response to sudden pressure changes would be very slow, some relaxation of the above conditions becomes necessary.

In the present research, surface pressure holes were drilled on thin steel tubes, glued in flush with the rod surface, to measure the static pressure distribution around the rod periphery. Extreme care was taken to ensure that the tubes did not have any protrusion or depression, and that the holes were burr-free with their axes normal to the rod surface.

Estimates of corrections that may have to be applied on wall static pressure measurements are given below.

(1) Effect of Hole Size

It has been shown that pressure overestimation error increases with increasing hole size (Franklin and Wallace, 1970). For slightly oversized holes this error generally tends to be insignificant. An upper limit for pressure error measured with the current surface pressure holes (corresponding to a maximum friction Reynolds number of 90; $Re^* = u^* d_{Hole}/\nu$; d_{Hole} = 0.3 mm; u^* = 0.3 m/s max.) is about 0.3% of the local wall shear stress.

5.2.2 Error Analysis for Preston Tube Data

(1) Errors due to Separation between Preston Tubes and Surface Pressure Holes

A small error was introduced in Δp due to the fact that the wall static holes were not positioned exactly at the Preston tube mouths, but slightly upstream of them, in order to reduce flow distortion near the pressure holes. To account for this, the static pressure at the Preston tube mouth was estimated from the measurement by interpolation or extrapolation using the measured axial mean pressure gradient.

(2) Wall Proximity Effects

Similarly to total head tubes, Preston tubes stationed in bundle rod gaps might also overestimate the impact pressure, due to presence of the opposite wall surface, which tends to produce deviations from the 'law of the wall', which is the basis for various calibration equations. However, there is some evidence (Tahir and Rogers,1986) that the law of the wall, in fact, apply to rod gaps, at least for y+ < 100. A very crude estimate of this error could be obtained from the one used for total head tubes in section 5.1.3; since in the present setup the Preston tube centre was slightly more than 2 diameters away from the opposite rod surface, a 2.8% overestimation in Δp might be expected.

(3) Pressure Gradient Effects

Pressure gradient effects on the Preston tube readings were estimated using Patel's (1965) approximate expression (equation 3-5). The value of was estimated to be -0.0006 (negative sign is used for favourable- pressure gradient, i.e. pressure drop along the streamwise direction) at the developing region and -0.0003 at the fully developed region for $Re_{bh} = 50000$; also $u^* d_p / \nu$ was found to be 175, and therefore, the maximum possible error in Preston tube reading due to pressure gradient is about 3% of τ_w.

5.3 METHODOLOGY FOR TURBULENCE MEASUREMENTS

5.3.1 Calibration Equations for Cross-Films

The modified King's law (equation 2-1) is a relation between the heat transfer from a single heated sensor and the velocity of the surrounding fluid. For a slanted film, an effective cooling velocity, that would produce the same heat loss as the velocity normal to the sensor, must be considered. For simplicity, one may neglect heat convection parallel to the sensor axis.

Then, U_{eff1}, the effective cooling velocity, normal to film 1, can be written as (Figure 26)

$$U_{eff1} = (\overline{U} + u + v) \cos 45^\circ \qquad (5\text{-}2)$$

and U_{eff2}, the effective cooling velocity normal to film 2, as

$$U_{eff2} = (\overline{U} + u - v) \cos 45^\circ \qquad (5\text{-}3)$$

Then King's law for films 1 and 2 can be written as

$$\frac{E_1^2}{T_{op1} - T_f} = A_1 + C_1 (\overline{U} + u + v)^{n_1} (\cos 45^\circ)^{n_1} \qquad (5\text{-}4)$$

and

$$\frac{E_2^2}{T_{op2} - T_f} = A_2 + C_2 (\overline{U} + u - v)^{n_2} (\cos 45^\circ)^{n_2} \qquad (5\text{-}5)$$

Decomposing instantaneous quantities into mean and fluctuating parts, equations (5-4) and (5-5) can be modified as

$$\frac{(E_1 + e_1)^2}{T_{op1} - T_f} = A_1 + B_1 (\overline{U} + u + v)^{n_1} \qquad (5\text{-}6)$$

and

$$\frac{(\overline{E}_2 + e_2)^2}{T_{op2} - T_f} = A_2 + B_2\,(\overline{U} + u - v)^{n_2} \qquad (5\text{-}7)$$

where $B_1 = C_1\,(\cos 45^\circ)^{n_1}$ and $B_2 = C_2\,(\cos 45^\circ)^{n_2}$.
Expanding equation (5-6) binomially and neglecting higher order terms, one can show that

$$\frac{(\overline{E}_1^{\,2} + 2\overline{E}_1 e_1)}{T_{op1} - T_f} = A_1 + B_1\,\overline{U}^{n_1}\left[1 + n_1\left(\frac{u}{\overline{U}} + \frac{v}{\overline{U}}\right)\right] \qquad (5\text{-}8)$$

On time averaging, equation (5-7) simplifies to

$$\frac{\overline{E}_1^{\,2}}{T_{op1} - T_f} = A_1 + B_1\,\overline{U}^{n_1} \qquad (5\text{-}9)$$

since time averaged fluctuating quantities ($\overline{e}_1$, $\overline{u}$ and $\overline{v}$) vanish by definition.

Following the same approach, equation (5-7) can be simplified to

$$\frac{\overline{E}_2^{\,2}}{T_{op2} - T_f} = A_2 + B_2\,\overline{U}^{n_2} \qquad (5\text{-}10)$$

The purpose of calibration is to determine optimum values of the empirical constants, A_1, B_1 & n_1 and A_2, B_2 & n_2, in equations (5-9) and (5-10) using measured sets of values of $\overline{E}_1$, $\overline{E}_2$, $\overline{U}$ and T_f.

5.3.2 The Cross-Film Calibration

Initial calibrations were performed in the open water jet of the calibration nozzle. The quality of hot-film signal in the calibration jet was found satisfactory (extremely low turbulence and electronic noise levels) by observation on the oscilloscope and with the use of a power spectrum analyzer. A typical calibration for a conical hot-film probe, calibrated in the calibration jet, is shown in Figure 27.

Although the calibration jet was found satisfactory, an alternate calibration procedure was followed for most single-bundle measurements. This procedure facilitated calibration of the hot-films under conditions nearly identical to those during measurements; in particular, it accounted for errors due to temperature variation and dirt accumulation on sensors. The cross-film probe was inserted in the empty, upstream section of the water tunnel and its outputs were calibrated with reference to a total tube inserted in the same section. The mean axial velocity profiles in the empty section were found similar to that in a fully developed channel flow, and also, were nearly identical at the two streamwise locations, where the cross-film probe and the pressure tube were inserted (Figure 28). A significant, steady increase in the recirculating water temperature was observed (Figure 29) during calibration as well as during measurements; for this reason, the mean water temperature was continuously monitored and accounted for in the hot-film response equations.

A typical calibration in the upstream empty section consisted of following general steps.

(1) Mean axial velocity profiles along the radial axis of the upstream empty section at two adjacent streamwise positions (8 cm apart) were determined by inserting two identical total head tubes (one in each) and measuring the impact pressure against a corresponding wall static pressure tap, located at the bottom flat surface; in the same plane as the inlet port. A correction for the small difference between the wall static pressure and the in-flow static pressure was applied. As seen from Figure 28, the mean velocity profiles at these adjacent streamwise locations were not only practically identical, but also had a flat region near the geometric centre of the channel.

(2) The (unheated) sensor resistances of the cross-film probes were estimated at different temperatures by immersing the probe tip in a hot-water bath. Linear relations of the form

$$R_1(T) = R_{01}\,(1 + \alpha_1 T)$$

$$R_2(T) = R_{02}\,(1 + \alpha_2 T) \qquad (5\text{-}11)$$

with $\bar{T}$ in °C, were fitted through each set of experimental points (Figure 30). The measured coefficient of resistance, α, and the operating resistance at T_{op} = 66.7 °C were very close to the manufacturer-supplied values.

(3) The hot-film probe was inserted, with great care, in the downstream port and a total head tube in the upstream port. The respective operating resistances of the sensors were set in the two resistance decades of the anemometer units, and the frequency response of the sensors was optimised using the standard square wave test, under typical flow conditions.

(4) Each calibration point consisted of the reference mean axial velocity, $\bar{U}$ (measured by the total head tube), the mean anemometer output voltages, $\bar{E}_1$ and $\bar{E}_2$ (time-averaged directly by the micro-computer, through the A/D to converter; see the following section) and the fluid temperature, T_f, measured by a mercury thermometer with 0.5 °C resolution. The flow velocity was varied using the various valves in the system, and at least ten calibration points were used to determine the optimum exponents, n_1 and n_2, of equations (5-8) and (5-9).

Two sample calibration equations, temperature corrected, are given below

$$\frac{\bar{E}_1^2}{T_{op1} - T_f} = 0.2487 + 0.3824\,\bar{U}^{0.4}$$

$$\frac{\bar{E}_2^2}{T_{op2} - T_f} = 0.2951 + 0.3674\,\bar{U}^{0.4}$$

An indication of the accuracy and reproducibility of the calibration equations is given in Figure 31, which compares the velocity calculated using these equations with the velocity measured using the pressure tube. The amount of scatter is significant, yet expected in view of the relatively large hot-film sensitivity to temperature changes and to dirt accumulation.

Despite filtering and frequent replacing of the water, rust and other impurities were found to accumulate in the system, with the result that the hot-film response was affected by the deposits on the film surface. To reduce such effects, the film surfaces were cleaned before each set of measurements, and the calibration was repeated as often as possible.

5.3.3 Signal Discretization and Processing System

The signal discretization and processing system consisted of an LSI -11/23 microcomputer with 64K byte memory as the main unit and an ADAC 1610 GPT 16-bit programmable timer and a 12-bit analog to digital converter (ADAC model 1012) as peripheral units.

The multiplexer of the A/D converter had 16 input channels which operated in a sequential mode. It was capable of accepting current loop inputs as well as voltage inputs. In the current investigation, the A/D converter was used to discretize only voltage signals. The input voltage range of the A/D converter could be adjusted using the software programmable gain amplifier, but it was normally set as -10 to 10 Volts. The digital output, Y, ranged from 0 to 4095, and was linearly related to the input voltage, X, as

$$X = 10Y/2048 \qquad \text{for } 0 < X < 10 \text{ Volts}$$

$$X = 10(Y-4095)/2048 \qquad \text{for } -10 < X < 0 \text{ Volts}$$

The discretization had an accuracy of 5 mV, and the minimum A/D conversion time was 40 , using the direct memory access.

Other peripheral units were an RX02 single disk drive unit, a Winchester drive, an LA50 printer and a VT100 CRT display monitor. Sampling was done using commercial subroutines in assembly language, while all computations were performed in FORTRAN IV

5.3.4 Hot-Film Measurements

Following a fresh calibration, the hot-film probe was carefully inserted into one of the three inlet ports of the test-section using the traversing system and mount, and measurements were taken at 5 mm intervals traversing the probe along the test-section radial axis. The flow rate and the gage pressure of the reference wall pressure tap were monitored to ensure that they remained constant throughout the experiment. After completing measurements at one axial station, the tunnel was shut off and partially emptied; the probe was then taken out and the sensors were cleaned. The entire calibration procedure was then repeated in the upstream empty section to evaluate new calibration constants. In most instances, the new constants were almost the same as the previous ones, although in some cases the difference between corresponding constants was as much as 5-10 %. For the next set of measurements at another axial location, the newly determined constants were always used. The problem of increasing fluid temperature, augmented with the possibility of contaminations getting entangled with the sensors, required to conduct data acquisition as quickly as possible, and for this reason, raw signals were instantaneously recorded in floppy diskettes to be processed at a later convenient time.

Figure 32 shows the data acquisition circuitry. As shown, the instantaneous anemometer outputs were directly fed to the A/D converter to determine and record the time averaged voltages $\overline{E}_1$ and $\overline{E}_2$. The same voltages, with the second one being delayed by 40 μs by a home-made analog delay line, were fed to the dual beam oscilloscope, amplified with a gain of 5 and low pass filtered at a frequency of 10 kHz (slightly less than the 'Nyquist-frequency', 12.5 kHz). The two oscilloscope outputs, AC coupled, were fed to the A/D converter. Using an interactive sampling program, it was possible to insert data such as the temperature of fluid at regular intervals.

The second signal was delayed by 40 μs, in order to permit simultaneous sampling of the two fluctuating signals by the sequential multiplexer. Thus, each set of fluctuating voltages, e_1 and e_2, recorded on the diskette, essentially originated at the same time from the two sensors. The electronic circuit of the delay line and its frequency response are shown in Figures 33 and 34. The signals had to be amplified at least 5 times to enhance the level of conversion accuracy, since the minimum possible resolution was only 5 mv for the -10 to 10 V range of the A/D converter.

For each position of the probe, typically 18 records (interspaced by a few seconds) of 1600 sets of data points were collected. The requirement for a large computer memory space, especially while computing autocorrelation and probability density functions, was the deciding factor in limiting the data acquisition to 18*1600 points. Inspite of having four channel inputs, it was possible to have a sampling frequency of 12.5 kHz (equivalent to a sampling time, Δt, of 80 μs) using special software.

5.3.5 The Computational Procedure

(A) Evaluation of Turbulence Parameters :

The procedure of computation of various turbulent parameters from the data stored on diskettes consisted of the following general steps.

(1) For each record,

(a) $\overline{U}$ was calculated from $\overline{E}_1$, $\overline{E}_2$ and T_f using,

$$\overline{U} = \frac{1}{2}\left[\frac{1}{B_1}\left(\frac{\overline{E}_1^{\,2}}{T_{op1} - T_f} - A_1\right)\right]^{1/n_1} + \frac{1}{2}\left[\frac{1}{B_2}\left(\frac{\overline{E}_2^{\,2}}{T_{op2} - T_f} - A_2\right)\right]^{1/n_2} \quad (5\text{-}12)$$

(b) $u+v$ and $u-v$, and thus u and v, were estimated from the first set of e_1 and e_2 using equations (5-6) and (5-7).

(c) Step (b) was repeated for all 1600 sets of e_1 and e_2 to create arrays of u and v (which were written on the same floppy disk replacing e_1 and e_2)

(d) One point moments such as $\overline{u^2}$, $\overline{u^3}$, $\overline{u^4}$, $\overline{v^2}$, $\overline{v^3}$ and $\overline{v^4}$ and the cross-correlation $\overline{uv}$ were then computed from these velocity arrays.

(2) Steps (a) to (d) were repeated for all 18 records and averaged to determine ensemble means.

(B) Evaluation of Autocorrelation Functions :

From the discrete time history, u_k^j, j = 1,2,3... m (m, the number of records = 18) and k = 1,2,3... n (n, number of points per record = 1600), the autocorrelation function $R_u^j(\tau)$ for each record was computed as

$$R_u^j(\tau) = \frac{\sum_{k=1}^{n-i} u_k^j\, u_{k+i}^j}{\sum_{k=1}^{n} u_k^j\, u_k^j}\left(\frac{n}{n-i}\right) \quad (5\text{-}13)$$

where the separation time, $\tau = i \times \Delta t$.

As before, the procedure was repeated for all m records, to evaluate the ensemble averaged autocorrelation function, $\mathcal{R}_u(\tau)$, as

$$\mathcal{R}_u(\tau) = \frac{1}{m} \sum_{j=1}^{m} \mathcal{R}_u^j(\tau) \qquad (5-14)$$

Following a similar analysis, the autocorrelation for the transverse velocity component, v , was determined as

$$\mathcal{R}_v(\tau) = \frac{1}{m} \sum_{j=1}^{m} \mathcal{R}_v^j(\tau) \qquad (5-15)$$

Using Taylor's hypothesis described in section 2.5, R_u and R_v were represented as a function of separation distance, α, as

$$R_u(\alpha) = \mathcal{R}_u(\tau)$$

and

$$(5-16)$$

$$R_v(\alpha) = \mathcal{R}_v(\tau)$$

where $\alpha = \overline{U}\tau$.

(C) Probability Density Calculations :

From each discrete time history, for example, u_k k = 1,2,3 ... N (N = 18*1600), a normalized time history was obtained as

$$b_k = \frac{u_k}{\sigma_u} \qquad (5-17)$$

where σ_u was the standard deviation of the ensemble.

The probability density of the normalized random variable was then computed as,

$$P_b(\beta) = \frac{P\left(\beta - \frac{\omega_b}{2} < b_k \leq \beta + \frac{\omega_b}{2}\right)}{\omega_b} \qquad (5\text{-}18)$$

where the numerator is the ratio between the number of points falling in the interval $(\beta - \frac{\omega_b}{2}, \beta + \frac{\omega_b}{2})$ and the total number of points, N. The window, ω_b, was chosen between 0.25 and 1 depending on the value of β (windows were narrower for lower values of β). By definition of probability,

$0 \leq P_b(\beta) \leq 1$ and also,

$$\int_{-\infty}^{\infty} P_b(\beta)\, d\beta = 1 \qquad (5\text{-}19)$$

For the bivariate probability of u and v, two normalized time histories were obtained as

$$b_k = \frac{u_k}{\sigma_u}$$

and (5-20)

$$l_k = \frac{v_k}{\sigma_v}$$

Then the joint probablity, density, $P_{b,\ell}(\beta,\lambda)$, was computed as

$$P_{b,\ell}(\beta,\lambda) = \frac{P\left(\beta - \frac{\omega_b}{2} < b_k \leq \beta + \frac{\omega_b}{2},\ \lambda - \frac{\omega_\ell}{2} < \ell_k \leq \lambda + \frac{\omega_\ell}{2}\right)}{\omega_b\ \omega_\ell} \tag{5-21}$$

By definition,

$$\int_{-\infty}^{\infty}\int_{-\infty}^{\infty} P_{b,\ell}(\beta,\lambda)\, d\beta\, d\lambda = 1 \tag{5-22}$$

It is interesting to note that

$$\int_{-\infty}^{\infty} P_{b,\ell}(\beta,\lambda)\, d\lambda = P_b(\beta)$$

and (5-23)

$$\int_{-\infty}^{\infty} P_{b,\ell}(\beta,\lambda)\, d\beta = P_\ell(\lambda)$$

5.3.6 Error Analysis for Hot-Film Measurements

(1) Yaw Effects

As described previously, using the traversing system and mount, it was possible to align the probe axis with the flow direction within $\pm 2^\circ$. The angular sensitivity of the probe was studied in an air jet by varying the angle between the probe axis and the flow direction using a swivelling arm, equipped with a micrometer-caliper that could read angles as small as 2'.

Figure 35 presents the variation of time averaged anemometer output voltage, $\overline{E}_1$, of one of the sensors of the cross-film probe with the mean velocity of the air jet for different yaw angles; θ represents the angle between the axis of the sensor and that of the jet. For a particular velocity, $\overline{E}_1$ increases monotonically with θ and reaches a maximum value at $\theta = 90^\circ$, where the axis of the sensor is normal to the axis of the jet. Figure 36 shows the response of the other sensor, where the output voltage, $\overline{E}_2$, presents a monotonic decrease with increasing value of and reaches the minimum value at $\theta = 90^\circ$, where the sensor axis is parallel to the jet axis. Figure 37 shows the sensitivity of the first sensor response with respect to $\overline{U}_J$ as well as to θ at a velocity of 22 m/s. The angular sensitivity of the sensor response decreases with increasing θ and suggests that small yaw might not affect the response significantly, when $\theta = 90^\circ$. The velocity sensitivity, however, demonstrates that the response of the sensor might vary significantly with velocity changes at $\theta = 90^\circ$, and very mildly at $\theta = 0^\circ$. Our interest, however, lies at $\theta = 45^\circ$, where both angular and velocity sensitivities are significant and equal to 0.038 V/m/s.

Figure 37 was obtained by fitting a least-square King's equation to each curve in Figure 35 as

$$\frac{\overline{E}_1^2}{T_{op1} - T_f} = A_1 + B_1 \left(\overline{U} \sin\theta \right)^{n_1} \qquad (5\text{-}24)$$

and then evaluating the velocity sensitivity, by differentiating the above equation with respect to $\overline{U}$, as

$$\frac{\partial \overline{E}_1}{\partial \overline{U}} = \frac{n_1 B_1}{2\overline{E}_1} \left(T_{op1} - T_f \right) \overline{U}^{\,n_1 - 1} \left(\sin\theta \right)^{n_1} \qquad (5\text{-}25)$$

and the angular sensitivity with respect to θ as

$$\frac{1}{\overline{U}} \frac{\partial \overline{E}_1}{\partial \theta} = \frac{n_1 B_1}{2\overline{E}_1} \left(T_{op1} - T_f \right) \overline{U}^{\,n_1 - 1} \left(\sin\theta \right)^{n_1 - 1} \cos\theta \qquad (5\text{-}26)$$

This method (based on King's law) is only approximate, since it assumes that the output voltage does not depend on the velocity parallel to the sensor. Corrections for parallel velocity have been developed (e.g. Champagne et al., 1967), but have not been considered at this stage.

(2) Temporal Resolution

The temporal resolution of the measuring system can be determined by comparing the characteristic times of the hot-film and the analog-todigital conversion system with the characteristic times of the flow. In the current flow field, a typical convection time (Corrsin, 1969) of the smallest relative motions (corresponding to viscous dissipation phenomenon) was

$$\left(\frac{1}{\overline{U}} \right) \left(\frac{\nu^3}{\epsilon} \right)^{1/4} \approx 13.5 \ \mu s \qquad (5\text{-}27),$$

while a typical convection time of the energy containing eddies was

$$\frac{L_u}{\bar{U}} \simeq 1.3 \quad ms \tag{5-28}$$

On the other hand, a characteristic time for the hot-film can be found as

$$\frac{d_{sensor}}{\bar{U}} \simeq 7.0 \ \mu s \tag{5-29}$$

while that for the data acquisition system (sampling time) was 80 μs. Therefore, it may be concluded that phenomena associated with energy production and transfer within the inertial subrange of the spectrum would be detected by the system; however, phenomena associated with energy dissipation, for example quantities such as $\overline{(\partial u/\partial t)^2}$ and $\overline{(\partial v/\partial t)^2}$, will be poorly estimated by the measurements.

(3) Spatial Resolution

The spatial resolution of cylindrical hot-film is limited by their finite length and also by the distance between sensors in the case of a cross-film probe. The length and spacing of the sensors can be compared with the characteristic length scales of the flow. In the present flow, the Eulerian integral length scale, L_u, was 4.71 mm, the Taylor microscale, λ_u, was 1.26 mm and the Kolmogoroff microscale, η_k, was 0.047 mm. For a probe with sensors having length $\ell_s \simeq$ 1.75 mm and spacing $\delta_s \simeq 0.5$ mm, one can determine

$$\frac{\ell_s}{L_u} = 0.37\,, \quad \frac{\ell_s}{\lambda_u} = 1.39\,, \quad \frac{\ell_s}{\eta_k} = 37.0$$

$$\frac{\delta_s}{L_u} = 0.11\,, \quad \frac{\delta_s}{\lambda_u} = 0.40\,, \quad \frac{\delta_s}{\eta_k} = 10.6 \tag{5-30}$$

The resulting errors in turbulence characteristics can be estimated from the above ratios and assuming a likely turbulence structure. For example, the measurement error in $\overline{u^2}$ can be estimated as (Corrsin, 1963)

$$\frac{\overline{u^2}_{measured}}{\overline{u^2}} = \frac{2\int_0^{\ell_s} (\ell_s - \kappa)\, R(\kappa)\, d\kappa}{\ell_s^2} \tag{5-31}$$

Using equation (2-44) one can simplify the above integral as

$$\frac{\overline{u^2} - \overline{u^2}_{measured}}{\overline{u^2}} \approx \frac{\ell_s^2}{24\,\lambda_u^2} \approx 0.08 \tag{5-32}$$

The spacial resolution of cylindrical cross-film sensors can be estimated in more detail using Wyngaard's (1968) spectral calculations. He provides the dependence of the ratio of measured and actual wave number spectra for cross-wire probes with $\delta_s/\ell_s = 0.5$ and various η_k/ℓ_s upon the dimensionless number $\kappa\,\ell_s$. The corresponding attenuation for typical conditions for the present experiments are as follows

κ	Streamwise Spectrum	Lateral Spectrum
$1/L_u$	7%	2%
$1/\lambda_u$	30%	20%
$1/\eta_k$	$\sim$ 100%	$\sim$ 100%

It can be concluded that the spatial resolution of the hot-film probe is adequate for measuring phenomena in the energy containing range of the spectrum but totally improper for those in the viscous range.

(4) End Conduction Effects

For a cylindrical hot-film sensor with an aspect ratio $\ell_s / d_s \approx 70$, conduction losses to supports can be neglected (Fingerson and Freymuth, 1983).

Chapter VI

THE MEASUREMENTS

PART A: MEASUREMENTS IN A SINGLE BUNDLE

6.1 AN OUTLINE OF MEASURING CONDITIONS

The majority of measurements with a single bundle were carried out at two flow rates with Reynolds numbers roughly equal to 62000 and 50000, based on the subchannel hydraulic diameter, the equivalent-pipe bulk velocity and an average water temperature (Table 2). Although some early measurements were performed at Reynolds numbers of about 100000, it was observed that at high Reynolds numbers, the long-time continuous operation of the water tunnel was hampered by the increasing rate of air suction into the system and also, due to the significant pressure drop along the bundle, the pressure inside the system was close to the vapour pressure of water, thus increasing the risk of water boiling near hot-films and sensor burn-out. Furthermore, our tests as well as those by several other investigators (e.g. Levchenko et al., 1967, and Rowe et al., 1974) have confirmed that in a fully developed turbulent flow, the friction factor and various turbulent parameters were relatively insensitive to Reynolds number. Therefore, there was no apparent need for collecting data at higher Reynolds numbers. According to Ibragimov et al. (1966), statistically stable turbulent flow can be achieved in a non-circular channel at a Reynolds number typically of about 10000, which is far below our experimental range.

Another concern during the experiments was whether the flow was fully developed at the measuring locations. The measuring stations were located at distances of $3d_h$, $8d_h$, $20d_h$, $23d_h$ and $35d_h$ from the entrance to the bundle. In a turbulent flow through a smooth circular pipe, in general, fully developed conditions are reached at an entrance length of 50-80 pipe diameters depending on the Reynolds number. According to Laufer(1954), fully developed conditions can be achieved after a distance of about 30 diameters, if the walls are rough enough to accelerate the boundary layer growth. Davies (1972) predicts that for pipes with sharp edges or bends, the entrance length can be as low as 30 diameters, or even less. Reynolds (1974) contends that the wall friction attains a fully developed value, after a distance of about 10-20 diameters. In the present geometry, the presence of endplates and Preston tubes enhances an earlier attainment of fully developed conditions. Therefore, it seems plausible that fully developed conditions would prevail at $x/d_h = 35$ and possibly at $x/d_h = 20\text{-}23$. The measured downstream development of mean pressure and mean velocity, presented in the following sections, has confirmed the validity of such an assumption.

6.2 MEAN STATIC PRESSURE

6.2.1 Wall Static Pressure

Figure 38 shows the wall static pressure distribution around the periphery of rod B, at $x/L = 0.20$ and 0.60. The pressure coefficient, C_p, was estimated using

$$C_p = \frac{\overline{P} - \overline{P}_{ref}}{\frac{1}{2}\rho U_{bt}^2} \qquad (6-1)$$

where $\overline{P}_{ref}$ is the static pressure at the reference wall pressure tap located in the upstream empty section.

A systematic variation of the wall static pressure was observed with the maxima approximately corresponding to the largest flow area and the minima to the rod gaps. The maximum variation in wall static pressure was about 8-10% for the upstream as well as for the downstream location. Within the central subchannel, the distributions appeared to be roughly symmetric about the central radial line of symmetry ($\phi = 45°$), consistent with the expectation that $\partial\overline{P}/\partial\phi = 0$, along the line of symmetry dividing identical, adjacent flow-cells. These distributions, however, must be treated with some reservation, since they are based on very few experimental points joined by a smooth cubic spline curve.

6.2.2 In-Flow Static Pressure

Figure 39 presents the distribution of mean static pressure along the test-section radial axis at x/L = 0.08, 0.50 and 0.91. The in-flow static pressure generally presented a low amplitude variation at all three locations, indicating that there was no significant pressure difference between the rod gap centre and the subchannel centre. It also indicated that blockage errors due to the presence of the pressure tubes were not significant.

The downstream evolution of mean static pressure at selective locations on the test-section radial axis and also the average mean static pressure at Re_{bh} = 50000 are shown in Figure 40 and only the average mean static pressure at Re_{bh} = 62000 in Figure 41. The broken vertical lines represent the entry and the exit planes of the test bundle. The mean static pressure of the reference wall pressure tap is represented at x/L = -0.08. Also shown on Figure 40, for comparison, are the corresponding wall static pressure values estimated from rod surface pressure distributions at x/L = 0.20 and 0.60. The static pressure loss at the bundle entry was equal to 10.8 kPa for Re_{bh} = 62000 and 7.85 kPa for Re_{bh} = 50000. The streamwise pressure gradient in the upstream half of the bundle was found to be about 21.58 kPa/m and 12.75 kPa/m length of the bundle, respectively for the two flow rates; At the downstream half of the bundle, the pressure gradients were found to decrease to approximately constant asymptotic values of 8.34 kPa/m and 5.59 kPa/m, respectively.

6.3 WALL SHEAR STRESS

Figure 42 shows the variation of local wall shear stress, $\tau_w(\phi)$, around the periphery of rod B, normalized with $\tau_{w_{av}}$, the average wall shear stress, computed from the asymptotic value of the average streamwise pressure gradient using equation (2-14).

The wall shear stress exhibited similar systematic variations at the developing region (x/L = 0.20) and at the borderline developed region (x/L = 0.60), having minima near the rod gaps and maxima near the largest flow area. The variation was about 15% of $\tau_{w_{av}}$ at x/L = 0.20 and 32% at x/L = 0.60. The shown cubic spline curve through the few experimental points is included as an aid to the eye, but should not be interpreted as exact. The measured wall shear stress distribution was compatible with the computational predictions of Bender and Switich (1968), derived using universal velocity distributions and neglecting secondary flows. Fakory and Todreas (1979) have also reported that in a triangular array of rods with s/d = 1.1 (close to our 1.14), the measured wall shear stress peaked at the largest flow area. On the other hand, many investigators, including Subbotin et al. (1971; s/d = 1.0 to 1.2), Hall and Swenningsson (1971; s/d = 1.217) and Trupp and Azad (1975;

s/d = 1.2 to 1.5), have observed a shift in peak of the local wall shear stress away from the largest flow area, slightly towards the rod gaps, and attribute this to the action of secondary flows. According to Kacker (1973), the effect of secondary flows on shear stresses can be neglected, only when the secondary velocities are less than 0.1 percent of the primary velocity. Kjellstrom (1978), among others, has measured secondary velocities in triangular arrays with s/d = 1.22 to be as much as 1% of the axial bulk velocity. For the present square subchannel with a smaller s/d of 1.14, the secondary velocities will probably be greater, and therefore, should not be ignored. In any case, the rather distant spacing and the relatively low accuracy of the Preston tubes do not permit an exact mapping of wall shear stress in our present setup.

The wall shear stress dependence on Reynolds number was studied separately using the same Preston tube instrumentation. This was done by measuring the wall shear stress at representative locations and at varying Reynolds numbers. The results of this brief study are presented in Figure 43. More discussion is included in section 7.1.

6.4 VELOCITY PROFILE

6.4.1 Mean Axial Velocity

Mean axial velocity distributions along the test-section radial axis are shown in Figures 44*, 45, 46 and 47. $\overline{U}_c$ is the mean axial velocity at the subchannel centre. The two vertical broken lines at r/R = 0.54 and 0.827 represent the central square subchannel boundaries. In all cases, as expected, the maximum axial mean velocity was found in the neighbourhood of the subchannel centre and the minimum near the rod gap centres.

At x/L = 0.5 and 0.91, the mean axial velocity distributions were roughly identical and the variation between the velocity in the rod gaps and that in the subchannel centre was about 20% of $\overline{U}_c$. At x/L = 0.08, closely behind the endplate, this variation was much larger, about 40% of $\overline{U}_c$, as expected considering that rod gaps were located in the wake of endplate peripheral ribs. Although the velocity profiles obtained using the hot-film probe as well as the pressure tubes look almost similar, the pressure tube measurements of mean velocity are more reliable; for a hot-film, the value of mean velocity is primarily determined

---

* Distributions of mean axial velocity and various turbulent parameters for two Reynolds numbers are presented almost throughout this chapter. Since most of these parameters were normalized, they appear to have approximately the same values at both Reynolds numbers. Often, a general and common discussion has been given without referring to any one particular Reynolds number. Nonetheless, wherever it was thought necessary, separate discussion (for each Reynolds number) has been provided.

by the value of A in the calibration equations (5-9) and (5-10), which, in turn, depends on the quality of the film surface, and in a slightly contaminated fluid flow as the present one, there is the possibility during operation that the value of A could change from time to time, thus resulting in an inaccurate estimate of the mean velocity. On the other hand, it should be added here that the slope of the calibration equation, B , however, would not be affected significantly (maximum variation of about 2-3%, observed from calibrations conducted at two consecutive days) by surface coating on the film, and therefore, reliable values for turbulence parameters might be expected, even when the mean velocity measurements are in error.

Figures 48, 49, 50 and 51 (correspond to Figures 44, 45, 46 and 47 respectively) show the downstream mean velocity development along selected lines parallel to the bundle axis. The mean axial velocity at the rod gaps increased gradually before reaching a nearly asymptotic value in the downstream half of the bundle; the velocity at the subchannel centre and its neighboring locations, however, was nearly constant in the entire bundle.

The downstream evolutions of mean pressure and mean axial velocity have shown that both quantities apparently reached asymptotic values in the downstream half of the bundle; thus it may be concluded that the flow was fully developed at $x/L = 0.91$ and probably so at $x/L = 0.50$.

6.4.2 Axial Turbulence Intensity

The variation of axial turbulence intensity $u'/\bar{U}_c$ (u' is defined as the root mean square value of u) along the radial axis is shown in Figures 52 and 53. At x/L = 0.91, u' was about 3.3% of $\bar{U}_c$ at the subchannel centre and had an average value of about 4.0% along the radial axis; these values are comparable to the 3.6% level in a fully developed pipe flow (Laufer,1974). The present distribution of axial turbulent intensity is in general agreement with that by Rowe et al. (1975; s/d = 1.125 and Re = 100000). At x/L = 0.5, the average value of u' was about 5.1% of $\bar{U}_c$, which is nearly 25% higher than the average intensity at x/L = 0.91. At x/L = 0.08, $u'/\bar{U}_c$ showed significant variation along the radial axis, from 1.4% at the subchannel centre to more than 10%, close to rod gap centres.

An interesting feature is the presence of relative minima of turbulence intensity generally at locations where the mean axial velocity gradient, $\partial\bar{U}/\partial r$, was near zero and of relative maxima at locations between rod gap centres and the subchannel centre, where the shear rate was maximum.

6.4.3 Radial Turbulence Intensity

The distribution of radial turbulence intensity, $v'/\bar{U}_c$, along the test-section radial axis is shown in Figures 54 and 55. In all three axial locations it can be observed that the radial turbulence intensity was minimum near the subchannel centre and maximum near the rod gap centres. At $x/L = 0.91$, the average value of v' was about 2.5% of $\bar{U}_c$; at $x/L = 0.5$, the typical v' was around 3.2% of $\bar{U}_c$. At $x/L = 0.08$, $v'/\bar{U}_c$ varied from a minimum of 2% at the subchannel centre to more than 10% near the inner rod gap centre.

Figures 56 and 57 present the variation of the ratio between radial and axial turbulence intensities, v'/u' , along the test-section radial axis. At the fully developed regions ($x/L = 0.91$ and 0.50), the ratio was typically 0.6 as is found in many other turbulent shear flows (Tavoularis, 1978).

6.5 MOMENTS AND CORRELATIONS

6.5.1 Skewness Factors

Skewness factor (defined as the third moment of a random variable, normalized by the cubic power of its standard deviation) is a measure of asymmetry of a random variable distribution. It is reminded that random variable with symmetric probability density functions, such as normal (or Gaussian) variables, have zero skewness.

Figures 58 and 59 show the variation of one point axial velocity skewness factor, $\overline{u^3}/u'^3$, along the test-section radial axis. At $x/L = 0.08$, the axial skewness factor demonstrated a significant variation, with near zero values in the rod gaps and negative values of about -2 at the subchannel centre. At x/L = 0.50 and 0.91, the skewness factors are small, never exceeding 0.5 in magnitude. Nevertheless, they also presented negative extrema at the subchannel centre and its adjacent locations. A negative skewness factor indicates that negative values of fluctuating velocity component, on the average, have higher amplitude than positive ones; since, by definition, the mean of a fluctuating quantity must vanish, the durations of typical events with negative fluctuations must be shorter than those with positive fluctuations. Stated differently, it also infers that high amplitude negative fluctuating velocity components occur more frequently than positive ones.

Figures 60 and 61 present the distribution of radial velocity skewness factor, $\overline{v^3}/v'^3$, along the test-section radial axis. At x/L = 0.08, the radial skewness factor has positive values (maximum of 2.1) in the inner half of the central square subchannel (0.54 < r/R < 0.68), indicating, of course, that high amplitude radial velocities occur more commonly in the direction of increasing r/R; the radial skewness factor in the outer half of the central square subchannel (0.68 < r/R < 0.83), however, has high negative values (minimum of -2.1) signifying that the high amplitude radial velocities are oriented more often in the reverse direction. The radial skewness factors at x/L = 0.50 and 0.91, present a relatively low amplitude variation, however maintaining approximately, if not exactly, a similar type of variation as at x/L = 0.08.

From the distribution of the two skewness factors (primarily from the data at x/L = 0.08), certain preliminary conclusions can be reached on the mechanism of momemtum transport at the entrance region of the bundle. At the inner half of the central subchannel, the dominant positive values of radial velocity component continuously carry fluid elements with negative momentum (corresponding to negative values of $\overline{u^3}/u'^3$) towards the subchannel centre and its adjacent locations, where the mean axial velocity is high. Similarly, at the outer half of the central subchannel, negative radial velocities, also, appear to transfer momentum deficit to the subchannel core, in an attempt to even out the shear, as postulated by phenomenological momentum transport theories.

6.5.2 Flatness Factors

Kurtosis or flatness factor of a random variable (defined as the fourth moment of a random variable normalized by the square of its variance) is a measure of the shape of the random variable probability density function. Results are often compared with the normal (Gaussian) random variable, which has a flatness factor of 3; any value lower than 3 would indicate a flatter probability density distribution (pdf) and vice versa.

Typical values of flatness factors of axial and radial turbulent velocities are presented in Table 3. At x/L = 0.50 and 0.91, the measured flatness factors were close to 3. However, at x/L = 0.08, at some locations, the flatness factors were as high as 20 indicating a peaky pdf with long tails on one or either side.

6.5.3 Reynolds Shear Stress and Correlation Coefficient

Figures 62 and 63 present the variation of Reynolds shear stress, $-\rho\overline{uv}$, normalized by the average wall shear stress, $\tau_{w_{av}}$ $(=\rho u_{av}^{*2})$, along the test-section radial axis. At x/L = 0.91, typical values of Reynolds shear stress were less than 15% of the average wall shear stress. The measured values were, generally, in agreement with the data presented by Trupp and Azad (1975). At x/L = 0.50, the maximum value of Reynolds shear stress was about 40% of $\tau_{w_{av}}$. At x/L = 0.08, the Reynolds stress showed significant variations with a positive maximum of 500% and a negative maximum of about 150-200% of $\tau_{w_{av}}$. The Reynolds shear stress at x/L = 0.50 and x/L = 0.91 was found comparable to the average wall shear stress computed from the asymptotic value of the average mean pressure gradient, $(\partial\bar{P}/\partial x)_{av}$. At the entrance region, however, $\tau_{w_{av}}$ apparently was not the appropriate scaling parameter, since the turbulence was dominated by the effects of sudden acceleration and obstruction by the endplate ribs.

Alternatively, Reynolds shear stress could be presented as 'correlation coefficient', by normalizing with the product of corresponding local standard deviations. The variation of correlation coefficient, $\overline{uv}/u'v'$, along the test-section radial axis is shown in Figures 64 and 65. At x/L = 0.50 and 0.91, the maximum value of the correlation coefficient was about 0.4-0.5, which is comparable to the typical value 0.4 in fully developed pipe flow and other shear flows.

In all cases, there was a systematic variation of the correlation coefficient with negative values in regions where the shear gradient, $\partial \bar{U}/\partial r$, was positive ($0.54 < r/R < 0.68$) and positive values in regions where the mean shear was negative ($0.68 < r/R < 0.83$). The correlation coefficient curves, in general, changed sign near points where the mean shear was zero, in confirmity with the gradient transport hypothesis.

6.5.4 Autocorrelation Coefficients

Autocorrelation coefficients, $R_u(\alpha)$ and $R_v(\alpha)$, at various locations along the test-section radial axis at x/L = 0.50 and x/L = 0.08 are presented in Figures 66 and 67. respectively. In all cases, the autocorrelation coefficients generally satisfied the relation

$$R_u(\alpha) > R_v(\alpha) \qquad (6\text{-}2)$$

except perhaps at large separations, where both curves had small amplitudes.

At x/L = 0.50, the autocorrelation coefficients decreased with separation time and presented no significant negative peak. This suggests that there were no apparent periodic pulsations in the flow. This differs from the findings of Rowe et al. (1975), who have reported that periodic pulsations were present at locations between rod gaps and the subchannel centre in a square array with s/d = 1.125 at Re_{bh} = 10000. Their conclusions were based on the relatively large amplitude of the first negative peak, which alone does not indicate conclusively the presence of such periodic pulsations.

At x/L = 0.08, the autocorrelation coefficients near the subchannel centre (r/R = 0.67 and 0.72) presented a decay which could be approximated as exponential (exponential vanish asymptotically at infinity and do not have any negative region; the present results, however, had a small negative region with a maximum amplitude of about 0.05-0.09), consistent with the fact that the flow was essentially isotropic near the subchannel centre. At r/R = 0.57 (see also Figure 68), behind the endplate peripheral rib, the autocorrelation coefficient presented a periodic oscillations, suggesting the possibility of vortex shedding from the endplate ribs. This possibility was confirmed by calculating the Strouhal number (e.g. Reynolds, 1974) as $St = fd/\overline{U}$

where f was the frequency of oscillation of the autocorrelation function in c/s, d was the nominal width of the rib and $\overline{U}$ was a typical velocity. Since the mean velocity upstream of the rib (2.85 m/s) was different from the downstream velocity (2.15 m/s), Strouhal number was calculated using each velocity; the values were equal to 0.13 and 0.18 respectively, which are in the same range as the Strouhal number for rectangular cylinders in uniform flows ($\simeq$ 0.15).

6.6 SCALES

6.6.1 Integral Length Scales

The longitudinal Eulerian integral length scale was evaluated as the product of the local mean axial velocity and the longitudinal integral time scale, as explained in section 3.6.1.

Ideally, the time scale, T_u, should be estimated by integrating $R_u(\tau)$ from zero to infinity. As is the common practice, however, it was calculated by integrating $R_u(\tau)$, until it first crossed the time axis, as

$$T_u = \int_0^{\tau_0} R_u(\tau)\, d\tau \qquad (6\text{-}3)$$

where τ_0 corresponds to the first occurrence of $R_u(\tau) = 0$.

In a similar way, T_v was estimated using

$$T_v = \int_0^{\tau_0} R_v(\tau)\, d\tau \qquad (6\text{-}4)$$

This procedure provides an unambiguous estimate of the integral length scale, when the autocorrelation function does not have a significant negative region.

At locations between the rod gap centre and the subchannel centre, where the autocorrelation function exhibits alternating regions with relatively large negative and positive peaks, this procedure results in scales larger (by as much as 10%) than scales computed by long time integration. This is a consequence of the fact that although negative and positive regions succeed each other, the peak magnitudes decrease monotonically, so that the contribution of the first negative region to the integral is stronger than the contribution of the subsequent positive region and so on. For such cases it would be preferable to integrate the autocorrelation function over a long interval, namely upto 25-30 integral scales or upto a point where the peaks have negligible amplitude (for example 0.01).

In the current investigation, since most of the autocorrelation functions did not show a strong negative peak, the integral length scales were computed using equations (6-3) and (6-4) and Taylor's hypothesis. Figure 69 presents the variation of integral length scales along the test-section radial axis. At the inner half of the central square subchannel, the average value of L_u was about $0.35\,d_h$, while at the outer half it was generally about $0.27\,d_h$; The present scales do not compare very well with the results of Rowe et al. (1975), who have reported that the typical L_u was about $0.6\,d_h$ for $s/d = 1.125$ and about $0.35\,d_h$ for $s/d = 1.25$ in a square subchannel. The difference is primarily attributed to the method of determining the length scale.. Rowe et al. have estimated the integral scale by fitting an exponentially decaying sinusoidal curve to the first eleven measured points of the autocorrelation function and then integrating the area under the fitted curve to infinity.

The Eulerian integral length scale for the radial component, L_v, shows systematic variation with high values ($0.28\,d_h$) corresponding to the rod gaps and low values ($0.14\,d_h$) to the neighbourhood of the subchannel centre. The fact that L_u and L_v in rod gaps are larger than the gaps is not necessarily contradictory, since these scales correspond to velocity components and separation in directions other than the line of minimum distance between rods.

6.6.2 Microscales

The variation of microscales, λ_u and λ_v, along the test-section radial axis, is shown in Figure 70. They were computed using equations (2-47) and (2-48).

The typical λ_u was about $0.08\,d_h$, which was nearly 23% of the corresponding integral length scale L_u. At $x/L = 0.50$, λ_v was about $0.05\,d_h$, which was also approximately 24% of the corresponding L_v. It is reminded that the ratio of Taylor's microscale to integral length scale decreases with increasing Reynolds number, following the increasing separation between energy containing eddies and dissipation eddies. Two alternative ways of evaluating microscales have been discussed and compared with the current estimate in the next chapter.

6.7 PROBABILITY FUNCTIONS

6.7.1 Single Variate Probability Density Functions

The probability density functions (pdf) of axial and radial velocity components at representative locations are shown in Figures 71 and 72. The presented pdf, estimated from normalized time histories, have a standard deviation of unity; also shown on these figures, is the pdf of a normal random variable with a unity standard deviation.

The pdf at $x/L = 0.50$ show minor departure from the normal pdf, consistent with the small values of their skewness factors; also, their maxima are close to 0.4, the maximum of a normal pdf, consistent with the fact that their flatness factors have a value of approximately 3. In contrast, at $x/L = 0.08$ the non-Gaussian character of the signal is demonstrated in the pdf, as also has been seen in skewness and flatness factors.

6.7.2 One-Point Bivariate Probability Density Functions

Isoprobability contours of the joint pdf, obtained from normalized time histories of u and v, are shown in Figure 73. Also shown, are the isoprobability contours of a jointly normal pdf, with the same value of the correlation coefficient, generated using

$$P^{N}_{b,\ell}(\beta,\lambda) = \frac{1}{2\pi\sqrt{1-\rho^2}} \exp\left[-\frac{1}{2(1-\rho^2)}(\beta^2 - 2\beta\lambda + \lambda^2)\right] \qquad (6\text{-}5)$$

where $\rho = \overline{b\ell}$. For the case presented, the two random variables appear nearly jointly normal. The small departure is partly due to experimental scatter and partly due to systematic deviations from normality.

From the isoprobability contours of the joint pdf, it is possible to evaluate, approximately, the correlation coefficient using

$$\frac{\overline{uv}}{u'v'} = \frac{a^2 - b^2}{a^2 + b^2} \qquad (6\text{-}6)$$

where a is the length of the axis of the ellipse, passing through the quadrants where uv is positive, and b is the length of the other (perpendicular) axis. Besides, the joint pdf could also be used to evaluate marginal probability (by integrating one of the two variables) and conditional probability (by keeping the value of one of the variables constant).

Joint pdf could be alternatively plotted on three-dimensional graphs with the horizontal axes representing the two random variables and the vertical axis the joint probability density. Figures 74(a) and 74(b) show sample jointly normal pdf corresponding to selected measured correlation coefficients. By rotating and tilting these solid figures using software, it is possible to have clear view of details in joint pdf.

PART B: MEASUREMENTS WITH AN UPSTREAM BUNDLE

6.8 DESCRIPTION OF MEASUREMENT CONDITIONS

After the upstream bundle was inserted, preliminary tests were conducted to determine the total pressure drop across the two bundles at various flow rates. Also, the air suction rate through flanges and ports into the system was visually monitored for different flow rates and elevations of the pressurizing tank. Following these preliminary investigations, a flow rate, at which the air suction rate would be insignificant, and also, the Reynolds number would be sufficiently high (about 45000), was chosen to conduct the initial set of mean flow measurements, reported in this chapter (see Table 4). Substantial modifications of the system would be required in order to produce suction-free, higher Reynolds number flow. Furthermore, although some hot-film measurements were attempted, it was realized that safe, stable operation of hot-films would not be possible without a complete disassembly and thorough cleaning of the water tunnel. For lack of time and funds for hot-film repairs, turbulence measurements in two-bundle settings were postponed. It was assessed, though, that mean wall shear stress and mean velocity measurements would be sufficient to demonstrate the gross effects of the upstream bundle orientation.

6.9 STATIC PRESSURE

6.9.1 Wall Static Pressure

The distribution of wall static pressure around the periphery of rod B is shown in Figure 75. The static pressure exhibited low-amplitude variation around the rod periphery, with the downstream holes having C_p values 17% higher than those of the upstream holes. Although the variation of mean static pressure around the rod periphery at x/L = 0.20 was roughly similar to that in the single bundle experiments, the variation at x/L = 0.60 showed minor deviation near the rod gap ($\phi = 0^\circ$) from the single bundle distribution. Since the mean static pressure variation was observed to be essentially uniform around the rod boundary, this could be attributed to experimental error.

6.9.2 In-Flow Static Pressure

The in-flow static pressure, measured at the three streamwise locations of the test bundle, did not reveal any apparent systematic variation along the test-section radial axis; therefore, the measurements are not presented here.

Figure 76 shows the downstream variation of average mean static pressure. As in the single bundle case, the streamwise pressure gradient reached an asymptotic value at the downstream half of the test bundle and was equal to 4.81 KPa/m. It might be interesting to note that in the upstream half of the bundle, the pressure gradient was about 7.50 kPa/m, only 1.6 times the downstream asymptotic value. This ratio was appreciably smaller than that in the single bundle experiments at identical conditions. This is consistent with the fact that the flow exiting from the upstream bundle was a fully developed turbulent flow, and therefore, it would take a much shorter length (about 15-20 d_h) to regain fully developed conditions in the test bundle.

6.10 MEAN AXIAL VELOCITY

Figure 77 presents the mean axial velocity distribution along the test-section radial axis. In all cases, the general systematic variation was consistent with the single bundle measurements, with minima corresponding to the rod gaps and maxima to the largest flow areas. As before, the velocity distributions at x/L = 0.50 and 0.91 were roughly identical, and the difference between the maximum and the minimum velocities was about 20% of $\overline{U}_c$. At $x/L = 0.08$, the mean axial velocity presented a sudden drop at $r/R = 0.42$, close to the centre of the inner square subchannel, adjacent to the central square subchannel. This is due to the presence of the upstream bundle rod, positioned at the first peripheral rib, which interferes with the flow through the inner square subchannel (see Figure 11). However, after about $r/R = 0.55$, the velocity profile was almost the same as that in the single bundle setting with the maximum variation about 40% of $\overline{U}_c$. This could be expected, since the two upstream rods in the second peripheral rib coincide exactly with the corresponding test bundle rods, and also, the influence of the upstream central rod in the third peripheral rib would be less persistent because of the relatively large flow area near the outer wall surface.

The downstream development of mean velocity along selected lines parallel to the bundle axis is shown in Figure 78. As observed in single bundle flow measurements, the mean axial velocity increases gradually in the rod gaps before reaching a nearly constant asymptotic value in the downstream half of the test-bundle, and also the velocity at the subchannel centre is essentially constant.

6.11 WALL SHEAR STRESS

The variation of local wall shear stress around the periphery of rod B is shown in Figure 79. The local wall shear stress at $x/L = 0.60$, exhibited the same type of variation, as before, with the maxima corresponding to the largest flow area and the minima roughly to the rod gaps. Also at $x/L = 0.20$, the wall shear stress variation was consistent with the single bundle measurements at all locations around the rod periphery, except at $\phi = -60^\circ$, where the new value was about 20% smaller than that in the single bundle. This decrease in wall shear stress is consistent with the sudden drop in the local mean axial velocity at $r/R = 0.42$ (explained in the previous section), which roughly corresponds to $\phi = -60^\circ$. Assuming that the friction factor is almost constant around the rod periphery for a given flow rate, the local wall shear stress then becomes a direct function of only the local bulk velocity (different from subchannel bulk velocity; see chapter II). Therefore, any drop in the local mean axial velocity (and hence, the local bulk velocity) would result in a decrease in the local wall shear stress (see equation 2-26).

Chapter VII

ANALYSIS AND DISCUSSION OF RESULTS

7.1 ANALYSIS OF FRICTION FACTOR

Friction factor represents a dimensionless form of wall shear stress and is generally used to compare the flow resistance of different channel geometries at identical Reynolds numbers or of a particular channel geometry at different Reynolds numbers. Since friction factor may vary along the periphery of non-circular channels, it was decided to present mainly the average friction factor for the central square subchannel of the test-section, f_{av}, which was computed from the measured average wall shear stress and the equivalent-pipe bulk velocity, using equation (2-24). Table 5 contains these values for three Reynolds numbers, 45000*, 50000 and 62000. It can be observed that the average friction factor decreases with increasing Reynolds number of the flow, as is normally the case in pipes and channels. Also presented in Table 5 is the friction factor, f_p, of a circular pipe evaluated at the above three Reynolds numbers using equation (2-22) (the values obtained from equation (2-21) were almost the same). The average friction factor of the central square subchannel was consistently

---

* Corresponds to two bundle measurements.

about 85% of the circular pipe friction factor for all three flow rates.

The present measurements of average friction factor were comparable to those by other investigators. As seen from Table 5, the measured f_{av} was within 5% from Trupp and Azad's (1975) results (equation 2-29). Also, the measured ratio f_{av}/f_p was between the theoretical values 0.777 and 1.028, suggested by Ibragimov (1967) and by Subbotin et al. (1971) respectively (equations 2-27 and 2-28).

The Reynolds number dependence of local friction factor at selected locations around the periphery of rod B was independently evaluated from Preston tube measurements of local wall shear stress, $\tau_w(\phi)$, at different flow Reynolds numbers. The local friction factor was then computed from the local wall shear stress, as

$$f(\phi) = \left(\frac{8\tau_w(\phi)}{\rho U_{bh}^2} \right) \qquad (7-1)$$

and the results, presented in Figure 80 for $\phi = 60^\circ$ at $x/L = 0.20$ and for $\phi = 60^\circ$ at $x/L = 0.60$, show that the friction factor decreased with increasing Reynolds number and approached a constant asymptotic value when the Reynolds numbers larger than about 60000.

Equation (7-1), of course, does not provide an exact estimate of local friction factor, since the local friction factor requires knowledge of the local bulk velocity, U_{bl} (equation 2-26). However, the local bulk velocity of an elementary area should be roughly proportional to the bulk velocity of the subchannel, and therefore, the shape of curves in Figure 80 should not be affected by the use of subchannel bulk velocity in equation (7-1).

7.2 EXPERIMENTAL AND THEORETICAL ESTIMATES OF EDDY VISCOSITY

As a first step in evaluating test-section radial eddy viscosity of axial momentum, $\nu_{T,r}^{u}$, the mean axial velocity gradient, $\partial \bar{U}/\partial r$, along the test-section radial axis was computed by fitting a cubic spline curve through the pressure tube velocity measurements, since as explained before, mean velocity profiles obtained using pressure tubes were more reliable than those obtained using hot-films. The other parameter required to estimate eddy viscosity, the Reynolds shear stress, was, however, measured using the hot-films. It should be reminded that turbulence parameters measured by the hot-film would be more accurate than the mean velocity because of their dependence primarily on the slope of the calibration equation, which did not change considerably during the operation of the hot-film, as discussed before. Since the Reynolds stress and the mean velocity gradient belonged to two different ensembles, the computed mean velocity gradient was multiplied by the ratio between the subchannel centreline velocity measured using the hot-film and that measured using the pressure tubes to compute the mean velocity gradient that would correspond to the hot-film ensemble. The normalized value of mean velocity gradient, $d_h/\bar{U}_c \cdot \partial\bar{U}/\partial r$, was typically about 0.16-0.24 at the high shear regions, at x/L = 0.50 and x/L = 0.91. At x/L = 0.08, the corresponding maximum value was 0.44-0.58.

From the velocity gradient data and the measured Reynolds shear stress, $\nu_{T\,r}^{\,u}$ at various locations along the test-section radial axis was computed using equation (2-54). In almost all cases, the mean velocity gradient and the Reynolds stress had the same sign, which resulted in positive eddy viscosity values. The computed eddy viscosity was generally one or two orders of magnitude higher than kinematic viscosity of the fluid, demonstrating the dominance of Reynolds stresses over viscous stresses along the centreplane of the test-section; the ratio between the average eddy viscosity and the kinematic viscosity was about 150 at x/L = 0.91, 400 at x/L = 0.50 and 550 at x/L = 0.08. Figure 81 shows the variation of $\nu_{T\,r}^{\,u}$ along the test-section radial axis at x/L = 0.91. There was a considerable scatter in the presented data, reflecting the relatively low accuracy of this procedure but also deviations from gradient transport. The accuracy of the above procedure was particularly poor near the rod gap centres and the subchannel centre where both the Reynolds shear stress and the velocity gradient were close to zero.

Despite the above reservations, it is assessed that a constant eddy viscosity across the subchannel might be sufficient as crude model of the flow, except near the rod surfaces. The values of eddy viscosity at the fully developed region (x/L = 0.91) are compared with results of other investigators in Table 6. Before comparing the results, an important point must be considered. Theoretical predictions, outlined in section 2.6.3, refer to flow-cell radial and peripheral eddy viscosities of axial momentum. Our results, however, would correspond to test-section radial eddy viscosity of axial momentum. Although the axial directions of both the test-section as well as the flow-cell are the same, their radial and peripheral directions are different.

Figure 82(a) corresponds to rod gap centre (and its adjacent locations), where the test-section radial direction coincides with the flow-cell peripheral direction, thus making $\nu_{T\,r}^{\,u}$ and $\nu_{T\,\phi}^{\,u_x}$ almost the same (where $\phi = 0°$ and $y = y_0$). Figure 82(c) corresponds to the subchannel centre (and its adjacent locations), where it can be assumed that $\nu_{T\,r}^{\,u} = \nu_{T\,\phi}^{\,u_x} = \nu_{T\,a}^{\,u_x}$, since near the subchannel centre (as near a pipe flow axis) the mean velocity gradient and the Reynolds shear stress are axisymmetric. Figure 82(b) corresponds to locations between the subchannel centre and the rod gap centre, where $\nu_{T\,r}^{\,u}$ is not equivalent to $\nu_{T\,\phi}^{\,u_x}$ or $\nu_{T\,a}^{\,u_x}$. At these locations, the measured values of

ν_{Tr}^{u} should however have the same order of magnitude as the theoretical estimates of $\nu_{T\phi}^{u_x}$ and $\nu_{Ta}^{u_x}$.

Table 6 presents ν_{Tr}^{u} normalized by local values of u^* and y_0, at three representative locations along the test-section radial axis. For each value of r/R, the corresponding angle, ϕ, was computed and then y_0 was evaluated using equation (2-7), while u^* was computed from the measured local wall shear stress using equation (2-25). As seen from Table 6, the variation of $\nu_{Tr}^{u}/y_0 u^*$ along the test-section radial axis was similar to the ones proposed by Nijsing et al. (1966) (equation 2-61) and Kattchee and Reynolds (1962) (equation 2-64). For r/R = 0.57 and 0.62 (ϕ = 11.84° and 22.21°), the measured value of eddy viscosity, in general, was closer to $\nu_{T\phi}^{u_x}$ rather than to $\nu_{Ta}^{u_x}$ and for r/R = 0.67 (near subchannel centre; ϕ = 42.25°), as expected, ν_{Tr}^{u} was almost the same as $\nu_{T\phi}^{u_x}$ and $\nu_{Ta}^{u_x}$. Some reservation would be necessary in drawing such conclusions, since the computed values of eddy viscosity were only approximate due to the procedure of computation of mean velocity gradient.

7.3 LOCAL ISOTROPY AND KOLMOGOROFF'S SCALES

7.3.1 Tests for Local Isotropy

(A) A minimum condition for the approximate applicability of local isotropy, as explained in section 3.5.3, is that $R_\lambda > 100$, although $R_\lambda > 1000$ has been suggested as a safer criterion. This condition was tested at a few representative locations of the test-section, and it was found that R_λ was typically about 250 at the fully developed region and about 350 at the entrance region. Therefore, deviations from local isotropy are expected to be rather small at nearly all locations in the test-section, except near the entrance, where the turbulence might be intermittent.

(B) Another condition due to Corrsin (1958) for the applicability of local isotropy in the mixed inertial-viscous range is

$$\left(\frac{\epsilon}{\nu}\right)^{1/2} \gg \left(\frac{\partial \bar{U}}{\partial r}\right) \qquad (7\text{-}2)$$

where ϵ is the turbulent kinetic energy dissipation rate (evaluated in the following section*). At the subchannel centres of the fully developed regions as well as the entrance regions, where the shear gradient was near zero, this condition was well satisfied. However, at high shear locations $(\epsilon/\nu)^{1/2} / (\partial \bar{U}/\partial r) \approx 12.5$ in fully developed regions and ≈ 4.5 in the entrance region. Corrsin's condition was, therefore, at best weakly satisfied at these locations.

---

* The dissipation rate, used in the local isotropy test, was actually evaluated from isotropic relations.

7.3.2 Turbulent Energy Dissipation Rate

The turbulent energy dissipation rate at various locations along the test-section radial axis was estimated, as an order of magnitude, using equation (2-49) under the assumption of isotropic turbulence. Figure 83 presents the variation of energy dissipation rate, along the test-section radial axis, at Re_{bh} = 50000. The dissipation rate appeared to be the lowest at the subchannel centre, where the shear rate was minimum. This is to be expected, since production of turbulent kinetic energy by mean shear would be small, and turbulence would be maintained by diffusion from high shear regions. Also shown on Figure 83 is the dissipation rate at a few locations in the square subchannel for Re_{bh} = 62000; the dissipation rate was generally higher for the higher flow rate at identical locations, as expected by scaling all terms in the turbulent kinetic energy equation.

7.3.3 Kolmogoroff's Scales

The fine structure scales of turbulence were computed from ϵ and ν using Kolmogoroff's equation (2-50). Figure 84 presents the variation of Kolmogoroff's length scales along the test-section radial axis for Re_{bh} = 50000. It is observed that the fine structure scales were typically larger at the subchannel centre, where the viscous dissipation was minimal and smaller at high shear regions where the viscous dissipation was higher. Also, the largest fine structure scales in the entire flow field, as expected, were present at the subchannel centre of the entrance region where the flow exiting from the upstream section was similar to a fully developed, core channel flow, and viscous dissipation would be extremely small. Also presented in Figure 84 are the Kolmogoroff's length scales at representative locations for $Re_{bh} = 62000$, which were about 10% smaller than those for $Re_{bh} = 50000$, in accordance with the expected trend that the dissipation scales decrease in size as Reynolds number increases.

The Kolmogoroff's time scales were typically about 1.8 ms to 2.5 ms at x = 0.50; at x/L = 0.08, they were typically about 1.0 ms at high shear regions and 4.6 ms at the subchannel centre for $Re_{bh} = 50000$.

7.4 ALTERNATIVE APPROACHES TO MICROSCALE COMPUTATION

7.4.1 Microscale from the Exact Time Derivative

The mean squared time derivative of the fluctuating velocity components in equation (2-47) were computed, for example, as

$$\left(\frac{\partial u}{\partial t}\right)^2 \simeq \left(\frac{\Delta u}{\Delta t}\right)^2 = \frac{\sum_{j=1}^{m} \sum_{k=1}^{n-1} \left(\frac{u_{k+1}^j - u_k^j}{\Delta t}\right)^2}{m\,(n-1)} \tag{7-3}$$

where the minimum possible sampling time for cross-film signals, Δt, was equal to 80 μs (for notation see section 5.3.5); when the smaller time scales in the flow field are smaller than 80 μs, the accuracy of this procedure is limited. An improved estimate of mean square derivations could, perhaps, be obtained by repeating the above calculations for several Δt and extrapolating the values to $\Delta t = 0$. In practice this was done by computing differences between samples separated by 1, 2, 3, 4, 5, and 6 minimum time steps of 80 μs. Figure 85(a) shows $\overline{(\Delta u/\Delta t)^2}$ as a function of Δt; as expected, $\overline{(\Delta u/\Delta t)^2}$ decreased monotonically with increasing time gap. A smooth polynomial was fitted through the points, and the point of intersection of this polynomial with the vertical axis was assumed to represent the exact value of $\overline{(\partial u/\partial t)^2}$. The thus estimated value was typically 15-20% higher than $\overline{(\Delta u/\Delta t)^2}_{\Delta t = 80\mu s}$, used in section 6.6.2, which would result in a 7-9% decrease in the value of Taylor's microscale of axial velocity component. Following the same procedure, the decrease in Taylor's microscale of radial velocity component was estimated, to be about 8-10% (Figure 85b).

7.4.2 Microscale from the Curvature of Autocorrelation Function

The Taylor's microscale of axial velocity component was computed as the curvature of autocorrelation coefficient, $R_u(\alpha)$ at $\alpha = 0$; this was done by fitting a parabola (equation 2-44) to the first few points of the autocorrelation function and determining the point of first intercept with the α-axis. Since the parabola fitting procedure is somewhat cumbersome, alternatively, in the, current study, equation (2-44) was modified to a linear form as

$$\log \alpha - \log \lambda_u = \frac{1}{2} \log 2(1 - R_u) \qquad (7\text{-}4)$$

and the experimental points were plotted with $\log \alpha$ as the vertical axis and $\frac{1}{2} \log 2(1-R_u)$ as the horizontal axis (Figure 86a). The intercept of the least square fitted straight line with the vertical axis should then represent the value of λ_u. The procedure was repeated for a few other locations in the test-section, and it was found that the Taylor's microscale of axial velocity component, computed using this procedure was typically 10-12% smaller than the one presented in section 6.6.2. Also, the typical value of Taylor's microscale of radial velocity component, estimated using a similar procedure, was found to be about 9-12% smaller than that presented in section 6.6.2 (Figure 87b). This level of agreement is assessed as satisfactory considering the large number of systematic and random error sources in these results.

Chapter VIII
CONCLUSIONS

The present study was successful in accomplishing most of its objectives. Although the pace of the research at the initial stage was hampered by certain operational problems, the progress was relatively faster at the later stage. It proved to be definitely advantageous to store raw turbulence signals and process them at a later time. This not only reduced the operation time of the water tunnel, but also made it possible to compute as many parameters as needed with the minimum number of experiments. Apart from the results presented in the study, the stored data will be also used to compute power spectra by evaluating the Fourier transform of the autocorrelation function. Furthermore, computations of such quantities as cross-correlation coefficient and cross-spectra are also planned.

Following are the main conclusions drawn from the results of the study on roughly square subchannels with $s/d \approx 1.14$.

1. The mean pressure is essentially uniform across a particular flow cross-section; the mean pressure gradient reaches a constant asymptotic value at an entrance length of about 20 hydraulic diameters in a single bundle and at a shorter distance when the bundle is preceded by a differently oriented bundle.

2. The local wall shear stress exhibits, a systematic variation with maxima corresponding to largest flow area and minima to rod gaps; the measured local wall shear stress is comparable to the average wall shear stress estimated from the average asymptotic pressure gradient.
3. The subchannel average friction factor is about 85% of that in pipe flow; the subchannel average friction factor as well as the local friction factor decrease with increasing Reynolds number.
4. The mean velocity distribution is comparable to that in a fully developed pipe flow, having maxima corresponding to subchannel centres and minima to rod gaps.
5. The streamwise turbulent intensity at the fully developed region is about 3.3-4.0% of the subchannel centreline velocity, which is comparable to the 3.6% level in a fully developed pipe flow (Laufer, 1974). The transverse turbulent intensity is about 60% of the streamwise turbulence intensity as generally observed in turbulent shear flows.
6. The magnitude of the shear stress correlation coefficient at the fully developed high shear region is about 0.4 as is in a fully developed pipe flow. It presents a systematic variation with negative values where the shear gradient is positive and

positive values where shear gradient is negative; it changes sign, in general, near locations where the shear gradient vanishes.

7. The eddy viscosity is typically one or two orders of magnitude larger than the kinematic viscosity; the measured eddy viscosity distribution is compatible with those predicted by Nijsing et al. (1966) and Kattchee and Reynolds (1962).
8. The turbulent flow at the fully developed region, in general, is comparable to turbulent channel flow; at the entrance region, near the subchannel centre, it preserves the upstream channel flow features, while behind endplate ribs vortex shedding is observed.
9. Streamwise and radial integral length scales at fully developed regions are roughly about 30% and 20% of the subchannel hydraulic diameter respectively, while the corresponding Taylor microscales are about 8% and 5% respectively. The Kolmogoroff scales are typically about 0.3% of the hydraulic diameter.
10. The turbulent kinetic energy dissipation rate is typically large at high shear regions and lower near subchannel centres, where the production of turbulent kinetic energy by mean shear is small.

Current continuation of the present investigation includes evaluation of the effects of realistic rod-spacers and wearpads on flow mixing and other mean flow quantities, as well as further assessment of the effects of upstream bundle orientation. Another part of the study will be concerned with cross-channel mixing by injection of heated water at different locations in the subchannels.

BIBLIOGRAPHY

Allen, J. M. (1976), Systematic study of error sources in skin-friction balance measurements, NASA TN D-8291.

Bankoff, S. G. and Rosler, R. S. (1962), Constant-temperature hot-film anemometers as a tool in liquid turbulence measurements, Rev. Sci. Instrum., Vol. 33, pp. 1209-1212.

Beckwith, T. G. and Buck, N. L. (1961), Mechanical Measurements, Addison-Wesley, Reading, Massachusetts.

Bellhouse, B. J. and Schultz, D. L. (1967), The determination of fluctuating velocity in air with heated thin-film gauges, J. Fl. Mech., Vol. 29, pp. 289-295.

Bender, D. J. and Switich, D. M. (1968), Turbulent velocity distribution in a rod bundle, ASME 68-WA/HT-36.

Benedict, R. P. (1977), Fundamentals of Temperature, Pressure and Flow Measurements (2nd edition), John Wiley & Sons, New York.

Bradshaw, P. and Unsworth, K. (1974), A note on Preston tube calibrations in compressible flow, AIAA J., Vol. 12, No. 9, pp. 1293-1294.

Brison, J. F., Charnay, G. and Comte-Bellot, G. (1979), Calculation of heat transfer between hot-film and substrate by means of a two-dimensional model: Prediction of the dynamic response of conventional probes, Int. J. Heat Mass Transfer, Vol. 22, pp. 111-119.

Bugg, J. (1984), Development of a twin needle conductance probe for two-phase flow measurements, APRP-AE-69, AECL, Chalk River Nuclear Laboratories, Chalk River, Ontario.

Champagne, F. H., Sleicher, C. A. and Wehrmann, O. H. (1967), Turbulence measurements with inclined hot-wires, J. Fl. Mech., Vol. 28, pp. 153-159.

Chue, S. H. (1975), Pressure probes for fluid measurement, Prog. Aerospace Sci., Vol. 16, pp. 147-223.

Coles, D. (1956), The law of the wake in the turbulent boundary layer, J. Fl. Mech., Vol. 1, pp. 191-198.

Corrsin, S. (1958), Local isotropy in turbulent shear flow, NACA Res. Memo. 58B11.

Corrsin, S. (1963), Turbulence: experimental methods, Handbuch der Physik, Vol. 8, Part 2, pp. 521-590, Springer-Verlag, Berlin.

Creer, J. M., Rowe, D. S., Bates, J. M. and Sutey, A. M. (1975), Effects of sleeve blockages on axial velocity and intensity of turbulence in a unheated 7x7 rod bundle, BNWL-1965, Pacific Northwest Laboratory, Richland, Washington.

Creer, J. M. and Bates, J. M. (1976), Effects of sleeve blockages on air velocity distributions in an unheated 7x7 rod bundle, BNWL-1975, Pacific Northwest Laboratory, Richland, Washington.

Creer, J. M., Rowe, D. S., Bates, J. M. and Sutey, A. M. (1979), Turbulent flow in model nuclear reactor bundles containing flow blockages, Nucl. Eng. and Design, Vol. 52, pp. 15-33.

D'Arcy, D. F. and Schenk, J. R. (1985), Velocity and turbulence measurements in water flowing axially through a 37-rod bundle (To be presented at Int. Symp. on Heat Transfer, Beijing, China, 15-18 October 1985).

Davies, P. O. A. L. (1957), The behaviour of a pitot tube in transverse shear, J. Fl. Mech., Vol. 3, pp. 441-449.

Davies, J. T. (1972), Turbulence Phenomena, Academic Press, New York.

Durst, F., Melling, A. and Whitelaw, J. H. (1976), Principles and Practice of Laser-Doppler Anemometry, Academic Press, New York. East, L. F. (1966), Measurement of skin friction at low subsonic speeds by razor blade technique, ARC R & M 3653.

Eifler, W. and Nijsing, ~~R.~~ (1967), Experimental investigation of velocity distribution and flow resistance in a triangular array of parallel rods, Nucl. Eng. and Design, Vol. 5, pp. 22-42.

Eskinazi, S. and Erian, F. F. (1960), Energy reversal in turbulent flows, The Physics of Fluids, Vol. 12, No. 10, pp. 1988-1998.

Fage, A. and Falkner, V. M. (1930), An experimental determination of the intensity of friction on the surface of an aerofoil, ARC R & M 1315.

Fakory, M. and Todreas, N. (1979), Experimental investigation of flow resistance and wall shear stress in the interior subchannel of a triangular array of parallel rods, J. Fl. Eng., Vol. 101, pp. 429-435.

Fenter, F. W. and Lyons, W. C. (1957), The direct measurement of local skin friction on Aerobee-Hi rockets in free flight, Univ. of Texas, DRL-391.

Fingerson, L. M. and Freymuth, P. (1983), Thermal anemometers, Fluid Mechanics Measurements, pp. 99-154 (ed. by R. J. Goldstein), Hemisphere Publishing Corp., Reading, Massachusetts.

Franklin, R. E. and Wallace, J. M. (1970), Absolute measurements of static hole error using flush transducers, J. Fl. Mech., Vol. 42, Pt. 1, pp. 83-92.

Freymuth, P. (1978), A bibliography of thermal anemometry, TSI Q., Vol. 4, p. 2.

Freymuth, P. (1981), Calculation of square wave test for frequency optimized hot-film anemometers, J. Phys. E, Vol. 14, pp. 238-240.

Ginder, R. B. and Bradbury, L. J. S. (1973), Measurements of the drag of some characteristic aircraft excrescences immersed in turbulent boundary layers, Paper No. 4, AGARD CP 124.

Goldstein, S. (1936), A note on the measurement of total head and static pressure in a turbulent stream, Proc. Roy. Soc. London A, Vol. 150, pp. 570-572

Groeneveld, D. C. (1984), Thermohydraulic experiments in support of CANDU reactors, APRP-TD-1, AECL, Chalk River Nuclear Laboratories, Chalk River, Ontario.

Hackett, E. (1984), Isokinetic velocity profiles in a 37-element fuel bundle, APRP-AE-70, AECL, Chalk River Nuclear Laboratories, Chalk River, Ontario.

Hanratty, T. J. and Campbell, J. A. (1983), Measurement of wall shear stress, Fluid Mechanics Measurements, pp. 559-615 (ed. by R. J. Goldstein), Hemisphere Publishing Corp., Reading, Massachusetts.

Head, M. R. and Rechenberg, I. (1962), The Preston tube as a means of measuring skin friction, J. Fl. Mech., Vol. 14, pp. 1-17.

Head, M. R. and Vasanta Ram, V. (1971), Improved presentation of Preston tube calibration, Dep' Aeronaut. Eng., Indian Inst. Tech., Kanpur, India, AE-10/1970; Aeronaut. Q. Vol.22, p. 3.

Hinze, J. O. (1975), Turbulence (second edition), McGraw-Hill, New York.

Hool, J. H. (1955), Measurement of skin friction using surface pressure tubes, Aircraft Eng., Vol. 28.

Hsu, E. Y. (1955), The measurement of local turbulent skin friction by means of surface pitot tubes, David Taylor Model Basin Report 957.

Ibragimov, M. Kh., Isupov, I. A., Kobzar, L. L. and Subbotin, V. I. (1966), Calculation of the tangential stresses at the wall of a channel and the velocity distribution in a turbulent flow of liquid, Soviet Atomic Energy, Vol. 21, pp. 731-739.

Ibragimov, M. Kh., Isupov, I. A., Kobzar, L. L. and Subbotin, V. I. (1967), Calculation of hydraulic resistivity coefficients for turbulent fluid flow in channels of noncircular cross-section, Soviet Atomic Energy, Vol. 23, pp. 1042-1057.

Kacker, S. C. (1973), Some aspects of fully developed turbulent flow in noncircular ducts, J. Fl. Mech., Vol. 57, pp. 583-602.

Kattchee, N. and Reynolds, W. C. (1962), An IBM 7090 Fortran computer program for heat transfer analysis of gas or liquid reactor, Hectic II, IDO-28595.

King, L. V. (1915), On the precision measurement of air velocity by means of the linear hot-wire anemometer, Phil. Mag., Vol. 29, pp. 556-563.

Kjellstorm, B. (1971), Studies of turbulent flow parallel to a rod bundle of triangular array, AB Atomenergi, Studsvik, 61101, Nykoping, Sweden, STU 68-263/u210.

Konstantinov, N. I. (1955), Energomashinostroenie, Trudy LPI 176, pp. 201-213 (English translation (1961), Comparative investigation of the friction stress on the surface of a body, DSIR RTS 1500).

Laufer, J. (1953), The structure of turbulence in fully developed pipe flow, NACA TN 2954.

Levchenko, Yu. D., Subbotin, V. I. and Ushakov, P. A. (1967), The distribution of coolant velocities and wall stresses in closely packed rods, Soviet Atomic Energy, Vol. 22, No. 3, pp. 262-269.

Ling, S. C. (1955), Measurement of flow characteristics by the hot-film technique, Ph. D. Dissertation, State Univ. of Iowa, Iowa City, Iowa.

Ludwieg, H. (1949), Ein Gerat Zur Messung der Wandschubspannung turbulenter Reibungsschichten, Ing. Arch., Vol. 17, pp. 207-218 (English translation (1950), Instrument for measuring the wall shearing stress of turbulent boundary layers, NACA TM 1284).

MacMillan, F. A. (1957), Experiments on pitot tubes in shear flow, ARC TN 30288.

McArthur, R. C. (1963), Transducer for direct measurement of skin friction in the hypersonic shock tunnel, CAL Report 129.

Merriam, K. G. and Spaulding, E. R. (1935), Comparative tests of pitot static tubes, NACA TN 546.

Merzkirch, W. (1974), Flow Visualization, Academic Press, New York.

Mueller, T. J. (1983), Flow visualization by direct injection, Fluid Mechanics Measurements, pp. 307-375 (ed. by R. J. Goldstein), Hemisphere Publishing Corp., Washington.

Nijsing, R., Gargantini, I. and Eifler, W. (1966), Analysis of fluid flow and heat transfer in a triangular array of parallel heat generating rods, Nucl. Eng. and Design, Vol. 4, pp. 375-398.

O'Donnell, F. B. (1964), A study of the effect of floating element misalignment on skin friction accuracy, Univ. of Texas DRL-515.

O'Donnell, F. B. and Westkaemper, J. C. (1965), Measurement of errors caused by misalignment of floating element skin-friction balances, AIAA J., Vol. 3, No. 1, pp. 163-165.

Ower, E. and Johansen, F. C. (1925), The design of pitot tubes, ARC R & M 981.

Ower, E. and Pankhurst, R. C. (1977), The Measurement of Air Flow (5th edition), Pergamon Press, Oxford.

Ozarapoglu, V. (1973), Measurements in incompressible turbulent flows, Thesis Universite' Laval.

Palmer, L. D. and Swanson, L. L. (1961), Measurements of heat transfer coefficients, friction factors and velocity profiles for air flowing parallel to closely spaced rods, ASME Int. Heat Transfer Conference, Part III, pp. 535-537.

Patel, V. C. (1965), Calibration of the Preston tube and limitations in its use in pressure gradients, J. Fl. Mech., Vol. 23, No. 1, pp. 185-208.

Patos, J. M. (1970), Application of the force-balance principle to pressure and skin friction sensors, 16th Annual Technical Meeting, Proc. Inst. Environmental Sci., pp. 363-368.

Prahlad, T. S. (1972), Yaw characteristics of Preston tubes, AIAA J., Vol. 10, No. 3, pp. 357-359.

Preston, J. H. (1954), The determination of turbulent skin friction by means of pitot tubes, J. Roy. Aeronaut. Soc., Vol. 58, pp. 109-121.

Quarmby, K. and Das, J. (1969), Displacement effects on pitot tubes with rectangular mouth, Aeronaut. Q., Vol. 20, pp. 129-139.

Rapier, A. C. and Redman, J. D. (1964), The calibration of velocity distributions in rod clusters, TRG Report 838(W).

Rapier, A. C. (1964), Forced convection heat transfer in passages with varying roughness and heat flux around the perimeter, Thermodynamics and Fl. Mech. Convention, Cambridge.

Rehme, K. (1978), The structure of turbulent flow through a wall subchannel of a rod bundle, Nucl. Eng. and Design, Vol. 45, p. 311.

Rehme, K. (1980), Turbulent momentum transport in rod bundles, Nucl. Eng. and Design, Vol. 62, p. 137.

Rehme, K. (1982), Distributions of velocity and turbulence in a parallel flow along an asymmetric rod bundle, Nucl. Technology, Vol. 59, pp. 148-159.

Reynolds, A. J. (1974), Turbulent Flows in Engineering, John Wiley & Sons, London.

Rogers, J. T. and Todreas, N. E. (1968), Coolant interchannel mixing in reactor fuel bundles-single phase coolants, Heat Transfer in Rod Bundles, ASME, New York, pp. 1-56.

Rowe, D. S. (1973), Measurement of turbulent velocity, intensity and scale in rod bundle flow channels, BNWL-1736, Pacific Northwest Laboratory, Richland, Washington.

Rowe, D. S. and Chapman, C. C. (1973), Measurement of turbulent velocity, intensity and scale in rod bundle flow channels containing grid spacer, BNWL-1757, Pacific Northwest Laboratory, Richland, Washington.

Rowe, D. S., Wheeler, C. L. and Fitzsimmons, D. E. (1973), An experimental study of flow and pressure in rod bundle subchannels containing blockages, BNWL-1771, Pacific Northwest Laboratory, Richland, Washington.

Rowe, D. S., Johnson, B. M. and Knudsen, J. G. (1975), Implications concerning rod bundle crossflow mixing based on measurements of turbulent flow structure, Int. J. Heat Mass Transfer, Vol. 17, pp. 407-419.

Schultz-Grunow, F. (1940), Neues Reiungswiderstandsgesetz, fur glatte Platten, Luftfahrtforschung, 17 239-246 (English translation (1941), New frictional law for smooth plates, NASA TM 986).

Staff of the Aerodynamics Division, N. P. L. (1958), On the measurement of local surface friction on a flat plate by means of Preston tubes, ARC R & M 3185.

Stanton, T. E., Marshall, D. and Bryant, C. W. (1920), On the condition at the boundary of a fluid in turbulent motion, Proc. Roy. Soc. London A, Vol. 97, pp. 413-434.

Subbotin, V. I., Ushakov, P. A., Levchenko, Yu. D. and Alexandrov, A. M. (1971), Velocity fields in turbulent flow past rod bundles, Heat Transfer - Soviet Res., Vol. 3, pp. 9-35.

Tahir, A. and Rogers, J. T. (1979), The mechanism of secondary flows in turbulent interchange in rod bundles, Proc. 7th Can. Cong. App. Mech., Sherbrooke, Ontario, pp. 773-774.

Tahir, A. and Rogers, J. T. (1986), Turbulent flow structure in a closely packed triangular array rod bundle (To be presented at 8th Int. Heat Transfer Conference, San Francisco, 1986)

Tavoularis, S. (1978), Experiments in turbulent transport and mixing, Ph. D. Dissertation, The Johns Hopkins Univ., Baltimore, Maryland.

Tavoularis, S. and Stapountzis, E. (1983), Subchannel flow visualization in a nuclear reactor fuel bundle, Proc. 3rd Int. Symp. Flow Visualization, Ann Arbor, Michigan, pp. 452-456.

Tennekes, H. and Lumley, J. L. (1973), A First Course in Turbulence, M. I. T. Press, Cambridge, Massachusetts.

Trupp, A. C. and Azad, R. S. (1975), The structure of turbulent flow in triangular array rod bundles, Nucl. Eng. and Design, Vol. 32, pp. 47-84.

Winter, K. G. (1977), An outline of the techniques available for the measurement of skin friction in turbulent boundary layers, Prog. Aerospace Sci., Vol. 18, pp. 1-57.

Wyngaard, J. C. (1968), Measurement of small-scale turbulence structure with hot-wires, Journal of Scientific Instruments, Vol. 1, pp. 1105-1108.

Young, A. D. and Maas, J. N. (1936), The behaviour of a pitot tube in a transverse total-pressure gradient, ARC R & M 1770.

Parameter	Symbol	Units	Reactor bundle	Test section
Operating fluid	--	--	Heavy water	Light water
Fluid temperature	T_f	°C	220-240	20-35
Fluid pressure	P	MPa	13.79	0.10
Flow cross-section area	A	mm^2	3425	2217
Bundle length	L	mm	500	610
Diameter of the rod	d	mm	12.6	25.4
Pitch to diameter ratio	s/d	--	1.14	1.14
Bundle hydraulic diameter	D_h	mm	7.42	13.18
Square subchannel hydraulic diameter	d_h	mm	7.85	15.70
Flow conditions	--	--	Single-phase, diabatic	Single -phase, isothermal
Mass flow rate	--	kg/s	17	5-14
Bundle Reynolds number	Re_{bt}	--	450000	32000-83000
Subchannel equivalent pipe Reynolds number	Re_{bh}	--	452000	45000-100000

Table 1 Comparison between the reactor bundle and and the test-section.

Measured parameter	Instrumentation used	Measuring locations	U_{bt} m/s	U_{bh} m/s	Re_{bh}	u^*_{av} m/s
In-flow static pressure	Static pressure tube	x/L = 0.08, 0.50, 0.91 (also, x/d_h = 3, 20, 35)	2.95 3.86	3.12 3.92	50000 62000	0.147 0.180
Mean axial velocity	Pressure tubes Cross-film	" "	2.95 2.95 3.86	3.12 3.12 3.92	50000 50000 62000	0.147 0.147 0.180
Turbulence intensity Skewness factor Flatness factor Reynolds stress Correlation coefficient Autocorrelation coefficient Integral length scale Microscale Probability density function	Cross-film	"	"	"	"	"
Wall static pressure	Surface pressure hole	x/L = 0.20, 0.60 (also, x/d_h = 8, 23)	2.95	3.12	50000	0.147
Wall shear stress	Preston tube	"	"	"	"	"

Table 2 Measurements in a single bundle.

x/L r/R	Re_{bh} = 50000 0.08	 0.50	 0.91	Re_{bh} = 62000 0.08	 0.50	 0.91
0.57	2.44*, 2.53	2.74, 2.87	2.90, 3.29	2.53, 2.91	2.83, 2.83	2.96, 3.59
0.67	22.4, 11.47	2.83, 3.31	3.31, 3.49	10.08, 8.50	2.92, 3.39	3.19, 3.29
0.72	10.68, 7.90	2.77, 3.09	2.94, 3.90	14.04, 13.54	2.76, 3.36	2.96, 3.10

* The first value denotes axial flatness factor and the second value radial flatness factor.

Table 3 Flatness factors at representative locations.

Measured parameter	Instrumentation used	Measuring locations	U_{bt} m/s	U_{bh} m/s	Re_{bh}	u^*_{av} m/s
In-flow static pressure	Static pressure tube	x/L = 0.08, 0.50, 0.91 (also, x/d_h = 3, 20, 35)	2.43	2.86	45000	0.137
Mean axial velocity	Pressure tubes	,,	,,	,,	,,	,,
Wall static pressure	Surface pressure hole	x/L=0.20, 0.60, (also, x/d_h = 8, 23)	,,	,,	,,	,,
Wall shear stress	Preston tube	"	,,	,,	,,	,,

Table 4 Measurements in the test-bundle with an upstream bundle.

Re_{bh}	f_{av} ×1000 (1)	f_p ×1000 (eq. 2-22) (2)	$\frac{f_{av}}{f_p}$	f_{av} ×1000 (eq. 2-29) (3)	$\frac{f_{av}}{f_p}$ (eq. 2-27) (4)	$\frac{f_{av}}{f_p}$ (eq. 2-28) (5)
45000	18.29	21.4	0.85	17.8	0.777	1.028
50000	17.97	20.9	0.86	17.2	0.777	1.028
62000	16.87	19.9	0.85	16.1	0.777	1.028

1 Present measurements; 2 Karman and Nikuradse (1933); 3 Trupp and Azad (1975); 4 Ibragimov (1967); Subbotin et al. (1971).

Table 5 Friction factor results.

r/R	$\frac{\nu_{Tr}^{u}}{u^* y_0}$ (1)	$\frac{\nu_{T\phi}^{u_x}}{u^* y_0}$ (eq. 2-59) (2)	$\frac{\nu_{T\phi}^{u_x}}{u^* y_0}$ (eq. 2-60) (3)	$\frac{\nu_{T\phi}^{u_x}}{u^* y_0}$ (eq. 2-61) (4)	$\frac{\nu_{T\phi}^{u_x}}{u^* y_0}$ (5)	$\frac{\nu_{T}}{u^* y_0}$ (eq. 2-64) (6)	$\frac{\nu_{Ta}^{u_x}}{u^* y_0}$ (eq. 2-58) (7)	$\frac{\nu_{Ta}^{u_x}}{u^* y_0}$ (8)
0.57	0.513	0.1	0.293	0.527	0.14-0.19	0.409	0.1	0.04-0.08
0.62	0.145	0.1	0.210	0.273	0.14-0.19	0.213	0.1	0.04-0.08
0.67	0.095	0.1	0.302	0.152	0.14-0.19	0.118	0.1	0.04-0.08

1 Present measurements; 2 Rapier (1964); 3,4 Nijsing et al. (1966); 5 Kjellstorm (1971) measurements;
6 Rattchee and Reynolds (1962); 7 Rapier and Redman (1964); 8 Kjellstorm (1971) measurements.

Table 6 Eddy viscosity results.

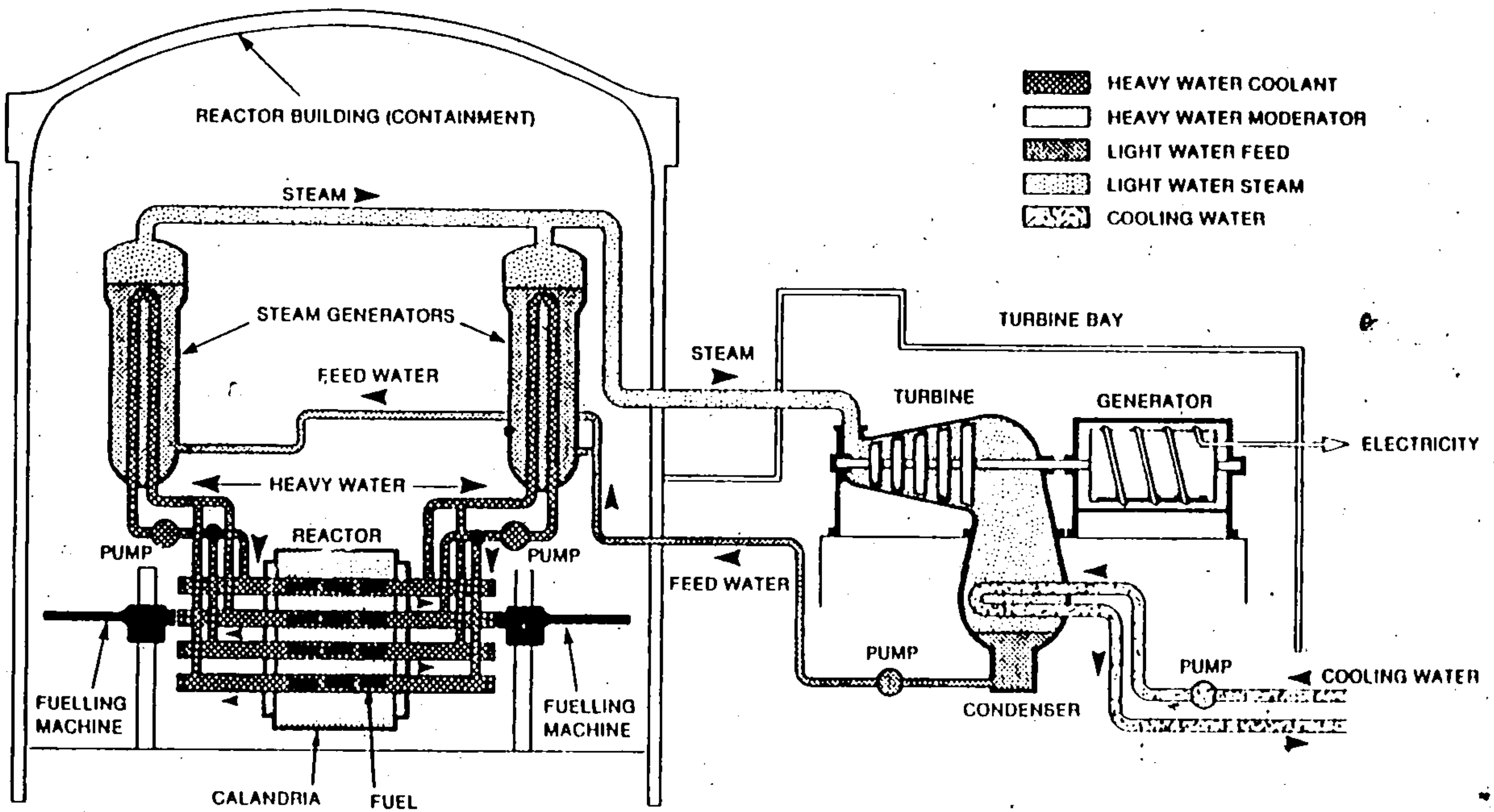

Figure 1 CANDU nuclear power system.

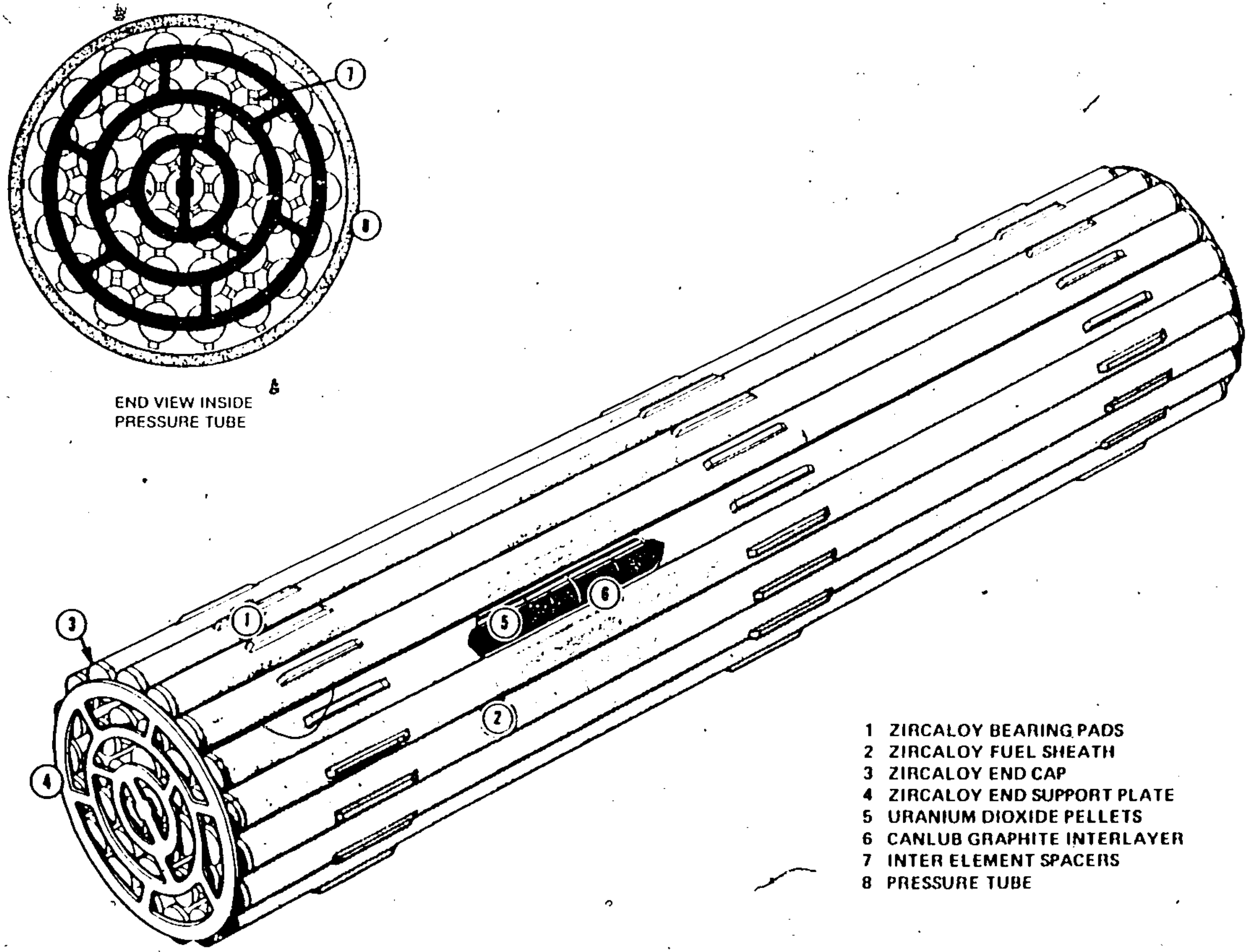

Figure 2 37-rod reactor bundle.

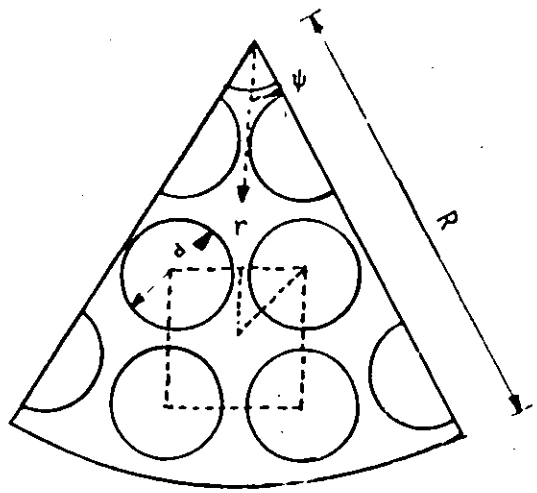

Figure 3 Test-section and central square subchannel.

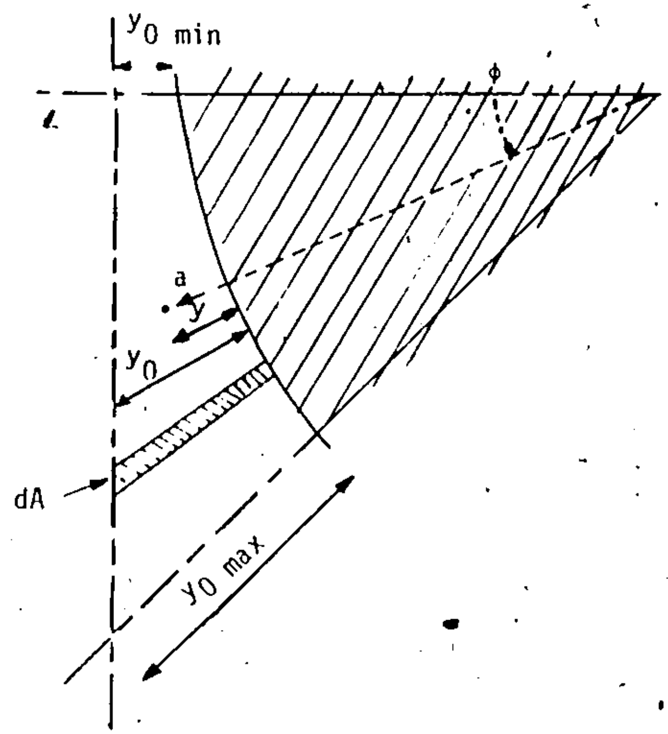

Figure 4 Flow-cell.

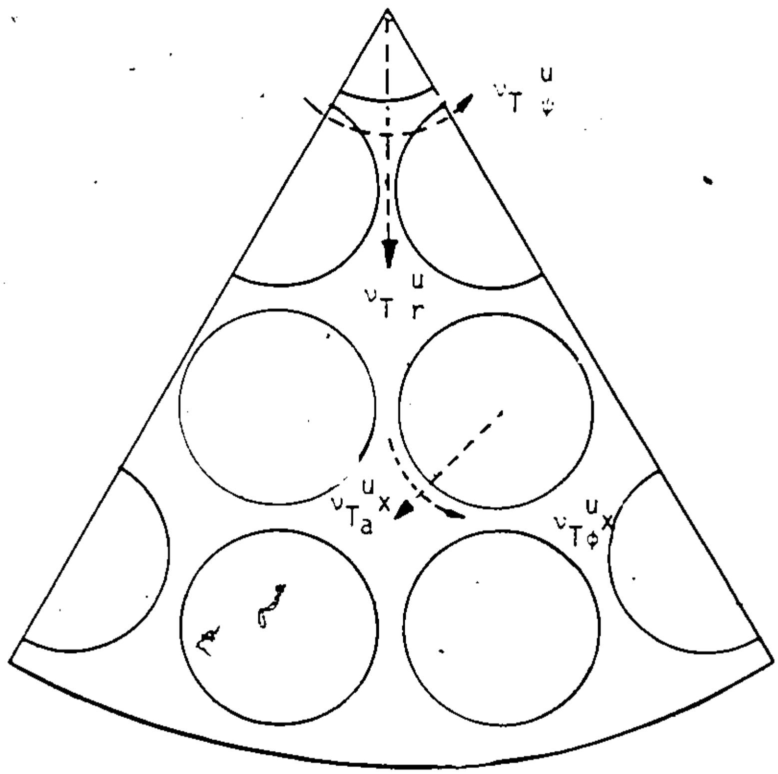

* arrow-heads indicate the direction of momentum transport

Figure 5 Representation of eddy viscosities.

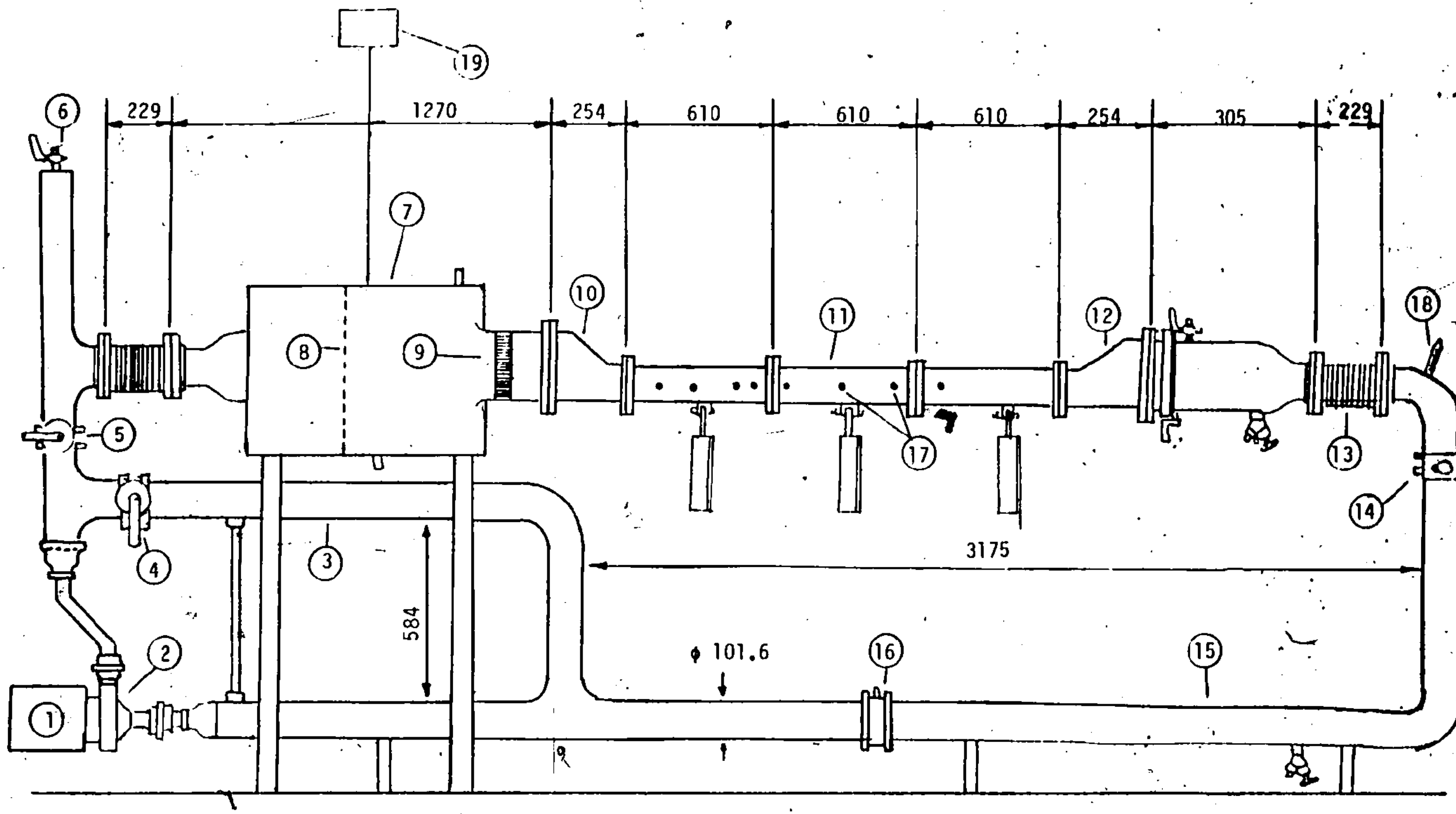

Figure 6 Water tunnel and parts (see p. 148 for Parts list).

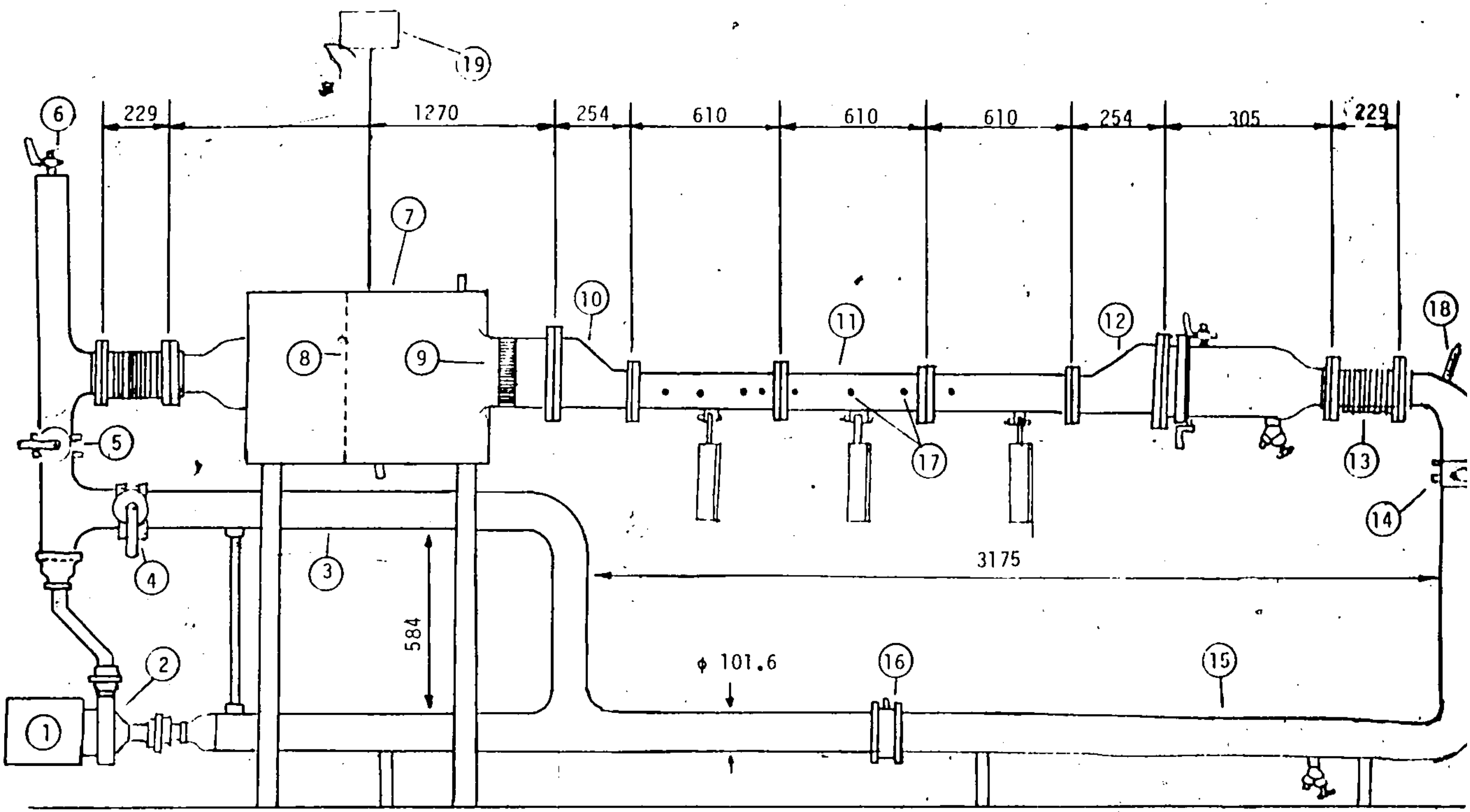

Figure 6 Water tunnel and parts (see p. 148 for Parts list).

WATER TUNNEL PARTS LIST

Number	Item
1	Electric motor
2	Water pump
3	By pass section pipe
4	By pass section valve
5	Main section valve
6	Relief valve
7	Plenum chamber
8	Thin wire gauze
9	Honeycomb screen
10	Contraction
11	Test-section
12	Expansion
13	Steel bellows
14	Control valve
15	Main pipe
16	Orifice plate
17	Probe insertion ports
18	Thermometer
19	Pressurizing tank

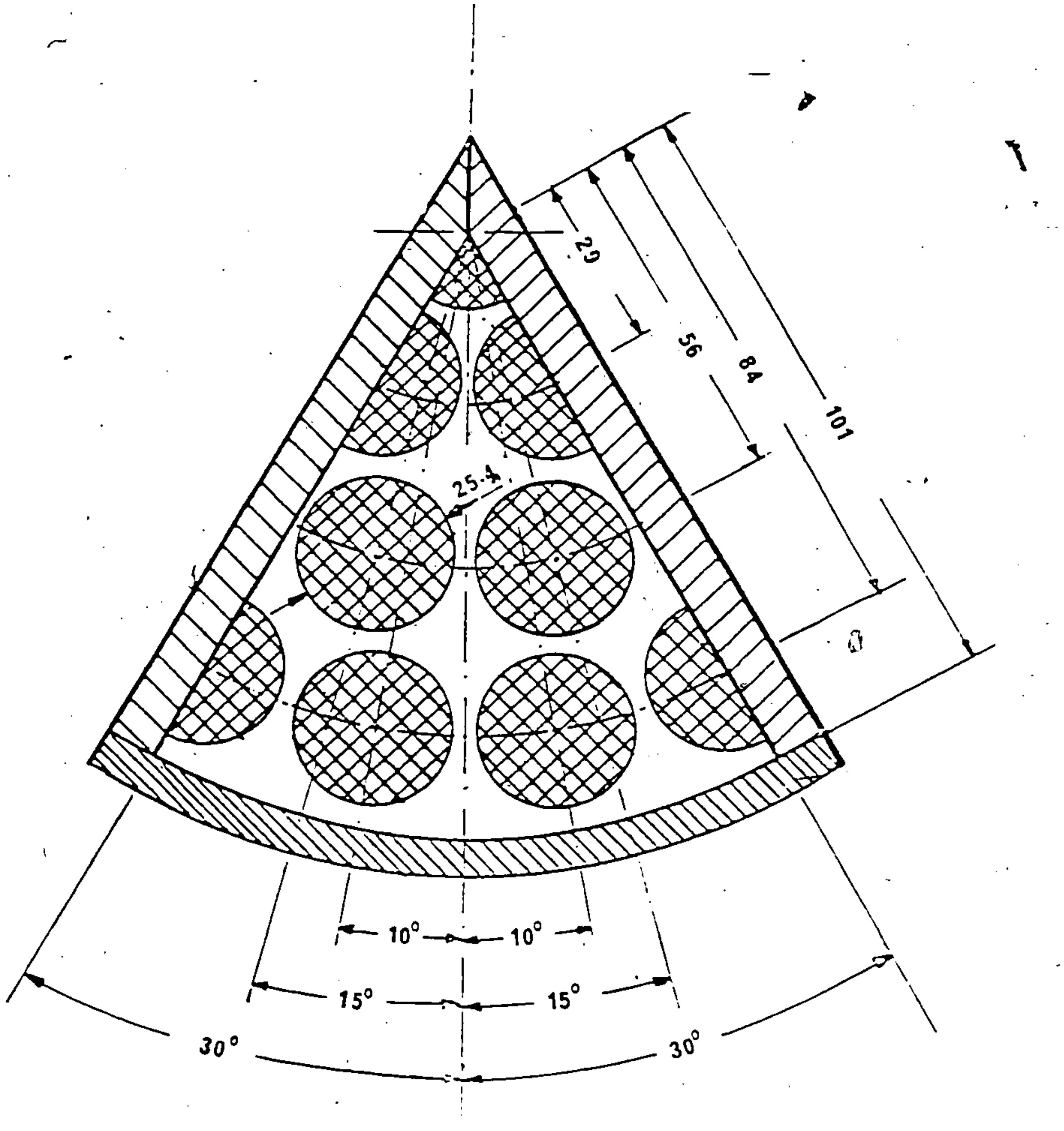

Figure 7 Cross-section of the bundle model.

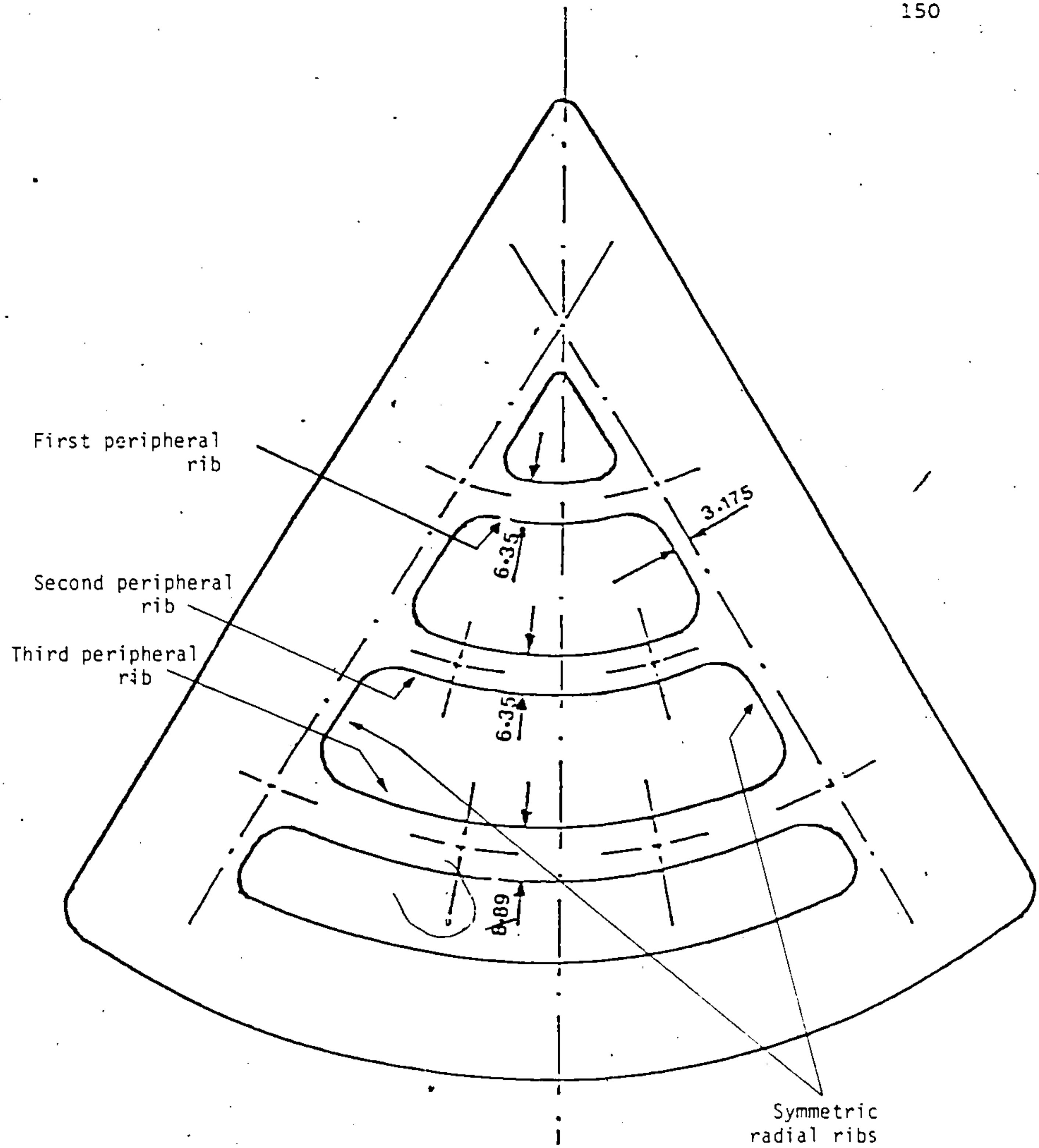

Figure 8 Endplate support.

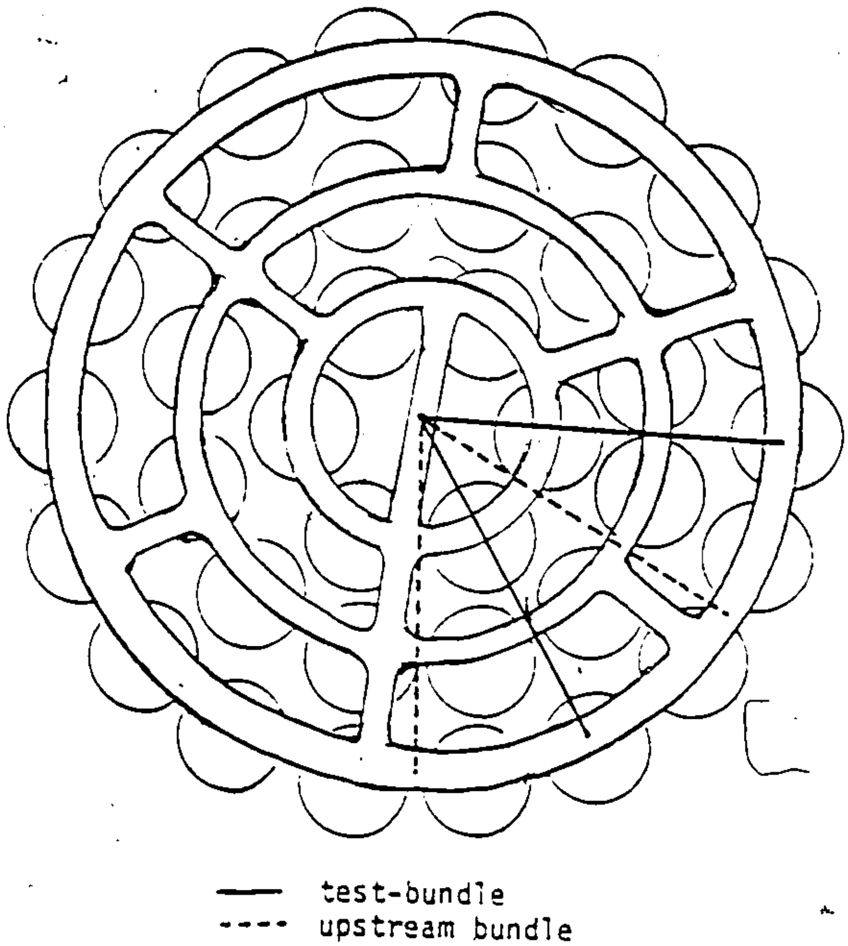

Figure 9 Reactor bundle endplate support.

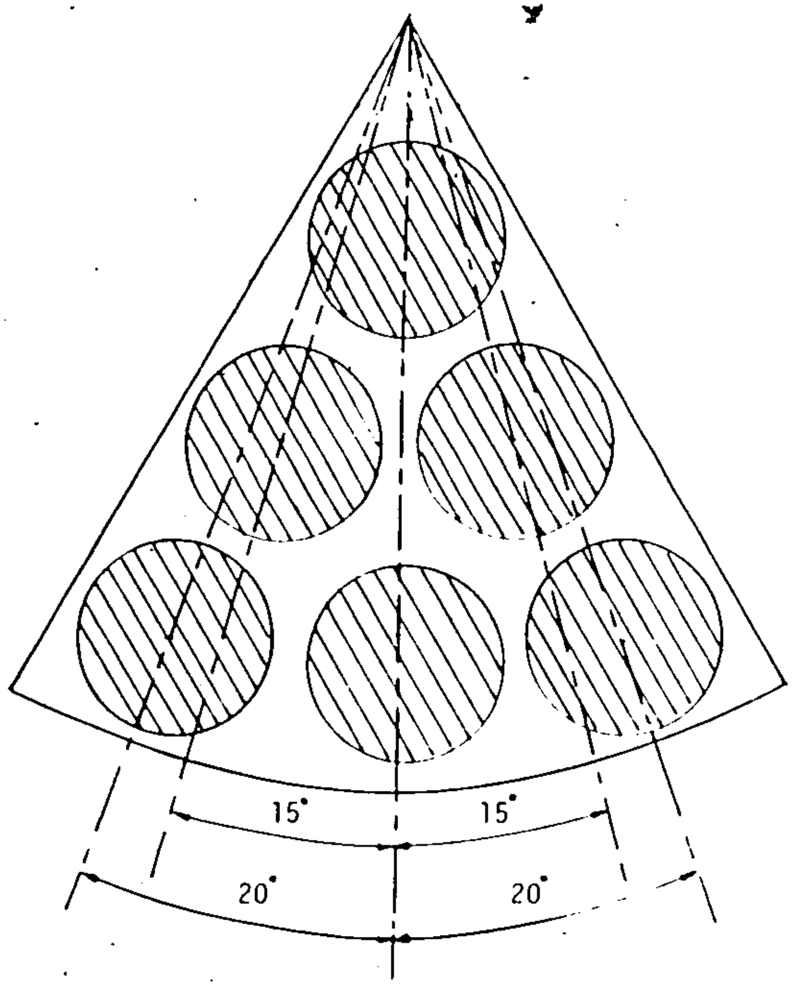

Figure 10 Cross-section of the 30° rotated bundle model.

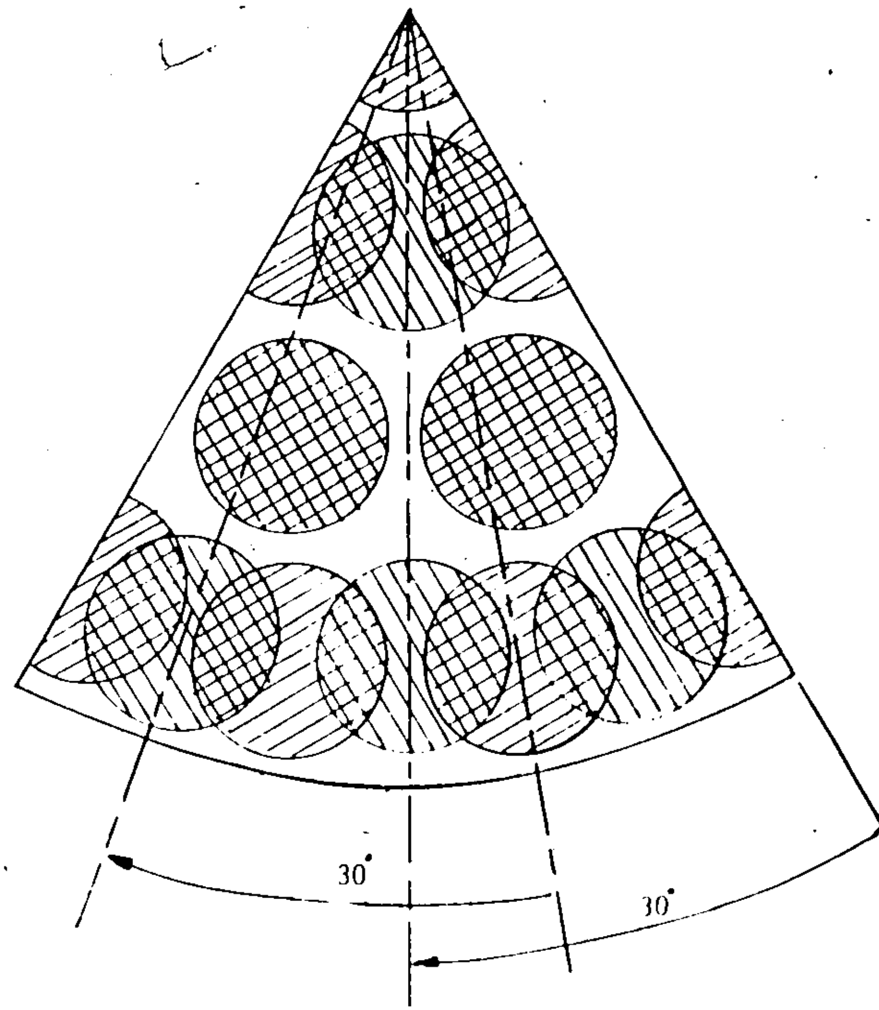

Figure 11 Relative subchannel interference between bundles in tandem.

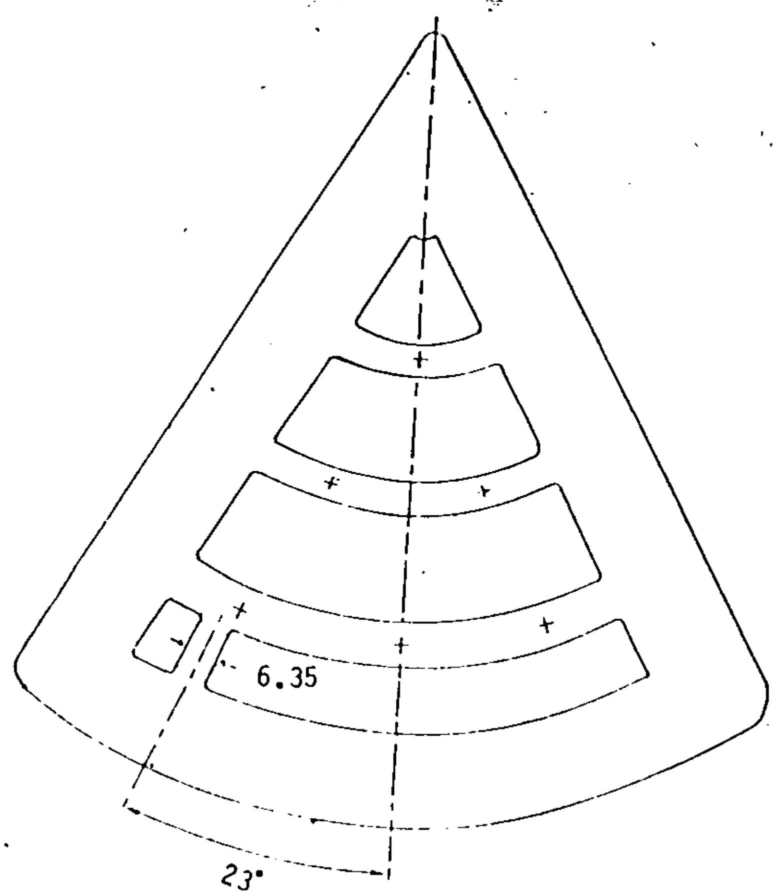

(a) downstream endplate of the upstream bundle

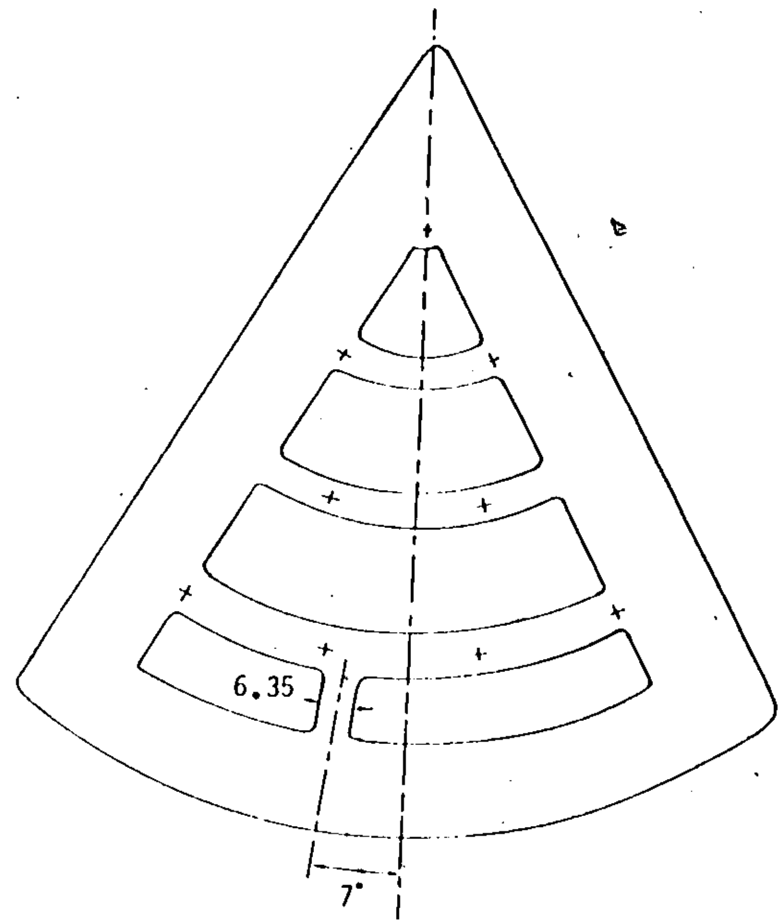

(b) upstream endplate of the test bundle

Figure 12 Modified endplate supports.

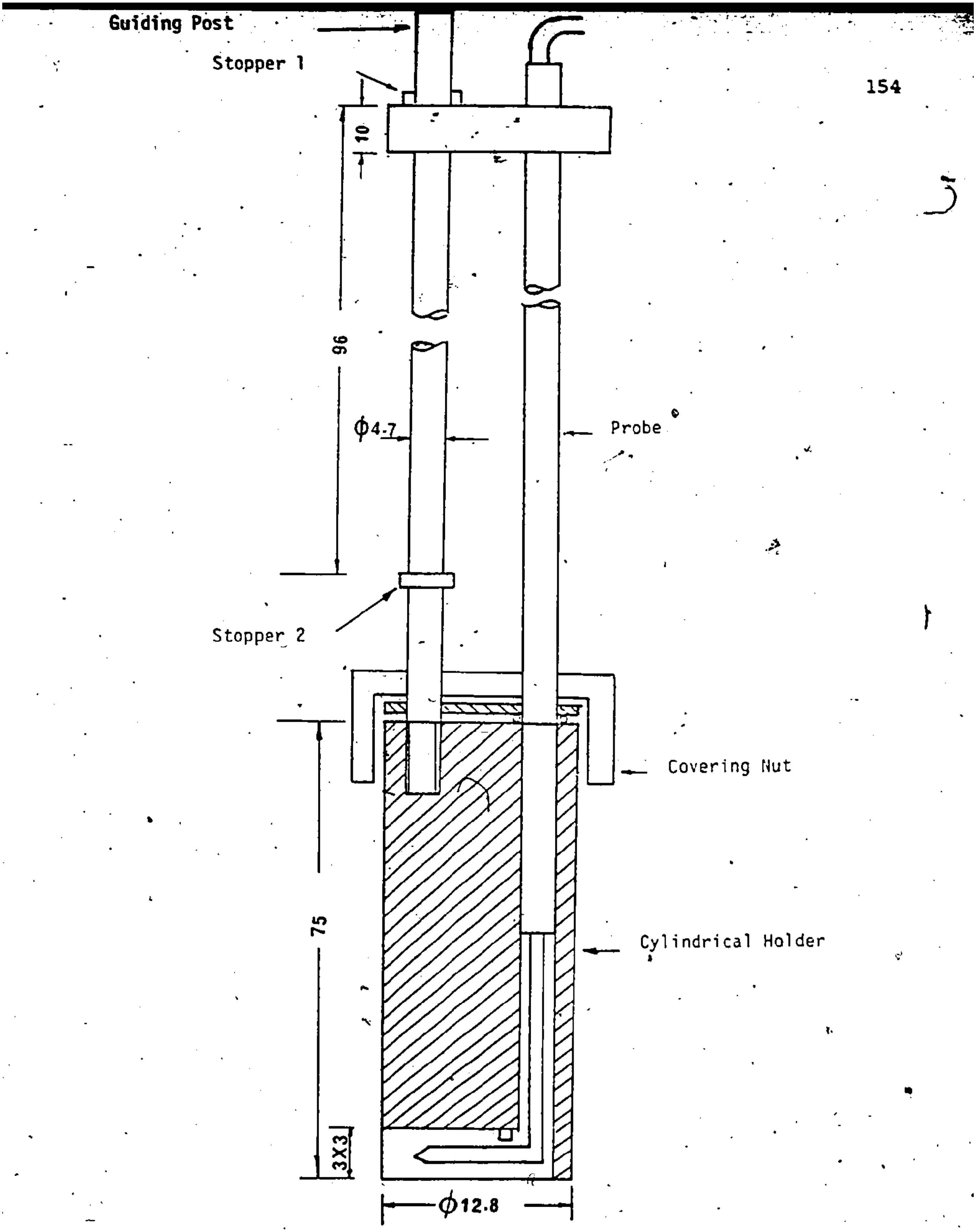

Figure 13 The probe mount.

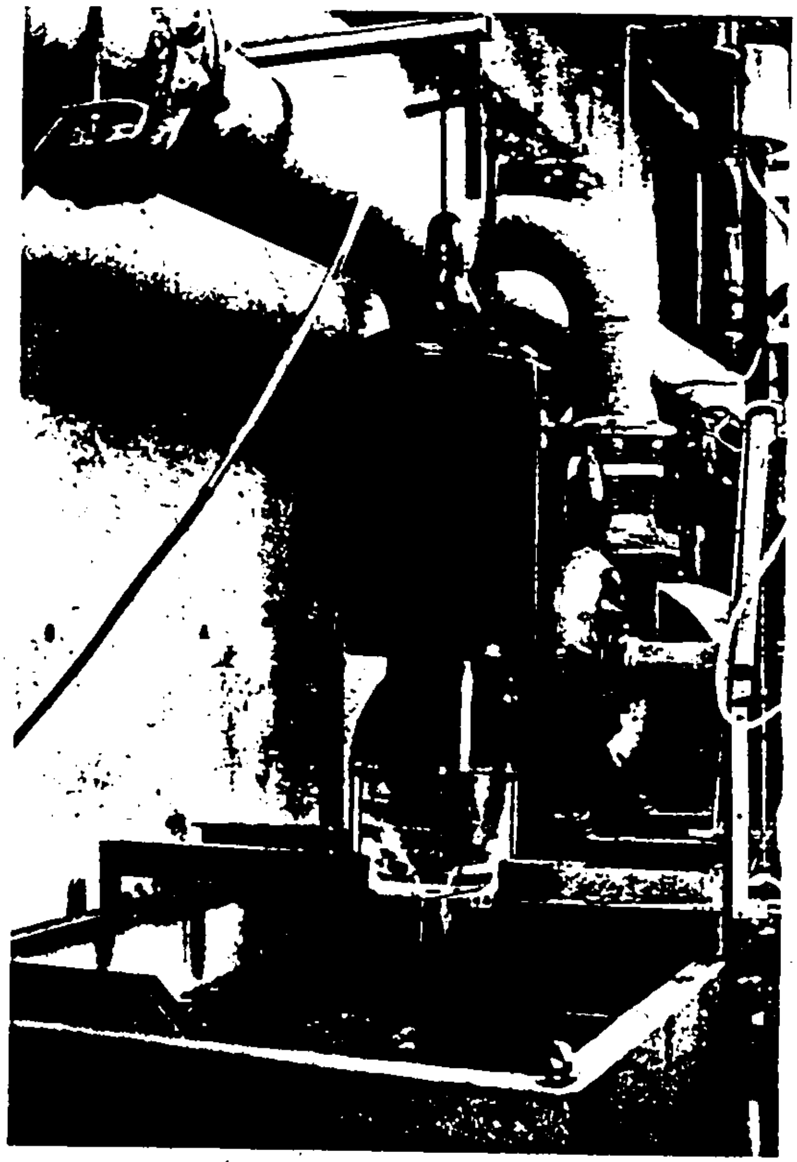

Figure 14 Calibration facility.

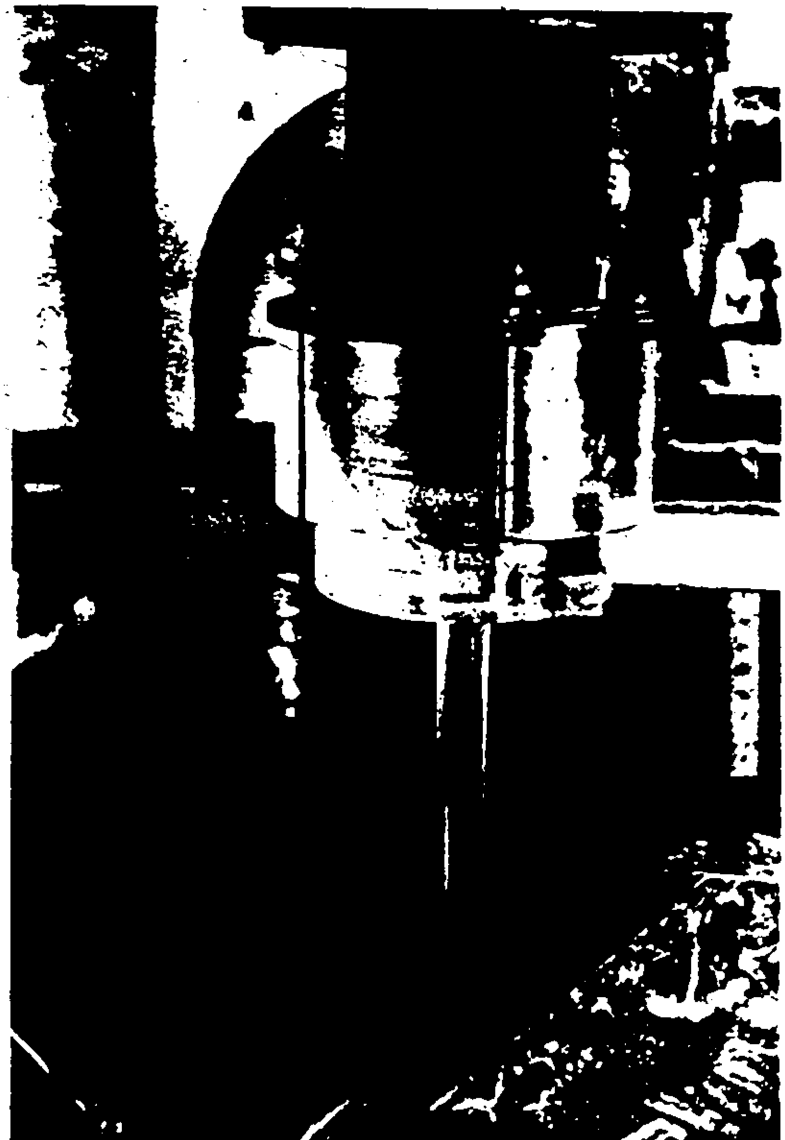

Figure 15 Calibration jet.

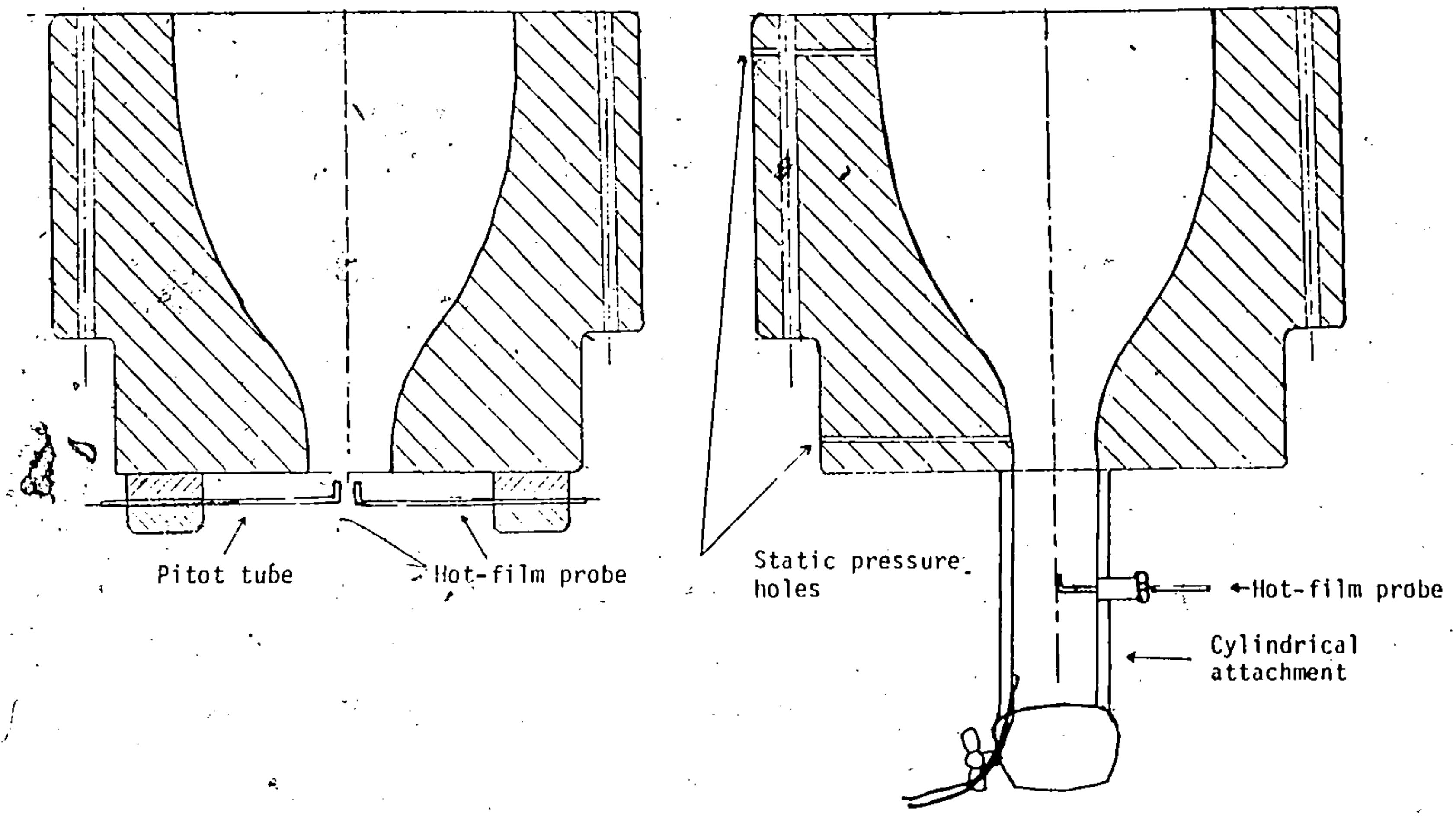

(a) Calibration in the open jet.

(b) Calibration in the closed jet

Figure 16 Hot-film positioning in the calibration nozzle.

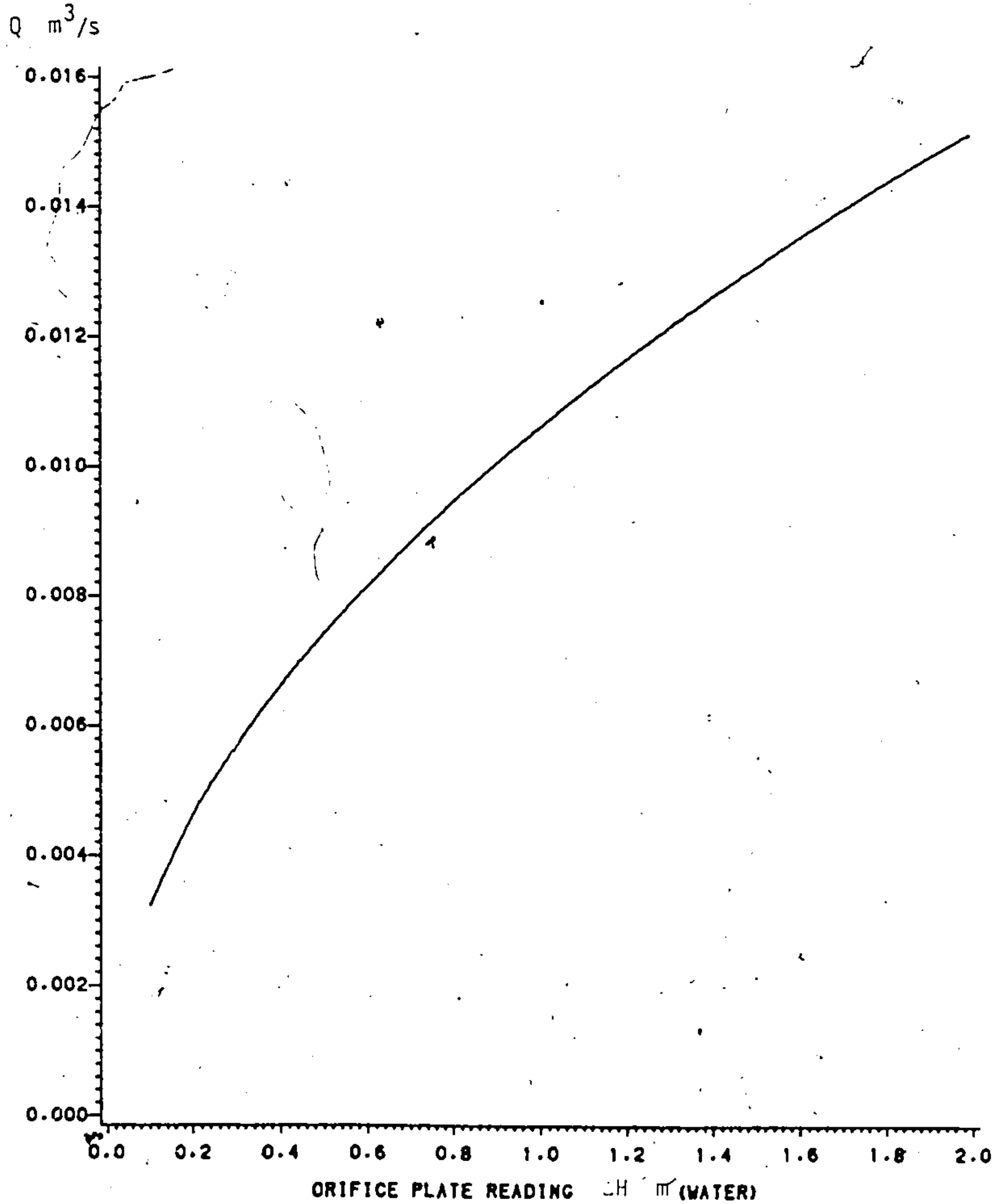

Figure 17 Calibration curve of the orifice plate.

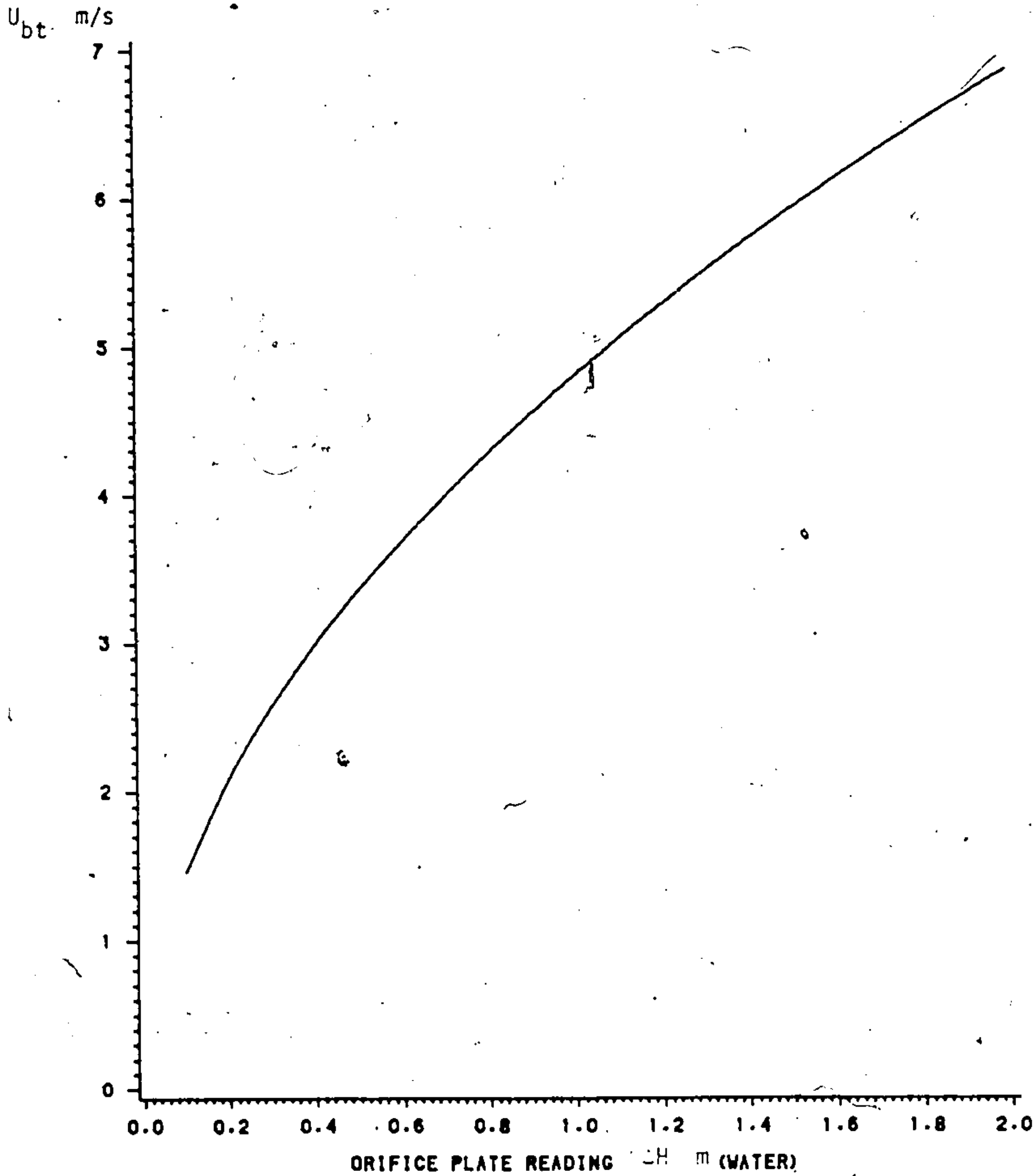

Figure 18 Test-section bulk velocity.

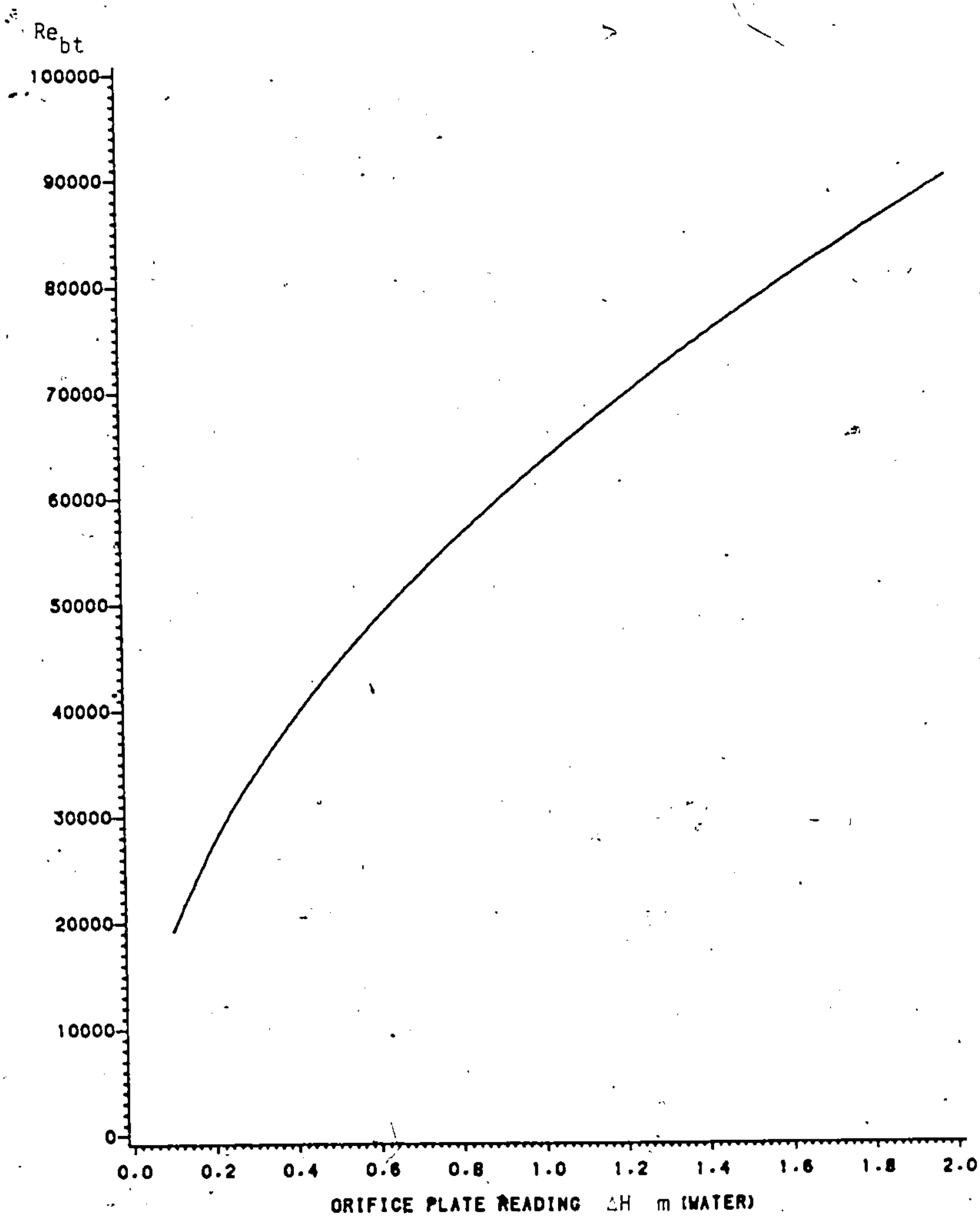

Figure 19 Test-section Reynolds number.

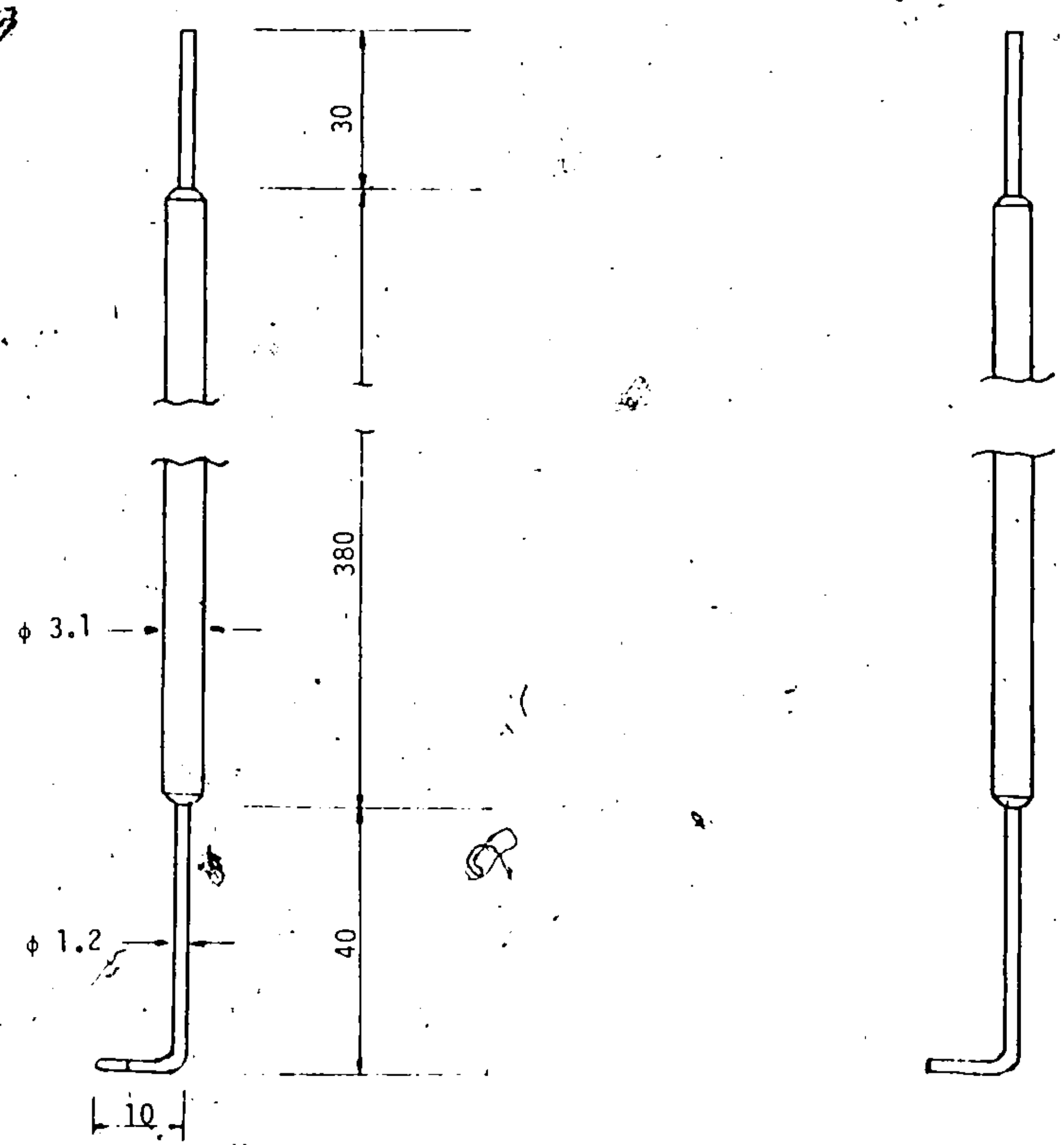

(a) static pressure tube

(b) total pressure tube

Figure 20 Pressure tubes.

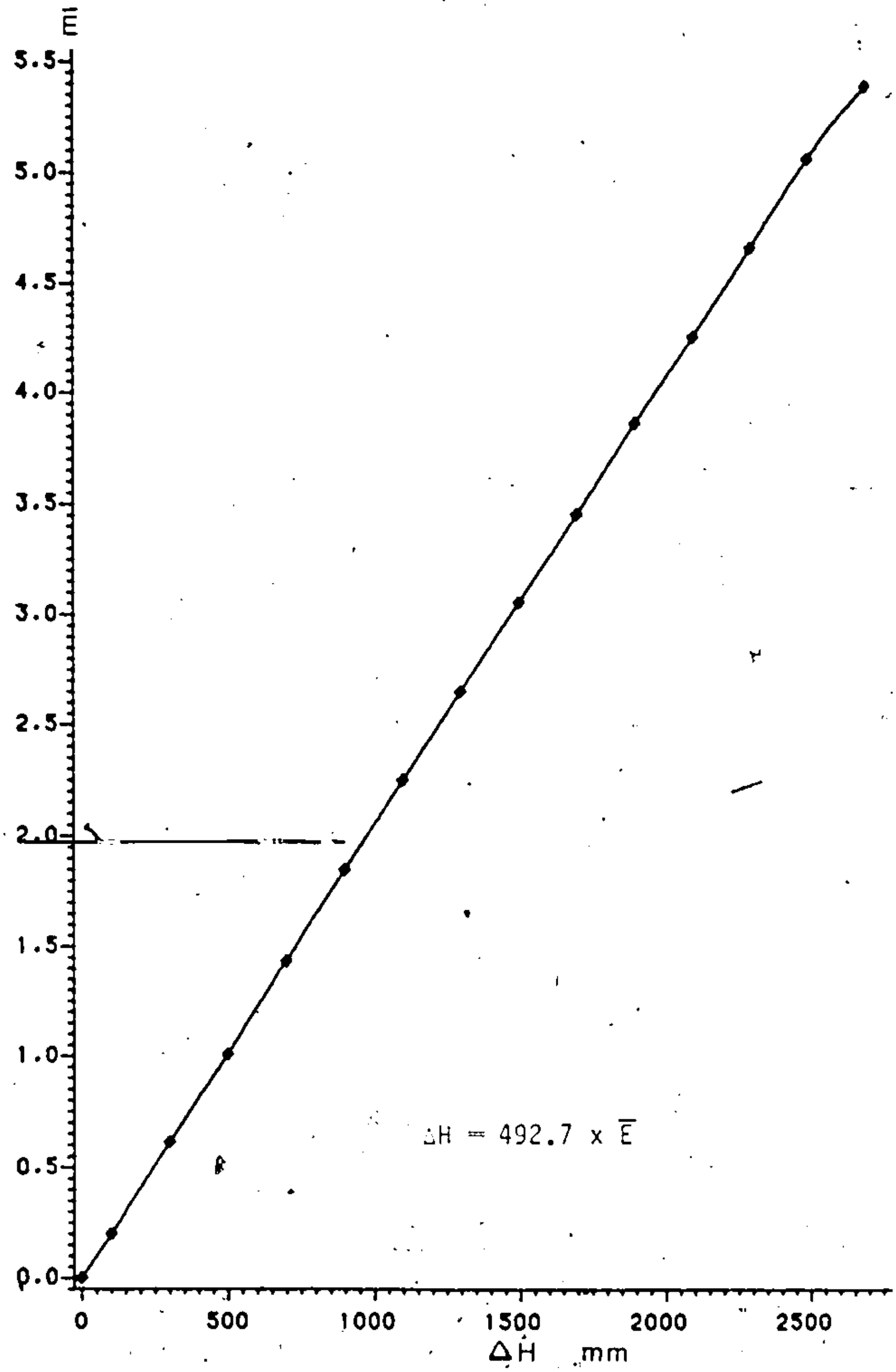

Figure 21 Calibration curve of the pressure transducer.

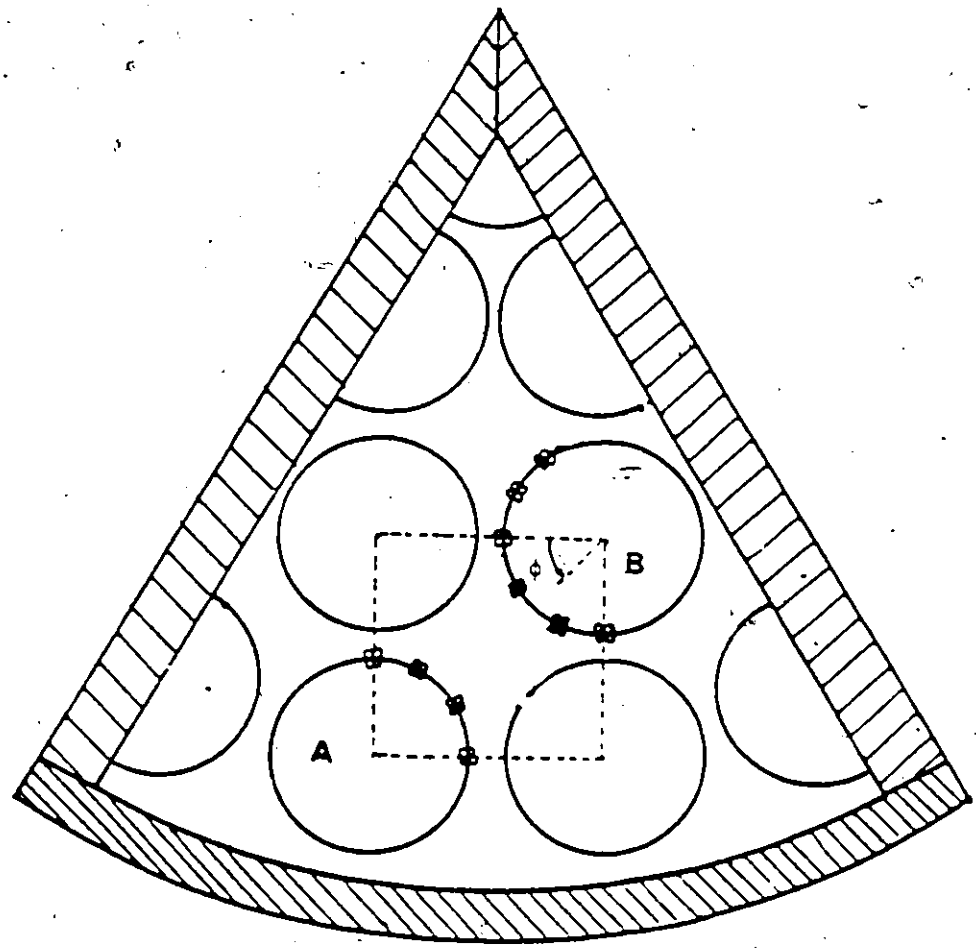

Figure 22 Peripheral position of static holes and Preston tubes.

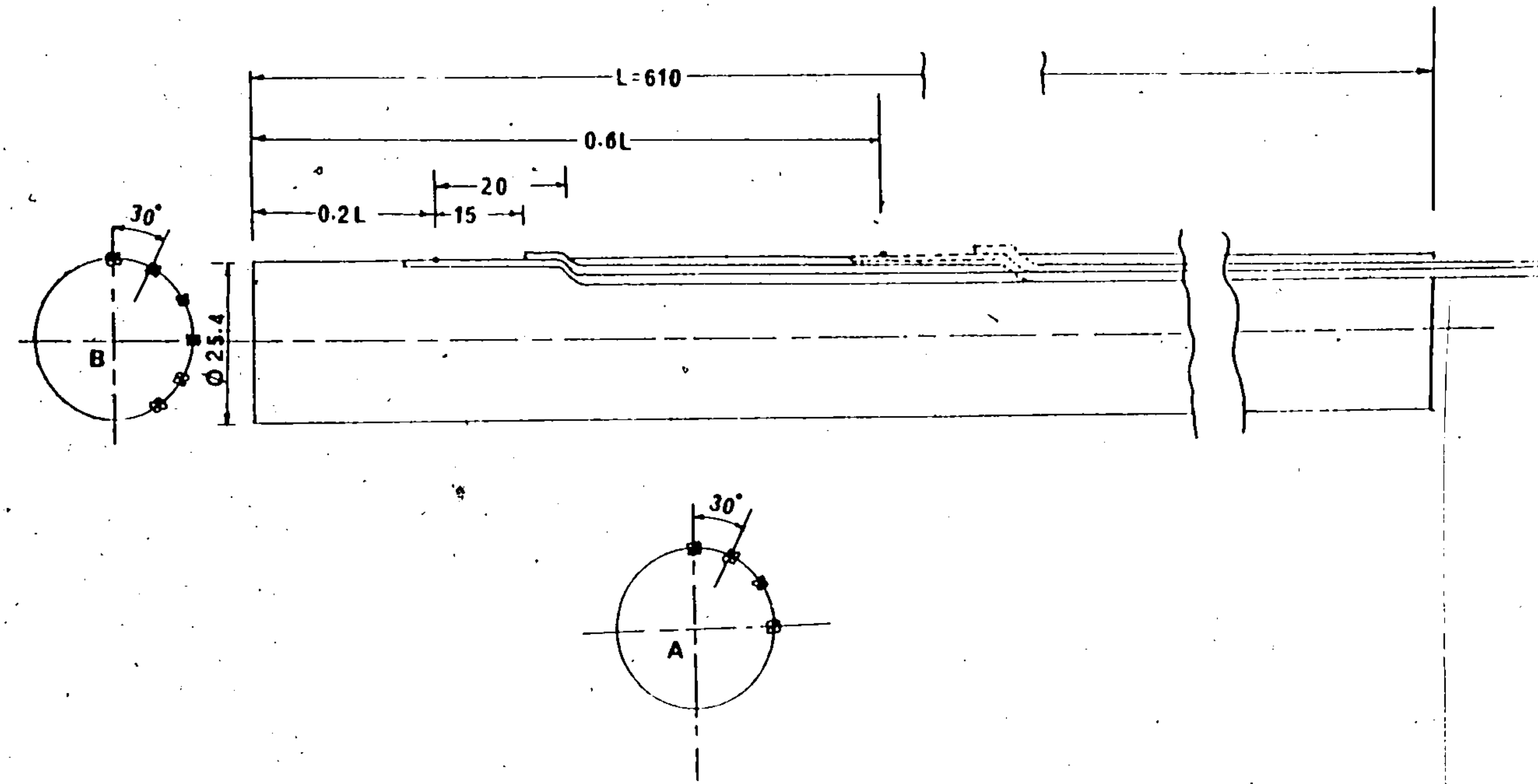

Figure 23 Axial position of static holes and Preston tubes

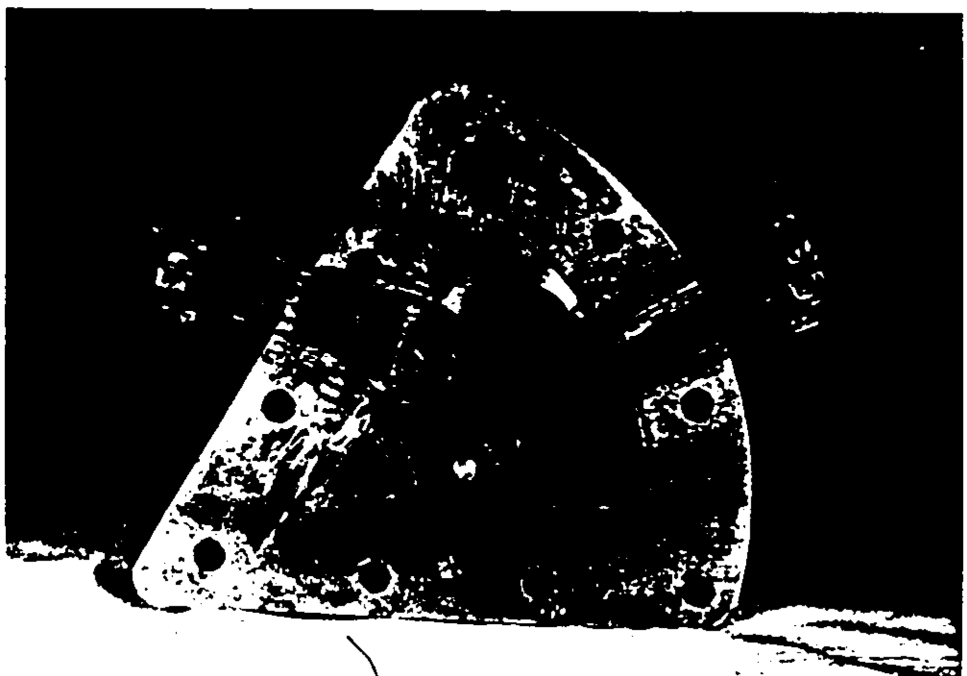

Figure 24 Endplate with surface tube assembly.

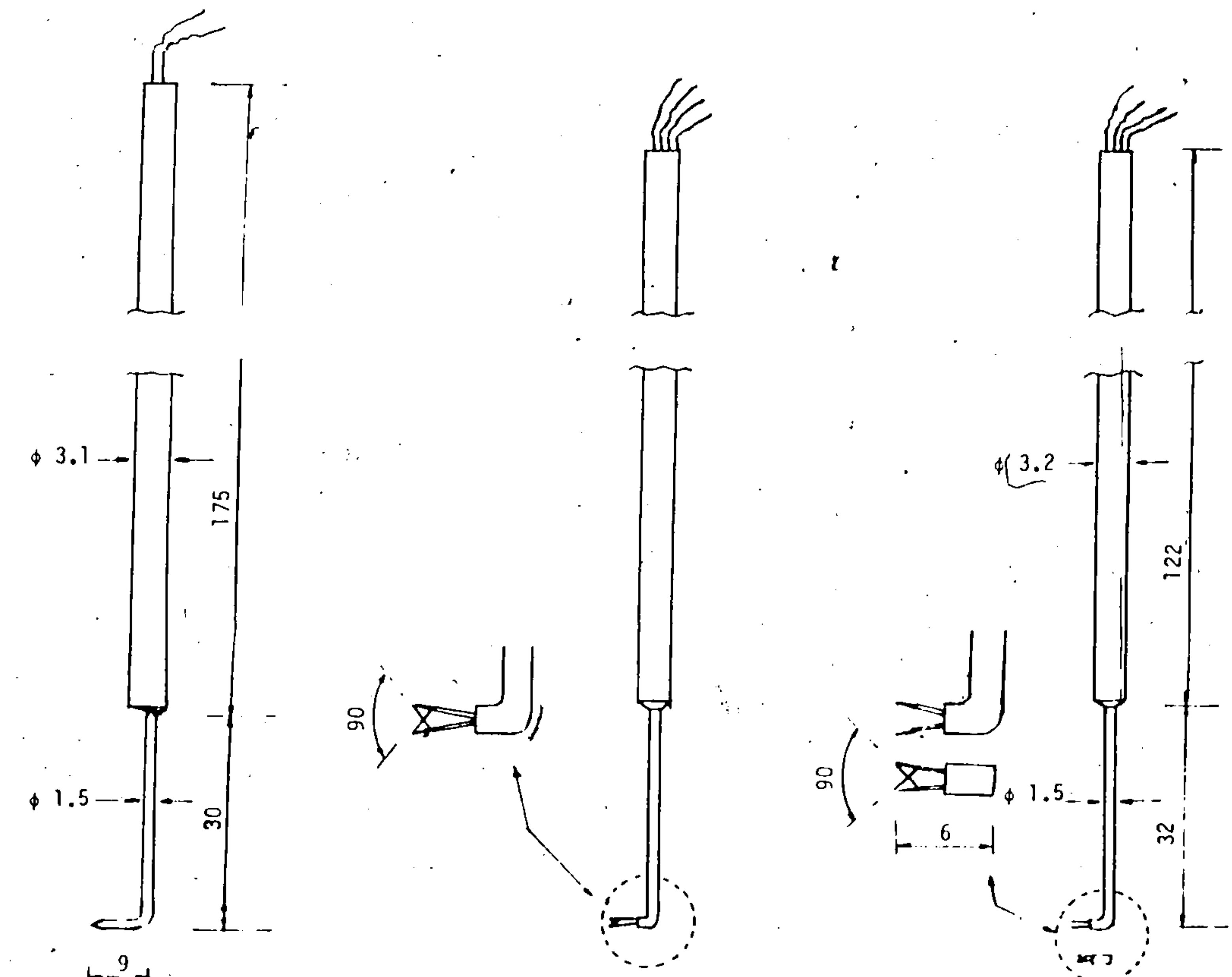

(a) conical film probe

(b) cross-film probe (U-V)

(c) cross-film probe (U-W)

Figure 25 Hot-film probes.

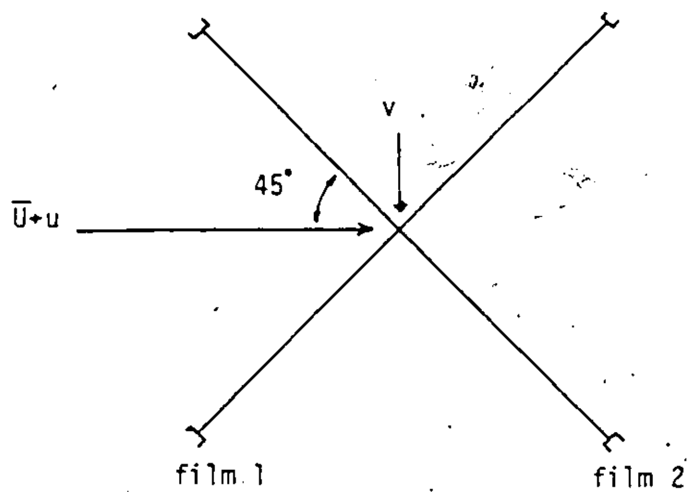

$$U_{eff1} = (\overline{U}+u+v)\cos 45^\circ$$
$$U_{eff2} = (\overline{U}+u-v)\cos 45^\circ$$

Figure 26 Cross-film and effective velocity.

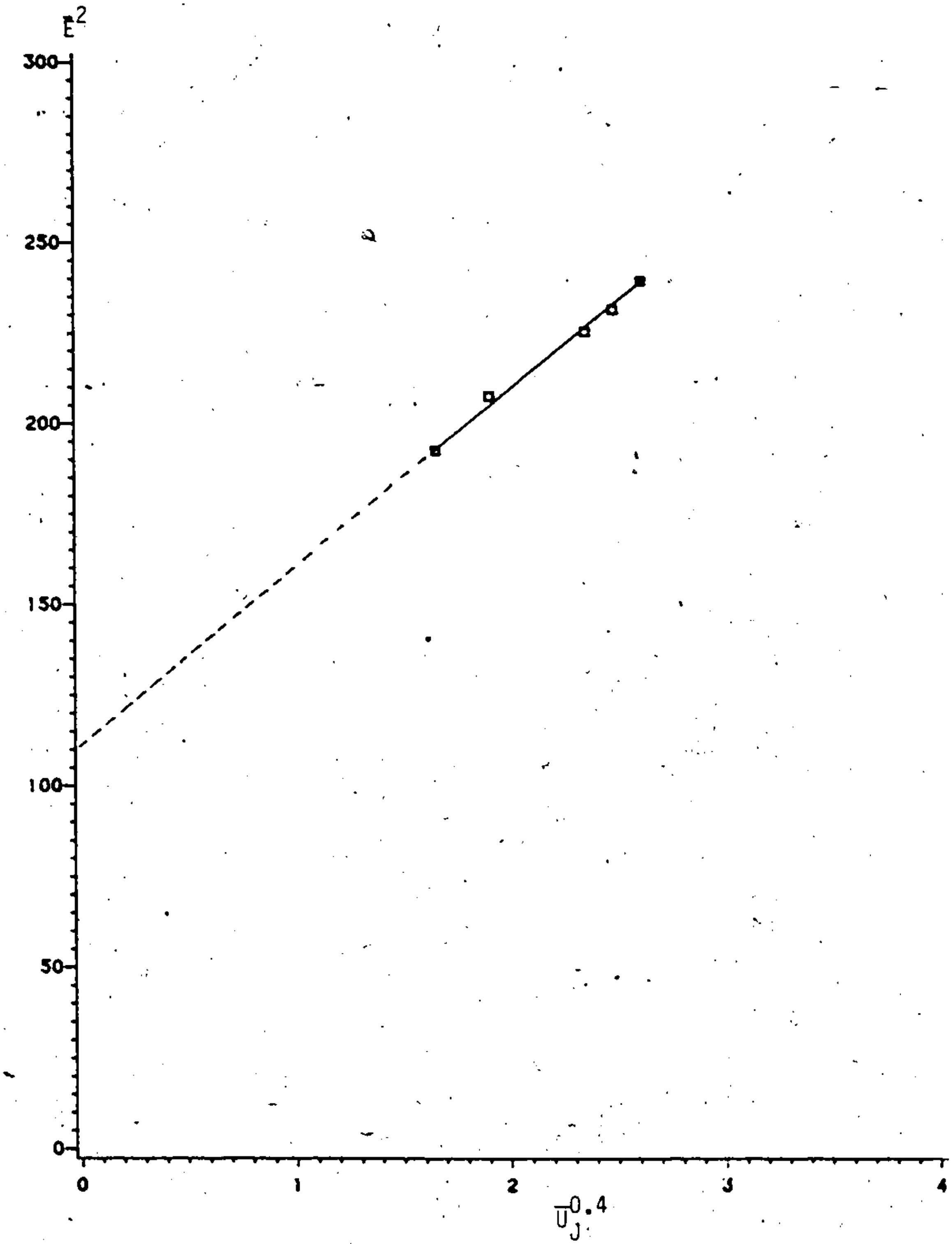

Figure 27 Conical film calibration curve.

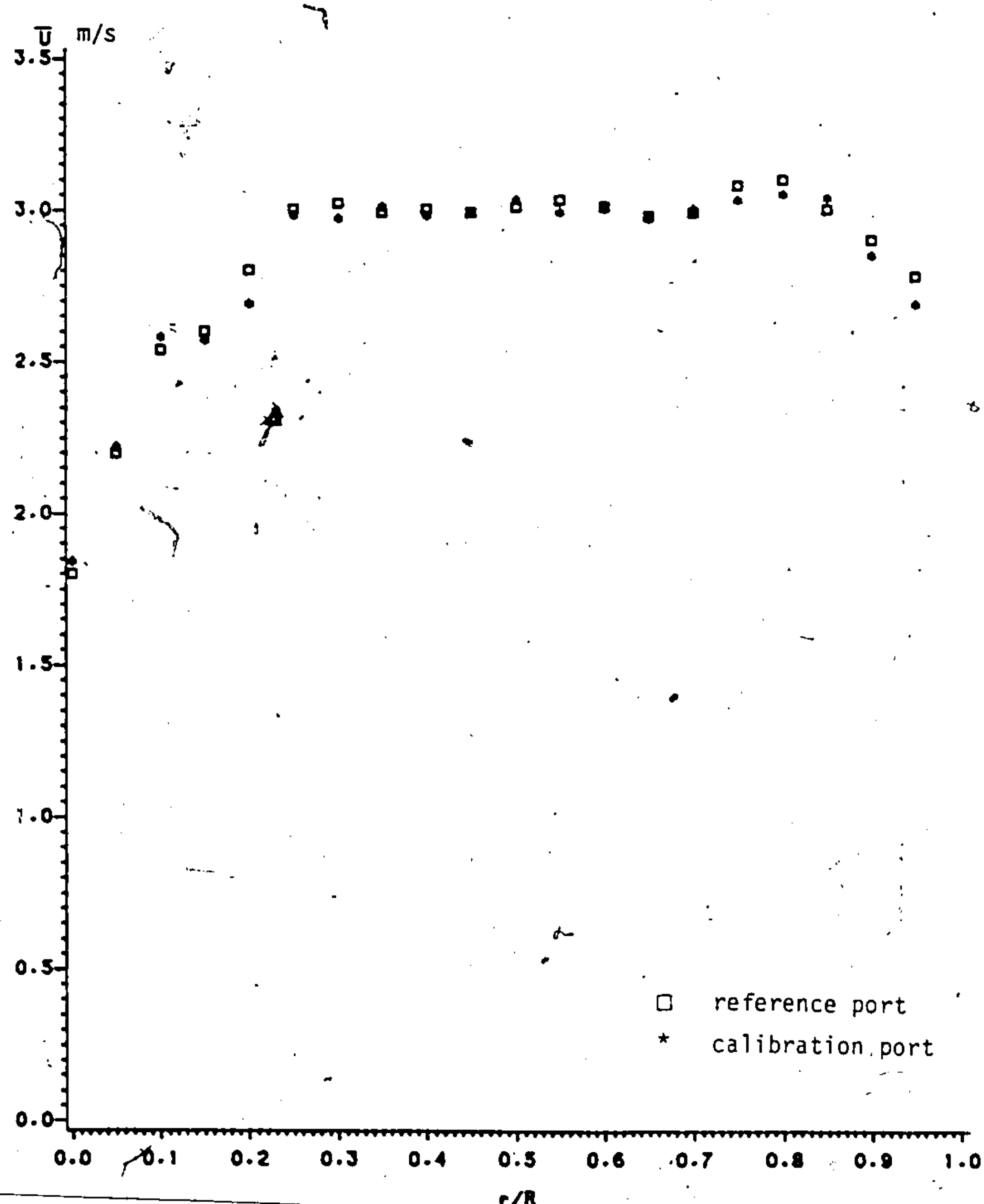

Figure 28 Mean axial velocity profile in the upstream empty section.

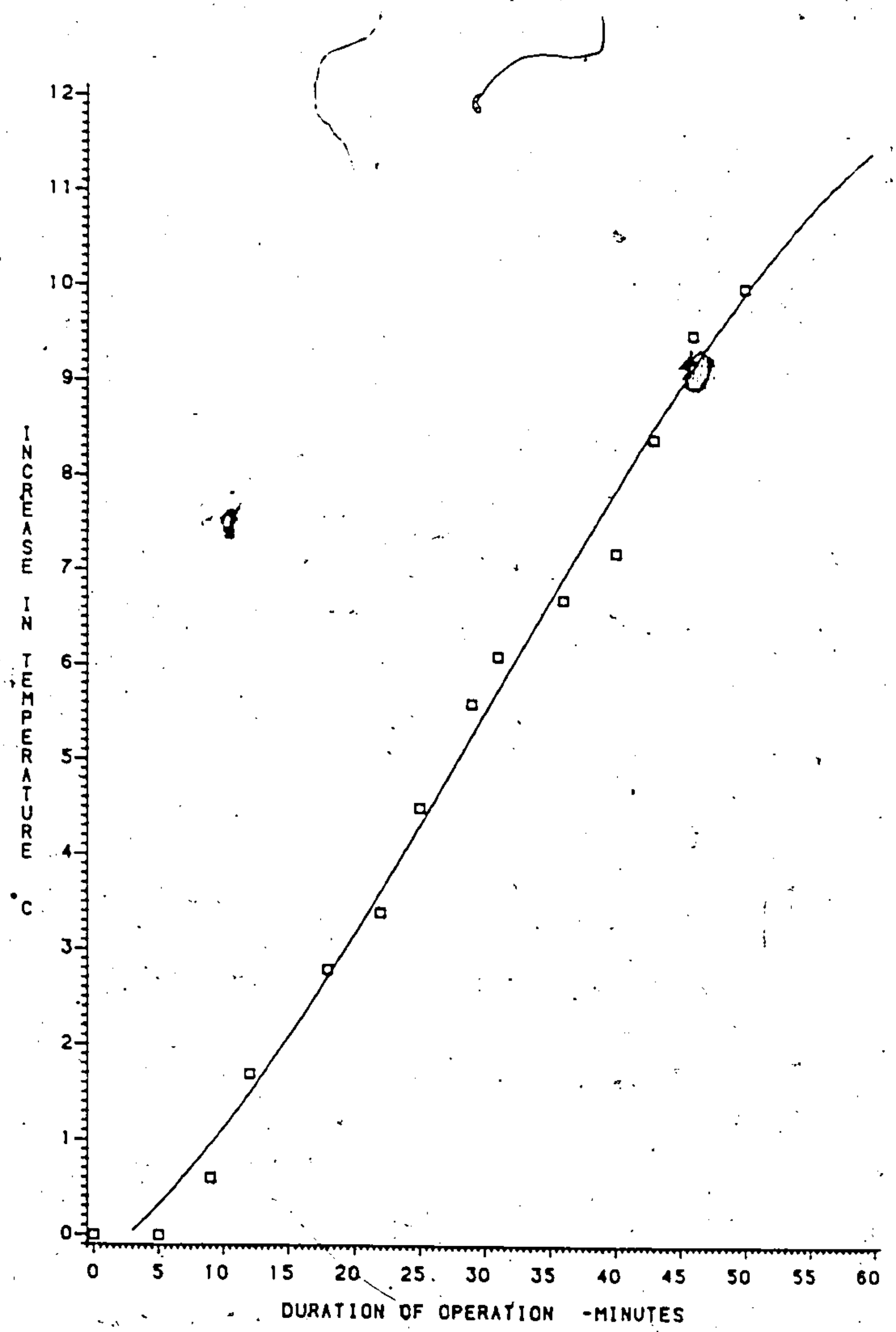

Figure 29 Water temperature rise with tunnel operation time.

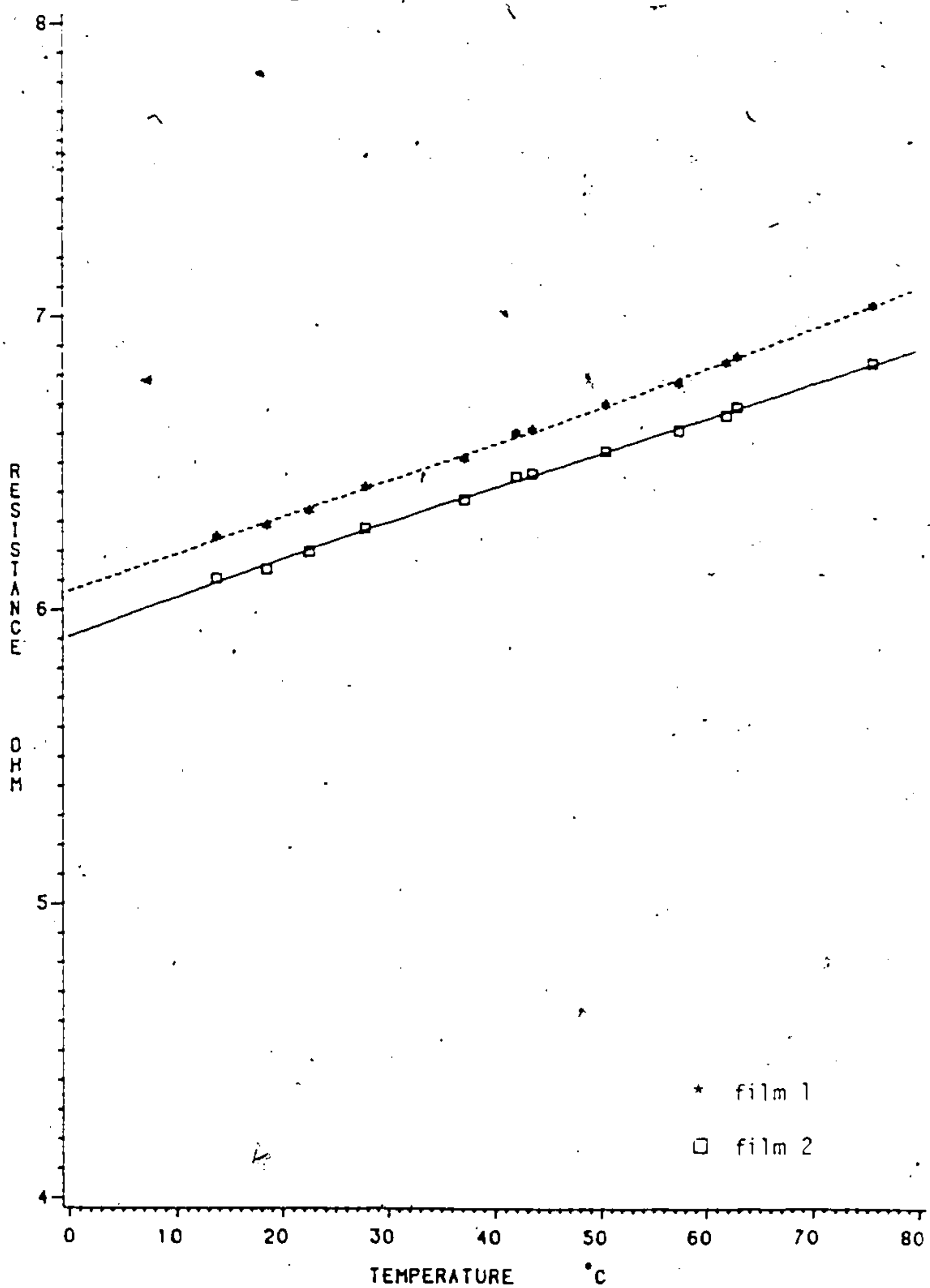

Figure 30 Temperature dependence of hot-film sensor resistance.

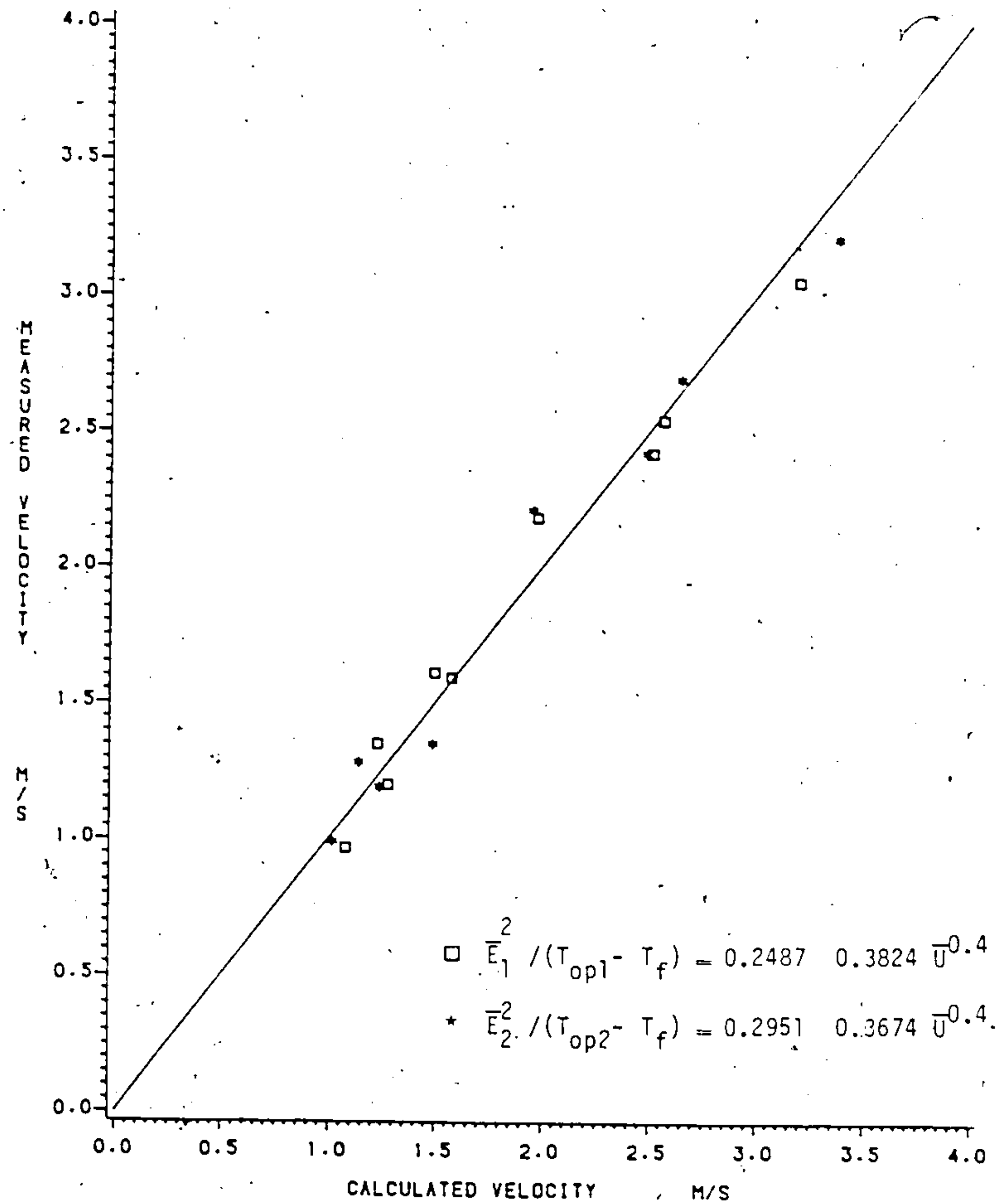

Figure 31 Accuracy of hot-film calibration equations.

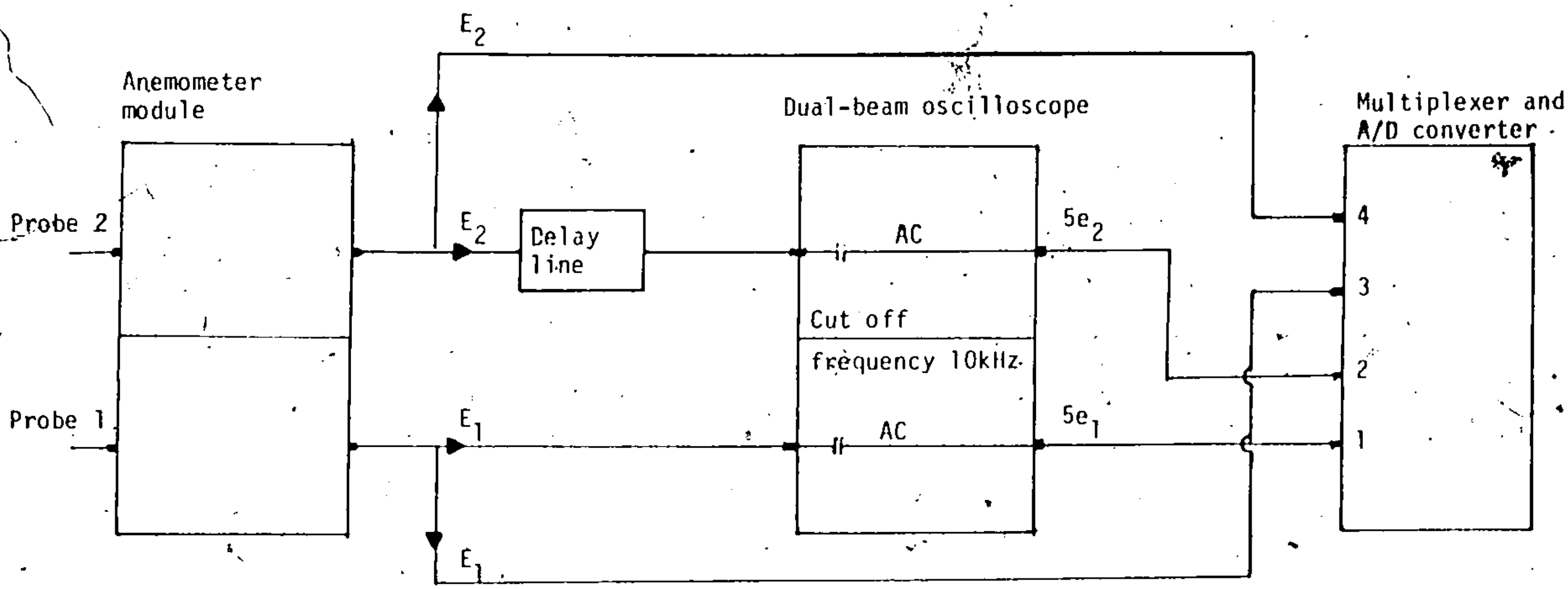

Figure 32 Data-acquisition circuitry.

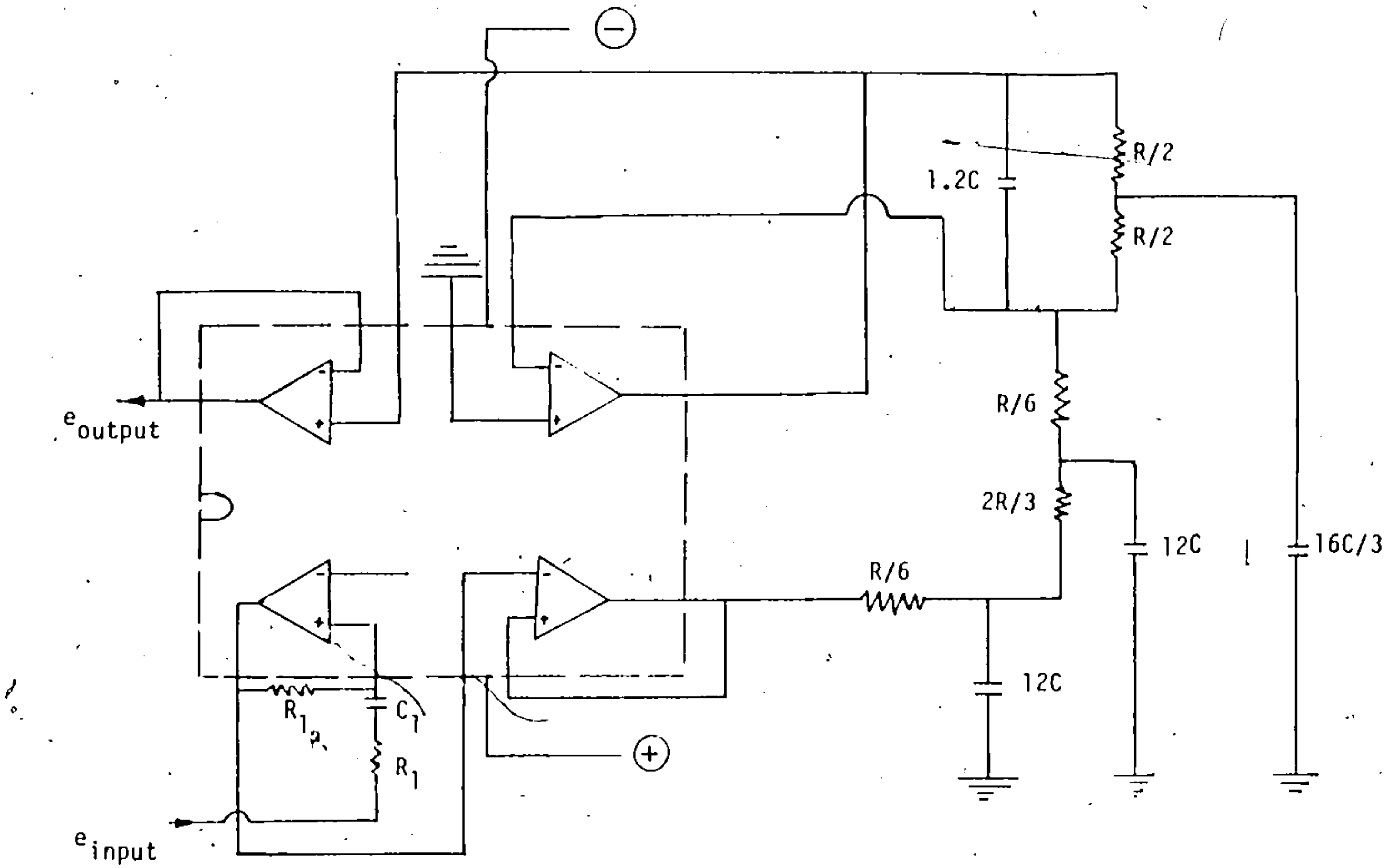

R 4256 Ω
R_1 330 kΩ

C 0.003 μF
C_1 4.7 μF

LM324D Quad op amp

Figure 33 Analog time-delay line circuit.

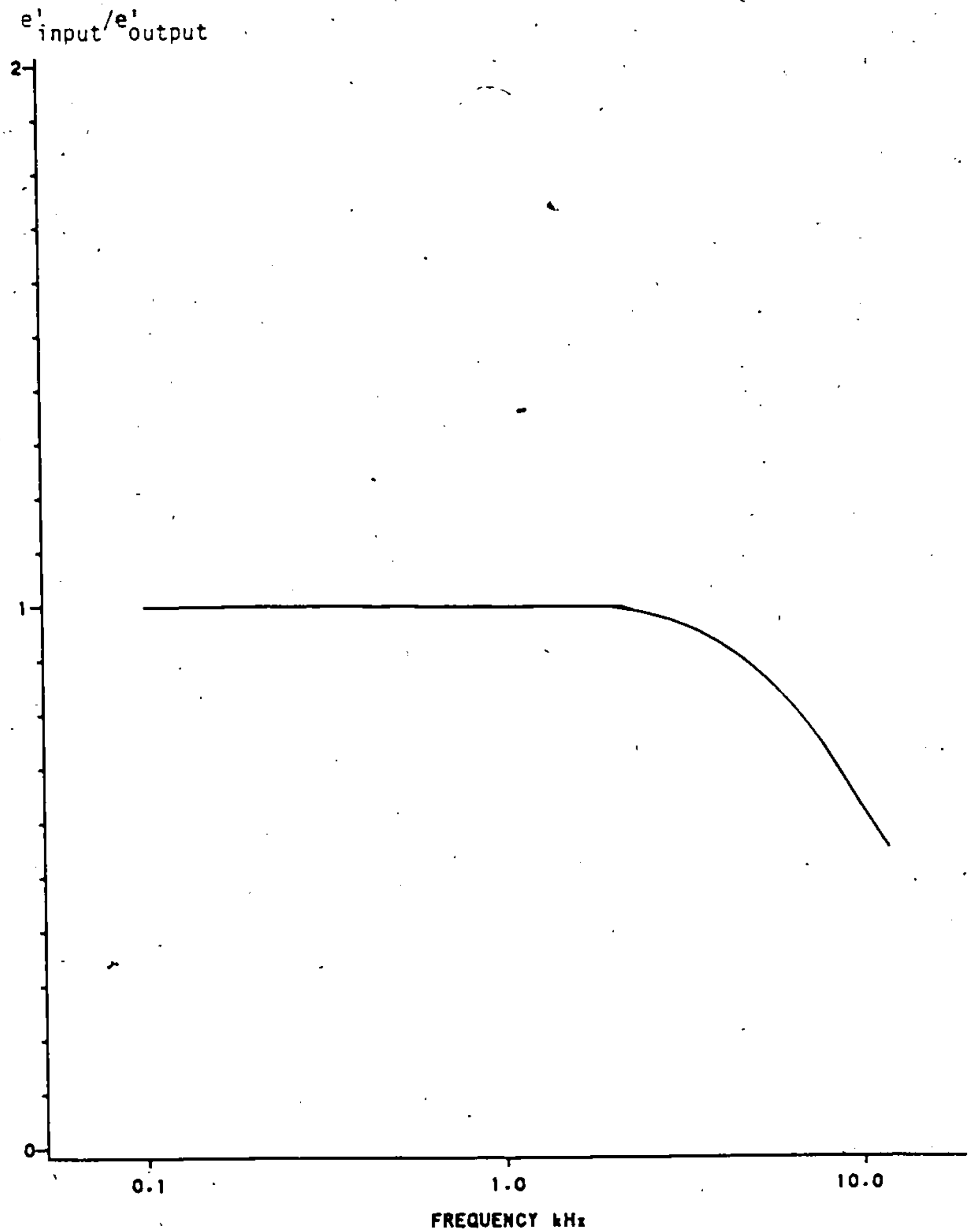

Figure 34 Frequency response of the analog time delay line.

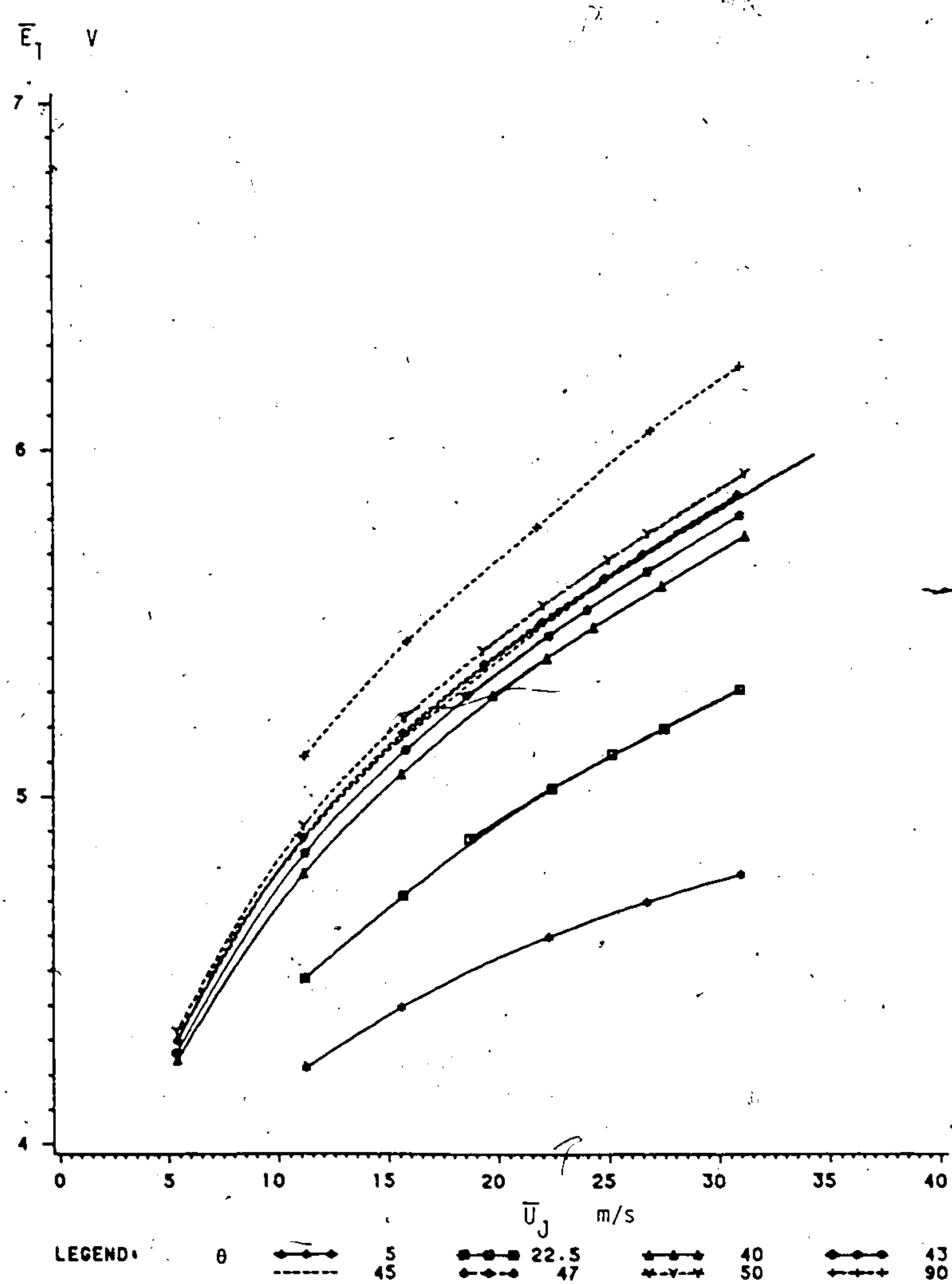

Figure 35 Yaw angle dependence of the first sensor output voltage.

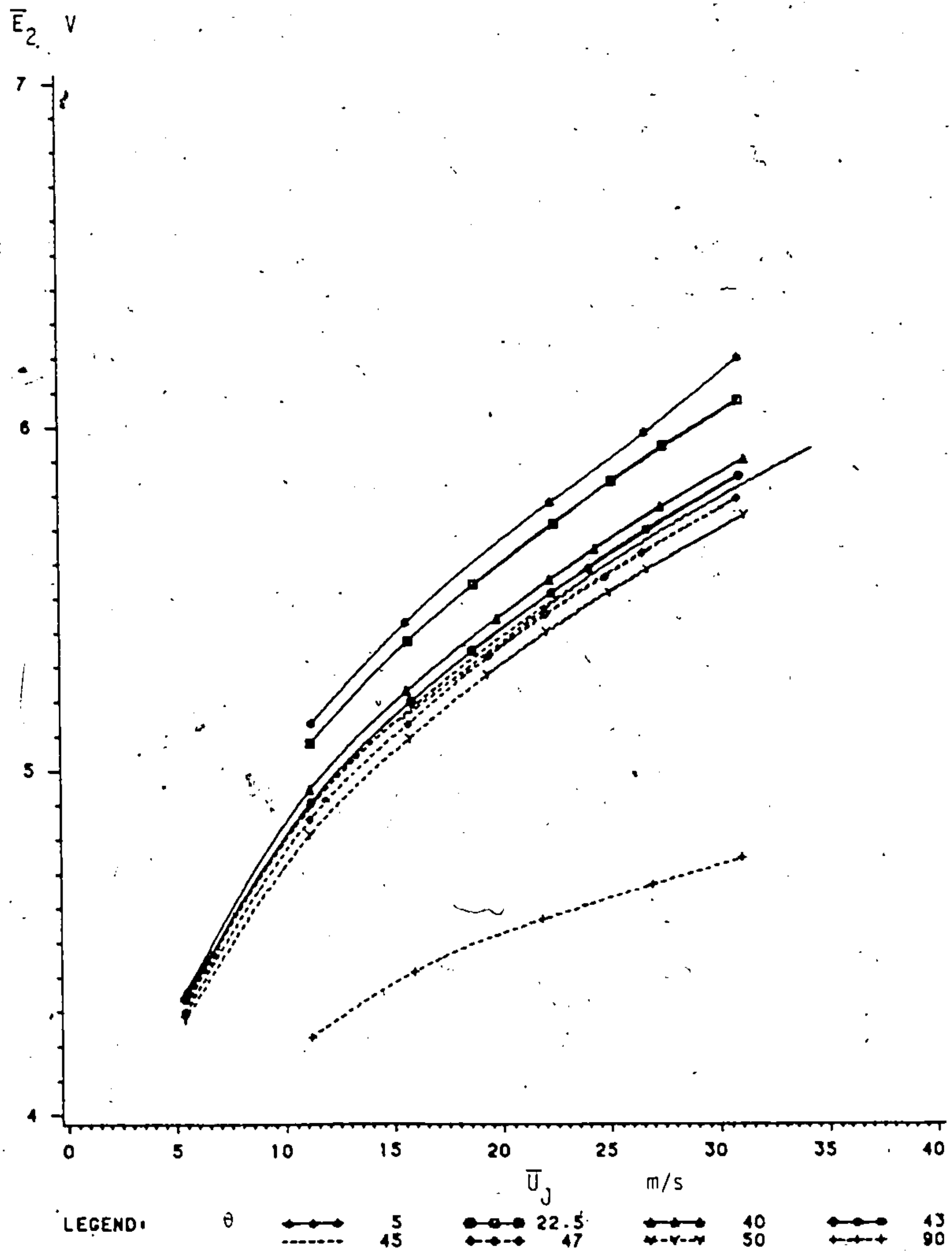

Figure 36 Yaw angle dependence of the second sensor output voltage.

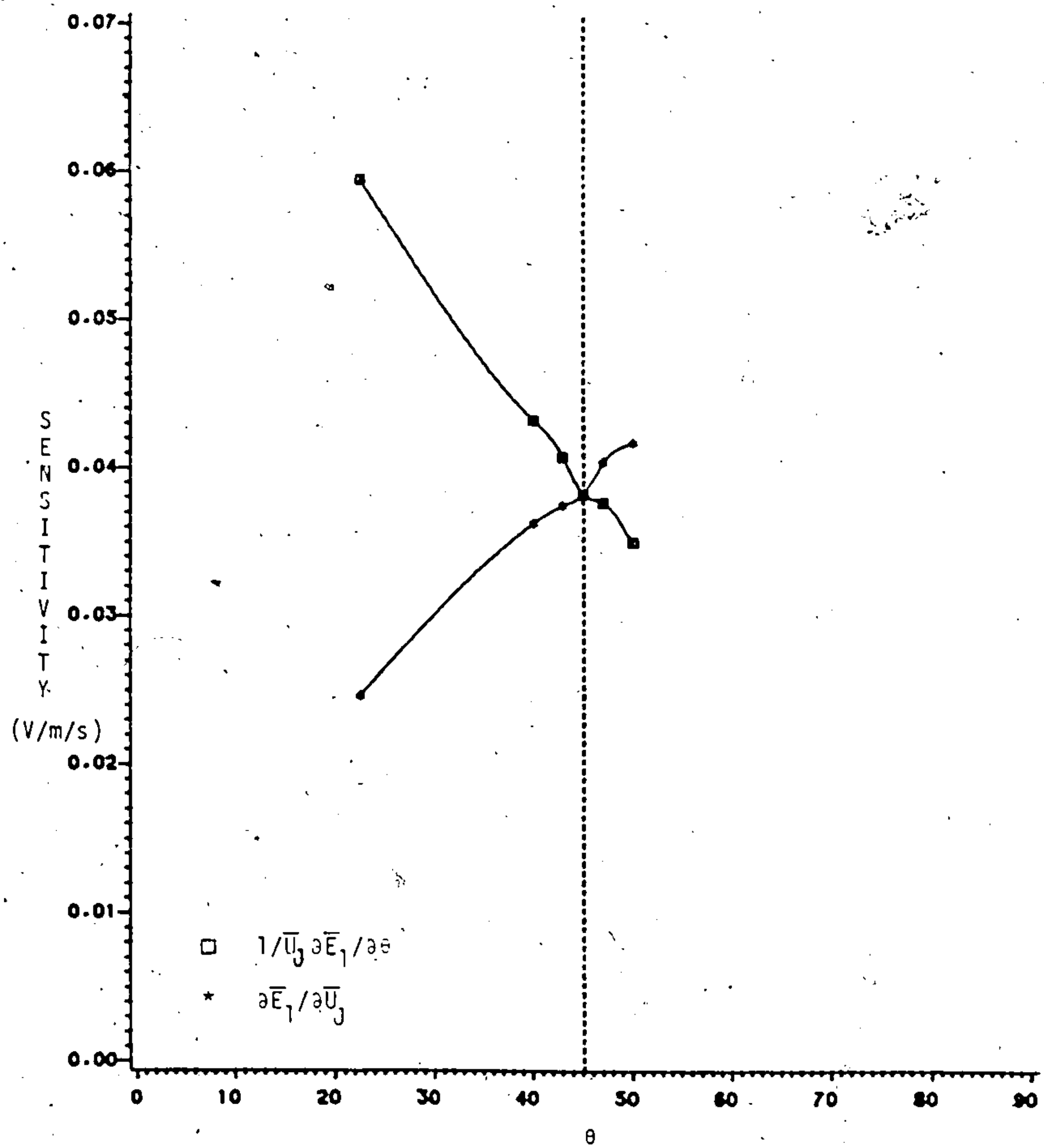

Figure 37 Angle and velocity sensitivity of the first sensor output voltage.

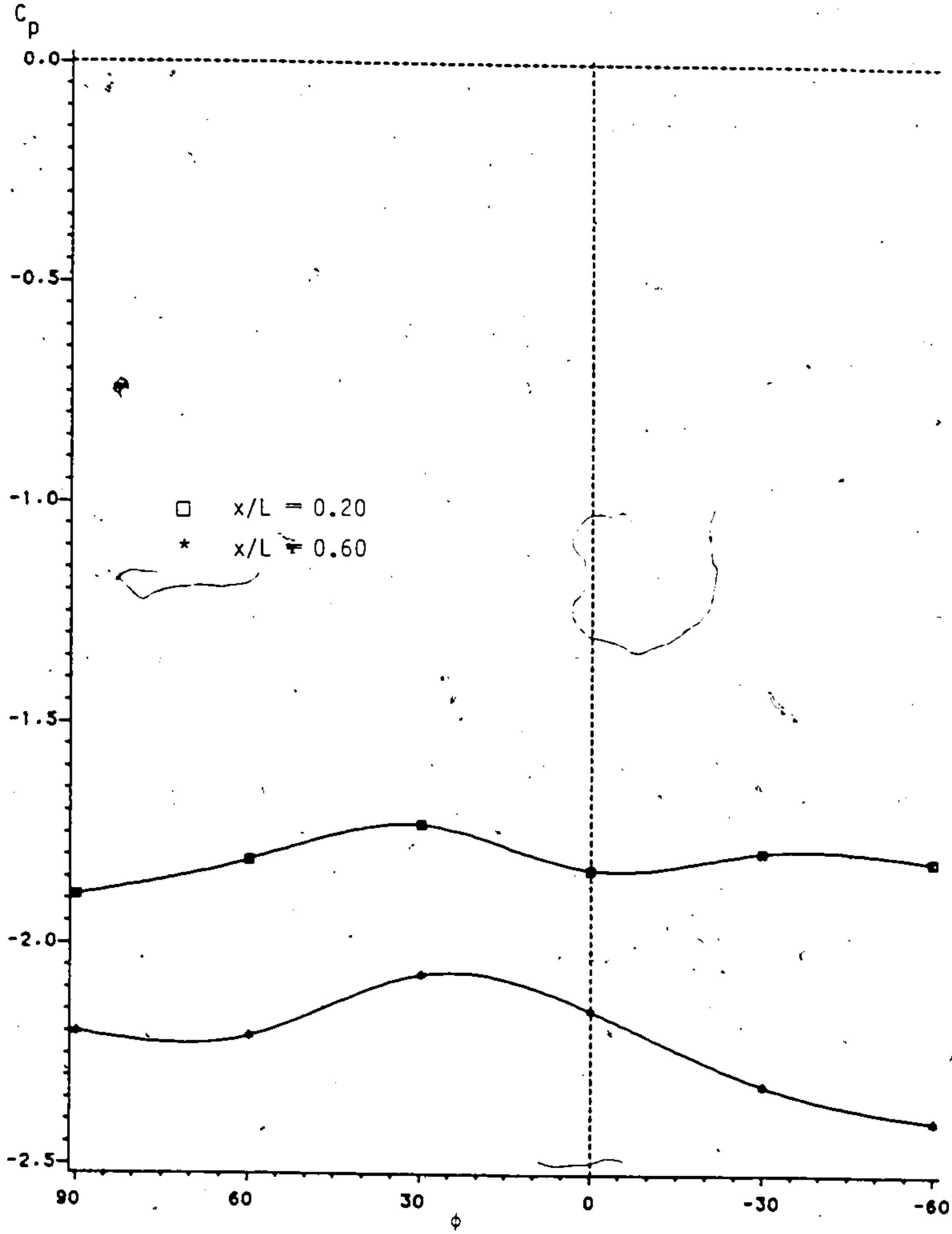

Figure 38 Peripheral variation of wall static pressure around rod B (Re_{bh} = 50000).

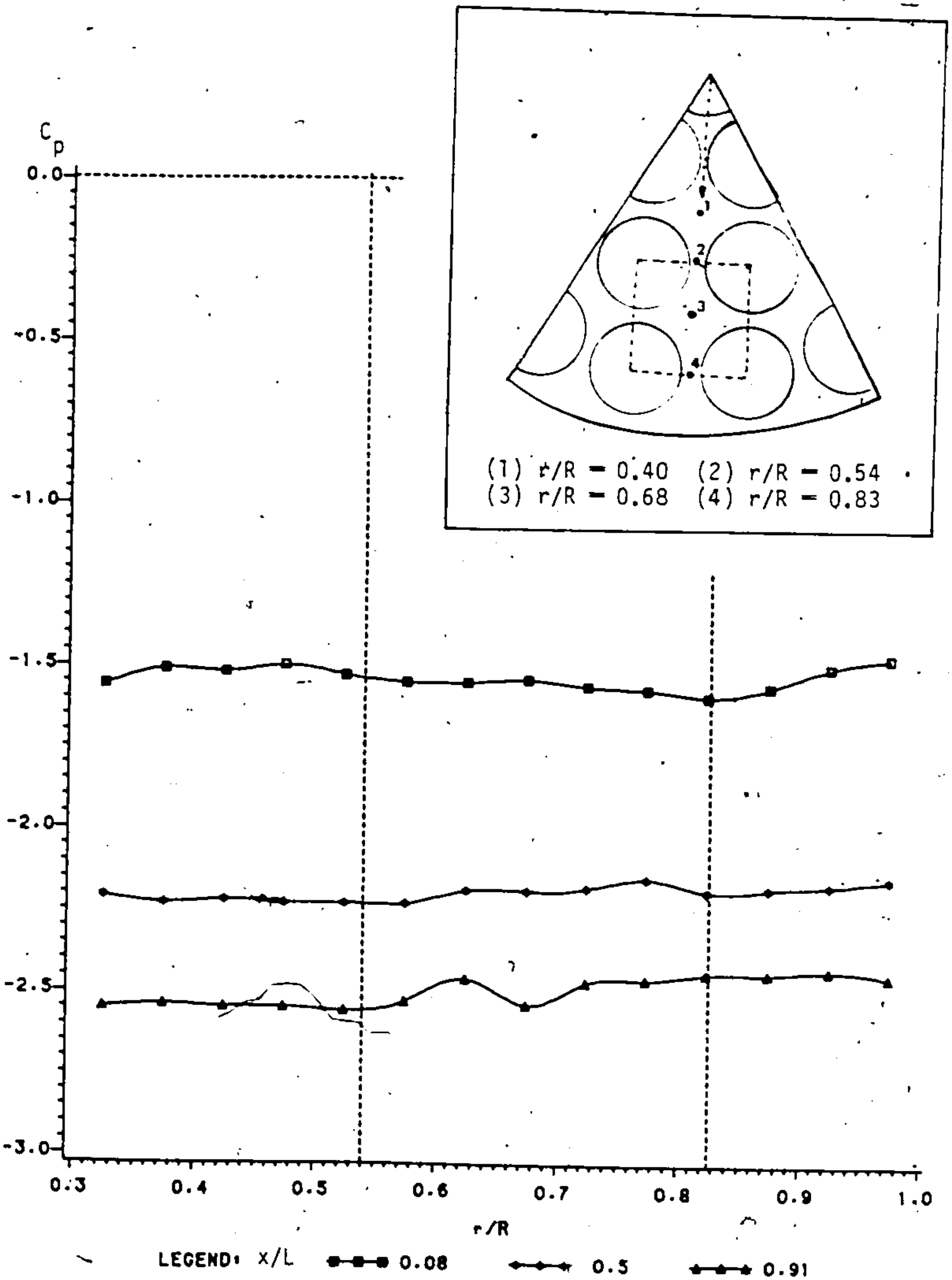

Figure 39 Variation of mean static pressure along the test-section radial axis (Re_{bh} = 50000).

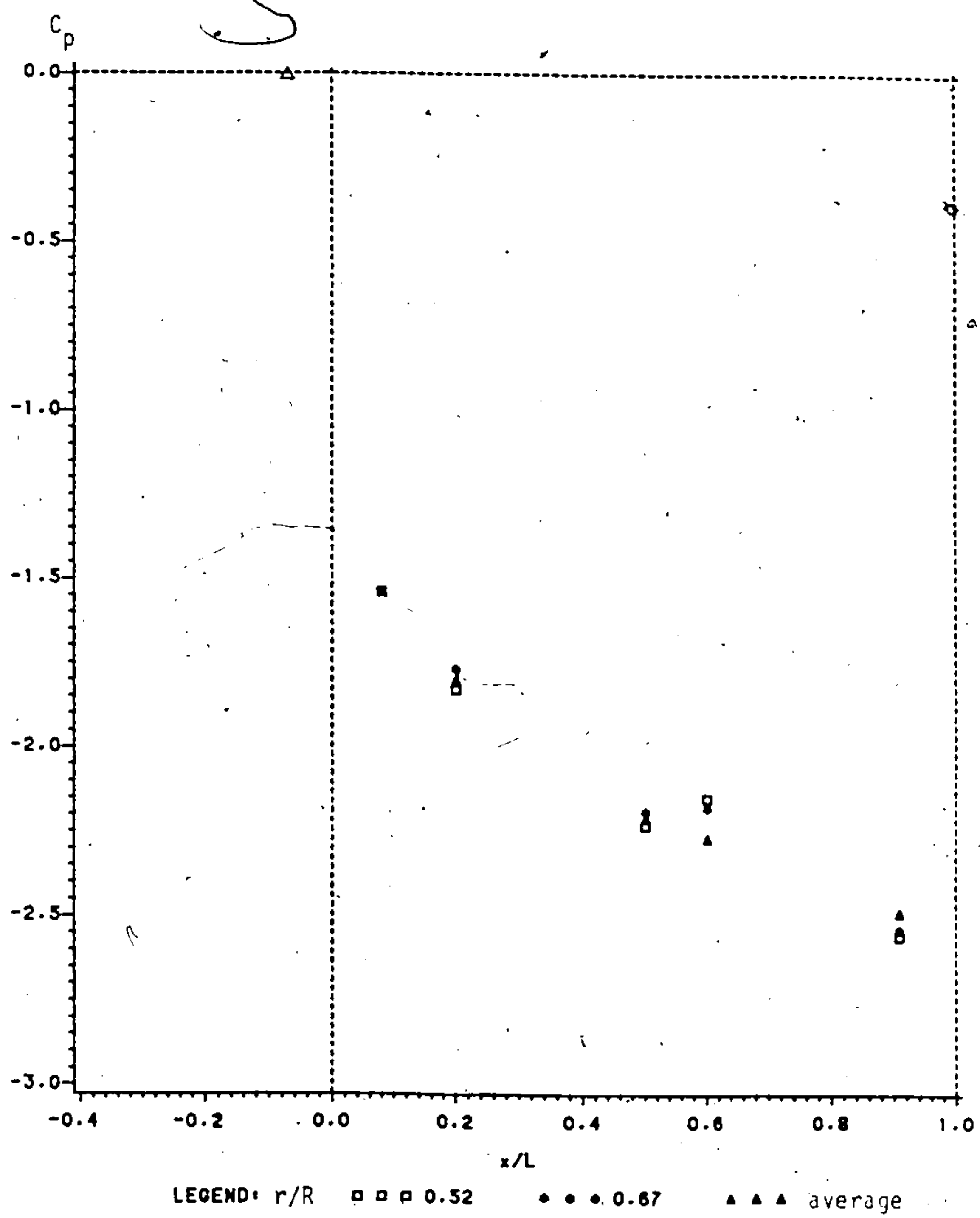

Figure 40 Downstream evolution of mean static pressure ($Re_{bh} = 50000$).

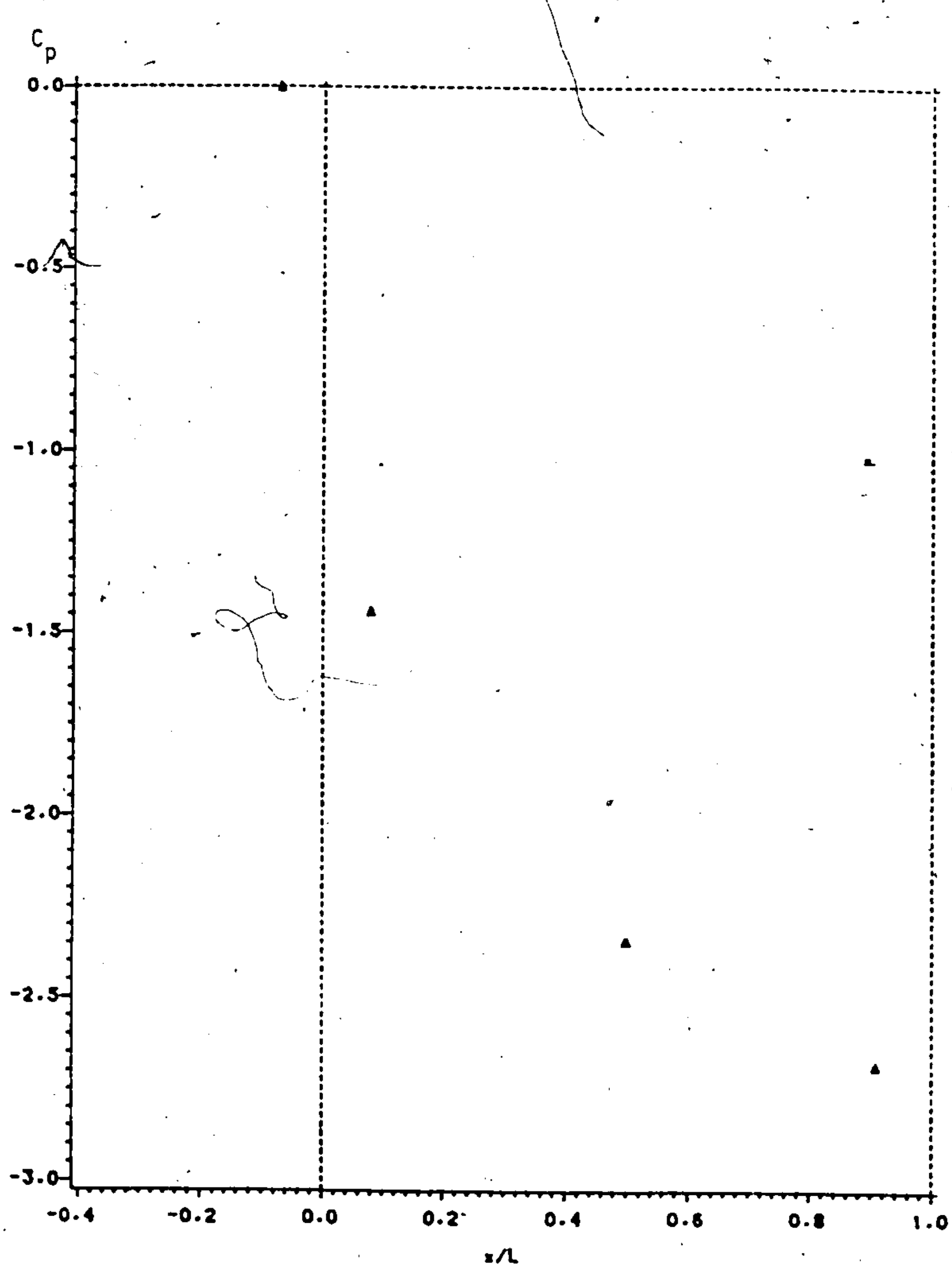

Figure 41 Downstream evolution of average mean static pressure (Re_{bh}= 62000).

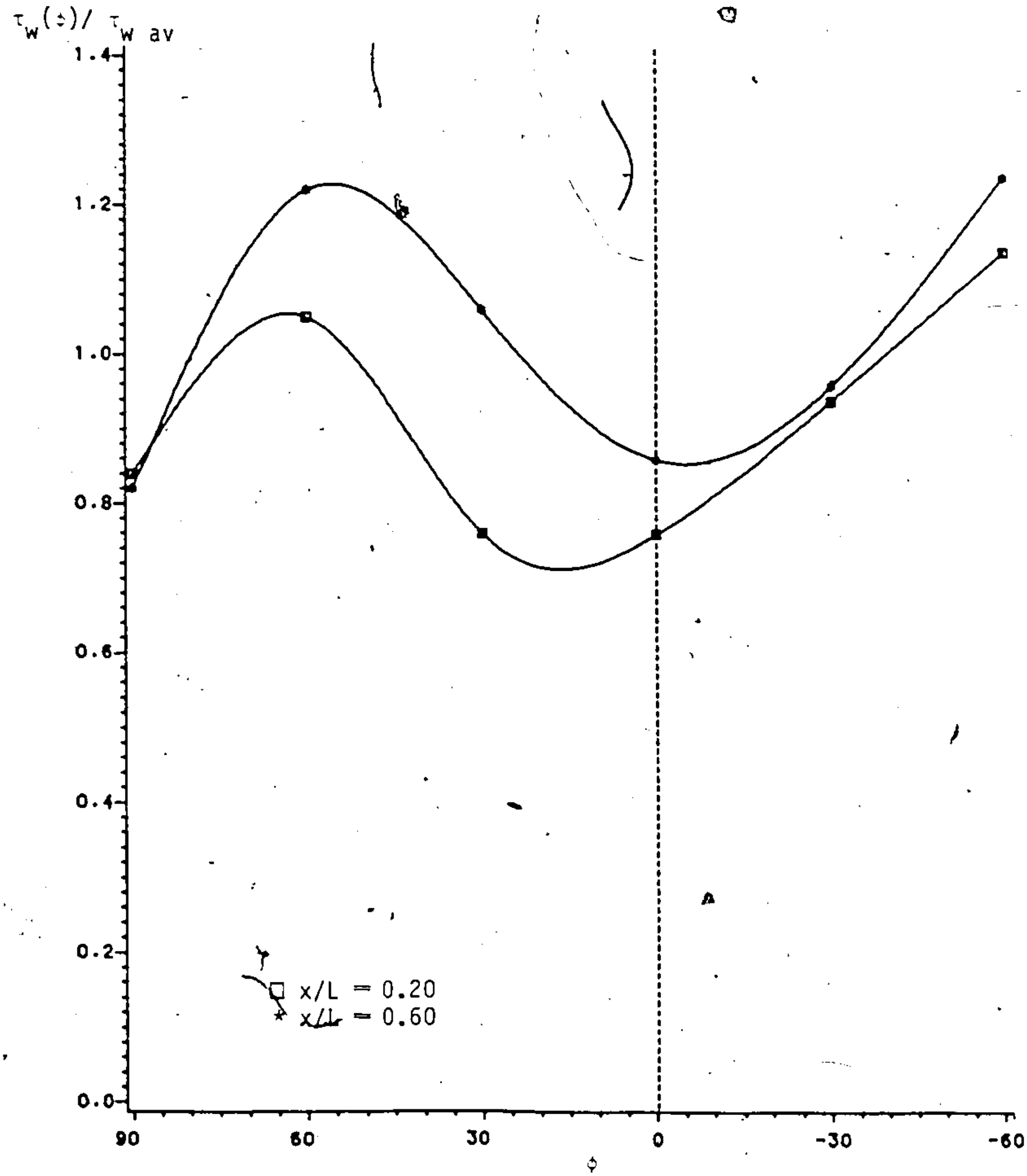

Figure 42 Peripheral variation of local shear stress around rod B (Re_{bh} = 50000).

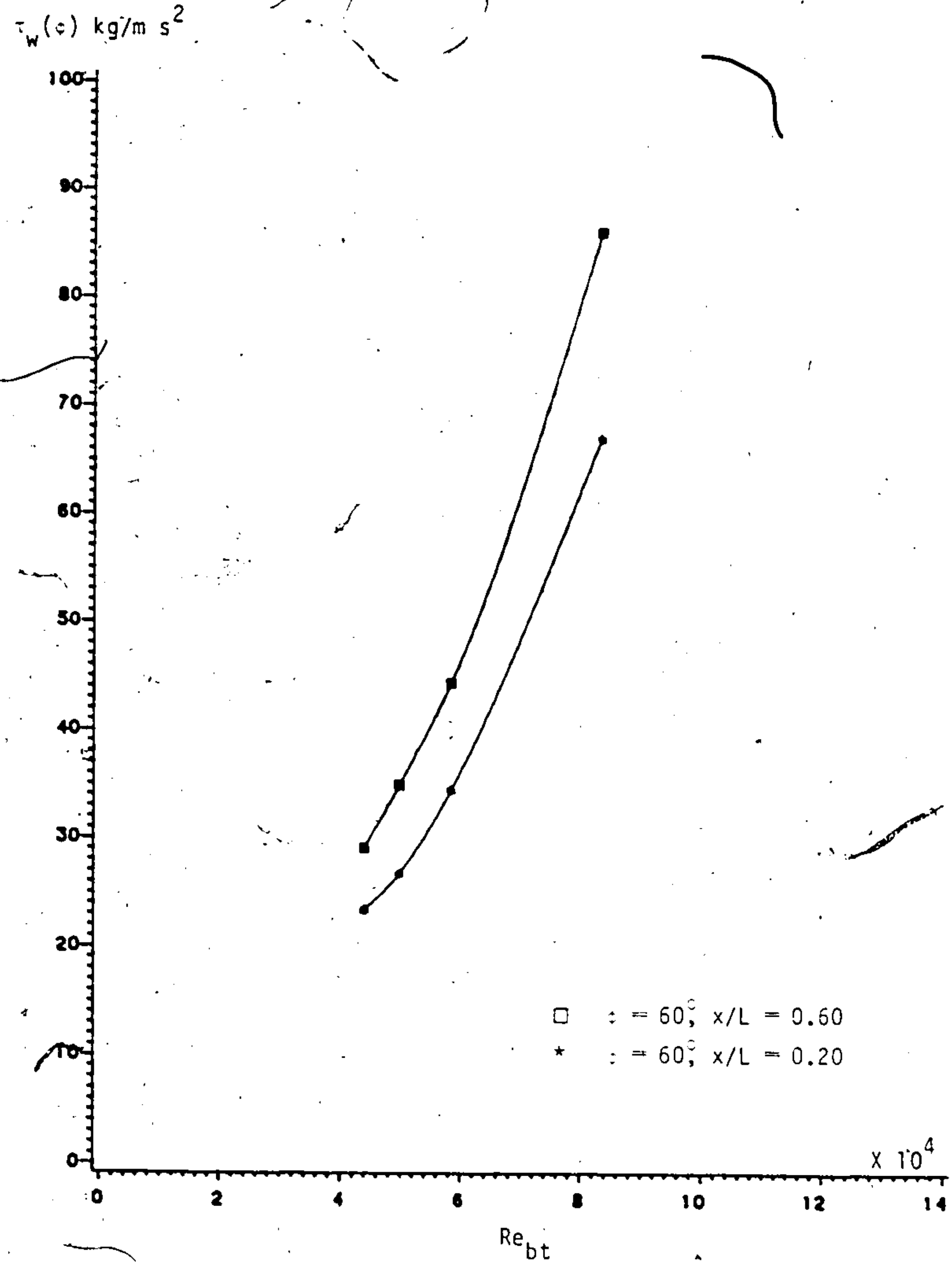

Figure 43 Reynolds number dependence of local wall shear stress.

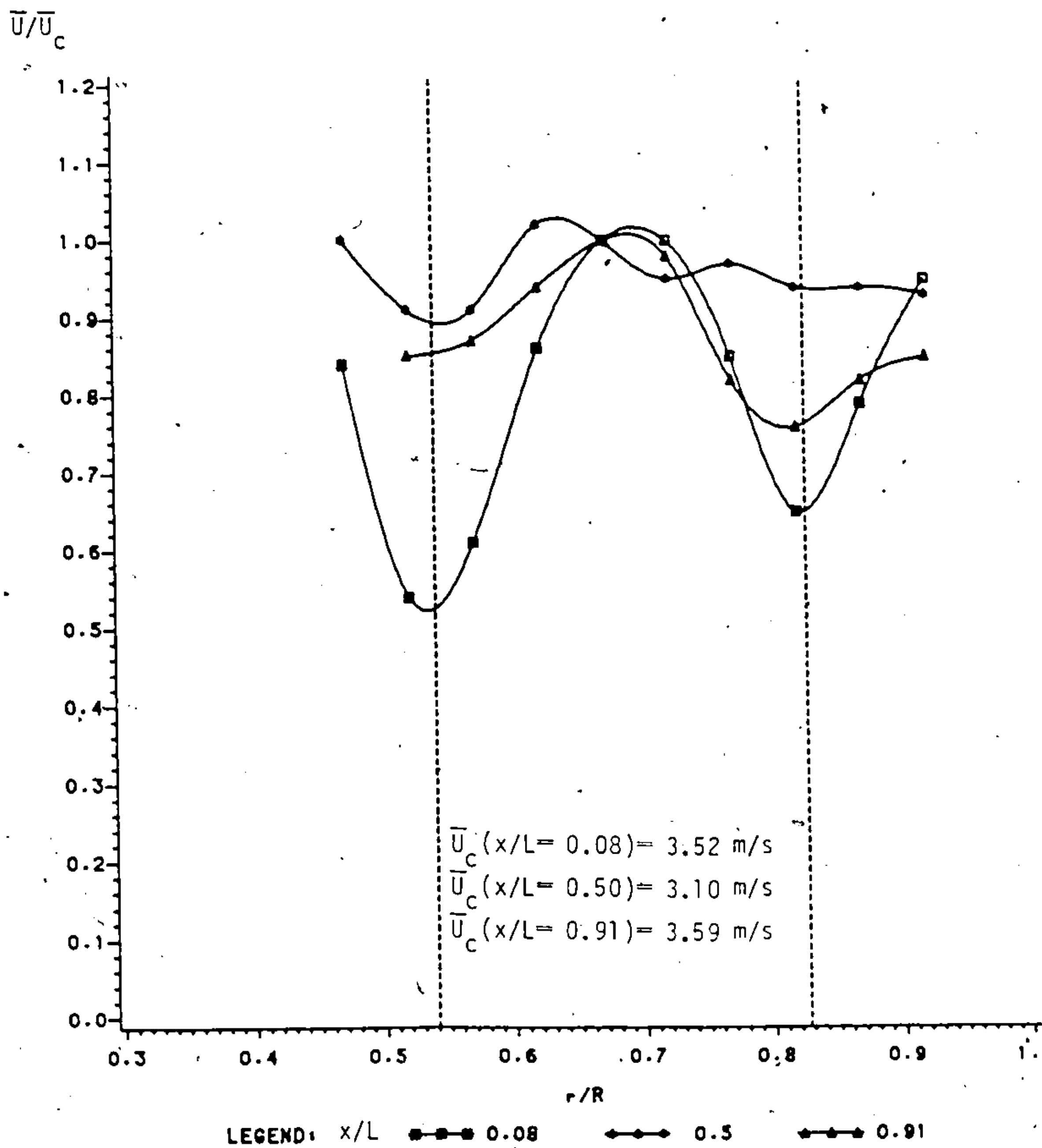

Figure 44 Variation of mean axial velocity along the test-section radial axis (Re_{bh} = 50000, hot-film).

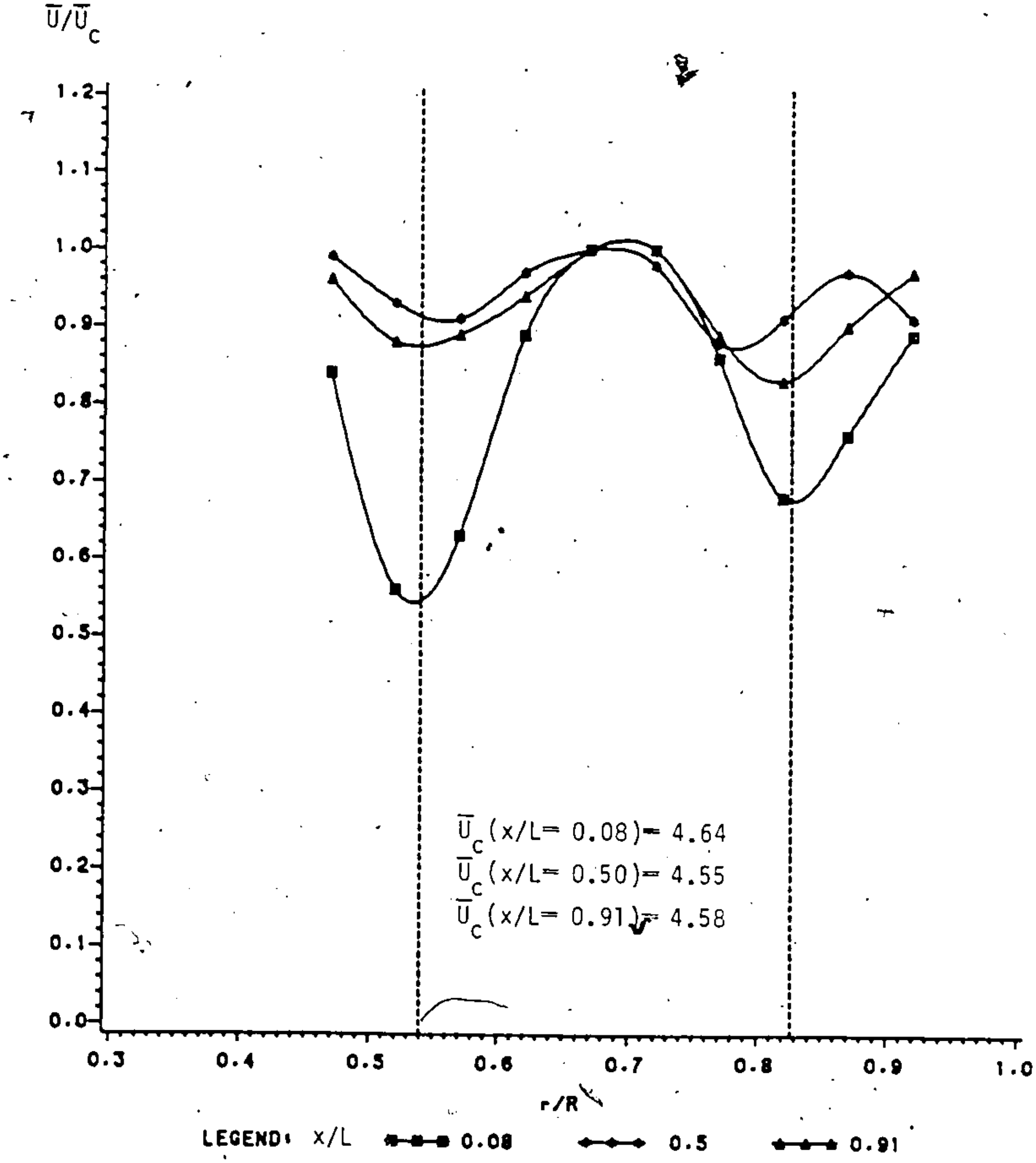

Figure 45 Variation of mean axial velocity along the test-section radial axis (Re_{bh} = 62000, hot-film).

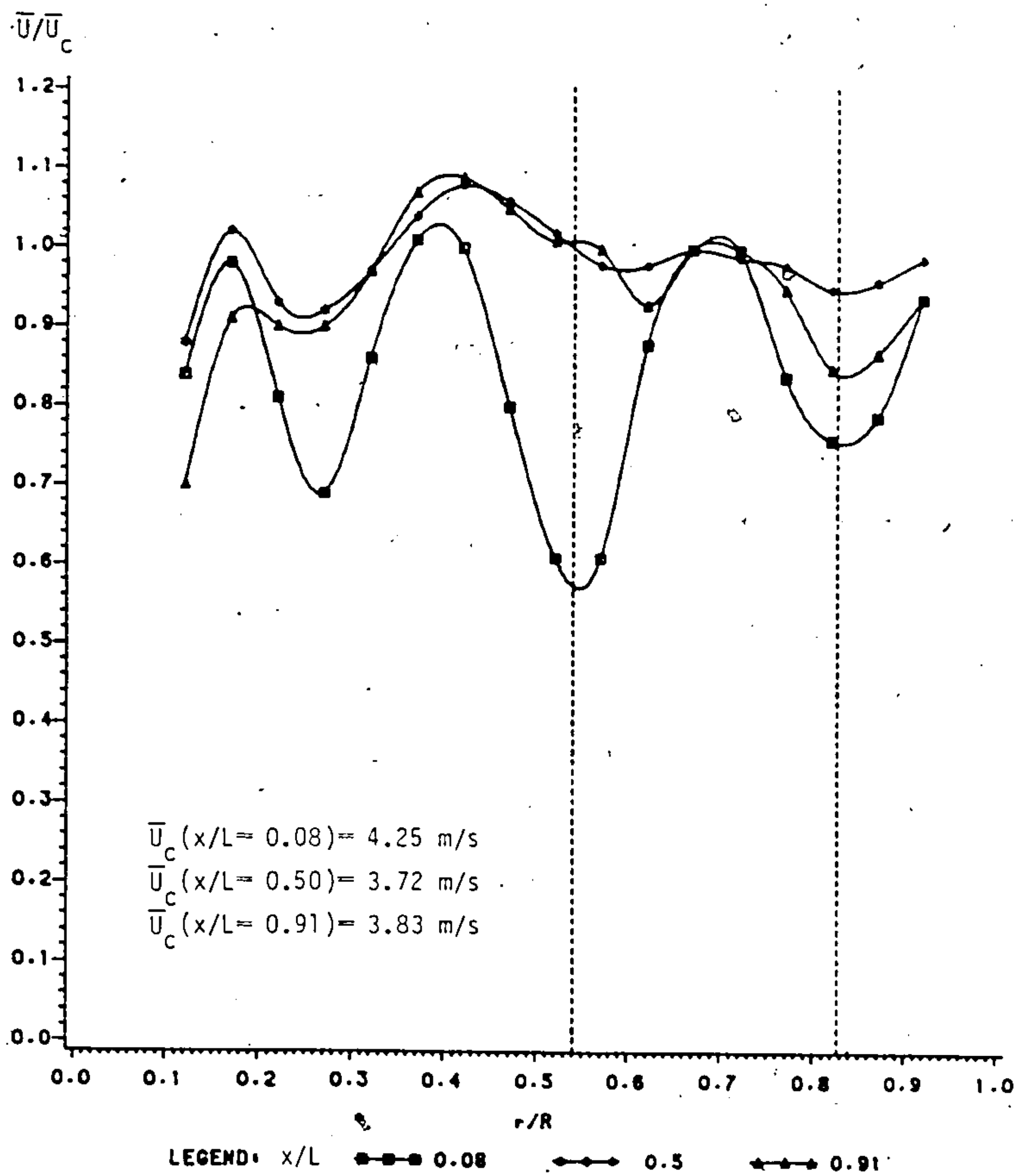

Figure 46 Variation of mean axial velocity along the test-section radial axis (Re_{bh} = 50000, pressure tubes).

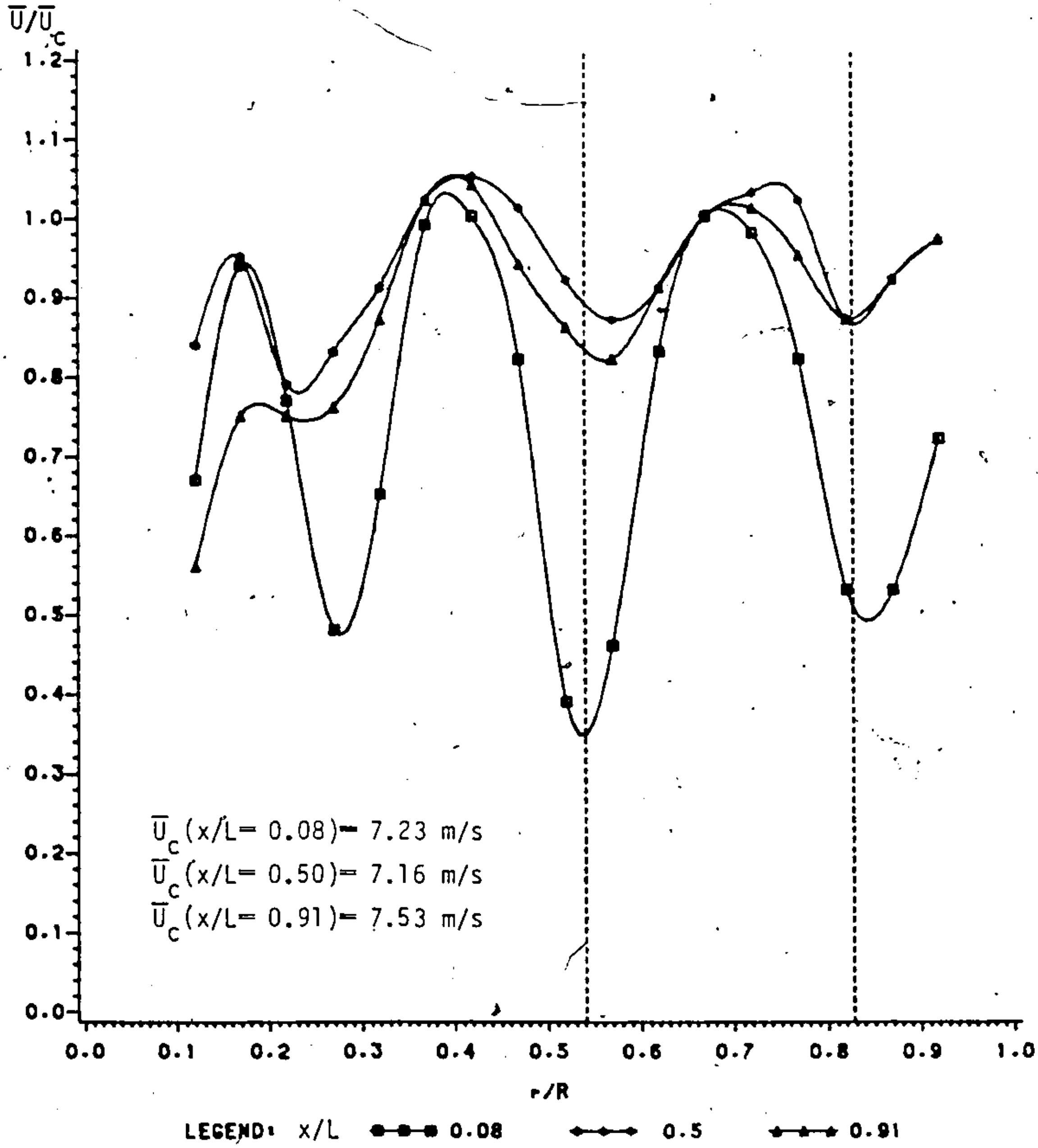

Figure 47 Variation of mean axial velocity along the test-section radial axis (Re_{bh} = 100000 , pressure tubes).

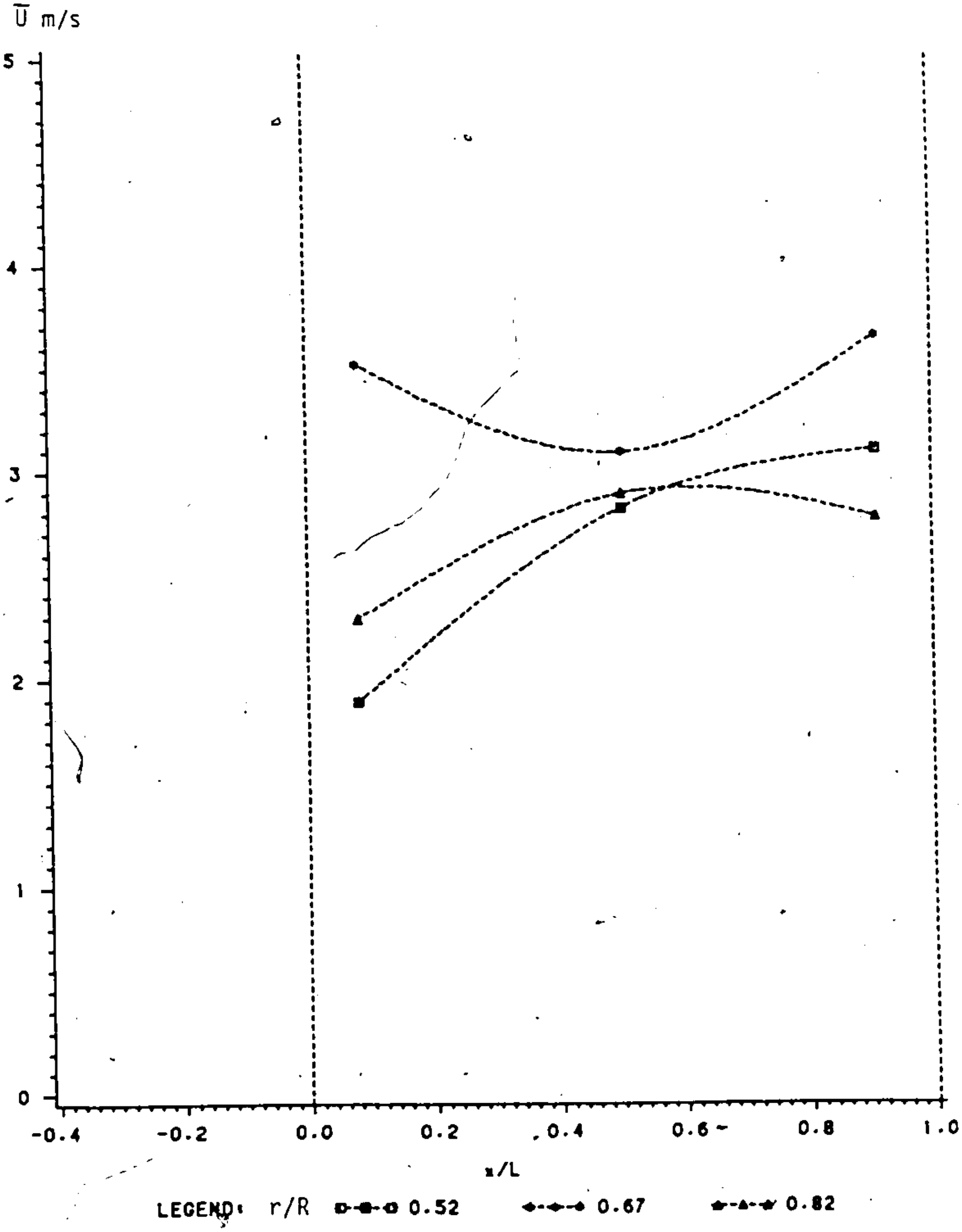

Figure 48 Downstream evolution of mean axial velocity (Re_{bh} = 50000).

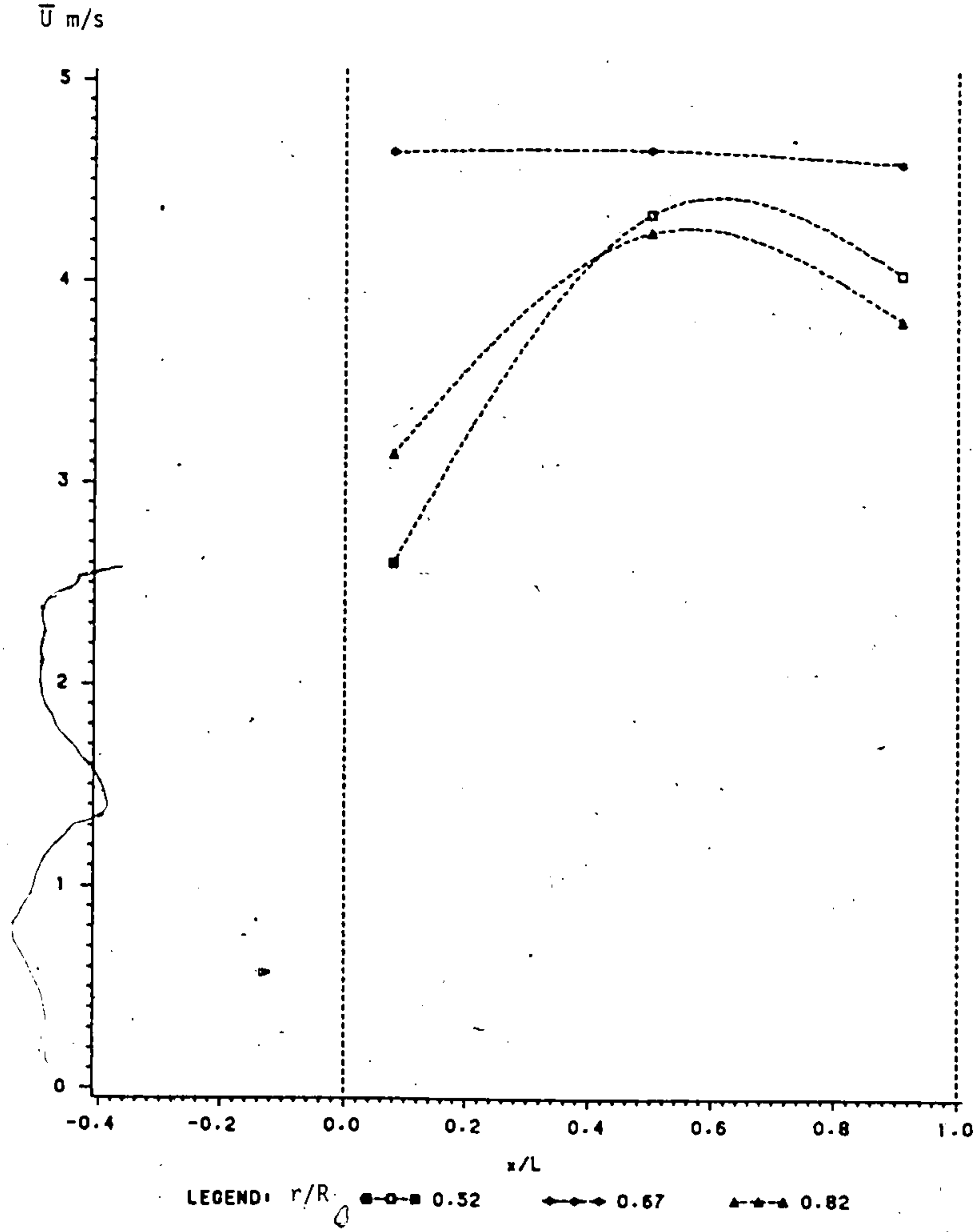

Figure 49 Downstream evolution of mean axial velocity (Re_{bh} = 62000, hot-film).

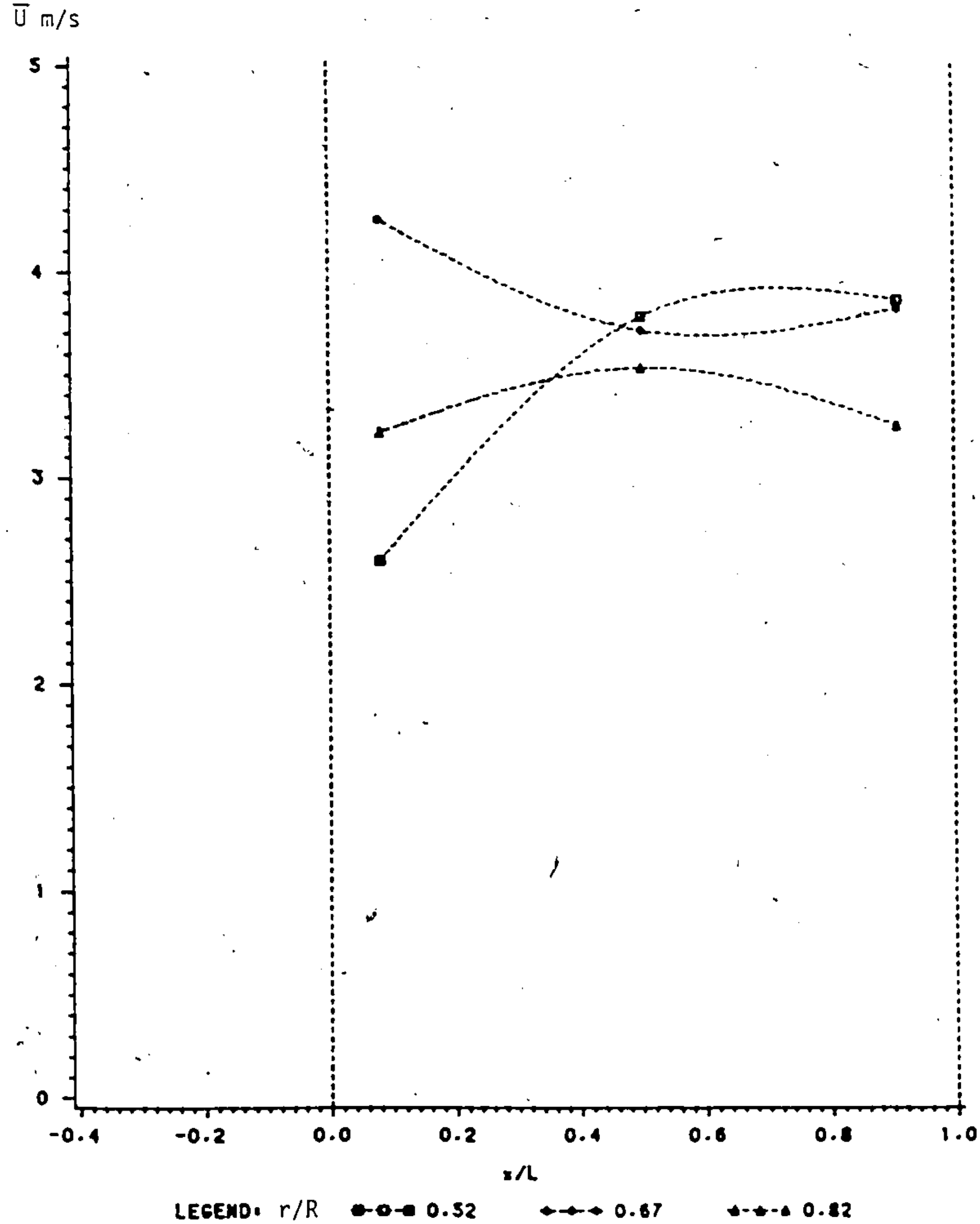

Figure 50 Downstream evolution of mean axial velocity (Re_{bh} = 50000, pressure tubes).

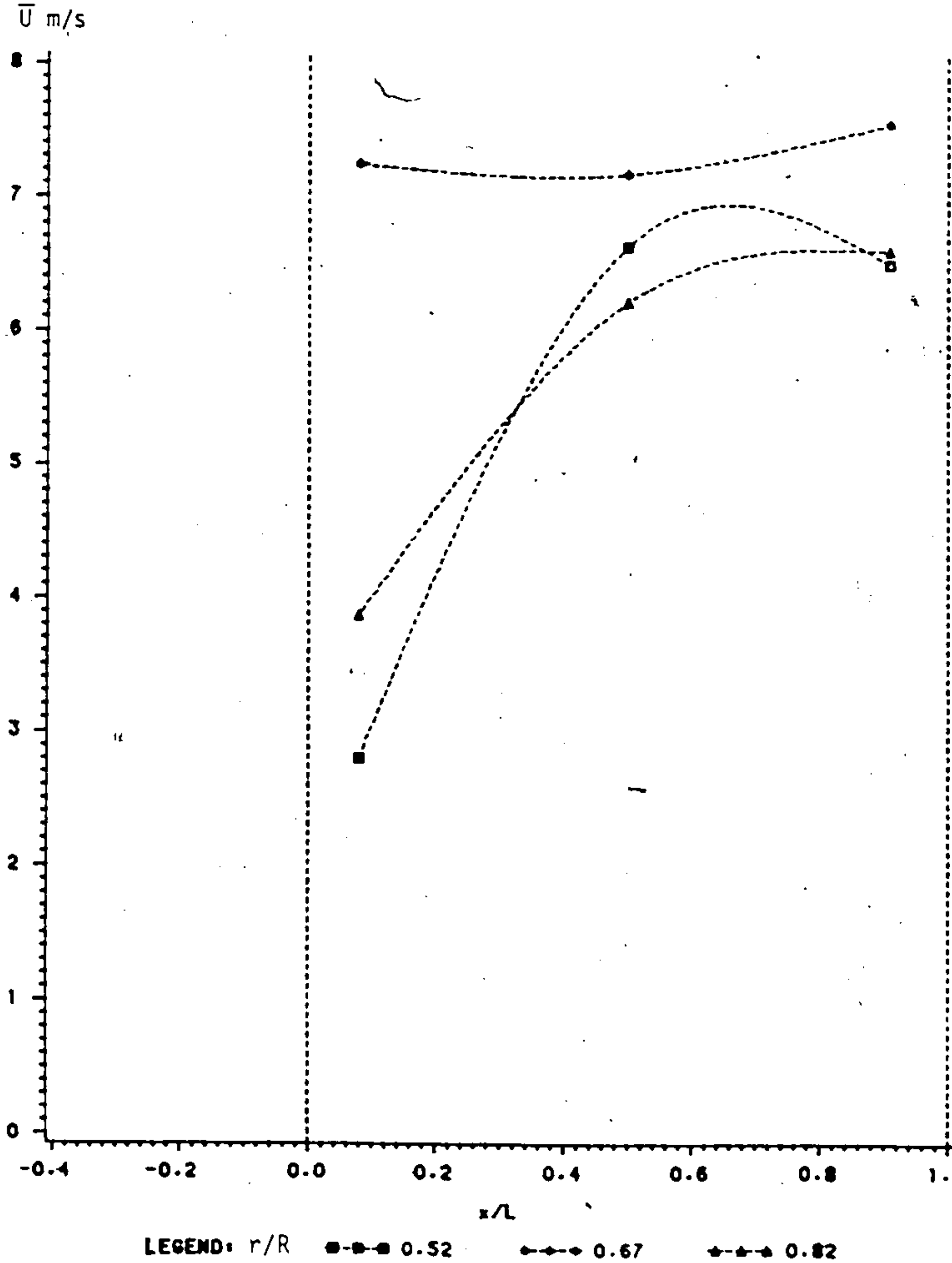

Figure 51 Downstream evolution of mean axial velocity (Re_{bh} = 100000, pressure tubes).

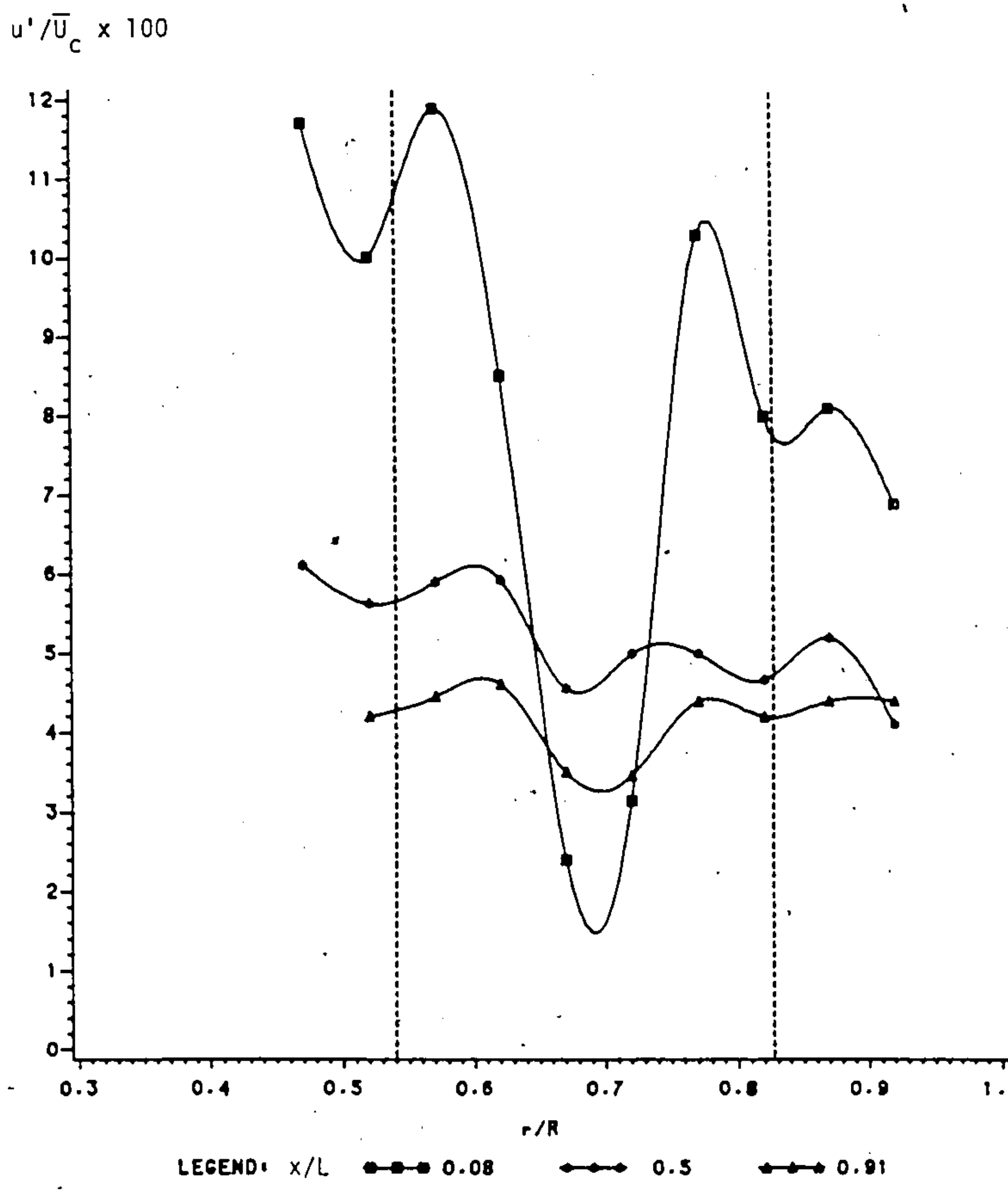

Figure 52 Variation of axial turbulence intensity along the test-section radial axis (Re_{bh} = 50000).

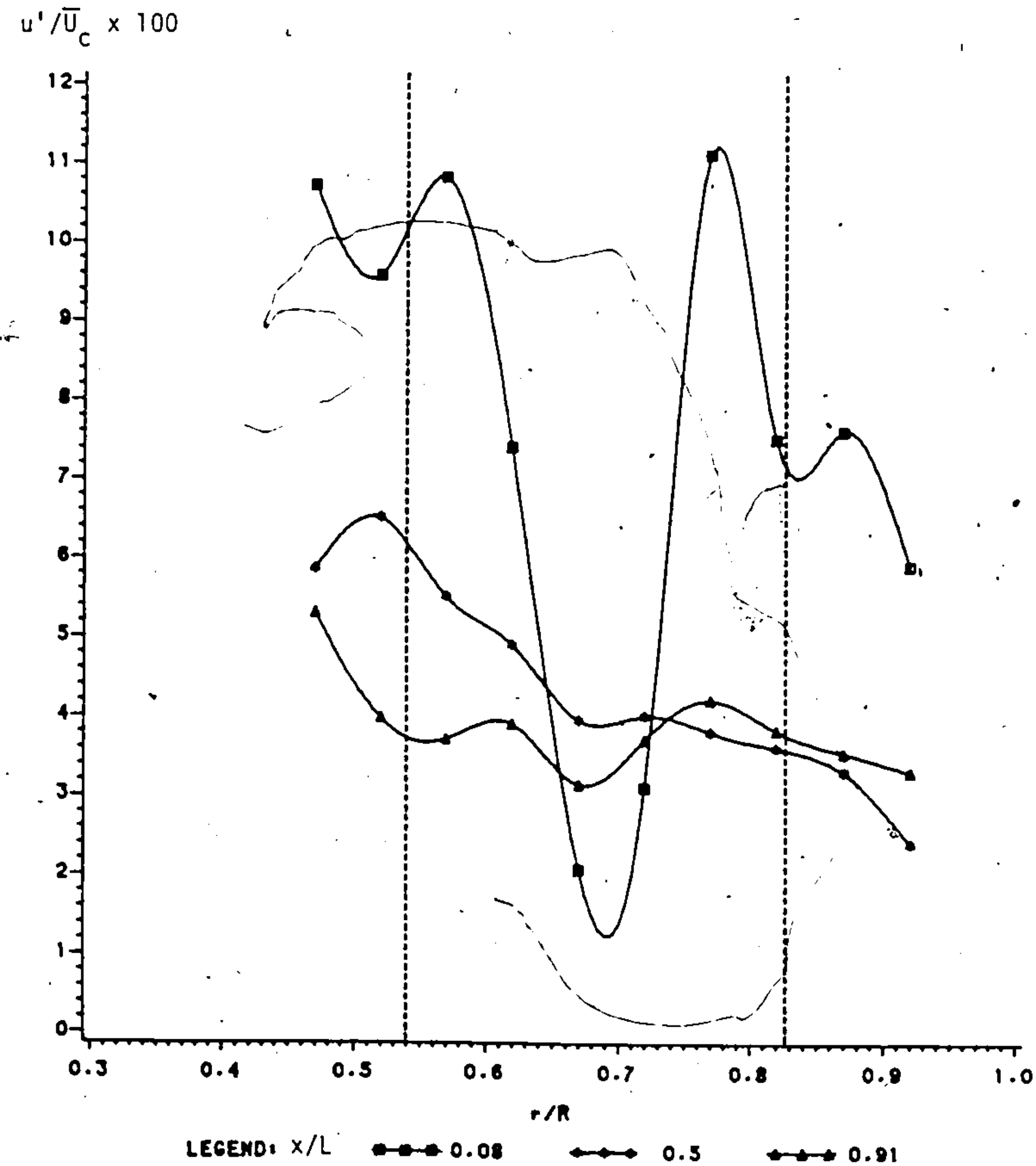

Figure 53 Variation of axial turbulence intensity along the test-section radial axis (Re_{bh} = 62000).

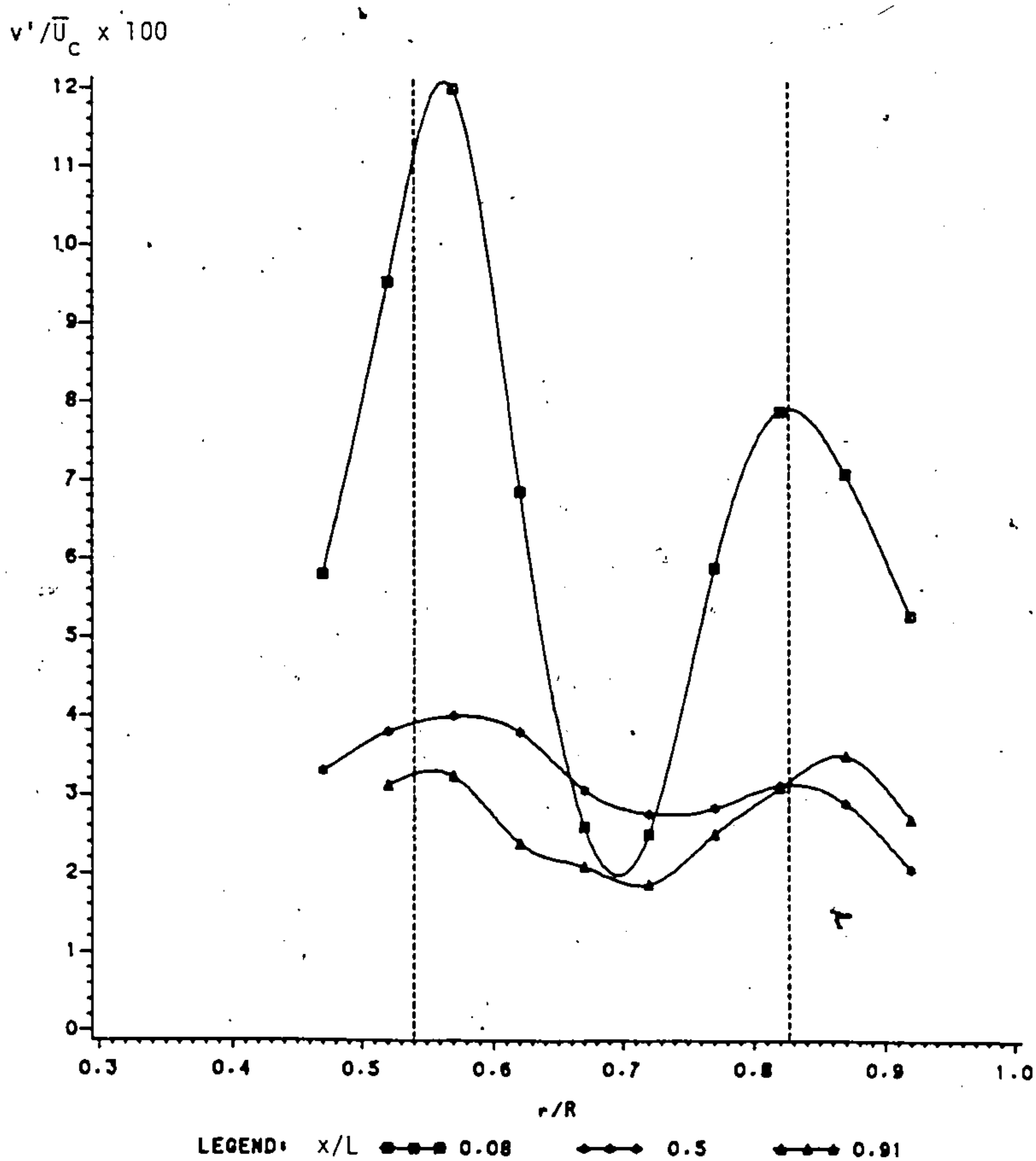

Figure 54 Variation of radial turbulence intensity along the test-section radial axis (Re_{bh} = 50000).

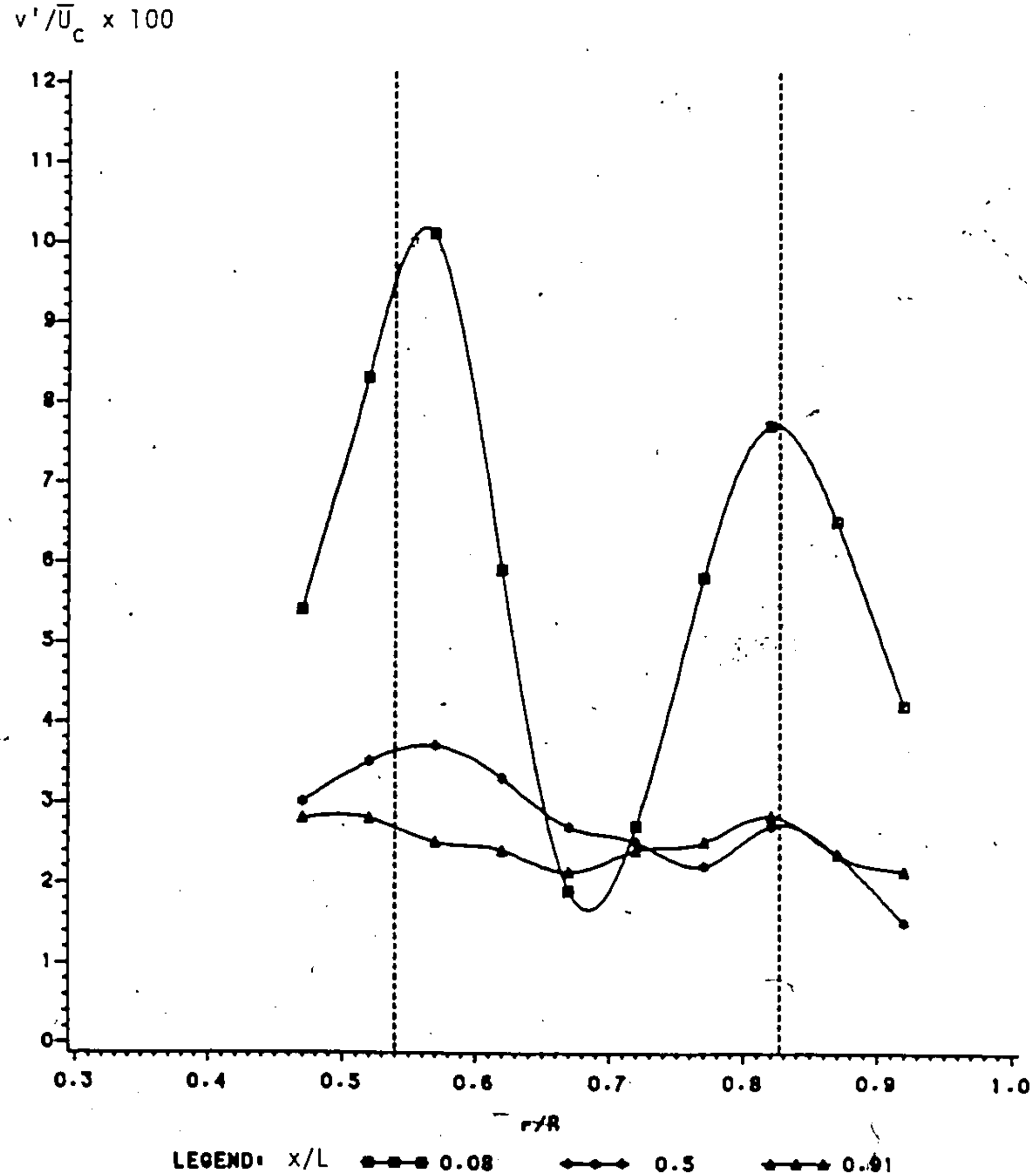

Figure 55 Variation of radial turbulence intensity along the test-section radial axis (Re_{bh} = 62000).

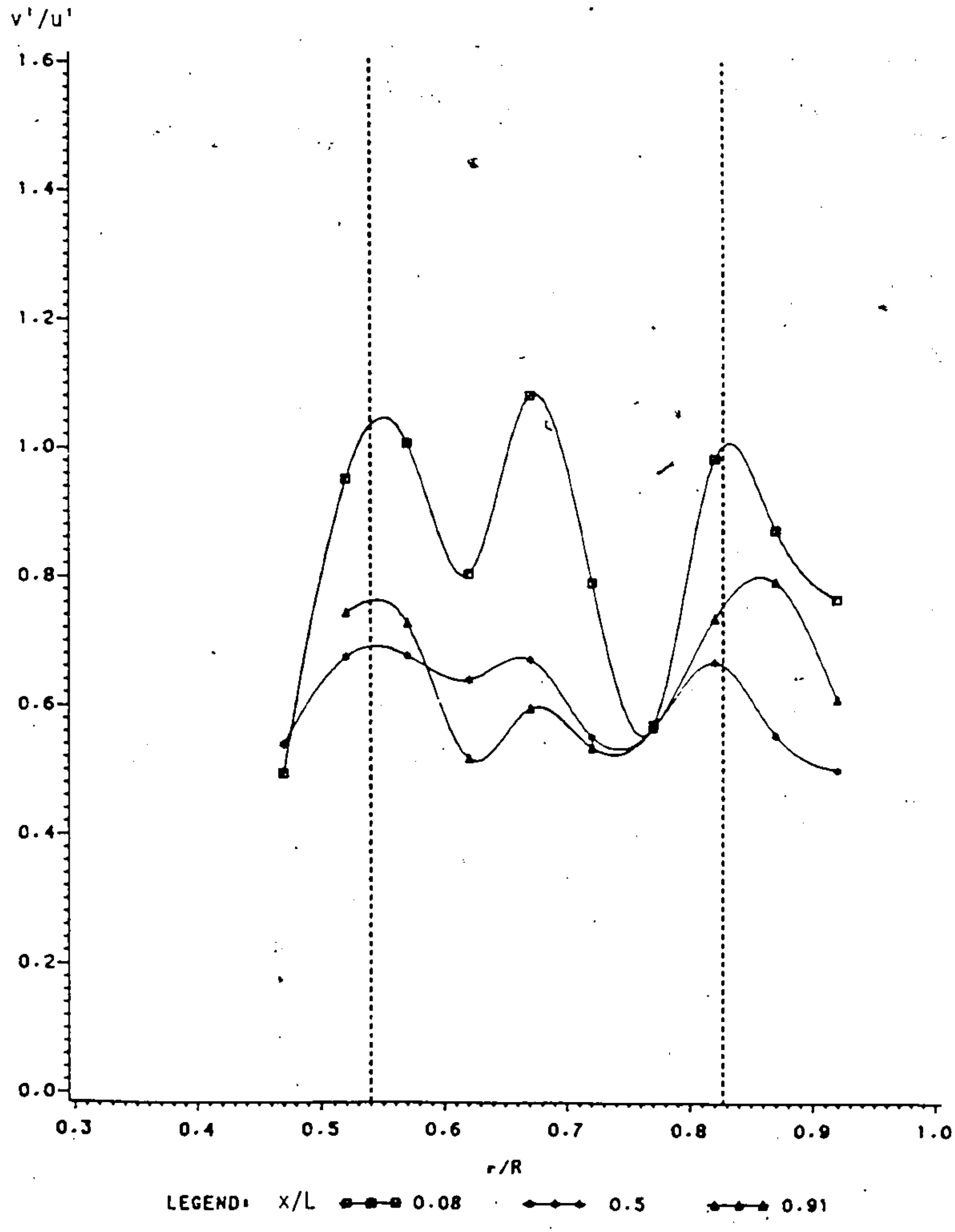

Figure 56 Relative magnitude of radial turbulence intensity with respect to axial turbulence intensity (Re_{bh} = 50000).

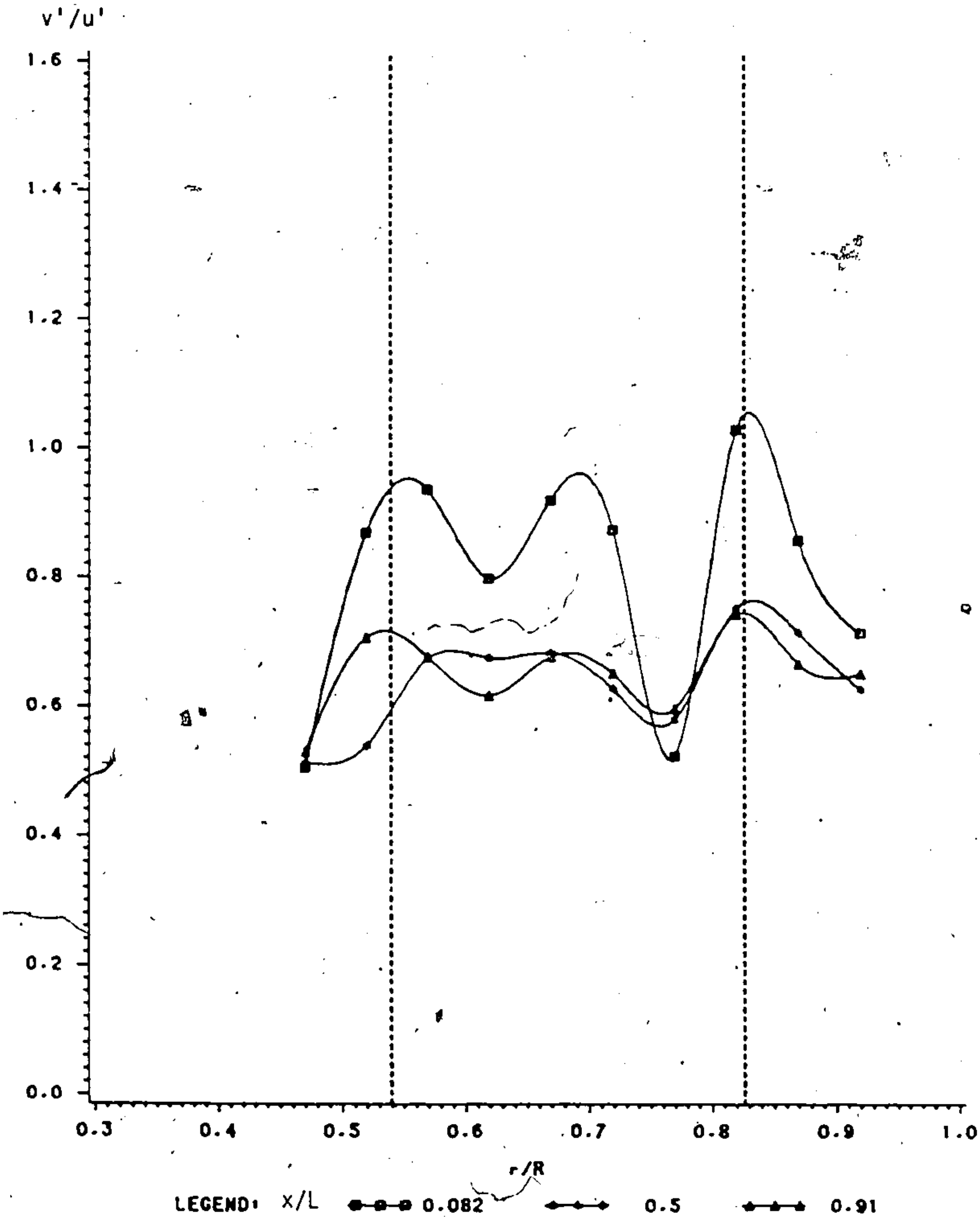

Figure 57 Relative magnitude of radial turbulence intensity with respect to axial turbulence intensity (Re_{bh} = 62000).

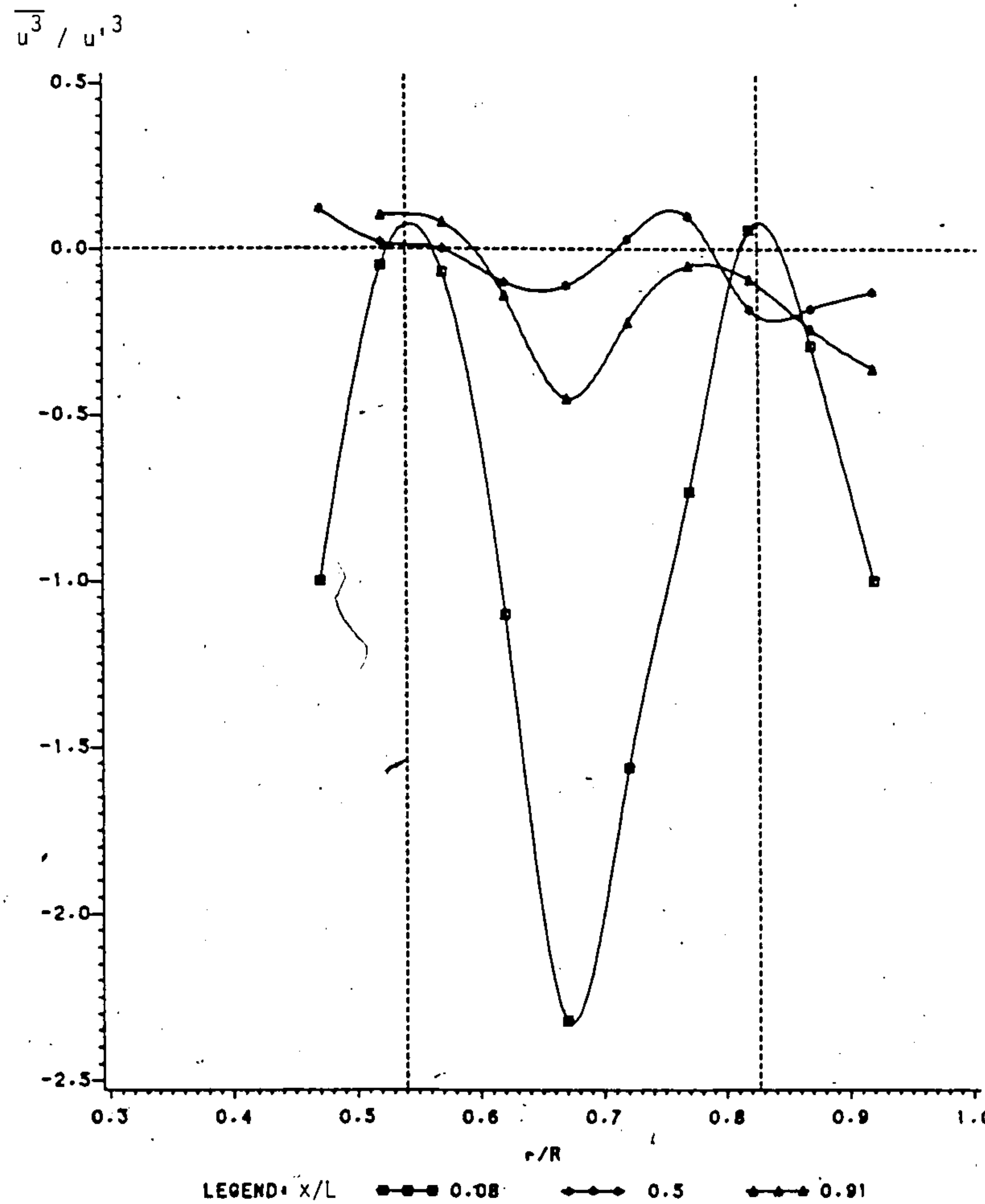

Figure 58 Variation of axial skewness factor along the test-section radial axis (Re_{bh}=30000).

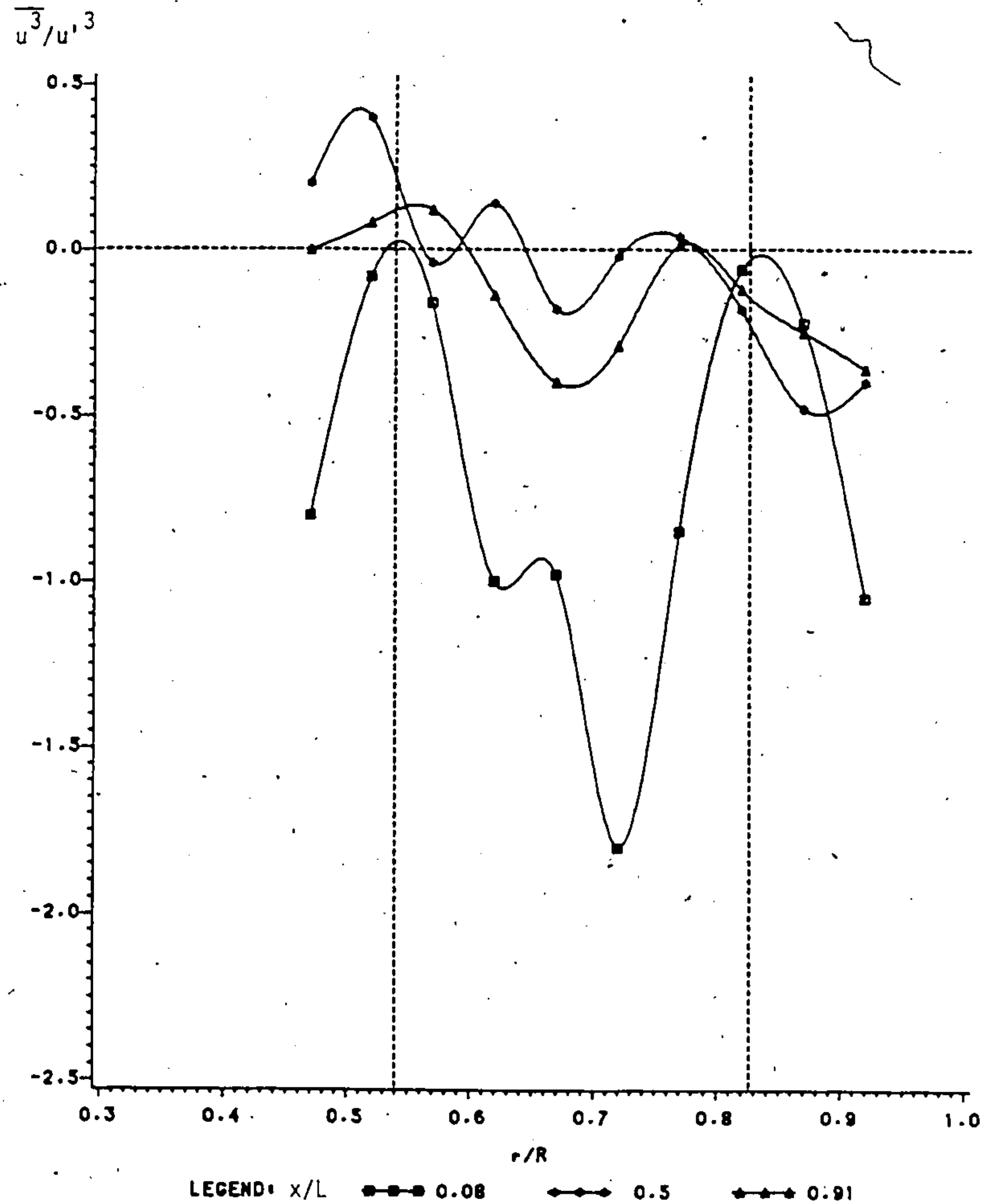

Figure 59 Variation of axial skewness factor along the test-section radial axis ($Re_{bh} = 62000$).

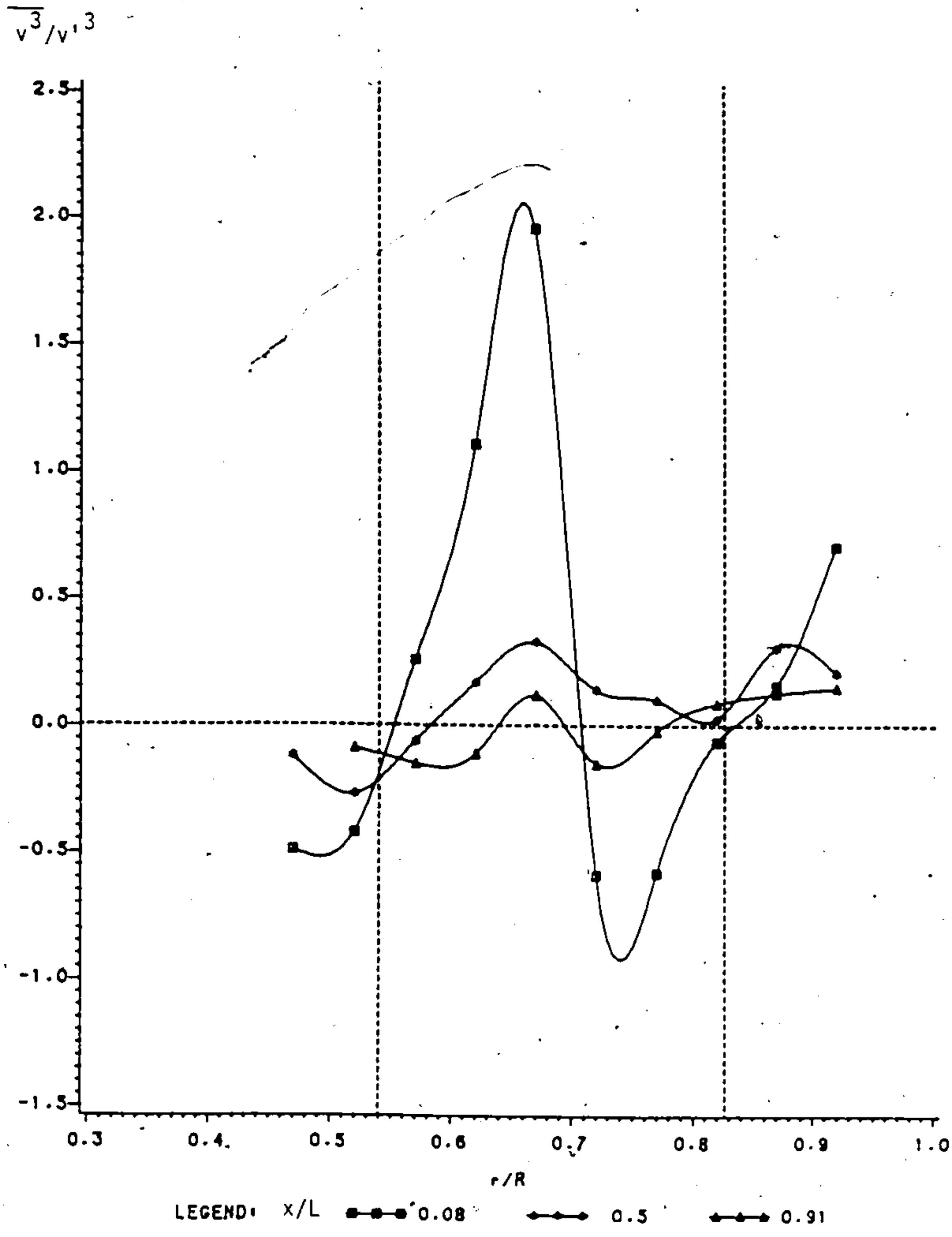

Figure 60 Variation of radial skewness factor along the test-section radial axis (Re_{bh} = 50000).

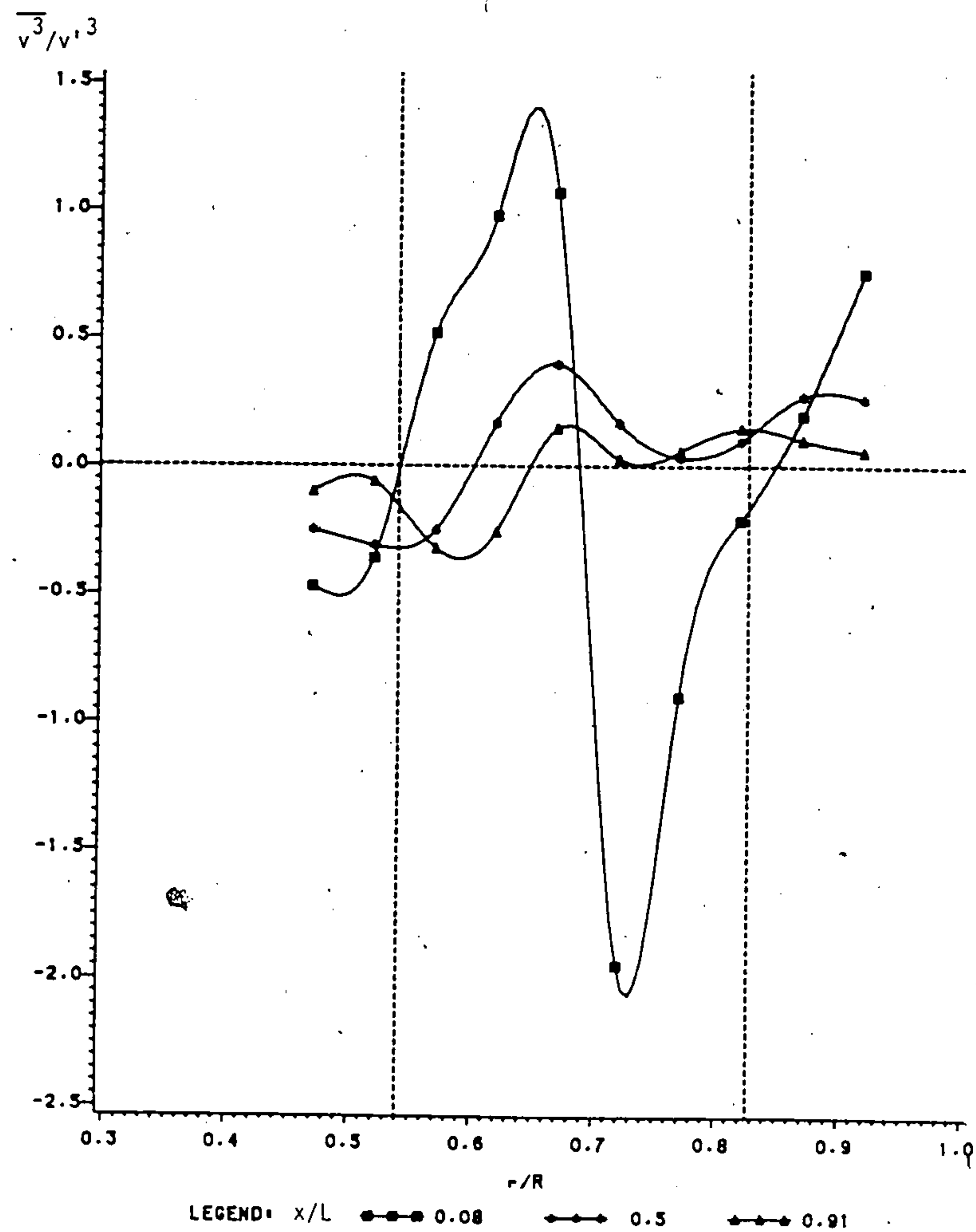

Figure 61 Variation of radial skewness factor along the test-section radial axis (Re_{bh} = 62000).

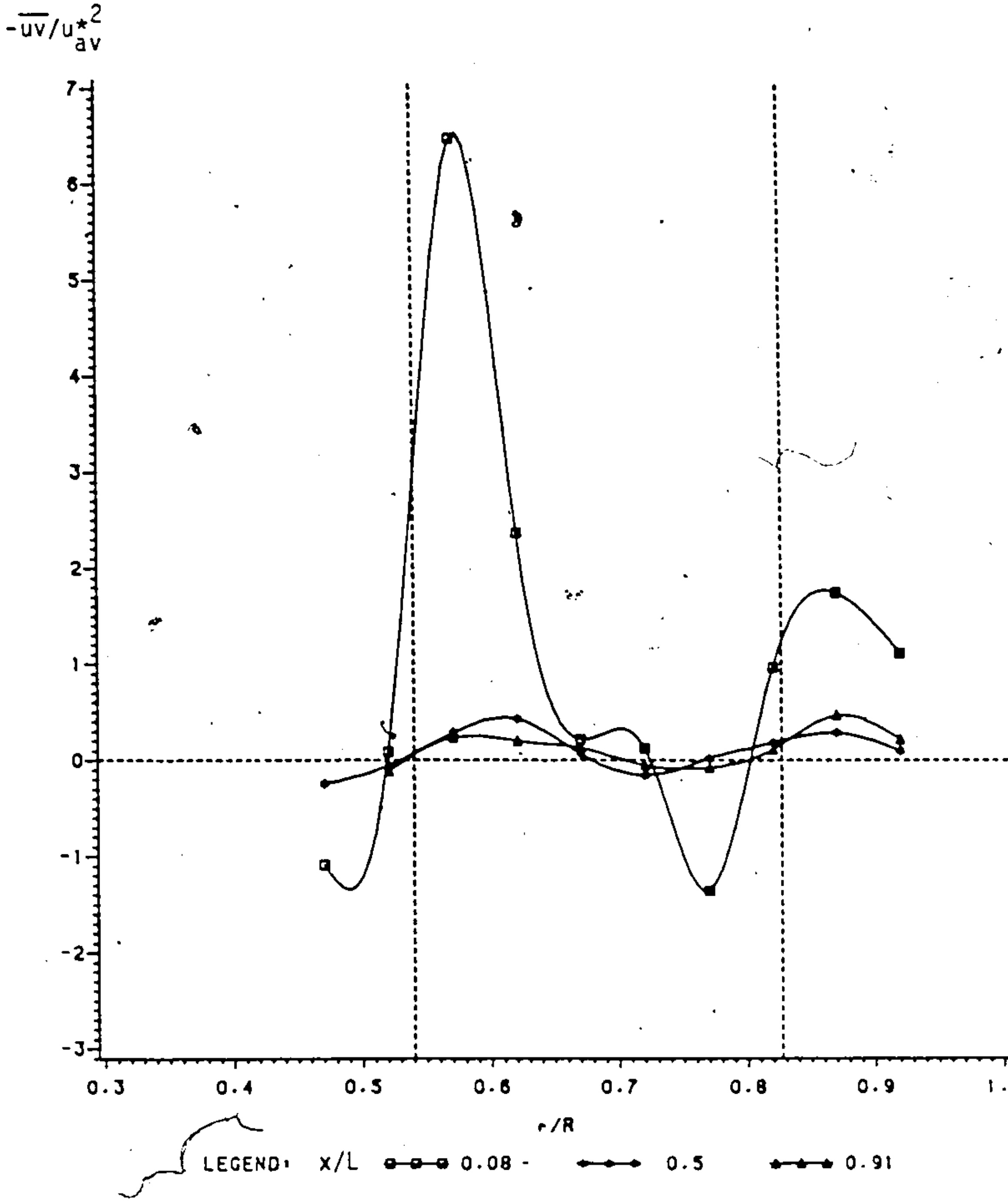

Figure 62 Variation of Reynolds shear stress along the test-section radial axis (Re_{bh} = 50000).

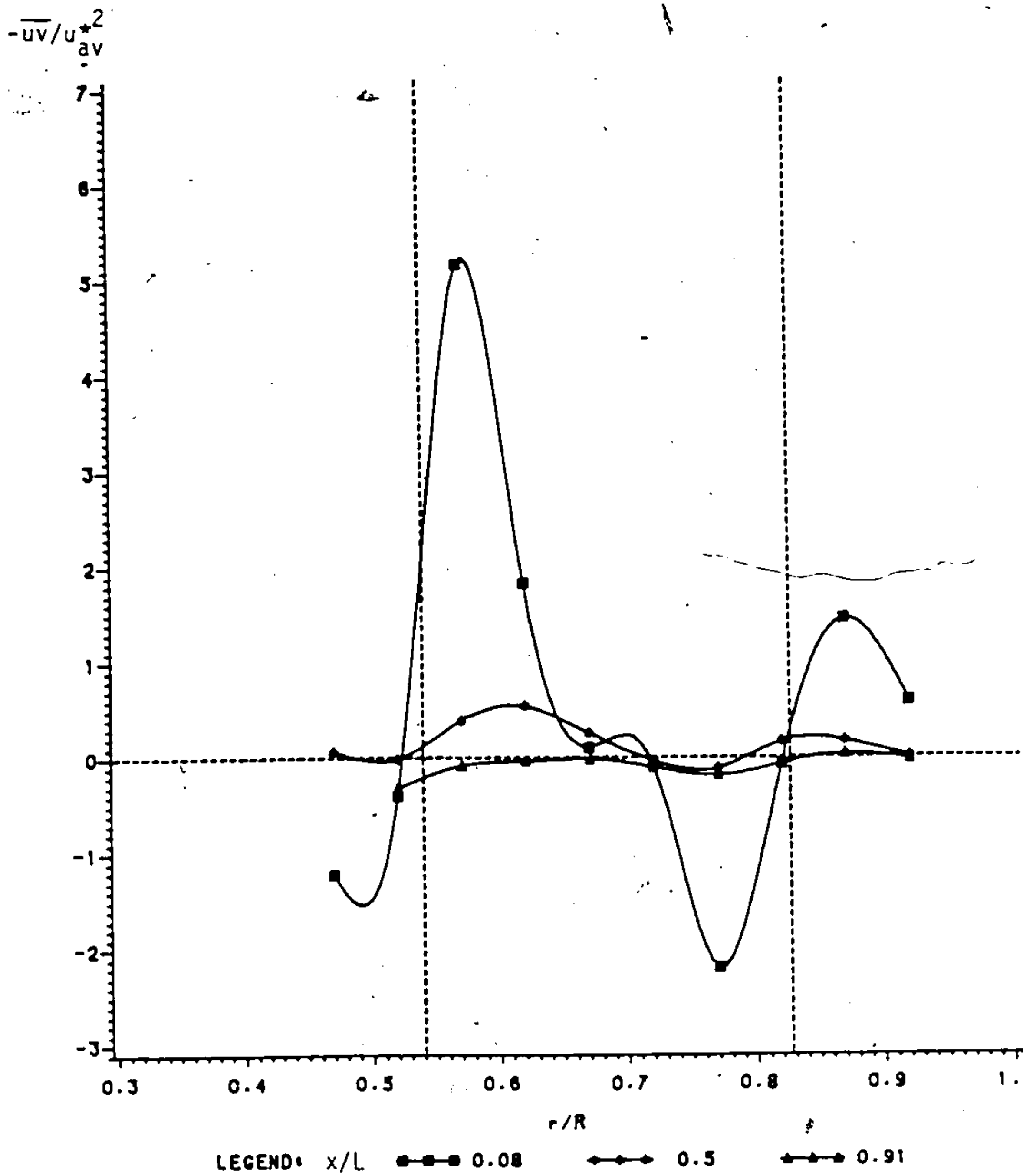

Figure 63 Variation of Reynolds shear stress along the test-section radial axis (Re_{bh} = 62000).

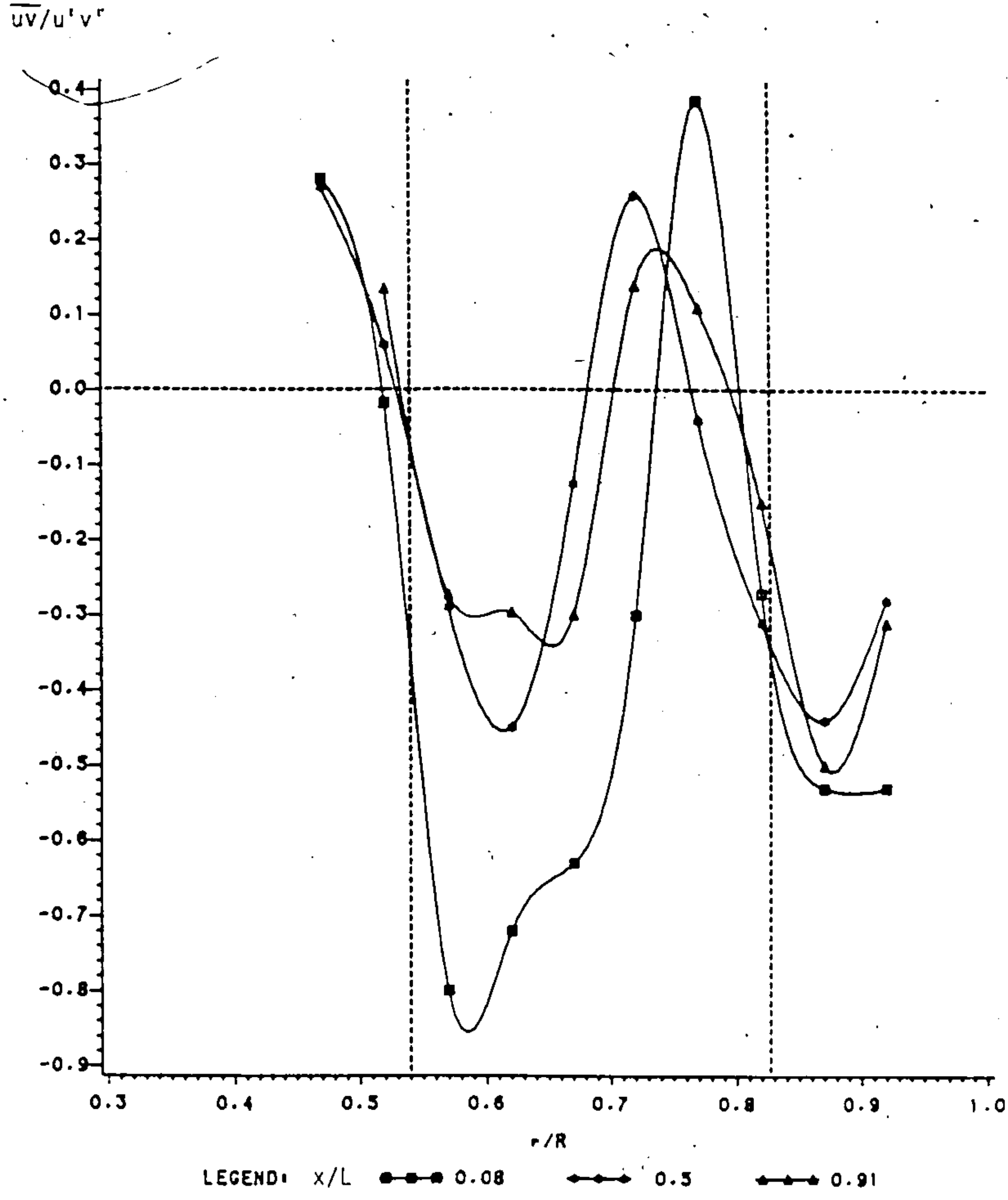

Figure 64 Variation of correlation coefficient along the test-section radial axis (Re_{bh} = 50000).

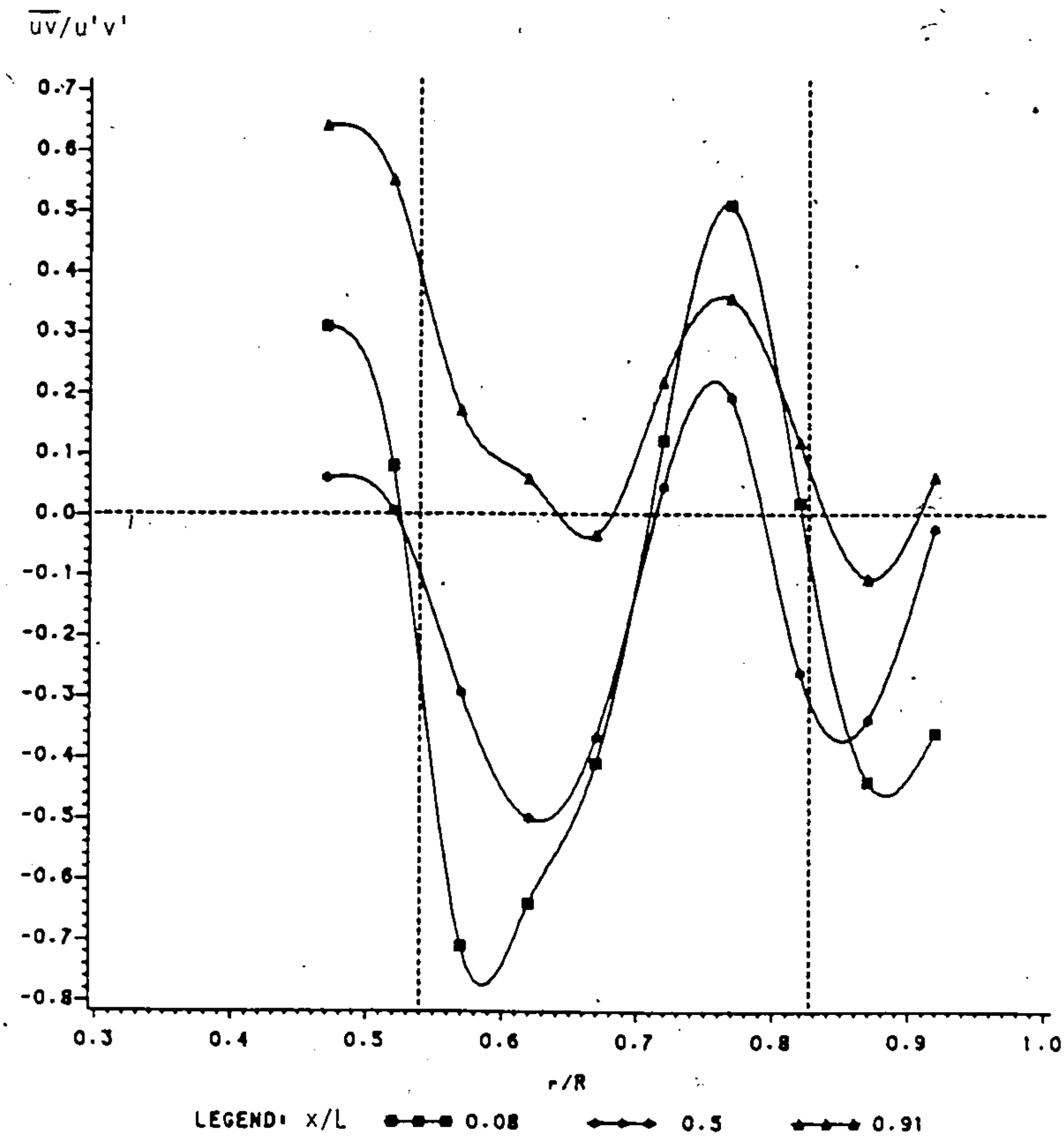

Figure 65 Variation of correlation coefficient along the test-section radial axis (Re_{bh} = 62000).

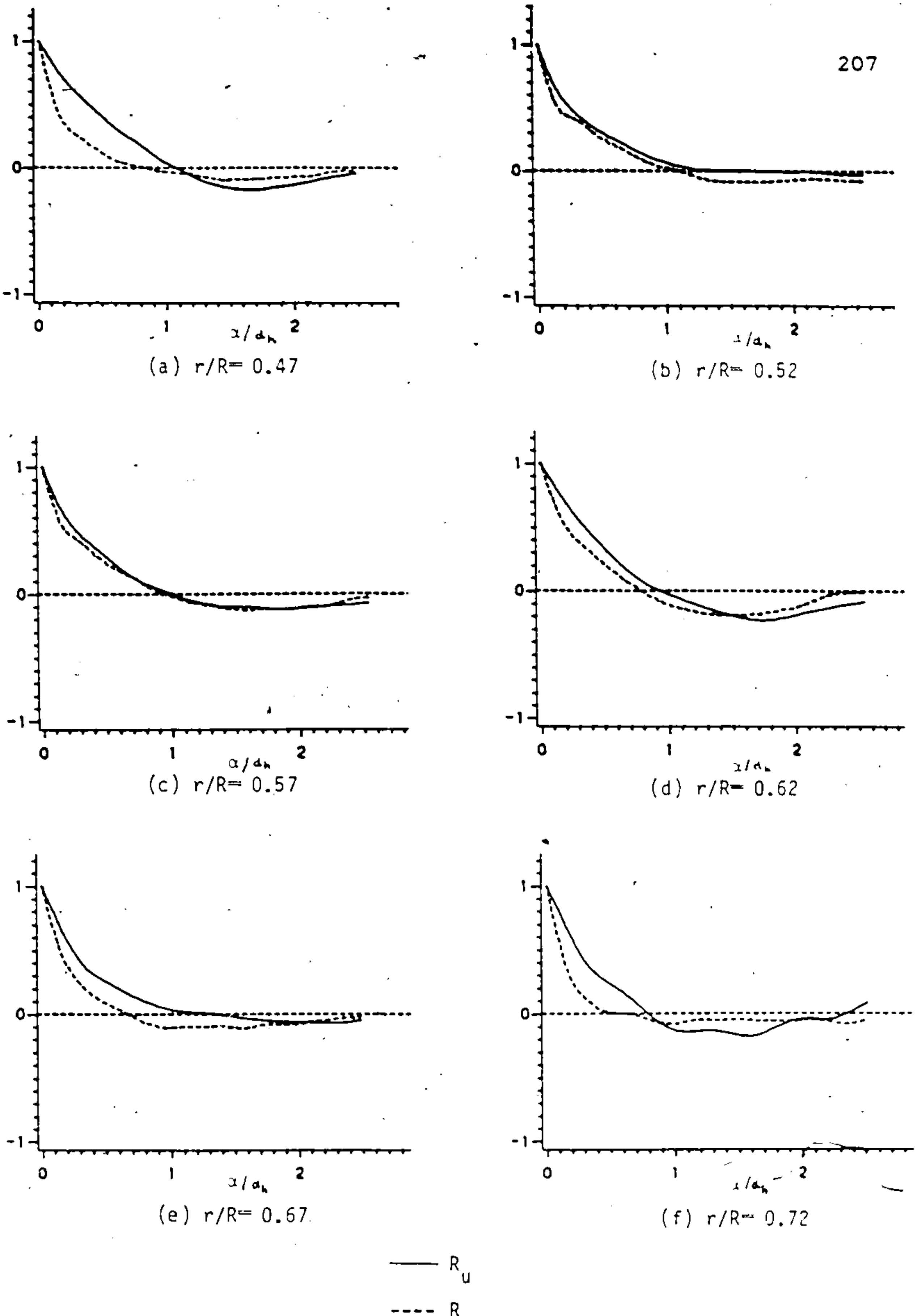

Figure 66 Autocorrelation coefficients at selected locations at x/L = 0.50 (Re_{bh} = 50000).

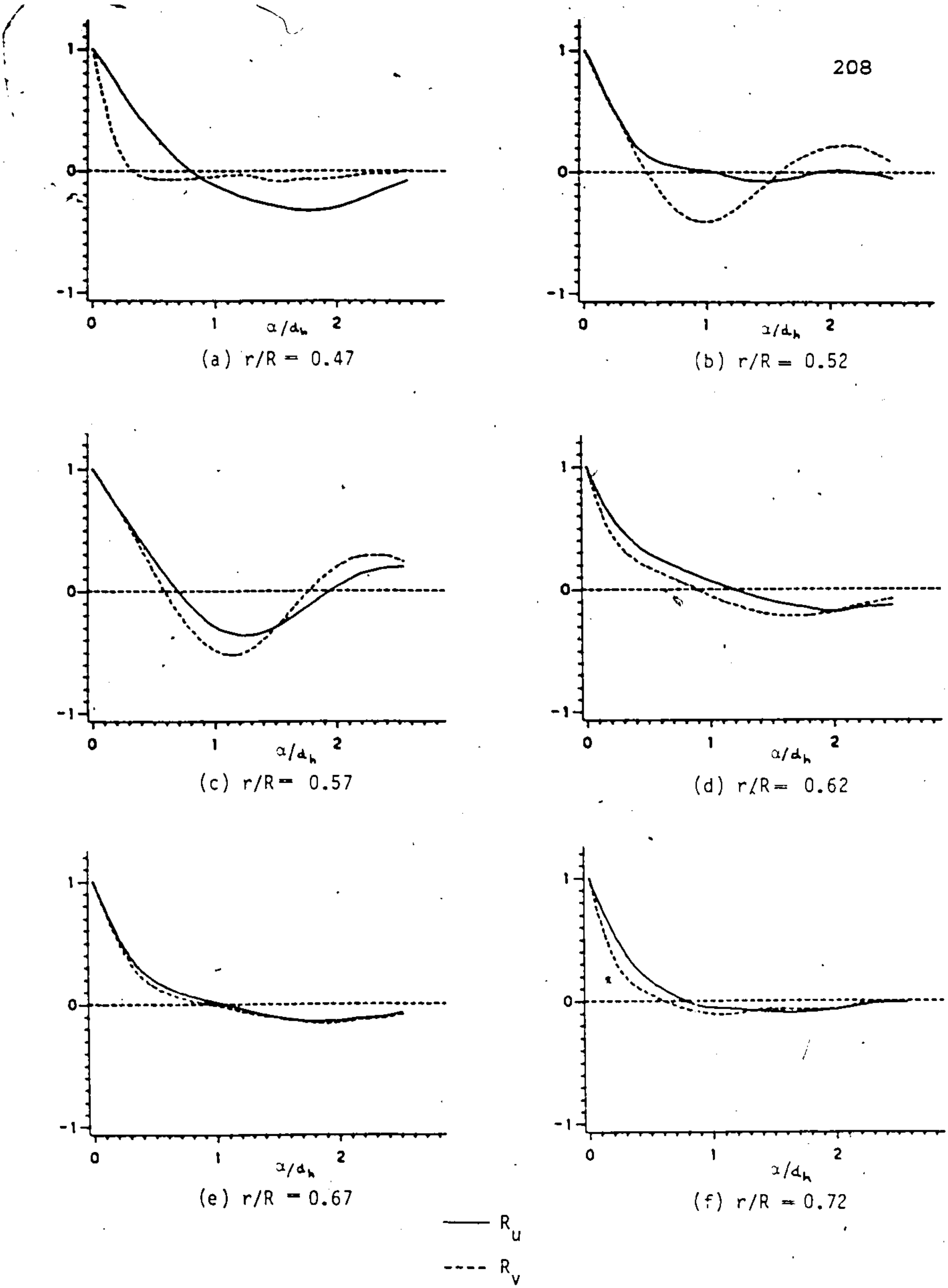

Figure 67 Autocorrelation coefficients at selected locations at $x/L = 0.08$ ($Re_{bh} = 50000$).

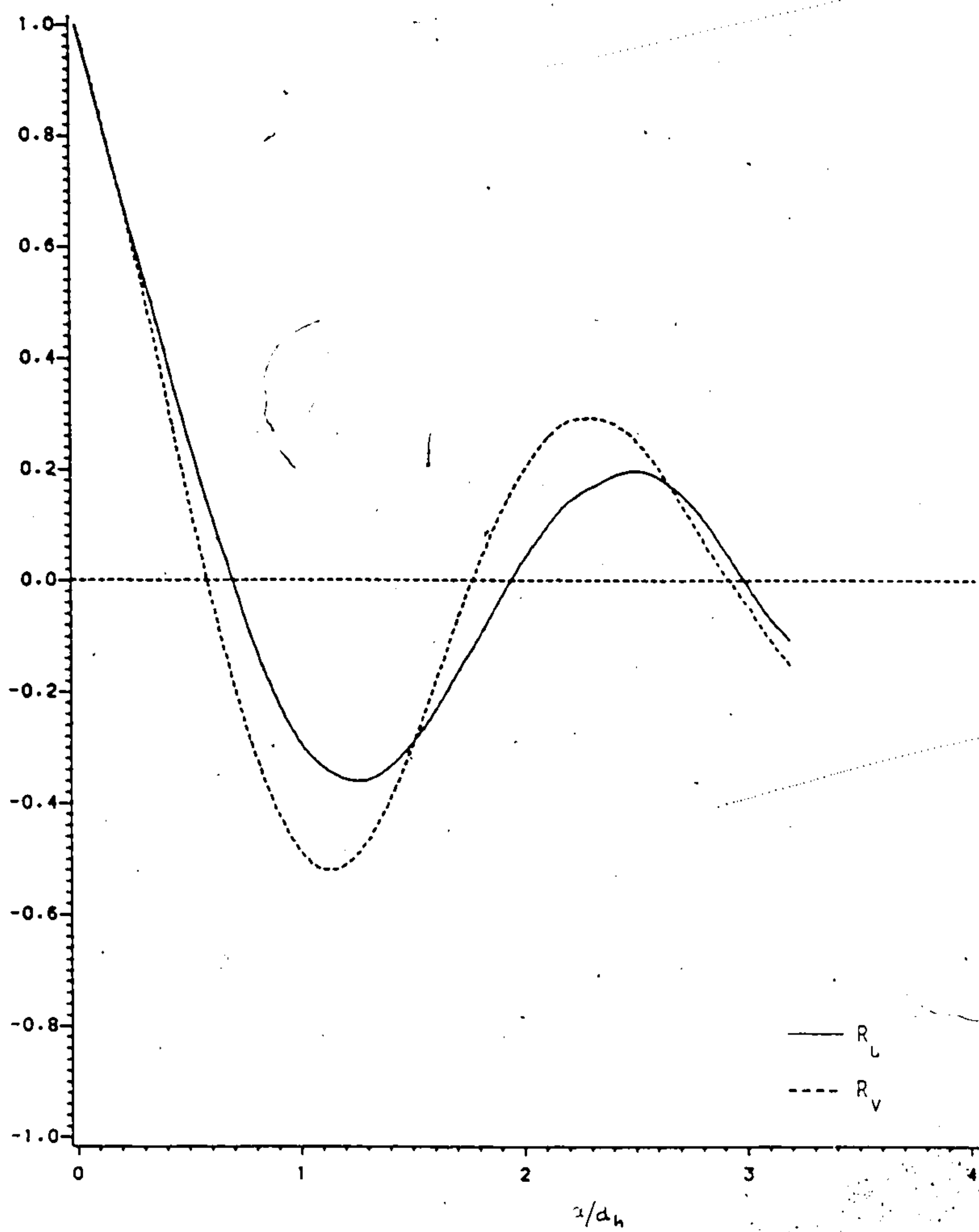

Figure 68 Autocorrelation coefficients at r/R = 0.57 at x/L = 0.08 (Re_{bh} = 50000).

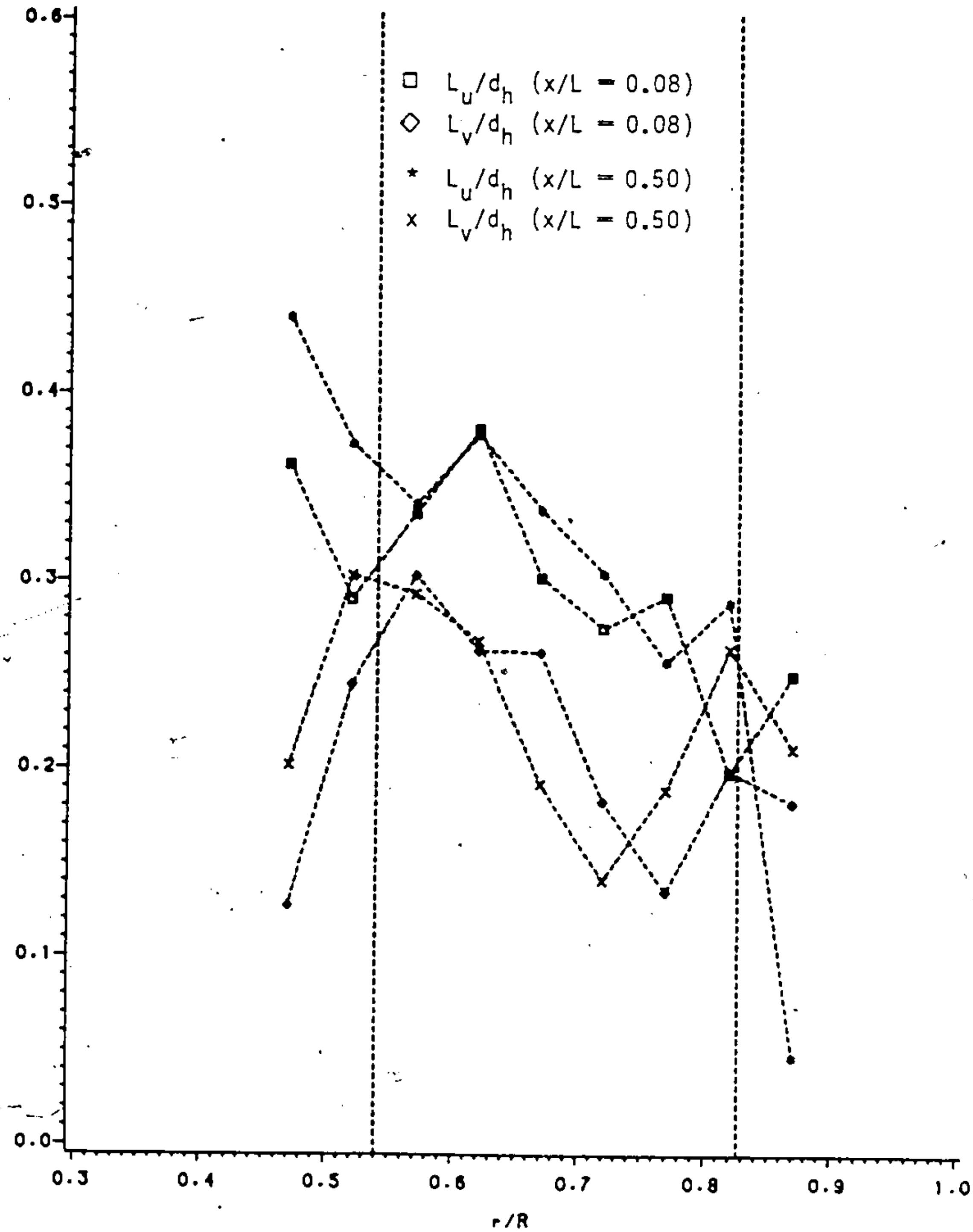

Figure 69 Variation of integral length scales along the test-section radial axis ($Re_{bh} = 50000$).

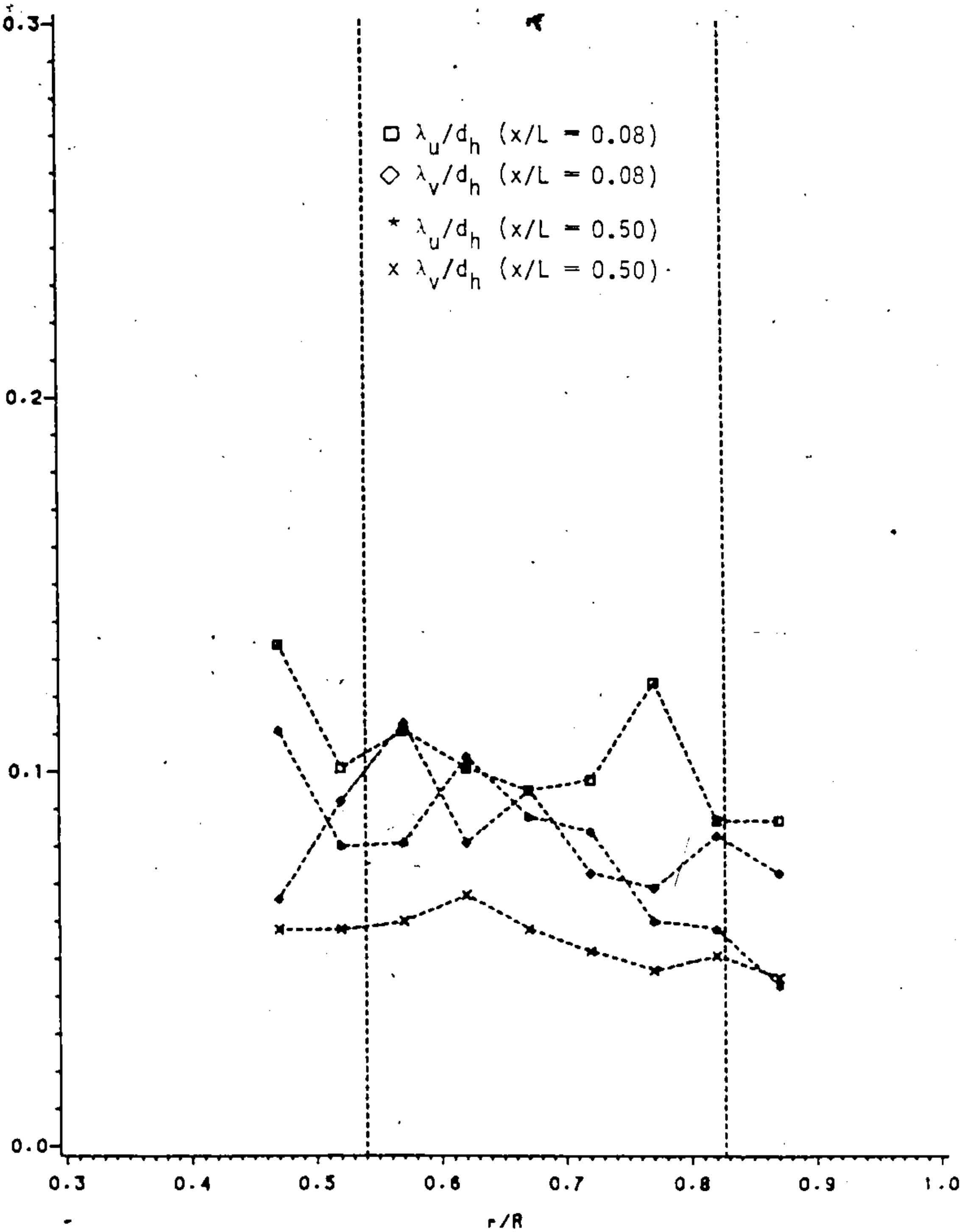

Figure 70 Variation of microscales along the test-section radial axis (Re_{bh} = 50000).

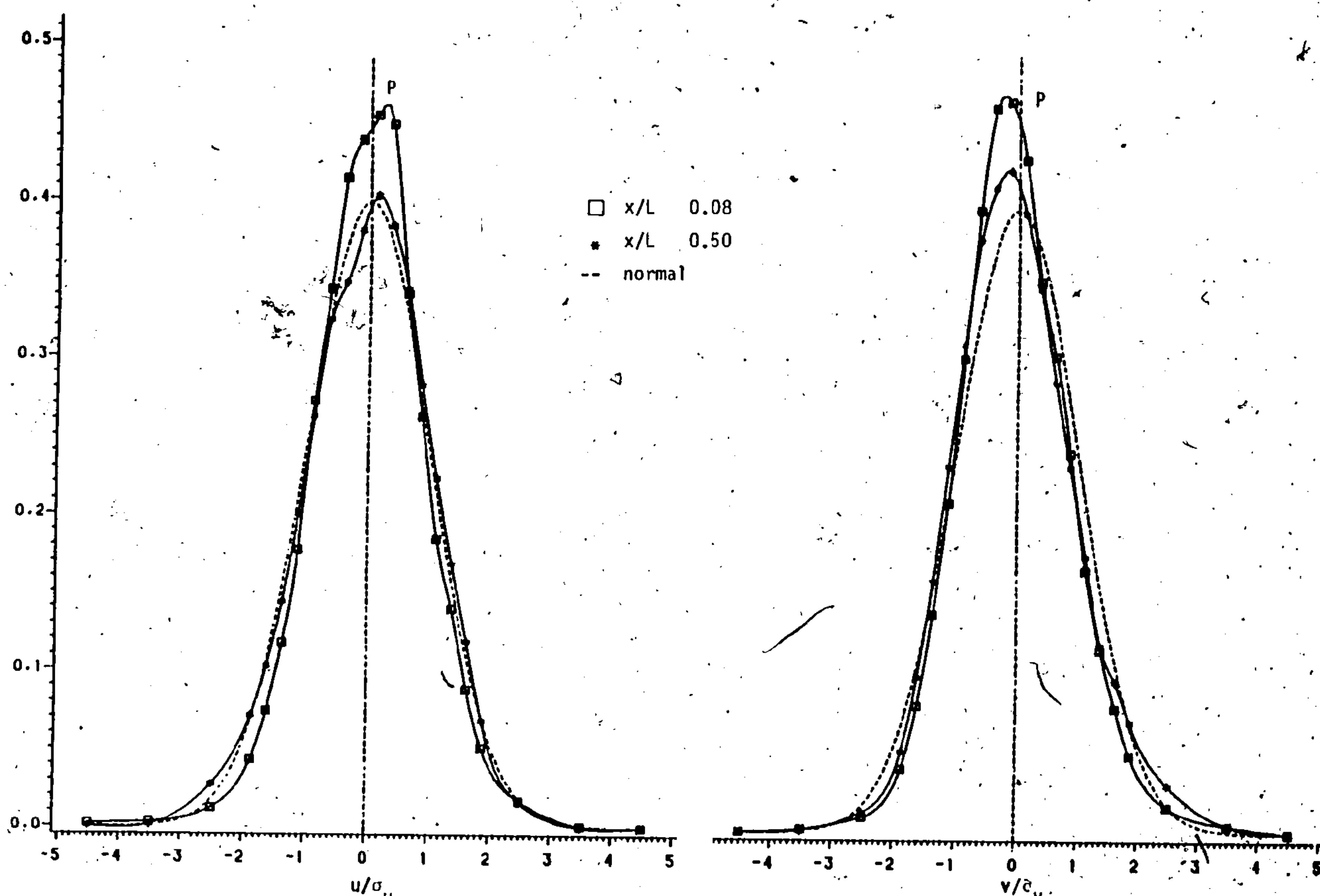

Figure 71 Probability density functions at $r/R = 0.57$ ($Re_{bh} = 62000$).

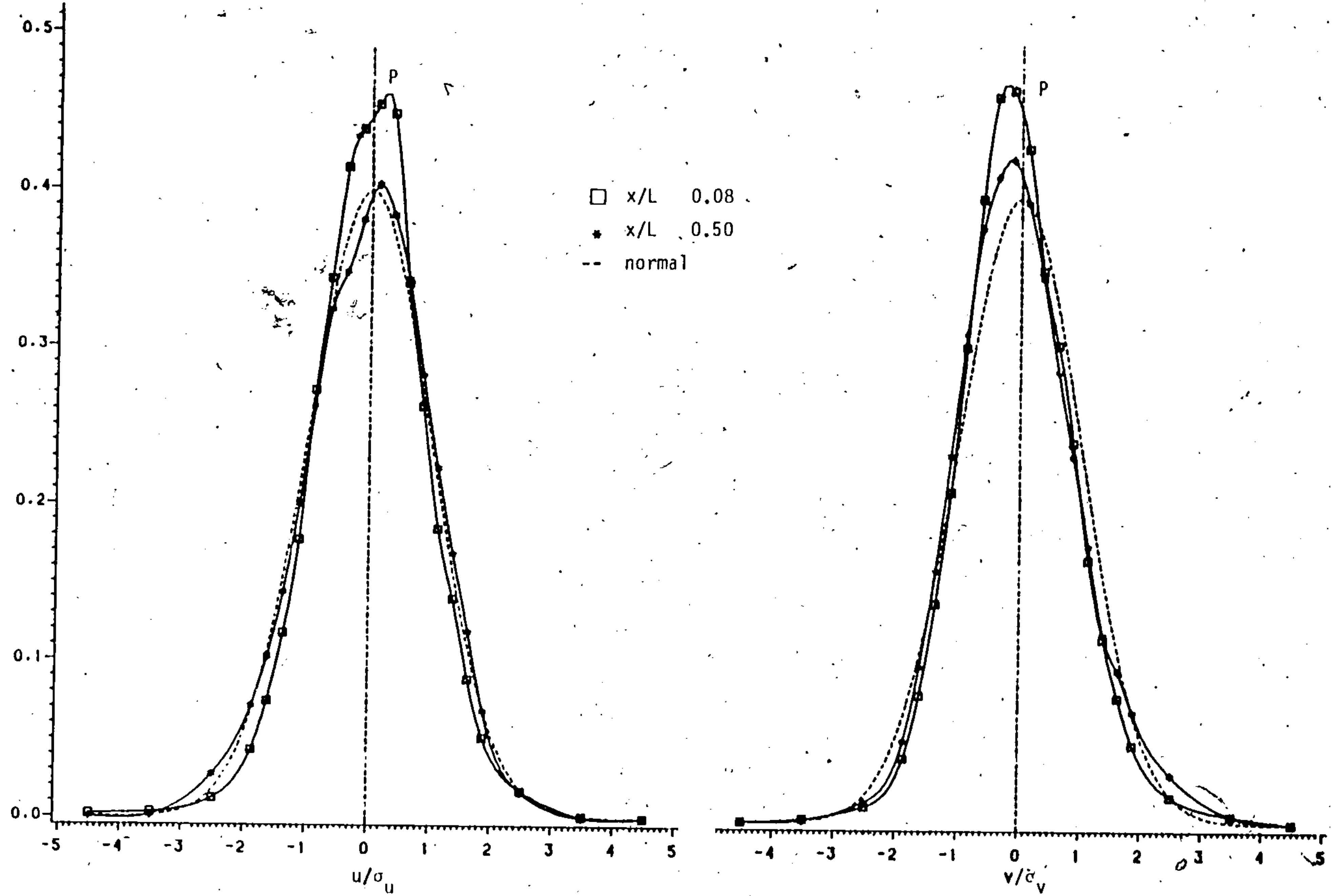

Figure 71 Probability density functions at r/R = 0.57 (Re_{bh} = 62000).

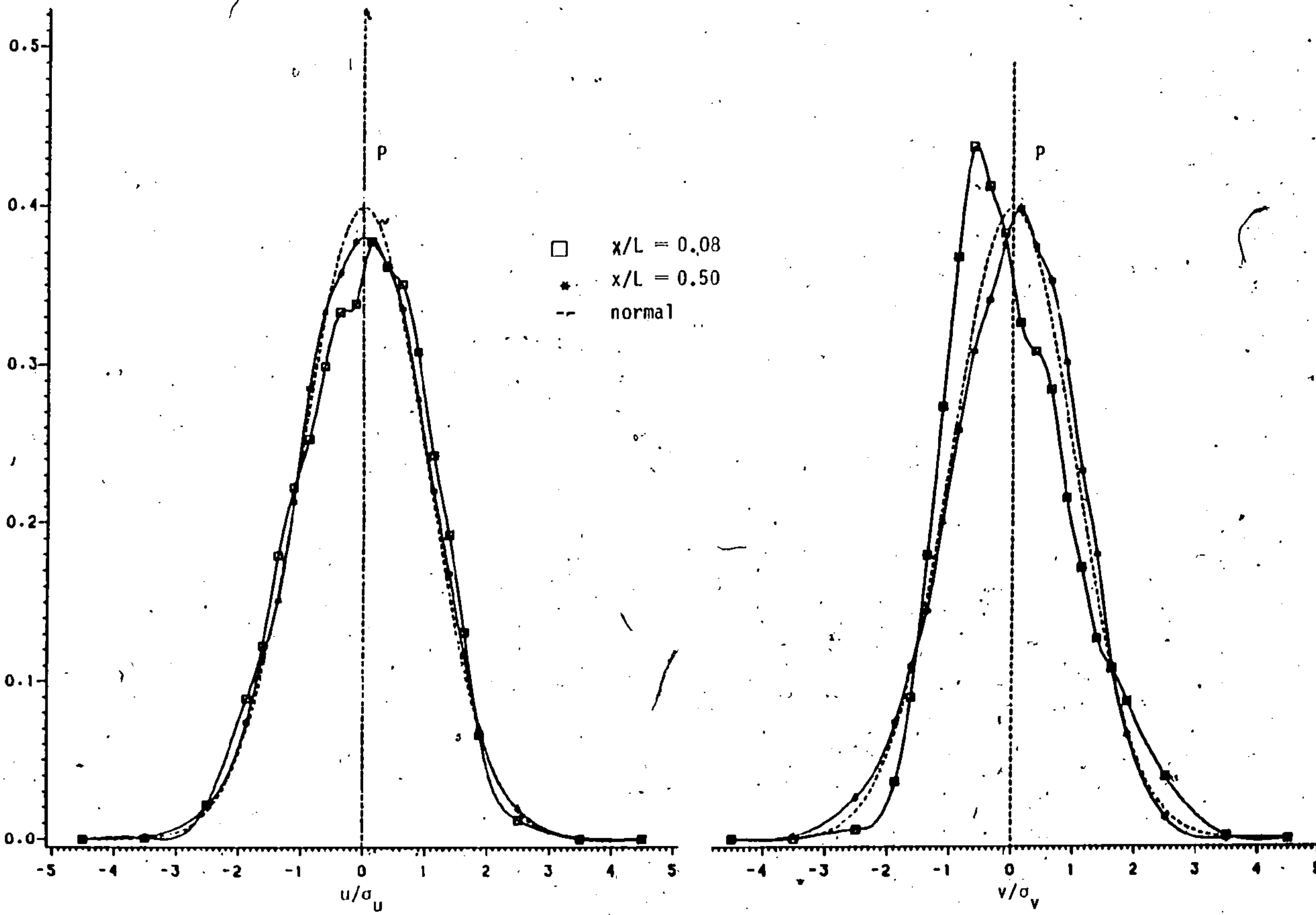

Figure 72 Probability density functions at $r/R = 0.67$ ($Re_{bh} = 62000$).

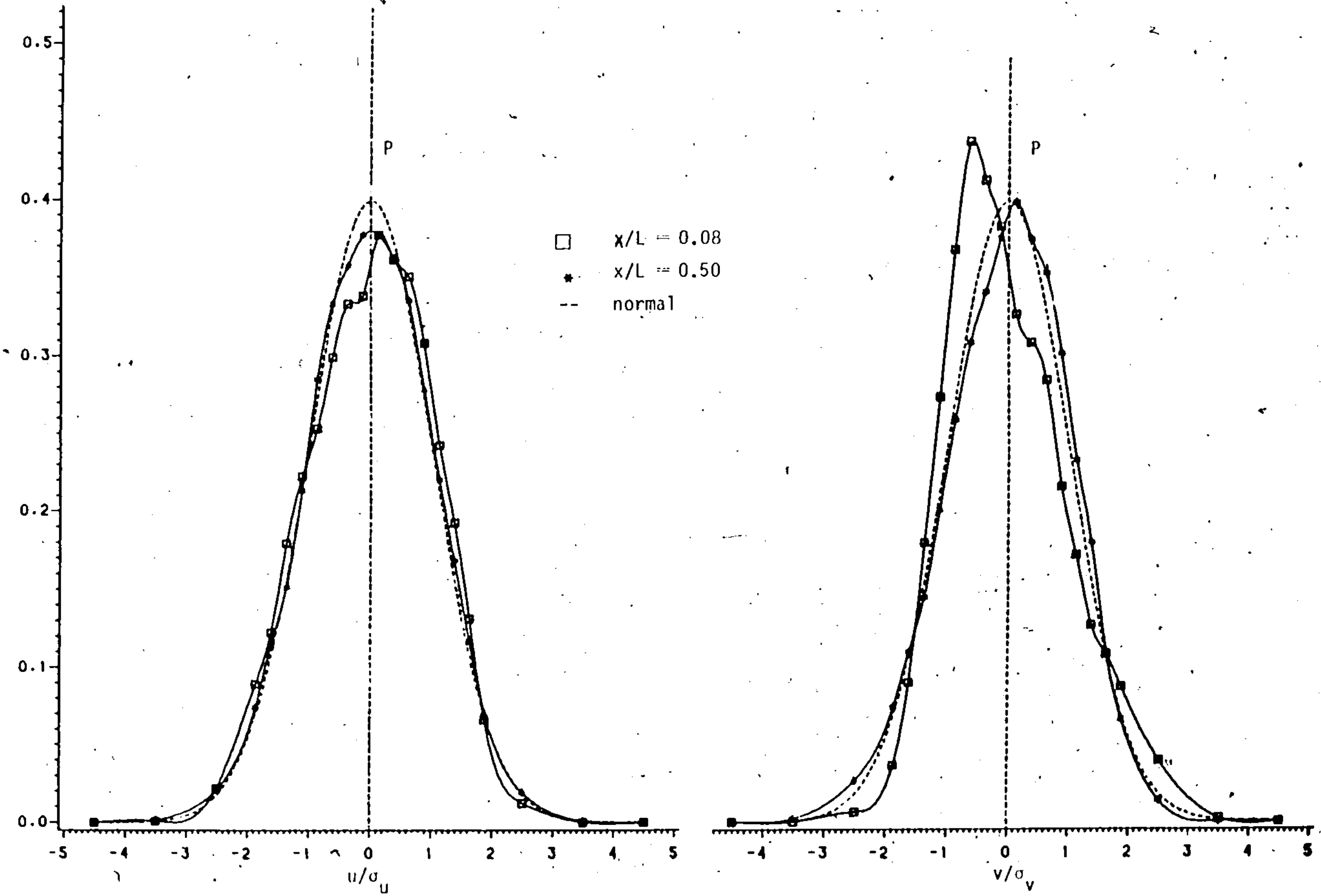

Figure 72 Probability density functions at $r/R = 0.67$ ($Re_{bh} = 62000$).

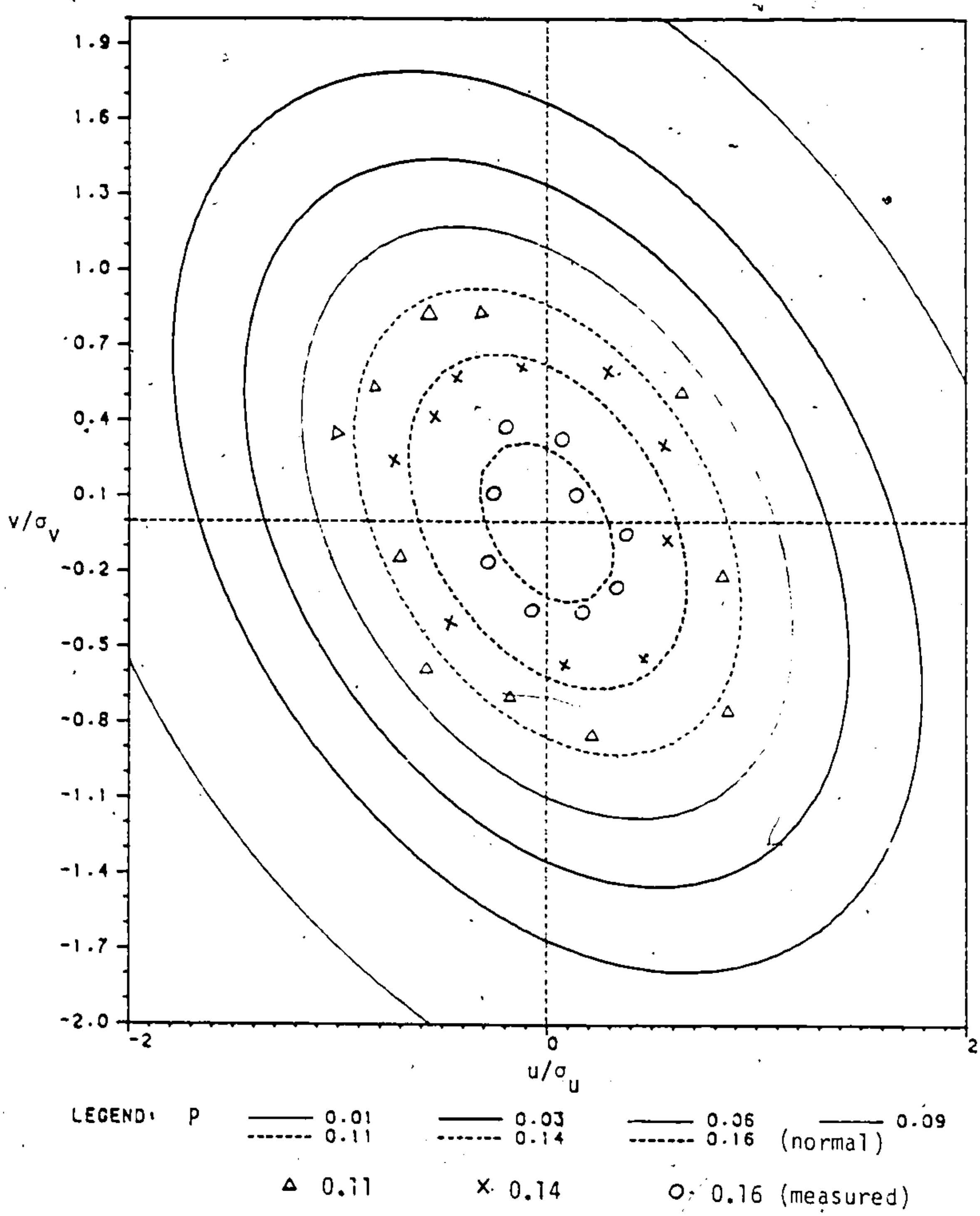

Figure 73 Isoprobability contours at r/R = 0.67 at x/L = 0.50 (Re_{bh} = 62000).

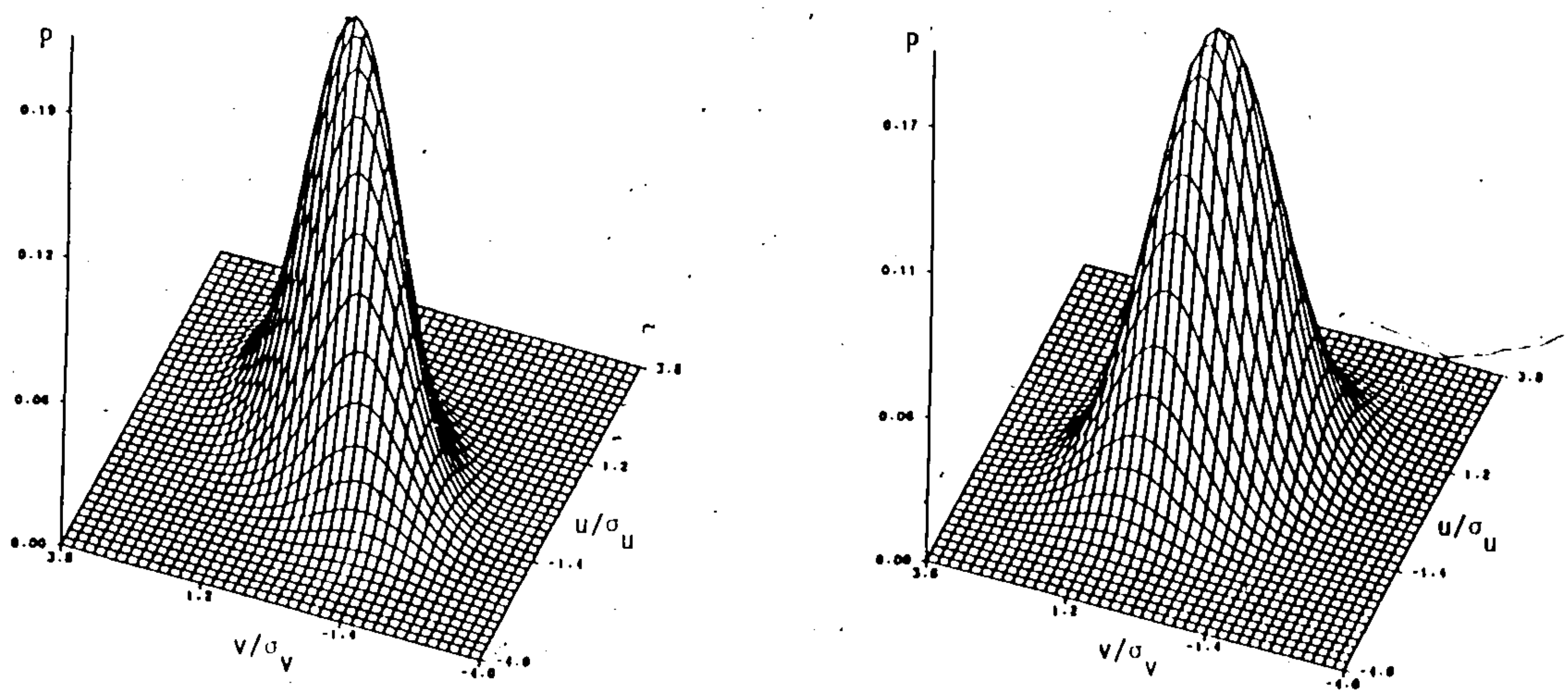

(a) $\rho = 0.51$; $r/R = 0.77$, $x/L = 0.08$.

(b) $\rho = -0.37$; $r/R = 0.67$, $x/L = 0.50$.

Figure 74 Bivariate normal probability density function ($Re_{bh} = 62000$).

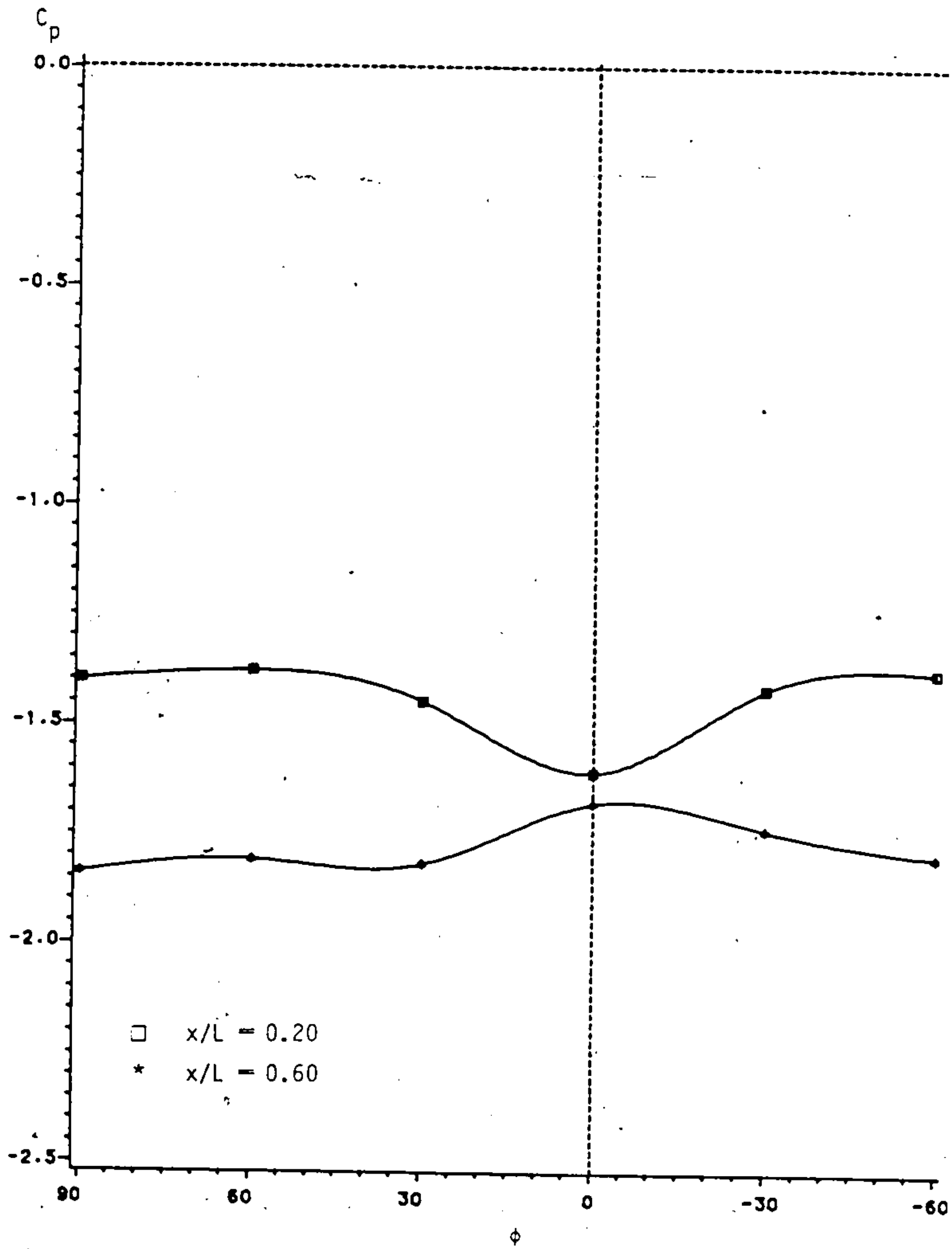

Figure 75 Peripheral variation of wall static pressure around rod B (Re_{bh} = 45000).

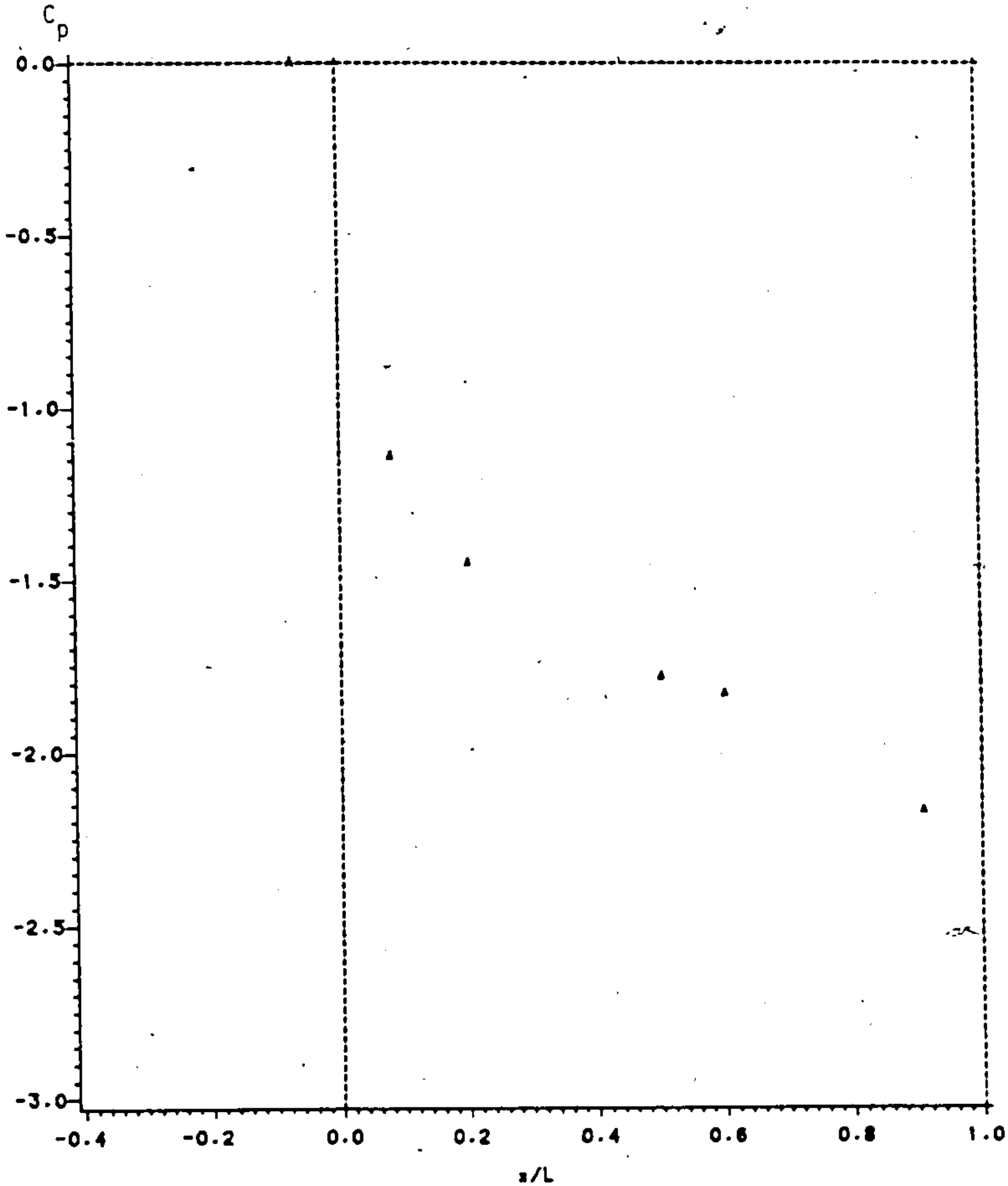

Figure 76 Downstream evolution of average mean static pressure (Re_{bh} = 45000).

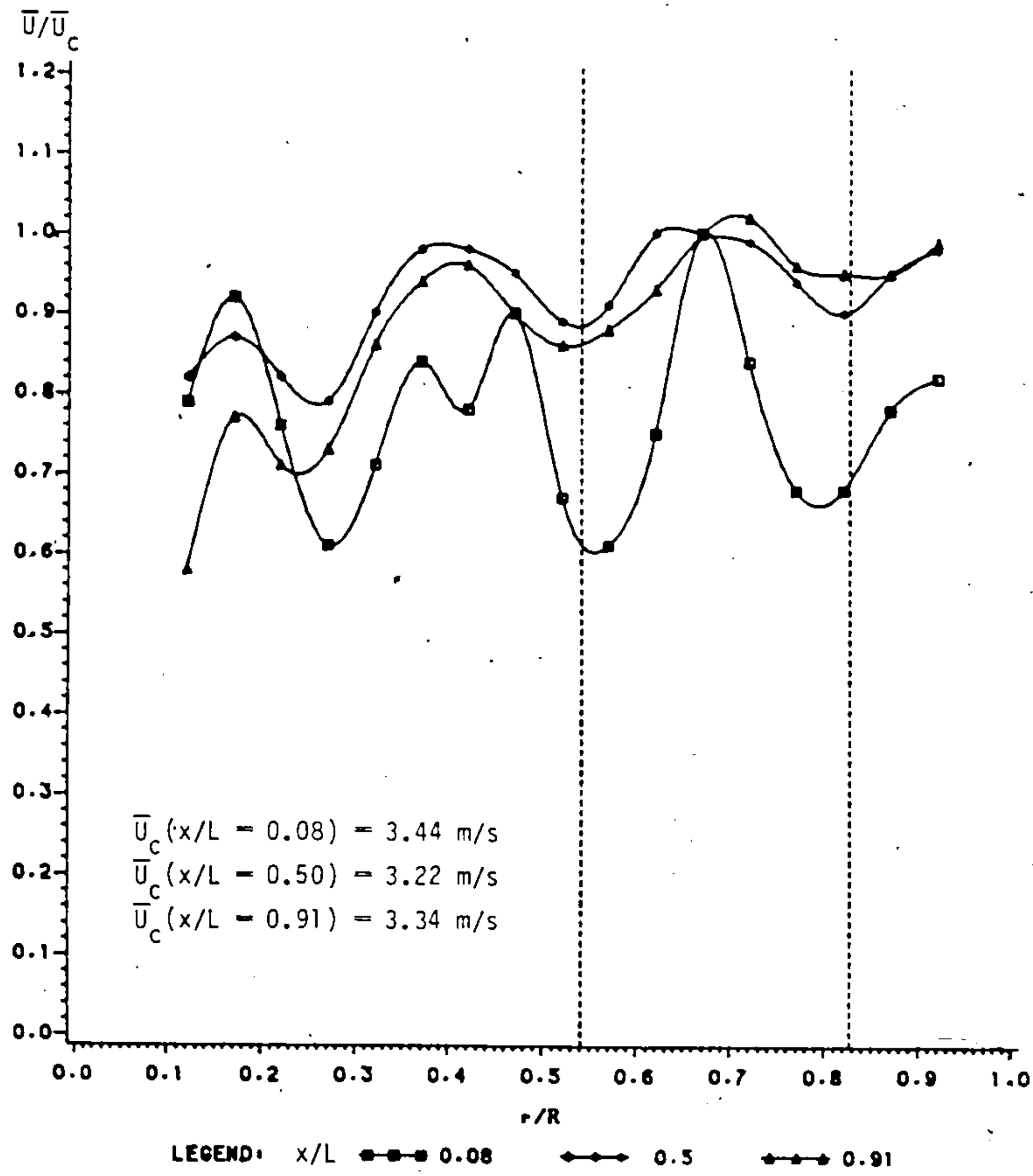

Figure 77 Variation of mean axial velocity along the test-section radial axis (Re_{bh} = 45000).

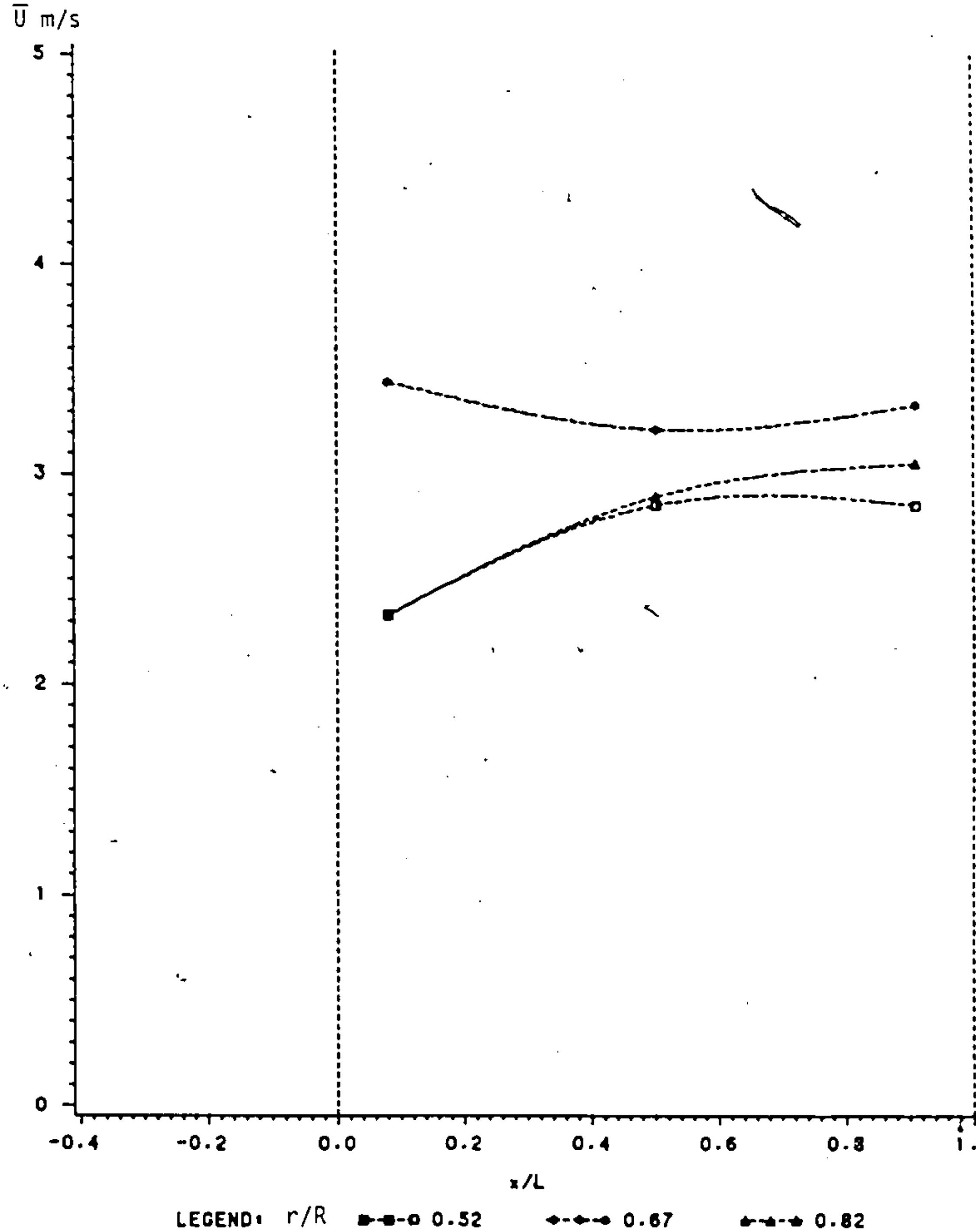

Figure 78 Downstream evolution of mean axial velocity (Re_{bh} = 45000).

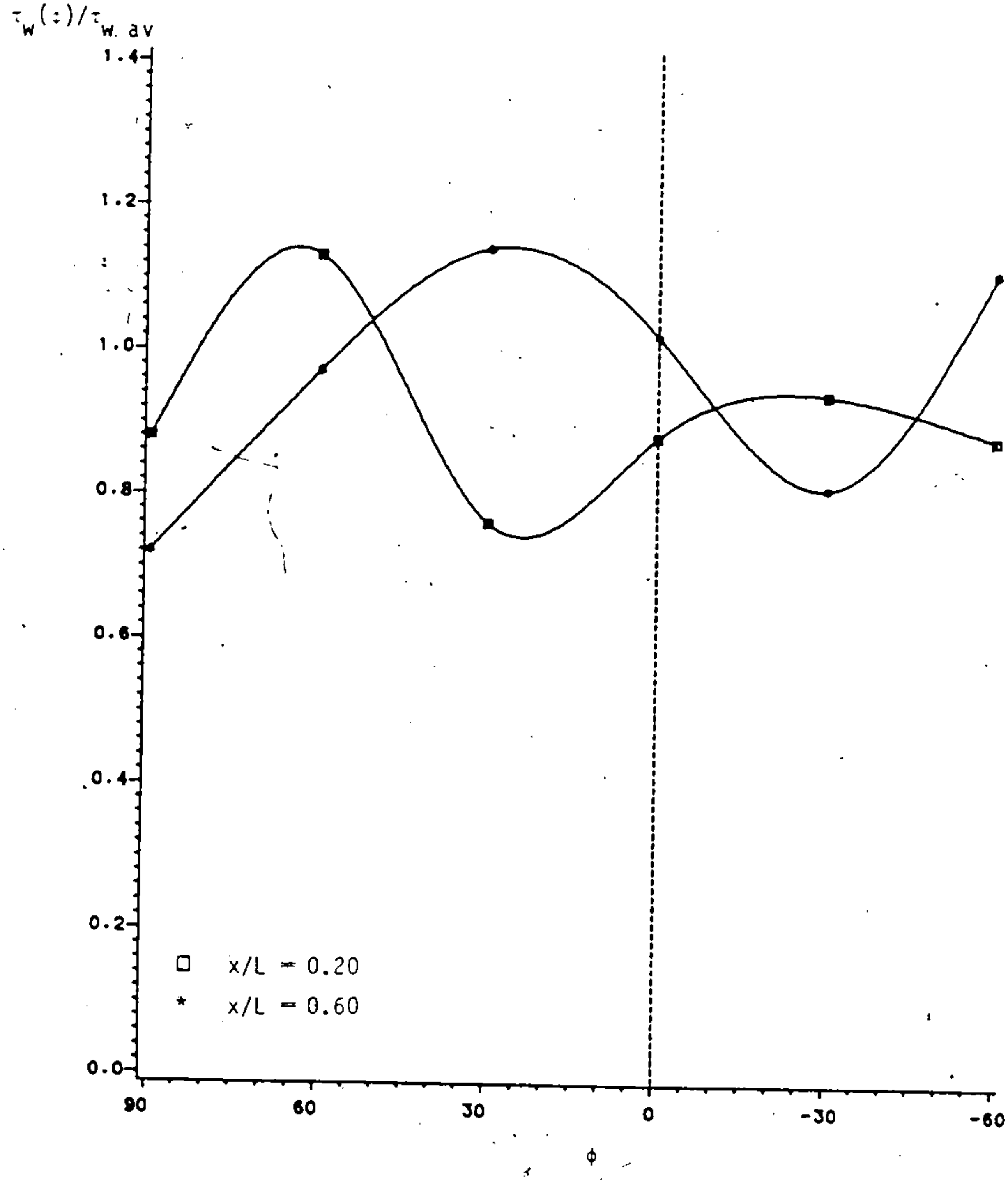

Figure 79 Peripheral variation of local wall shear stress around rod B (Re_{bh} = 45000).

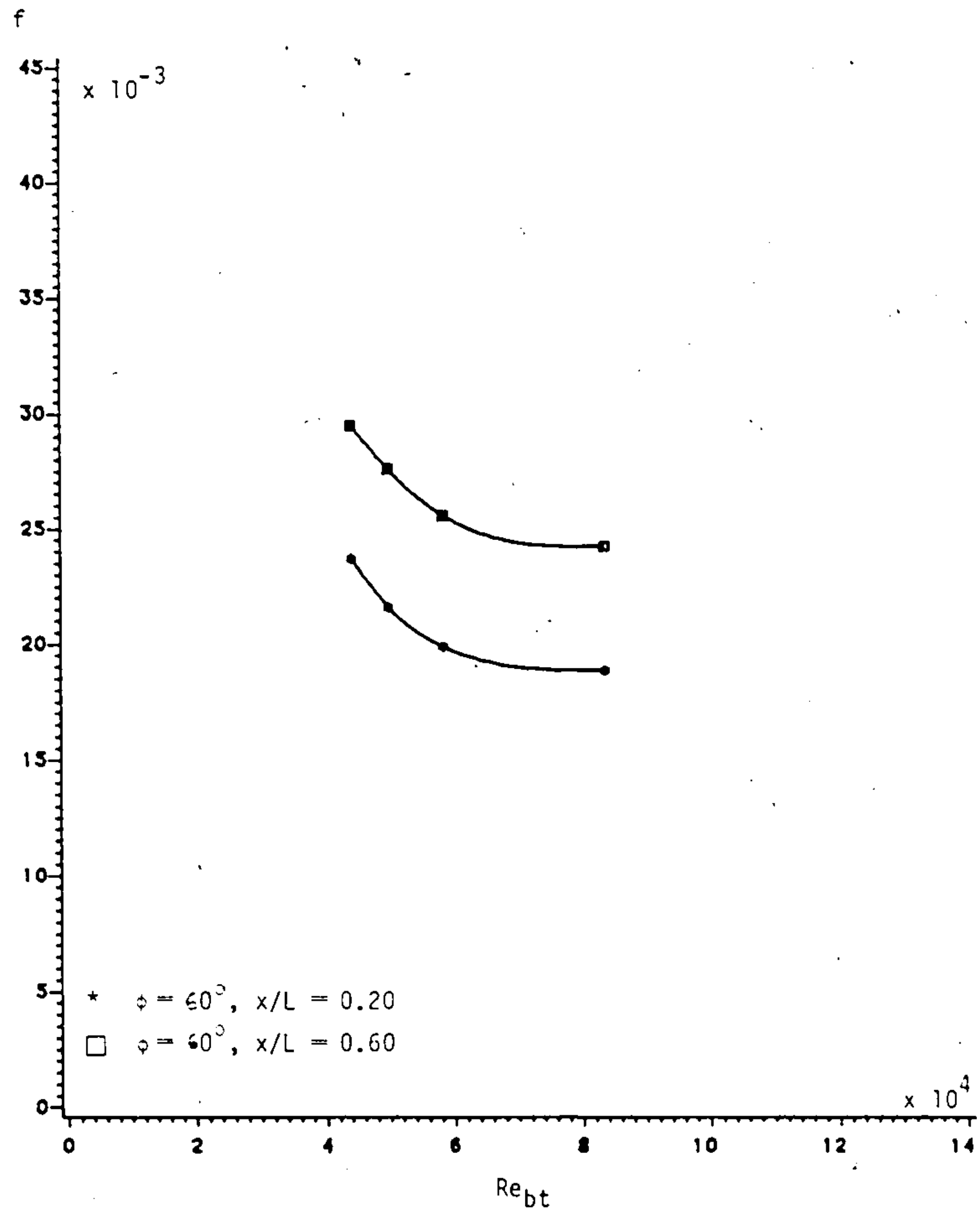

Figure 80 Reynolds number dependence of local friction factor.

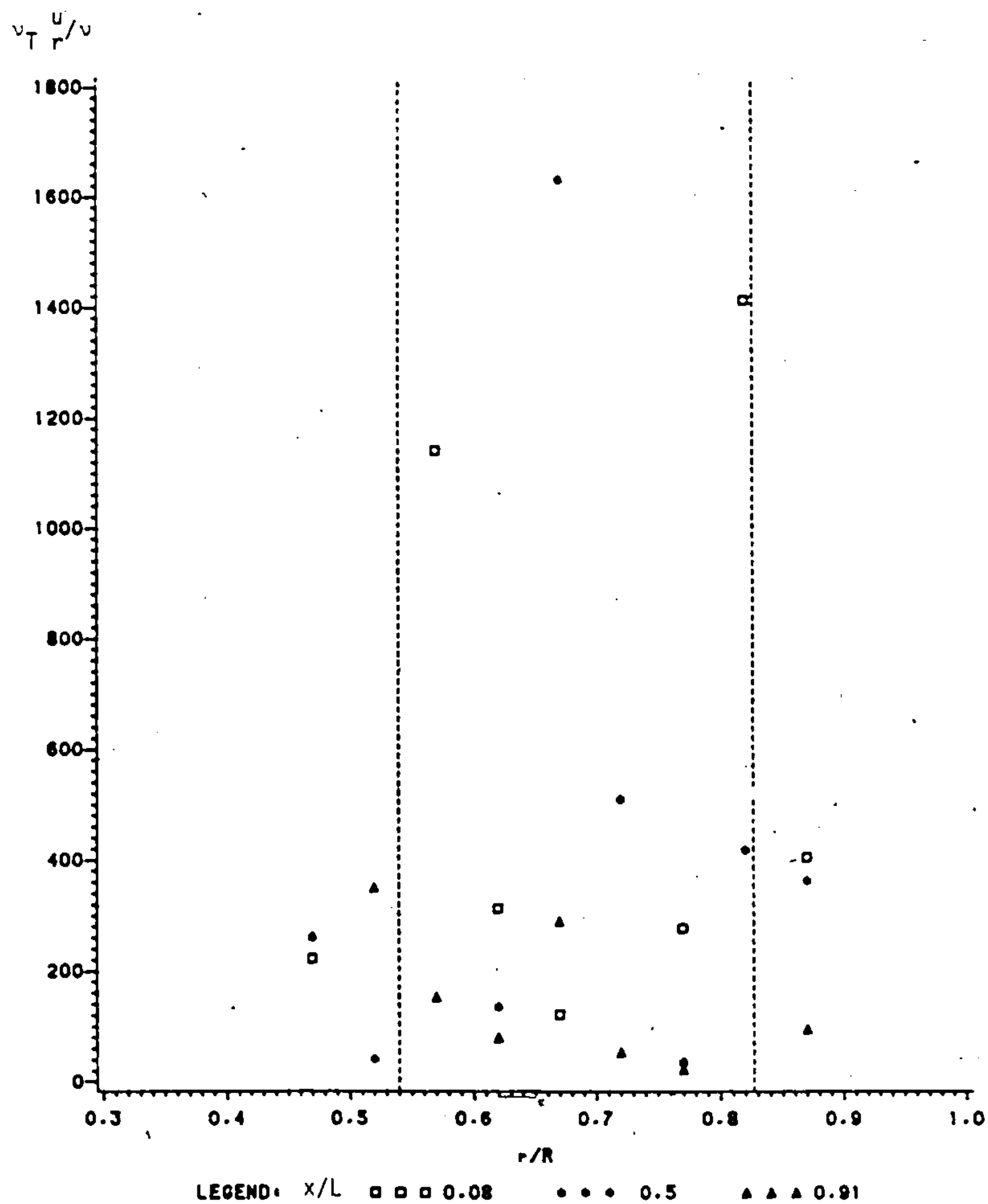

Figure 81 Variation of eddy viscosity along the test-section radial axis (Re_{bh} = 50000).

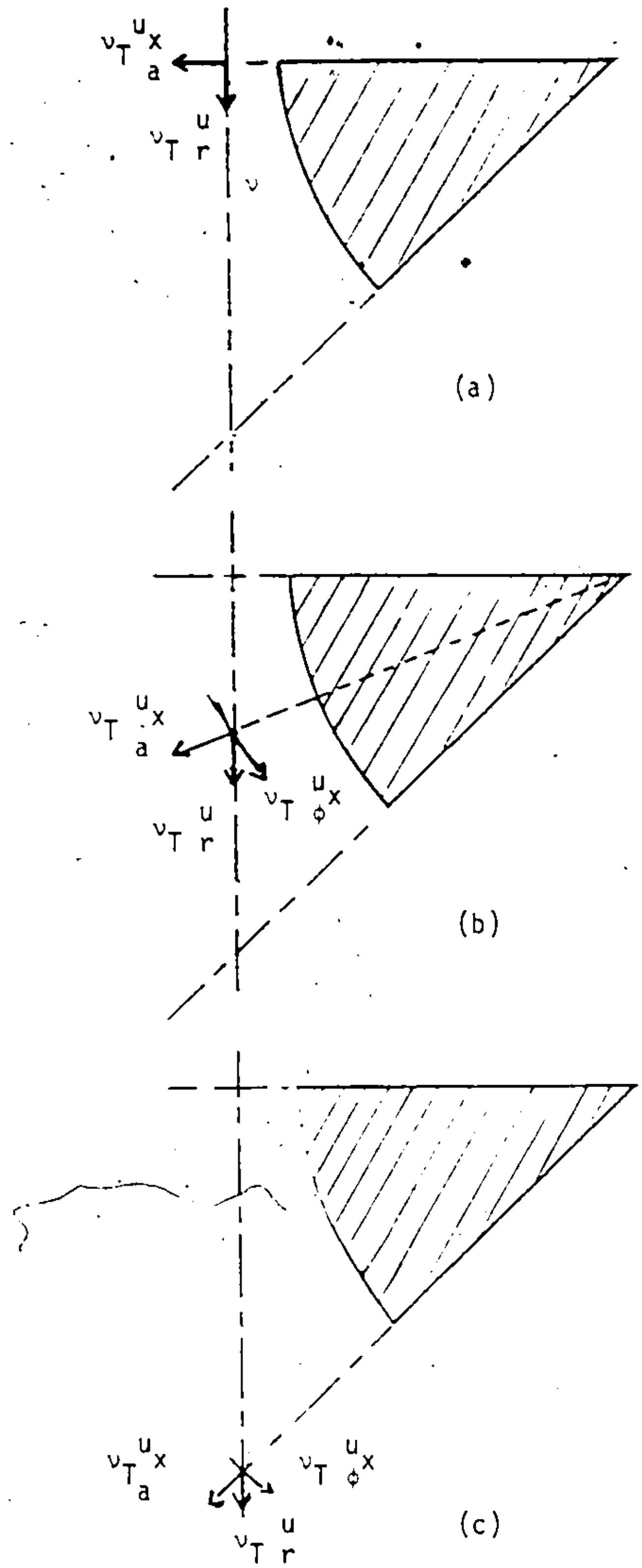

Figure 82 Illustration of eddy viscosities at representative locations along the test-section radial axis.

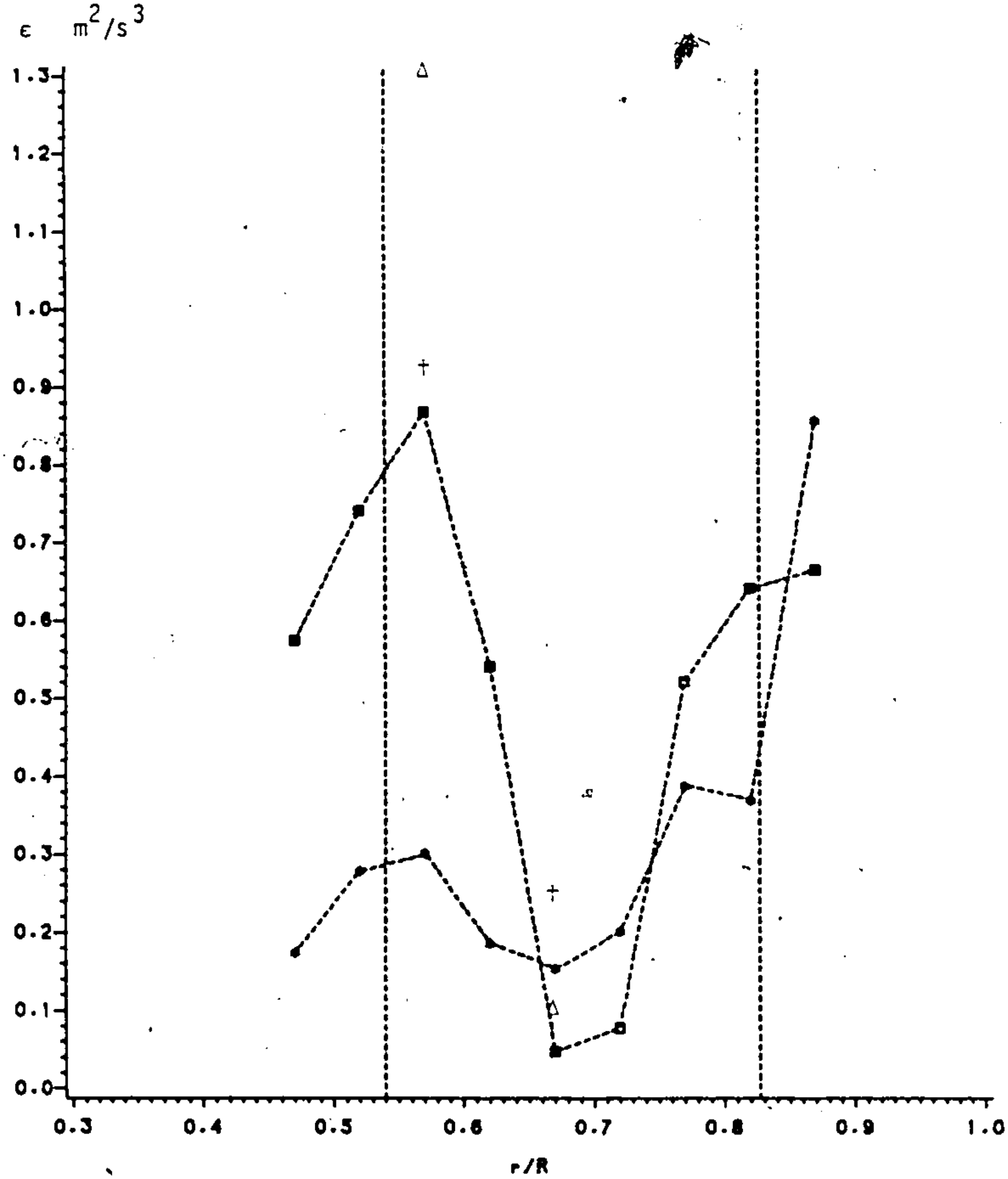

□ x/L = 0.08 * x/L = 0.50 (Re_{bh} = 50000)
Δ x/L = 0.08 + x/L = 0.50 (Re_{bh} = 62000)

Figure 83 Variation of energy dissipation rate along the test-section radial axis.

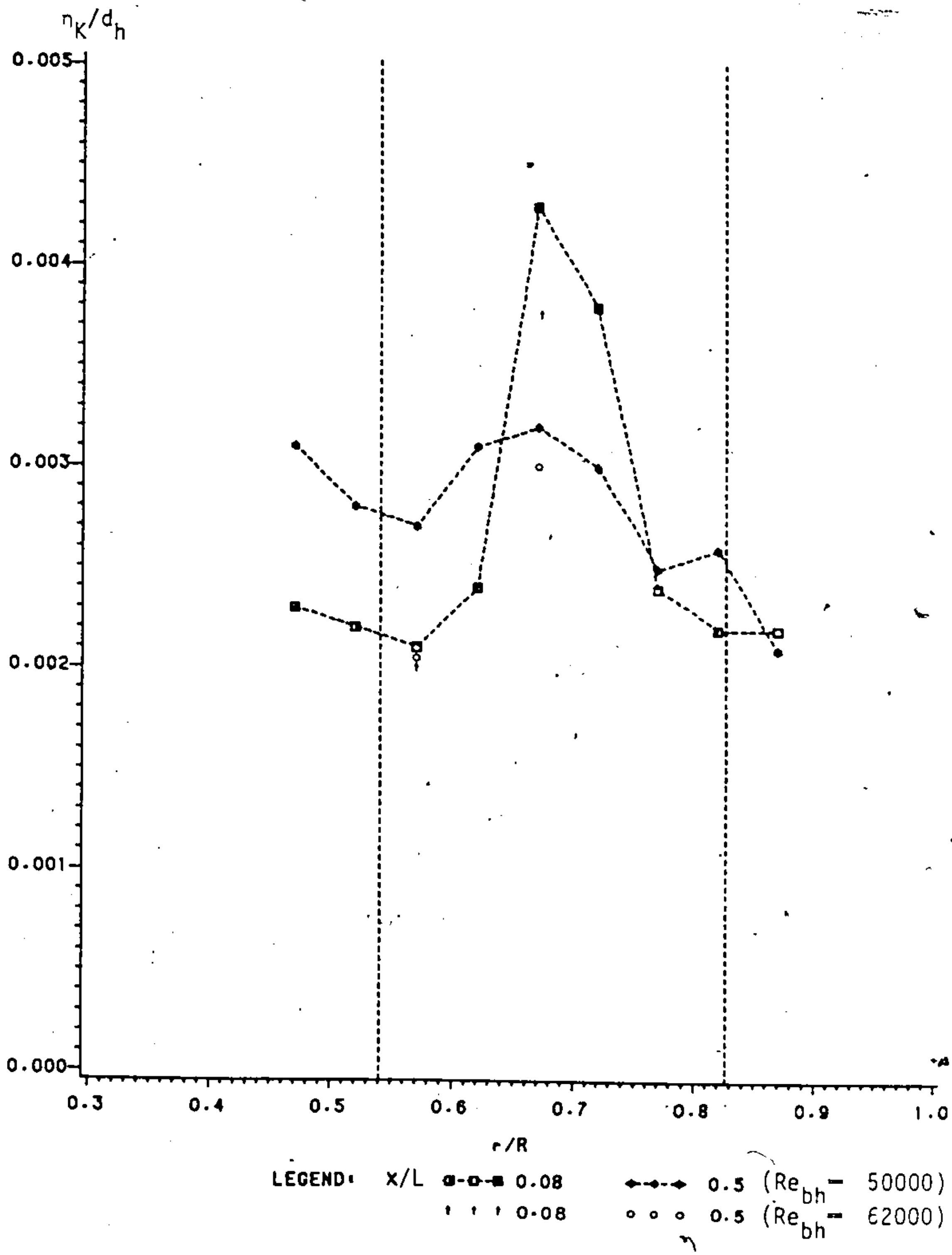

Figure 84 Variation of Kolmogoroff's length scale along the test-section radial axis.

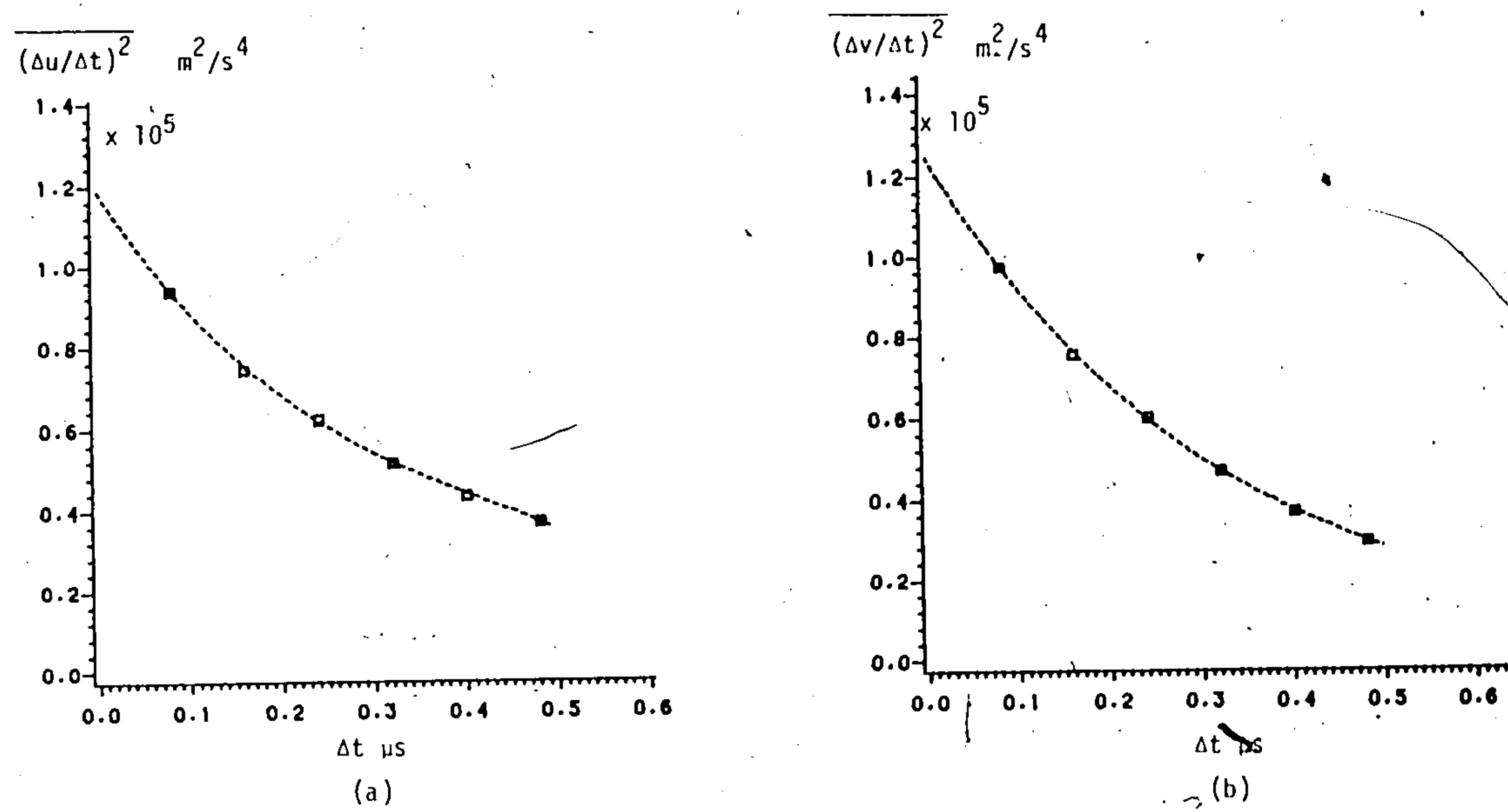

Figure 85 Sampling time dependence of velocity time derivative ($r/R = 0.67$, $x/L = 0.50$, $Re_{bh} = 50000$).

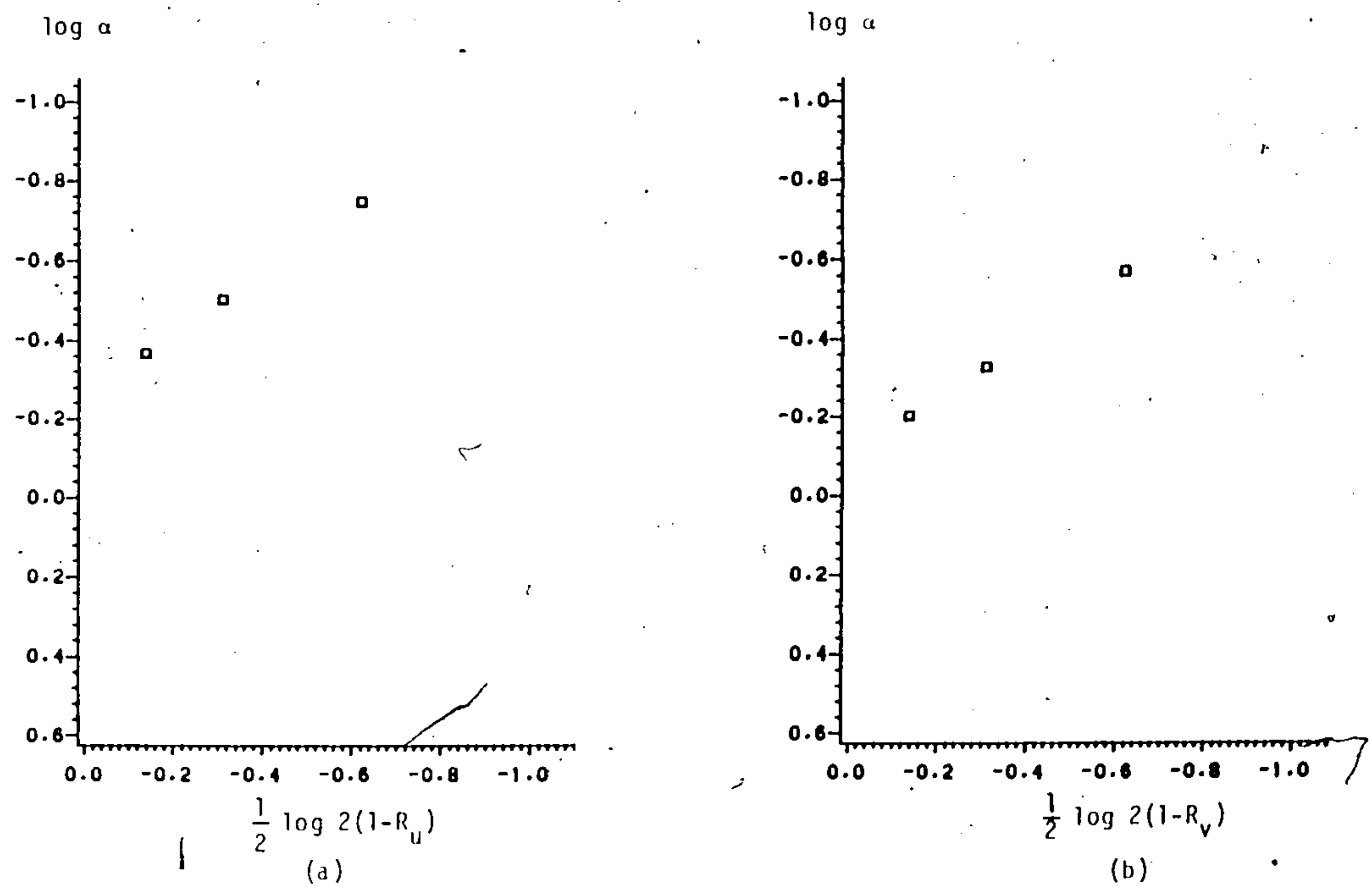

Figure 86 Sampling distance dependence of autocorrelation coefficient
(r/R 0.67, x/L = 0.50, Re_{bh} = 50000).